# Shear Resistance of Circular Concrete-Filled Steel Tubes

Ashley E. Heid

A thesis
submitted in partial fulfillment of the
requirements for the degree of

Master of Science in Civil Engineering

University of Washington

2016

Committee:
Charles W. Roeder
Dawn E. Lehman
Jeffrey W. Berman

Program Authorized to Offer Degree:
Department of Civil and Environmental Engineering

©Copyright 2016
Ashley E. Heid

University of Washington

**Abstract**

Shear Resistance of Circular Concrete-Filled Steel Tubes

Ashley E. Heid

Co-Chairs of the Supervisory Committee:
Professor Charles W. Roeder
Civil and Environmental Engineering

Professor Dawn E. Lehman
Civil and Environmental Engineering

Concrete-filled steel tubes (CFSTs) and reinforced concrete-filled steel tubes (RCFSTs) are used throughout the world in tall buildings and bridges. They are becoming increasingly popular in the United States transportation sector as bridge piers, piles, or shafts where lateral spreading and liquefaction potentials can create large shear demands that control member design. Prior research indicates that CFSTs have superior strength, stiffness, and inelastic deformation capacity compared to their reinforced concrete and structural steel counterparts. This has been well defined for flexural and axial behavior; however, few studies have been done to assess the shear carrying capacity of these members. For design, most provisions either reference one of the two materials, steel and concrete, or some combination of the two, without acknowledging the increased capacity that comes from their interaction.

Past research has been performed on small diameter CFSTs ($\sim 6$ *in.*) that has shown these methods greatly underestimate shear resistance. This program extends this knowledge with the experimental testing of larger-scale CFSTs (20 *in.* in diameter) and the development of a finite element model, validated against these tests, that was used for further

parametric studies. The experimental study varied parameters including aspect ratio ($a/D$), diameter-to-thickness ratio ($D/t$), concrete compressive strength, tube type, tail length, internal reinforcement, and interface condition. Parameter studies then expanded this data set to include variation in tube steel yield strength and axial load ratio ($P/P_0$). The results from these investigations, and prior research studies, were used to develop limit state criterion and quantify shear capacity with a new design expression incorporating the composite nature of all components and enhanced properties due to axial load.

# TABLE OF CONTENTS

Page

List of Figures . . . . . vi

List of Tables . . . . . xiii

Chapter 1: Introduction . . . . . 1
1.1 Concrete-Filled Steel Tubes . . . . . 1
1.2 Research Program and Objectives . . . . . 2
1.3 Report Overview . . . . . 3

Chapter 2: Literature Review and Current Design Provisions . . . . . 4
2.1 Introduction . . . . . 4
2.2 Current Design Provisions . . . . . 4
2.2.1 Summary of Available Provisions . . . . . 4
2.2.2 Axial and Flexural Capacities . . . . . 5
2.2.3 Shear Capacity . . . . . 9
2.3 Previous Experimental Research on Shear Capacity of CFSTs . . . . . 11
2.3.1 Summary of Programs to be Evaluated . . . . . 11
2.3.2 Previous Research Results and Conclusions . . . . . 16
2.3.3 Comparison of Previous Research to Current Shear Provisions . . . . 27
2.3.4 Assessment of Experimental Specimens and Setups . . . . . 29
2.4 Previous Analytical Modeling of CFSTs . . . . . 31
2.4.1 Summary of Available Analytical Programs . . . . . 31
2.4.2 Bending and Combined Loading of Circular CFSTs - Moon et al. (2012, 2013) . . . . . 31
2.4.3 Cyclic Behavior of Circular Steel Columns with In-Filled Concrete - Goto et al. (2010) . . . . . 34

2.4.4 Finite Element Modeling of CFSTs Subjected to Constant Axial Compression and Shear Loads - Han et al. (2008) . . . 36

Chapter 3: Experimental Program Summary . . . 38
3.1 Introduction . . . 38
3.2 Experimental Setup and Procedure . . . 38
3.3 Test Matrix . . . 46
3.3.1 Specimens . . . 46
3.3.2 Materials . . . 49
3.4 Results . . . 51
3.4.1 Specimen Failure . . . 51
3.4.2 Failure Mode Characteristics . . . 56
3.4.2.1 Flexural Failure in CFST . . . 60
3.4.2.2 Shear Failure in CFST . . . 68
3.4.2.3 Flexure-Shear Interaction in CFST . . . 71
3.4.2.4 Significant Bond Slip in CFST . . . 76
3.4.3 Additional Specimens of Interest . . . 83
3.4.3.1 Specimen 5 - CFST with muddy interface . . . 83
3.4.3.2 Specimen 12 - RCFST . . . 86
3.4.3.3 Specimen 13 - CFST with axial load . . . 89
3.4.3.4 Specimen 21 - Steel tube with gravel fill . . . 92
3.5 Parameter Influence . . . 95
3.5.1 Composite Action due to Tail Length, $L_T$, and Steel-Concrete Interface Condition . . . 95
3.5.2 Comparison of RCFST and CFST, $\rho_{int}$ . . . 99
3.5.3 Effect of Concrete Strength, $f'_c$ . . . 100
3.5.4 Shear Span to Depth Ratio, $a/D$ . . . 101

Chapter 4: Analytical Model . . . 103
4.1 Introduction . . . 103
4.2 Model Description . . . 104
4.2.1 Base Model . . . 104
4.2.1.1 General Approach to Problem . . . 105
4.2.1.2 CFST . . . 105

4.2.1.3 Test Setup . . . 112
4.2.1.4 Base Model Results . . . 119
4.2.2 Modeling Issues . . . 126
4.2.3 Refined Base Model . . . 130
4.2.3.1 Large Strain Approach . . . 131
4.2.3.2 Remove Cotton Duck Bearing Pads . . . 132
4.2.3.3 Replace Support Setup with Springs . . . 133
4.2.3.4 Concrete Confinement . . . 134
4.2.3.5 Refined Base Model Summary . . . 136
4.3 Model Validation . . . 138

Chapter 5: Parameter Studies . . . 140
5.1 Introduction . . . 140
5.2 Axial Load Ratio, $P/P_0$ . . . 141
5.3 Tube Diameter to Thickness Ratio, $D/t$ . . . 147
5.4 CFST Materials . . . 152
5.4.1 Concrete Strength, $f'_c$ . . . 152
5.4.2 Tube Steel Yield Strength, $F_{yt}$ . . . 157
5.5 Internal Reinforcement Ratio, $\rho_{int}$ . . . 162

Chapter 6: Proposed Design Expression . . . 168
6.1 Introduction . . . 168
6.2 Equation Development Utilizing Experimental Results . . . 170
6.2.1 Proposed Limit State Criterion . . . 170
6.2.2 Tube Steel Contribution . . . 172
6.3 Equation Development Utilizing Parameter Studies . . . 172
6.3.1 Internal Reinforcement Contribution . . . 172
6.3.2 Concrete Contribution . . . 174
6.4 Proposed Design Expression, $V_{n(prop)}$ . . . 176
6.4.1 Comparison of $V_{n(prop)}$ to Experimental Results . . . 177
6.4.2 Comparison of $V_{n(prop)}$ to Analytical Results . . . 179
6.4.3 Assessment of RCFSTs with $V_{n(prop)}$ . . . 180
6.4.4 Comparison of $V_{n(prop)}$ to All Data . . . 181

6.4.5 Summary of Component Contributions According to $V_{n(prop)}$ . . . . . 183

Chapter 7: Conclusions and Future Work . . . . . 187
7.1 Summary . . . . . 187
7.2 Conclusions . . . . . 187
7.2.1 Proposed Limit State Criterion and Design Expression . . . . . 187
7.2.2 Experimental Results . . . . . 190
7.2.3 Parameter Studies . . . . . 192
7.3 Future Work . . . . . 193
7.3.1 Experiments . . . . . 193
7.3.2 Analytical Modeling . . . . . 194

References . . . . . 196

Appendix A: NOTATION LIST . . . . . 201

Appendix B: Experimental Test Rig . . . . . 202

Appendix C: Supplementary Experimental Data Calculations . . . . . 206
C.1 Specimen Deflection Target Locations . . . . . 206
C.2 Optotrak Data Correction . . . . . 207
C.2.1 Step 1: Fill Gaps . . . . . 208
C.2.2 Step 2: Smooth Spikes and Plateaus . . . . . 210
C.2.3 Filtering Results . . . . . 212
C.2.4 MATLAB Script . . . . . 214
C.3 Match Optotrak and LabVIEW Data . . . . . 221
C.3.1 MATLAB Script . . . . . 222
C.4 CFST Deflection Correction Procedure . . . . . 226
C.4.1 MATLAB Script . . . . . 230

Appendix D: Further Validation of Analytical Model . . . . . 235
D.1 Shear Force vs. Vertical Deflection . . . . . 236
D.2 Shear Force vs. Relative Displacement . . . . . 238
D.3 Local Behaviors . . . . . 242

Appendix E: Supplementary Parameter Study Results . . . 249
E.1 Axial Load Ratio, $P/P_0$ . . . 250
E.1.1 Model Details and Results . . . 250
E.1.2 Shear Force vs. Vertical Deflection . . . 251
E.2 Tube Diameter to Thickness Ratio, $D/t$ . . . 252
E.2.1 Model Details and Results . . . 252
E.2.2 Shear Force vs. Vertical Deflection . . . 253
E.3 Concrete Strength, $f'_c$ . . . 255
E.3.1 Model Details and Results . . . 255
E.3.2 Shear Force vs. Vertical Deflection . . . 256
E.4 Tube Steel Yield Strength, $F_{yt}$ . . . 258
E.4.1 Model Details and Results . . . 258
E.4.2 Shear Force vs. Vertical Deflection . . . 259
E.5 Internal Reinforcement Ratio, $\rho_{int}$ . . . 261
E.5.1 Model Details and Results . . . 261
E.5.2 Shear Force vs. Vertical Deflection . . . 262

Appendix F: Design Expression Results . . . 264
F.1 Linear Regression of Shear Controlled Models . . . 264
F.1.1 Axial Load Ratio, $P/P_0$ . . . 265
F.1.2 Tube Diameter to Thickness Ratio, $D/t$ . . . 266
F.1.3 Concrete Strength, $f'_c$ . . . 267
F.1.4 Tube Steel Yield Strength, $F_{yt}$ . . . 268
F.1.5 Internal Reinforcement Ratio, $\rho_{int}$ . . . 269
F.1.6 Summary of Fit Lines . . . 270
F.2 Equation Evaluation Results for All Models . . . 271

# LIST OF FIGURES


Figure Number Page

2.1 Methods for Predicting CFST Resistance . . . 6
2.2 Geometry used for Closed-Form CFST PSDM Derivation . . . 7
2.3 Geometry used for Closed-Form RCFST PSDM Derivation . . . 8
2.4 Effect of End Caps on CFST Specimen Behavior (Xu et al., 2009) . . . 21
2.5 $V_c/(f_{ct}A_c)$ vs. $a/D$ (or $\lambda$) (Qian et al., 2007) . . . 24
2.6 Shear Force vs. Deflection Behaviors of CFST Specimens with Varying $D/t$ and Concrete Strength (Qian et al., 2007) . . . 24
2.7 Validation of Model by Moon et al. (2012) with Simulated and Observed Local Behaviors . . . 32
2.8 Validation of Model by Moon et al. (2012) with Moment vs. Drift Relationships . . . 33
2.9 Validation of Model by Goto et al. (2010) with Hysteretic Behaviors . . . 35
2.10 Validation of Model by Han et al. (2008) with Select Experimental Data Sets 37

3.1 Schematic of Experimental Apparatus . . . 39
3.2 Experimental Apparatus Details . . . 41
3.3 In-Place Experimental Apparatus . . . 42
3.4 Typical Experiment Instrumentation . . . 44
3.5 Optotrak Layout for $a/D = 1.0$ . . . 45
3.6 Optotrak Layout for $a/D = 0.5$ . . . 45
3.7 Optotrak Layout for $a/D = 0.375$ . . . 46
3.8 Optotrak Layout for $a/D = 0.25$ . . . 46
3.9 Deformed Geometry of Experimental Apparatus . . . 52
3.10 Shear Span Deformation . . . 53
3.11 Failure Mode Results . . . 58
3.12 Characteristics of Flexural Failure Mode in CFSTs (as demonstrated by Specimen 17) . . . 61
3.13 Specimen 17 Normalized Shear vs. Vertical Deflection Behavior . . . 63

3.14 Specimen 17 Normalized Moment vs. Vertical Deflection Behavior . . . . . 63
3.15 Specimen 1 Photos . . . . . 64
3.16 Specimen 1 Normalized Shear vs. Vertical Deflection Behavior . . . . . 65
3.17 Specimen 1 Normalized Moment vs. Vertical Deflection Behavior . . . . . 65
3.18 Specimen 2 Photos . . . . . 66
3.19 Specimen 2 Normalized Shear vs. Vertical Deflection Behavior . . . . . 67
3.20 Specimen 2 Normalized Moment vs. Vertical Deflection Behavior . . . . . 67
3.21 Characteristics of Shear Failure Mode in CFSTs (as demonstrated by Specimen 14 and *Specimen 8) . . . . . 68
3.22 Specimen 14 Tear in Top of Steel Tube . . . . . 69
3.23 Specimen 14 Normalized Shear vs. Vertical Deflection Behavior . . . . . 70
3.24 Specimen 14 Normalized Moment vs. Vertical Deflection Behavior . . . . . 70
3.25 Characteristics of Flexure-Shear Behavior in CFSTs (as demonstrated by Specimen 10) . . . . . 71
3.26 Specimen 10 Normalized Shear vs. Vertical Deflection Behavior . . . . . 72
3.27 Specimen 10 Normalized Moment vs. Vertical Deflection Behavior . . . . . 73
3.28 Specimen 16 Photos . . . . . 74
3.29 Specimen 16 Normalized Shear vs. Vertical Deflection Behavior . . . . . 75
3.30 Specimen 16 Normalized Moment vs. Vertical Deflection Behavior . . . . . 75
3.31 Characteristics of Bond Slip Behavior in CFSTs . . . . . 77
3.32 Specimen 9 Deformed State of Steel Tube . . . . . 78
3.33 Specimen 9 Normalized Shear vs. Vertical Deflection Behavior . . . . . 79
3.34 Specimen 9 Normalized Moment vs. Vertical Deflection Behavior . . . . . 79
3.35 Specimen 11 Photos . . . . . 81
3.36 Specimen 11 Normalized Shear vs. Vertical Deflection Behavior . . . . . 82
3.37 Specimen 11 Normalized Moment vs. Vertical Deflection Behavior . . . . . 82
3.38 Specimen 5 Photos . . . . . 84
3.39 Specimen 5 Normalized Shear vs. Vertical Deflection Behavior . . . . . 85
3.40 Specimen 5 Normalized Moment vs. Vertical Deflection Behavior . . . . . 85
3.41 Placement of reinforcement steel cage in RCFST prior to casting . . . . . 86
3.42 RCFST (Specimen 12) vs. CFST (Specimen 2) Photos . . . . . 87
3.43 Specimen 12 Normalized Shear vs. Vertical Deflection Behavior . . . . . 88
3.44 Specimen 12 Normalized Moment vs. Vertical Deflection Behavior . . . . . 88

3.45 Specimen 13 Photos . . . 90
3.46 Specimen 13 Normalized Shear vs. Vertical Deflection Behavior . . . 91
3.47 Specimen 13 Normalized Moment vs. Vertical Deflection Behavior . . . 91
3.48 Specimen 21 Photos . . . 93
3.49 Specimen 21 Normalized Shear vs. Vertical Deflection Behavior . . . 94
3.50 Specimen 21 Normalized Moment vs. Vertical Deflection Behavior . . . 94
3.51 Composite Action Specimens Comparisons . . . 98

4.1 Typical ABAQUS Base Model . . . 104
4.2 Tube Steel Stress vs. Strain Relationship by Moon et al. (2012) . . . 106
4.3 Base ABAQUS Model Tube Steel Stress vs. Strain Relationship (Specimen 17, $a/D = 0.5$) . . . 107
4.4 Concrete Uniaxial Stress vs. Strain Behavior (Specimen 17, $a/D = 0.5$) . . . 108
4.5 Concrete Damaged Plasticity Parameter Influence on Yield Function (Dassault Systemes Simulia Corp., 613) . . . 110
4.6 Concrete Damaged Plasticity Parameter Influence on Flow Rule . . . 111
4.7 Simulated Test Setup Movement * Note that the cotton duck is not visible here

and that the 'mirror' effect was used to create this image, as only one-quarter of the test is actually modeled. . . . 113
4.8 Cradle to CFST Tube Surfaces for ABAQUS Interaction Definition . . . 115
4.9 Loading Procedure in ABAQUS Model . . . 116
4.10 Support Cradle Sliding Surface in ABAQUS Model . . . 117
4.11 Elastomeric Bearing and Cotton Duck Pads in ABAQUS Model . . . 118
4.12 Measured, $V_{ed}$, and Predicted Normalized Normalized Shear vs. Vertical Deflection for Flexurally Dominated Specimen using Base Model (Specimen 17, $a/D = 0.5$) . . . 120
4.13 Observed and Simulated Local Behaviors of Flexurally Dominated Specimen using Base Model (Specimen 17, $a/D = 0.5$) . . . 122
4.14 Measured, $V_{ed}$, and Predicted Normalized Shear vs. Vertical Deflection for Shear Yielding Specimen using Base Model (Specimen 16, $a/D = 0.375$) . . . 124
4.15 Observed and Simulated Local Behaviors of Shear Yielding Specimen using Base Model (Specimen 16, $a/D = 0.375$) . . . 125
4.16 Illustration of Symmetry Issue in Analytical Models . . . 127
4.17 Experiment Nonlinear Setup Deformations . . . 129

4.18 Measured and Predicted Normalized Shear vs. Vertical Deflection for Shear Yielding Specimen using Refined Base Model (Specimen 16, $a/D = 0.375$) . 131
4.19 Measured and Predicted Normalized Shear vs. Vertical Deflection for Shear Yielding Specimen with Cotton Duck Removal (Specimen 16, $a/D = 0.375$ ABAQUS model) . . . . . 133
4.20 Illustration of the Final Model Boundary Conditions . . . . . 134
4.21 Concrete Stress vs. Strain Behavior (Specimen 17, $a/D = 0.5$ model) . . . . 136

5.1 Application of Axial Load in ABAQUS Simulations . . . . . 142
5.2 Illustration of Predicted Moment, $M_{pr}$, for Following Figures ($a/D = 0.375$) 143
5.3 Variation of Axial Load Ratio vs. Normalized Maximum Moment . . . . . 144
5.4 $V_{prmax}$ vs. Axial Load Ratio . . . . . 145
5.5 $\eta$ vs. Axial Load Ratio for Axial Load Ratio Study . . . . . 146
5.6 Bilinear Relationship of $\eta$ vs. Axial Load Ratio for $a/D = 0.375$ Model in Figure 5.5 . . . . . 146
5.7 Variation of Axial Load Ratio vs. Normalized Maximum Moment with Different $D/t$ Ratios . . . . . 149
5.8 $V_{prmax}$ vs. Axial Load with Different $D/t$ Ratios . . . . . 150
5.9 $\eta$ vs. Axial Load Ratio with Different $D/t$ Ratios . . . . . 151
5.10 Variation of Axial Load Ratio vs. Normalized Maximum Moment with Different Concrete Strengths, $f'_c$ . . . . . 154
5.11 $V_{prmax}$ vs. Axial Load Ratio with Different Concrete Strengths, $f'_c$ . . . . . 155
5.12 $\eta$ vs. Axial Load Ratio with Different Concrete Strengths, $f'_c$ . . . . . 156
5.13 Variation of Axial Load Ratio vs. Normalized Maximum Moment with Different Tube Steel Strengths, $F_{yt}$ . . . . . 158
5.14 $V_{prmax}$ vs. Axial Load Ratio with Different Tube Steel Strengths, $F_{yt}$ . . . . 159
5.15 $\eta$ vs. Axial Load Ratio with Different Tube Steel Strengths, $F_{yt}$ . . . . . 161
5.16 Illustration of Rebar Layout in ABAQUS Simulation . . . . . 163
5.17 Variation of Axial Load Ratio vs. Normalized Maximum Moment with Different Internal Reinforcement Ratios, $\rho_{int}$ . . . . . 164
5.18 $V_{prmax}$ vs. Axial Load Ratio with Different Internal Reinforcement Ratios, $\rho_{int}$ 165
5.19 $\eta$ vs. Axial Load Ratio for CFST with Different Internal Reinforcement Ratios, $\rho_{int}$ . . . . . 167

6.1 Increase in $V_{prmax}$ with Increasing Steel Area from $D/t$ Parametric Study . 173

6.2 Increase in $V_{prmax}$ with Increasing Internal Reinforcement Area from $\rho_{int}$ Parametric Study . . . 173
6.3 Example of Least Squares Linear Regression Fit Line using CFST having: $D/t = 80$, $f'_c = 6\ ksi$, $F_{yt} = 56.8\ ksi$, and $\rho_{int} = 0\%$ . . . 175
6.4 Comparison of $\eta = 5\,(1 + 5 \cdot P/P_0) \leq 10$ to Shear Controlled Models, Meeting Proposed Limit State Criterion . . . 176
6.5 Comparison of $V_{n(prop)}$ to Experimental Results Meeting Proposed Limit State Criterion, Including Axial Load . . . 178
6.6 Comparison of $V_{n(prop)}$ to Shear Controlled Models, Meeting Limit State Criterion . . . 179
6.7 Comparison of $V_{n(prop)}$ to Experimental and Analytical RCFST Shear Specimens, Meeting Proposed Limit State Criterion . . . 181
6.8 Comparison of $V_{n(prop)}$ to Experimental and Analytical Shear Specimens, Meeting Proposed Limit State Criterion . . . 182
6.9 Contribution of Tube Steel, Internal Reinforcement, and Concrete to Total Shear Resistance According to $V_{n(prop)}$ . . . 184
6.10 Contribution of Tube Steel, Internal Reinforcement, and Concrete to Total Shear Resistance According to $V_{n(prop)}$ using All Data . . . 185
6.11 Contribution of Tube Steel, Internal Reinforcement, and Concrete to Total Shear Resistance According to $V_{n(prop)}$ using Typical CFST Design . . . 186

B.1 Support Cradle . . . 202
B.2 Elastomeric Bearing . . . 203
B.3 Load Cradle . . . 203
B.4 Steel Base . . . 204
B.5 Steel Base Assembly . . . 205

C.1 Illustration of Targets used for Deflection in Force-Displacement Plots in Chapter 3 (as demonstrated by the Optotrak layout for a/D = 0.375) . . . 206
C.2 Sample Correction for Gaps in Raw Data . . . 209
C.3 Sample Correction for Spikes and Plateaus in Raw Data . . . 211
C.4 Sample of Data after Complete Data Filtering . . . 213
C.5 Illustration of Placement of Optotrak Data Origin for Subsequent Calculations 222
C.6 Illustration of Procedure for Elastomeric Bearing and Steel Base Correction (as demonstrated by the Optotrak layout for a/D = 0.25) . . . 228

C.7 Illustration of Targets used for CFST Deflection Correction in MATLAB Script (as demonstrated by the Optotrak layout for a/D = 0.375) . . . . . 230

D.1 Measured, $V_{ed}$, and Predicted Normlaized Shear vs. Vertical Deflection . . . 237

D.2 Illustration of Locations of Points for Relative Displacement Calculation in Simulation and Experiments . . . . . 239

D.3 Illustration of Points used For Calculation in Equations D.1 and D.2 . . . . 240

D.4 Measured, $V_{ed}$, and Predicted Normalized Shear vs. Relative Displacement . 241

D.5 Observed and Simulated Local Behaviors of Flexurally Dominated Specimen (Specimen 1, a/D = 1.0) . . . . . 243

D.6 Observed and Simulated Local Behaviors of Flexurally Dominated Specimen (Specimen 17, a/D = 0.5) . . . . . 244

D.7 Observed and Simulated Local Behaviors of Flexurally Dominated Specimen (Specimen 2, a/D = 0.5) . . . . . 245

D.8 Observed and Simulated Local Behaviors of Shear Yielding Specimen (Specimen 16, a/D = 0.375) . . . . . 246

D.9 Observed and Simulated Local Behaviors of Shear Yielding Specimen (Specimen 10, a/D = 0.375) . . . . . 247

D.10 Observed and Simulated Local Behaviors of Shear Dominated Specimen (Specimen 14, a/D = 0.25) . . . . . 248

E.1 Variation of Normalized Predicted Shear Force vs. Normalized Vertical Deflection with Axial Load Ratio for CFST with $a/D = 0.375$ . . . . . 251

E.2 Variation of Normalized Predicted Shear Force vs. Normalized Vertical Deflection with Axial Load Ratio for CFST with $a/D = 0.25$ . . . . . 251

E.3 Variation of Normalized Predicted Shear Force vs. Normalized Vertical Deflection with Axial Load and $D/t$ Ratios for CFST with $a/D = 0.375$ . . . . 253

E.4 Variation of Normalized Predicted Shear Force vs. Normalized Vertical Deflection with Axial Load and $D/t$ Ratios for CFST with $a/D = 0.25$ . . . . . 254

E.5 Variation of Normalized Predicted Shear Force vs. Normalized Vertical Deflection with Axial Load Ratio and Concrete Strength, $f'_c$, for CFST with $a/D = 0.375$ . . . . . 256

E.6 Variation of Normalized Predicted Shear Force vs. Normalized Vertical Deflection with Axial Load Ratio and Concrete Strength, $f'_c$, for CFST with $a/D = 0.25$ . . . . . 257

E.7 Variation of Normalized Predicted Shear Force vs. Normalized Vertical Deflection with Axial Load Ratio and Steel Tube Strength, $F_{yt}$, for CFST with $a/D = 0.375$ . . . . . 259
E.8 Variation of Normalized Predicted Shear Force vs. Normalized Vertical Deflection with Axial Load Ratio and Steel Tube Strength, $F_{yt}$, for CFST with $a/D = 0.25$ . . . . . 260
E.9 Variation of Normalized Predicted Shear Force vs. Normalized Vertical Deflection with Axial Load Ratio and Internal Reinforcement Ratio, $\rho_{int}$, for CFST with $a/D = 0.375$ . . . . . 262
E.10 Variation of Normalized Predicted Shear Force vs. Normalized Vertical Deflection with Axial Load Ratio and Internal Reinforcement Ratio, $\rho_{int}$, for CSFT with $a/D = 0.25$ . . . . . 263
F.1 Least Squares Linear Regression with Different Axial Load Ratios, $P/P_0$ . . 265
F.2 Least Squares Linear Regression with Different $D/t$ Ratios . . . . . 266
F.3 Least Squares Linear Regression with Different Concrete Strengths, $f'_c$ . . . 267
F.4 Least Squares Linear Regression with Different Tube Steel Strengths, $F_{yt}$ . . 268
F.5 Least Squares Linear Regression with Different Internal Reinforcement Ratios, $\rho_{int}$ . . . . . 269

# LIST OF TABLES


Table Number Page

2.1 Previous Experimental Research Summary . . . 12
2.2 Summary of Specimens and Results (Xiao et al., 2012) . . . 16
2.3 Summary of Specimens and Results (Xu et al., 2009) . . . 20
2.4 Summary of Specimens and Results (Qian et al., 2007) . . . 23
2.5 Summary of Specimens and Results (Nakahara and Tokuda, 2012) . . . 25
2.6 Summary of Specimens and Results (Ye et al., 2016) . . . 26
2.7 Results using AISC Method 1, without Axial Load or Expansive Concrete . 27
2.8 Results using AISC Method 2, without Axial Load or Expansive Concrete . 28
2.9 Results using WSDOT Method (prior to 2016 BDM), without Axial Load or Expansive Concrete . . . 28

3.1 Test Matrix . . . 48
3.2 CFST Material Properties . . . 50
3.3 CFST Reinforcing Bar Material Properties . . . 50
3.4 Moment and Shear Test Results . . . 55
3.5 Specimen Failure Mode Classification . . . 59
3.6 Composite Action Series Specimen Summary . . . 96
3.7 RCFST Series Specimen Summary . . . 99
3.8 Concrete Strength Series Specimen Summary . . . 101
3.9 Shear Span to Depth Ratio Series Specimen Summary . . . 102

4.1 Summary of Specimens used for Analytical Model Validation . . . 103
4.2 Concrete Damaged Plasticity Parameters . . . 111
4.3 Elastomeric Bearing and Cotton Duck Spring Stiffnesses ($kips/in.$) in ABAQUS . . . 118
4.4 Base Model Maximum Shear Force Results for Flexurally Dominated Specimen (Specimen 17, $a/D = 0.5$) . . . 120

4.5 Base Model Maximum Shear Force Results for Shear Yielding Specimen Specimen (Specimen 16, $a/D = 0.375$) . . . 123
4.6 Refined Base Model Maximum Shear Force Results for Shear Yielding Specimen (Specimen 16, $a/D = 0.375$) . . . 130
4.7 Summary of Error in Predicted Ultimate Shear Resistance . . . 139

5.1 Base CFST Properties in Axial Load Parameter Study . . . 142
5.2 Base CFST Properties in D/t Parameter Study . . . 147
5.3 Base CFST Properties in $f'_c$ Parameter Study . . . 152
5.4 Base CFST Properties in $F_{yt}$ Parameter Study . . . 157
5.5 Base CFST Properties in $\rho_{int}$ Parameter Study . . . 163

6.1 Results using AISC Method 1 for Reported Shear Failures, without Axial Load or Expansive Concrete, by UW and Others . . . 168
6.2 Results using AISC Method 2 for Reported Shear Failures, without Axial Load or Expansive Concrete, by UW and Others . . . 169
6.3 Results using WSDOT Method (prior to 2016 BDM) for Reported Shear Failures, without Axial Load or Expansive Concrete, by UW and Others . . . 169
6.4 Summary of Specimens Meeting Proposed Limit State Criterion used for $V_{n(prop)}$ Analysis . . . 178
6.5 Statistical Evaluation of $V_{n(prop)}$ for Specimens Meeting Proposed Limit State Criterion, Including Axial Load . . . 179
6.6 Statistical Evaluation of $V_{n(prop)}$ for Shear Controlled Models, Meeting Limit State Criterion . . . 180
6.7 Statistical Evaluation of $V_{n(prop)}$ for Experimental and Analytical RCFST Shear Specimens, Meeting Proposed Limit State Criterion . . . 181
6.8 Statistical Evaluation of $V_{n(prop)}$ for Experimental and Analytical Shear Specimens, Meeting Proposed Limit State Criterion . . . 182

C.1 Summary of Targets used for Force-Deflection Plots in Chapters 3, 4, and Appendix D . . . 207

D.1 Summary of Specimens used for Analytical Model Validation . . . 235

E.1 Summary of Models for $P/P_0$ Study . . . 250
E.2 Summary of Models for $D/t$ Study . . . 252
E.3 Summary of Models for $f'_c$ Study . . . 255
E.4 Summary of Models for $F_{yt}$ Study . . . 258

E.5 Summary of Models for Internal Reinforcement Ratio, $\rho_{int}$, Study . . . . . 261
F.1 Summary of Fit Lines for Models with $M_{pr}/M_{PSDM} < 1.1$ and $P/P_0 \leq 0.2$ . 270
F.2 Previous Experimental Research Summary . . . . . 272

# ACKNOWLEDGMENT

I would first like to thank my advisors, Professor Charles Roeder and Professor Dawn Lehman, for their continued support and guidance throughout the completion of this work. Each provided me invaluable counsel, with their diverse knowledge and experience, on a one-on-one basis, and as a team, that gave me the encouragement to push through. I would also like to thank Professor Jeff Berman for taking the time to give constructive input to this project as part of my reading committee.

Furthermore, thank you to the Washington State Department of Transportation for their support and funding of this research. Mr. Bijan Khalieghi and his team provided the practical knowledge and advice that helped form this project to be relevant to structural engineering work today.

However, before this research program gave me the opportunity to work among these talented individuals, the Valle Scholarship and Scandinavian Exchange Program is to be credited for affording me the opportunity to come to the University of Washington. I am honored to be called a Valle scholar.

In addition to the support of the professors and programs though, several other individuals had a large hand in helping to complete this work. This help included: Vince Chaijaroen's time, training, and exhaustive efforts in the lab; Todd Maki's collaboration and knowledge that set the groundwork for my continuation of the project; Max Stephens's continuous advice and efforts both in the lab and throughout analyses; and numerous undergraduates' laborious work alongside Todd and I in the lab. Thank you Becky Gilbertson, Truc Thai, Marisa Gelms, Nate Clemens, and Anthony Gasca.

And finally to my family and friends, because of your support during this period and

beyond, I have achieved so much. These victories are yours and mine. I'm so thankful to have my family's never-wavering encouragement throughout the evolutions in life that bring us both near and far from each other. My sisters, brother, and I are very lucky to have parents that work so hard to afford us so many of these opportunities. Andrea Meza, my BFF4LYFE, for the last 14 years and the remaining to come, you will always give me the strength through example to continue to make goals and see them through to completion.

To my fellow grad students, particularly those in More 109C, thank you for the laughs, the patience, and the camaraderie. (Shout out to the Chambray Squad.) Your intelligence and hard work kept me motivated through this entire process. My Core Crew, Kristina Tsvetanova, 'Kray-K', the Bulgarian princess, and Tianye Yang, 'T-Yay', my fellow summer warrior, was there with me from day one to what feels like day 1,000 at times, and I am eternally grateful for their friendship. And to the Extended Crew, Andrew Winter, 'A-Dubs', and Ryan Ganey, the 'Lil' King', thanks for being with us through the thick and thin of grad school, with the sarcasm and laughter along the ride that I value so much. Ryan, you da, you da best.

# Chapter 1

# INTRODUCTION

## *1.1 Concrete-Filled Steel Tubes*

Concrete-filled steel tubes (CFSTs) offer superior strength and ductility to the design of building and transportation structures throughout the world as beams, columns, braces, truss elements, and foundation components. The combination of steel and concrete create an efficient and economical solution to structural engineering problems. CFSTs utilize the strengths of each individual material in typical design applications and when together, improve upon each others' weaknesses. Steel is highly ductile and very strong in tension, while concrete has a very high compressive strength. In a composite CFST, the concrete fill restrains the tube from local buckling, and the steel tube confines the concrete fill and prevents spalling. Added strength then comes from the potential for composite action to develop by chemical bond, mechanical interlock, and/or binding action. This combination results in high stiffness, strength, and large inelastic deformation capacities. Additional benefits of CFSTs are their rapid construction and cost cutting capabilities with the steel tube acting as formwork and shoring during placement, and the elimination of the need for internal reinforcement bars or vibration of concrete.

CFSTs can be constructed with either rectangular or circular steel tubes. Research by Roeder et al. (2009) showed that circular tubes provide better concrete confinement and better bond stress between the tube and concrete fill, both improving the composite performance of the member. Reinforced concrete-filled steel tubes (RCFSTs) are also used when connections to other reinforced concrete members, or other design limitations require.

While the axial and flexural properties of CFSTs have been well researched, little research has been done on the shear resistance and behaviors of CFSTs and RCFSTs. Currently,

AISC, ACI, AASHTO, and WSDOT all include provisions for the determination of shear resistance. Each either uses the noncomposite shear capacity of one of the components of the CFST, or some combination of them, without recognizing the increased load carrying capacity from composite action. For this reason, current provisions significantly underestimate the shear resistance of CFSTs, resulting in unnecessary cost and conservatism, particularly in foundation systems.

The stiffness, strength, ductility, and efficient constructability of CFSTs make them attractive alternatives to conventional reinforced concrete bridge piers and deep foundations. In a deep pile or shaft though, lateral spreading and liquefaction in high seismic regions can create large transverse forces between thin soil layers. Because of the current limitations on predicted shear resistance of CFSTs, these foundation systems often are designed overly conservative.

The limited prior research on the shear resistance of CFSTs was performed in Japan and China, where they are frequently used in construction. In the United States, CFSTs are underutilized due to the lack of awareness and limited research base on which to implement into design provisions. With further research, the benefits of CFST construction will make them more commonplace.

### *1.2 Research Program and Objectives*

The primary purpose of this research program was to investigate and quantify the shear resistance and behavior of CFSTs and RCFSTs. Thorough evaluation of prior research results on the subject was completed and used to develop the program completed here. A new experimental and analytical study was performed to collect data on the the general behaviors and impacts of various parameters on the shear behavior of CFSTs.

First, experimental testing was performed on twenty-one 20 *in.* diameter CFSTs. With this data, analytical models were developed and calibrated to experimental results. The developed models were then used to perform parameter studies and gather additional information that could be used with the experimental data to determine a limit state criterion

and propose a shear capacity design expression that includes the composite benefits of a CFST. Conclusions on the failure modes and impacts of the various parameters studied were also to be made.

### *1.3 Report Overview*

This research program is summarized in the following chapters, with a list of notations used throughout provided in Appendix A.

- *Chapter 2* includes the study and analysis of current design provisions on CFST member resistance, previous experimental work on CFST shear, and previous analytical modeling of CFST members.

- *Chapter 3* summarizes the experimental testing in this program reported by Maki (2015), with further analysis completed in this work, including setup design, test matrix, results, and the influence of various parameters.

- *Chapter 4* details the developed analytical model and the techniques required to overcome modeling challenges in mimicking the experiments. The model was calibrated to the test results of six specimens.

- *Chapter 5* discusses the parameter studies performed with the validated model and conclusions on the behaviors of the various simulations.

- *Chapter 6* proposes a limit state criterion used to determine shear-controlled specimens and simulations, so that a new design expression could be developed and compared to research results.

- *Chapter 7* provides a summary of the key findings of this thesis and recommends additional work that could be done to further define the shear response of CFSTs and RCFSTs.

# Chapter 2

# LITERATURE REVIEW AND CURRENT DESIGN PROVISIONS

## *2.1 Introduction*

Concrete-filled steel tubes have been widely researched for various applications, including design strength, cyclic performance, and others. However, clear consensus on all of their behaviors is still not made. The research presented in this thesis builds upon and references the previous works presented in this chapter for completeness and further insight. The following sections summarize current design provisions, previous experimental studies on CFST shear strength, and previous CFST modeling results.

## *2.2 Current Design Provisions*

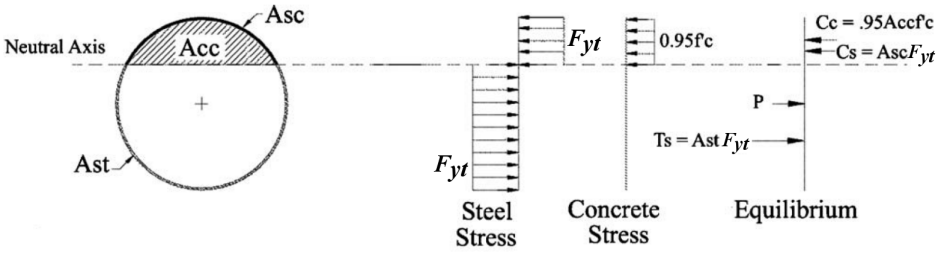
### *2.2.1 Summary of Available Provisions*

Significant research has been performed on the flexural, axial, and combined flexural and axial strengths of CFSTs (Roeder et al., 2010; Moon et al., 2013) and are included in various design provisions, including the American Institute of Steel Construction specifications (ASIC, 2010), the American Concrete Institute specifications (ACI, 2011), and the American Association of State Highway and Transportation Officials specifications (AASHTO, 2016). However, there is wide variation among these design methods. More recently though, AASHTO LRFD specification changes have closed this gap, with modifications making it more similar to those found in AISC, because research results have better supported the accuracy of the AISC provisions (Bishop, 2009). For the shear resistance of CFST members, variability in design method is still prominent, largely due to limited research in this area. The research program presented in this thesis aims to improve this limitation. Nevertheless,

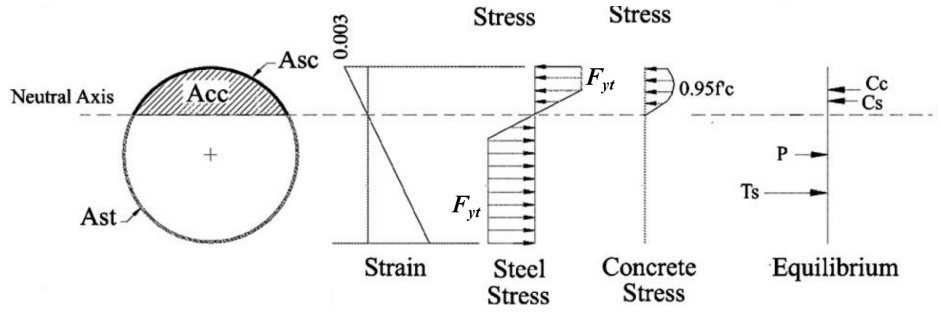
current specifications include predictions of shear resistance. The following sections describe the approaches by each specification for flexural, axial, and shear resistance. Additionally, the Washington Department of Transportation (WSDOT, 2012) has supported considerable research on CFSTs and also has equations for predicting these strengths. These are also included in this evaluation.

### *2.2.2 Axial and Flexural Capacities*

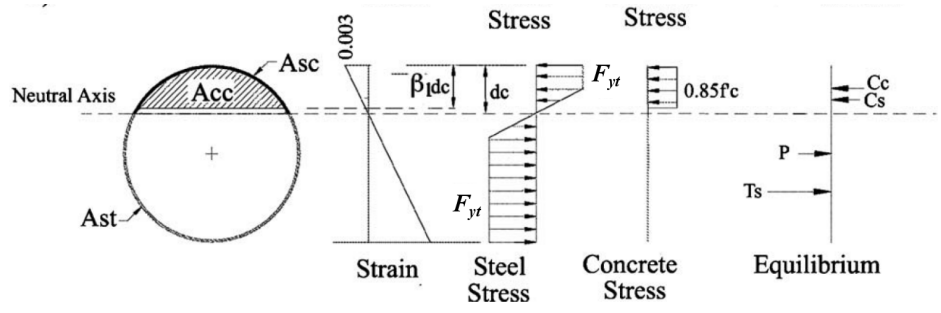
The AASHTO and AISC provisions permit both the plastic stress distribution method (PSDM) and the strain compatibility method for evaluating axial, flexural, and combined axial and flexural capacities of CFST and RCFT members. Figure 2.1 illustrates these models. Experimental research though has demonstrated the the PSDM provides consistently more accurate, while conservative, predictions of resistance than the strain compatibility method, because the latter requires a strain, or deformation, limit which is not well defined for CFSTs. Strain limits on steel or concrete are far less meaningful for CFSTs and RCFSTs than for reinforced concrete, because the steel tube is extremely efficient at confining and preventing the spalling of concrete. The PSDM assumes that the concrete fill reaches a compressive stress of $0.95f_c'$ for circular sections, due to axial or flexural loading, and that the steel tube, and any internal reinforcement, approach their yield stress, $F_{yt}$, in either tension or compression.




(a) Plastic Stress Distribution Method




(b) AISC Strain Compatibility Method




(c) ACI Method

Figure 2.1: Methods for Predicting CFST Resistance

In the WSDOT memorandum, a closed form solution is provided using the PSDM method for circular CFSTs and RCFSTs. Equation 2.1 and Figure 2.2 illustrate the methodology for CFSTs, and Equation 2.2 and Figure 2.3 show that for RCFSTs.

$$r_m = r - \frac{t}{2} \tag{2.1a}$$

$$\theta = sin^{-1}\left(\frac{y}{r_m}\right) \tag{2.1b}$$

$$c = r_i \cos\theta \tag{2.1c}$$

$$P = F_{yt} t r_m \{(\pi - 2\theta) - (\pi + 2\theta)\} + \frac{0.95 f'_c}{2}\{(\pi - 2\theta) r_i^2 - 2yc\} \tag{2.1d}$$

$$M = 0.95 f'_c c \left\{ \left(r_i^2 - y^2\right) - \frac{c^2}{3} \right\} + 4 F_{yt} t c \frac{r_m^2}{r_i} \tag{2.1e}$$

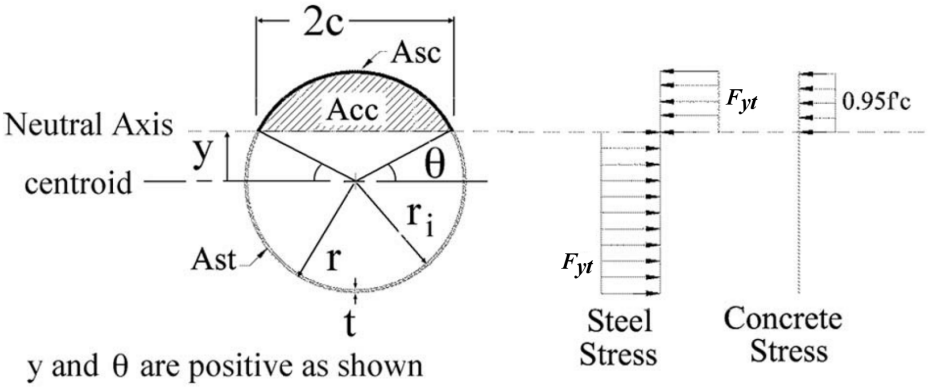



Figure 2.2: Geometry used for Closed-Form CFST PSDM Derivation

$$r_m = r - \frac{t}{2} \tag{2.2a}$$

$$\theta_s = sin^{-1}\left(\frac{y}{r_m}\right) \; and \; \theta_b = sin^{-1}\left(\frac{y}{r_b}\right) \tag{2.2b}$$

$$c = r_i \cos\theta_s \; and \; c_b = r_b \cos\theta_b \tag{2.2c}$$

$$t_b = \frac{nA_{srl}}{2\pi r_b} \tag{2.2d}$$

$$P = F_{yt} t r_m \{(\pi - 2\theta_s) - (\pi + 2\theta_s)\} + t_b r_b \left\{F_{yrl}(\pi - 2\theta_b) - (F_{yrl} - 0.95f_c')(\pi + 2\theta_b)\right\} + \frac{0.95f_c'}{2}\{(\pi - 2\theta_s)r_i^2 - 2yc\} \tag{2.2e}$$

$$M = 0.95f_c' c\left\{\left(r_i^2 - y^2\right) - \frac{c^2}{3}\right\} + 4F_{yt} t c \frac{r_m^2}{r_i} + 4F_{yrl} t_b c_b r_b \tag{2.2f}$$

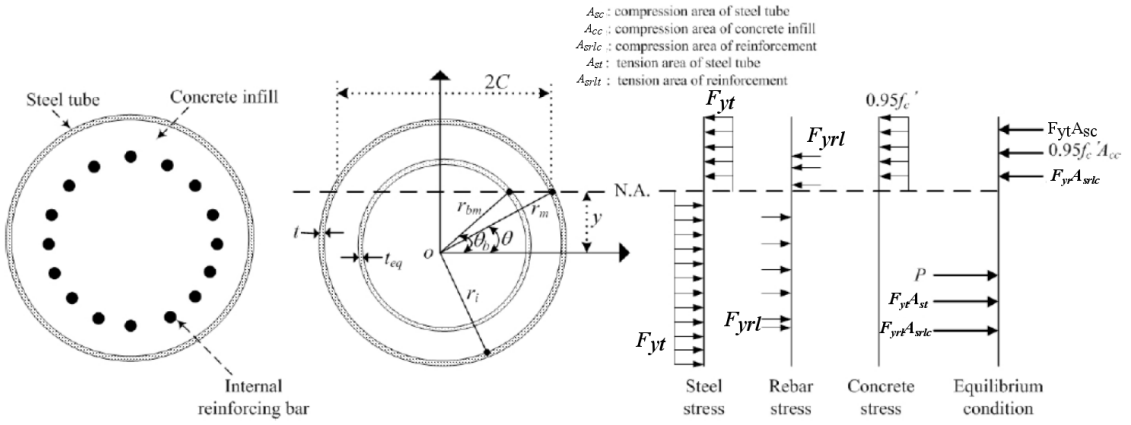



Figure 2.3: Geometry used for Closed-Form RCFST PSDM Derivation

For both cases, $P$ defines the axial force, positive being a compressive load; $M$ defines the moment of the section; and $y$ the distance from the centroid to the neutral axis, N.A., ranging from $+/-r_i$, with the positive direction as shown in Figures 2.2 and 2.3. Axial-moment interaction curves for material behavior can be developed by solving $P-M$ pairs for varying neutral axis depths, $y$. These equations can be used for nominal capacities in both strength and extreme limit states, and utilized with the appropriate resistance factors per LRFD provisions.

Lastly, the nominal compressive strength, often noted as a CFST's crushing load, is specified for short, compact CFSTs and RCFSTs by Equation 2.3.

$$P_0 = A_{st}F_{yt} + A_{srl}F_{yrl} + 0.95A_c f'_c \tag{2.3}$$

### *2.2.3 Shear Capacity*

When it comes to looking at the shear capacity of CFSTs, the AISC provisions permit three methods. The first, Equation 2.4, is defined by the available shear strength of the steel tube, neglecting any contribution by the concrete fill. The second approach, Equation 2.5, relies solely on the shear strength of the concrete fill and any internal shear reinforcement used, without regard to the steel tube. Finally, the the third method, Equation 2.6, is a sort of combination of the first two, utilizing the shear strength of the steel tube and any shear reinforcement present in the concrete fill. Still, though, the concrete fill is ignored here.

- *AISC Method 1*

$$V_{n(AISC_1)} = V_{st} \tag{2.4a}$$

$$where:\ V_{st} = 0.6F_{yt}(0.5A_{st}) \tag{2.4b}$$

- *AISC Method 2*

$$V_{n(AISC_2)} = V_c + V_{srt} \tag{2.5a}$$

$$where: \ V_c = 2\sqrt{f'_c}A_c$$

$$(f'_c \ is \ in \ psi \ units) \tag{2.5b}$$

$$V_{srt} = \frac{A_{srt}F_{yrt}D}{s} \tag{2.5c}$$

- *AISC Method 3*

$$V_{n(AISC_3)} = V_{st} + V_{srt} \tag{2.6a}$$

$$where: \ V_{st} = 0.6F_{yt}(0.5A_{st}) \tag{2.6b}$$

$$V_{srt} = \frac{A_{srt}F_{yrt}D}{s} \tag{2.6c}$$

In ACI, the shear strength is limited to that of the concrete fill, comparable to AISC Method 2. The AASHTO specification then limits the CFST shear resistance to the steel tube only, comparable to AISC Method 1. The WSDOT shear design expression, though, combines the respective strengths of the concrete fill and steel tube, but still neglects the composite benefits. Equation 2.7 presents this approach. This expression has since been updated in the 2016 BDM based on preliminary analysis of this research program. Nevertheless, the presented equation used prior to the 2016 BDM is evaluated in this thesis.

$$V_{n(Method \ 4)} = V_{st} + 0.5V_c \tag{2.7a}$$

$$where: \ V_{st} = 0.6F_{yt}(0.5A_{st}) \tag{2.7b}$$

$$V_c = 0.0316\beta\sqrt{f'_c}A_c, \ if \ P \ is \ compressive$$

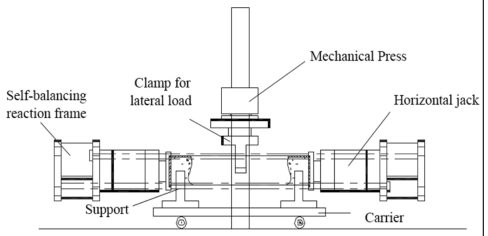
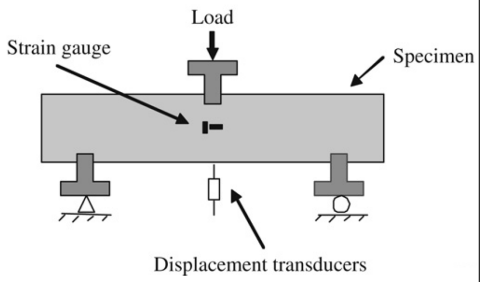
$$(f'_c \ is \ in \ ksi \ units \ and \ \beta = 2) \tag{2.7c}$$

## *2.3 Previous Experimental Research on Shear Capacity of CFSTs*

### *2.3.1 Summary of Programs to be Evaluated*

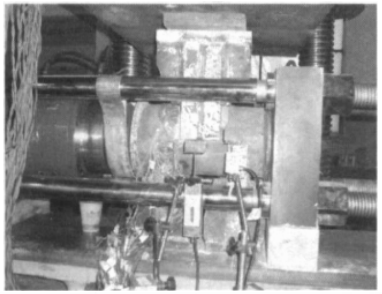
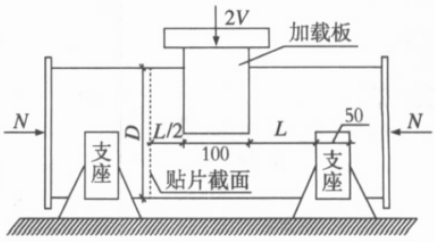
A limited number of research programs have focused on the shear capacity of circular, CFSTs, and all evaluated small diameter tubes ($\sim 6\ in.$). This section highlights five experimental programs on small circular, CFSTs (Xiao et al., 2012; Xu et al., 2009; Qian et al., 2007; Nakahara and Tokuda, 2012; Ye et al., 2016). A summary of the specimens, variables, and testing apparatuses of these programs is given in Table F.2, with the variable $P/P_0$ defining axial load divided by the crushing load given in Equation 2.3. Three of the researchers tested CFSTs under monotonic three-point bending, one performed cyclic, double-curvature tests, and the last a similar double-curvature setup but with two shear spans and monotonic loading. All five studies concluded that the effects of shear span to depth ratio, $a/D$, are significant for shear resistance. Further details of these research programs are discussed in the following passages and in Maki (2015).

Table 2.1: Previous Experimental Research Summary

| Researcher | Program Description | Setup | Proposed Equation |
|---|---|---|---|
| Xiao, C. et al. (2012) | • Specimens: 58 total, all with end caps<br>• Geometry: Dia. of 160 to 166 mm (6.3 to 6.5 in.)<br>• Parameters: $a/D$, $D/t$, $f'_c$, and $P/P_o$<br>• Testing: 3 point bending with monotonic transverse load | <br>Xiao et al. (2012) | **Pure Shear Capacity (a/D = 0):**<br>$V_0 = A_c f_{cv} + A_{st} f_{yv} = 2A_c f_{ct} + 0.6A_{st} f_s$<br>$\approx 0.2A_c f'_c(1 + 3\theta)$<br>**Shear Capacity (a/D > 0):**<br>$V_n = (V_0 + 0.1P)\left(1 - 0.45\sqrt{a/D}\right)$<br>*where P is the axial compressive force*<br>$Concrete\ Shear\ Strength: \ f_{cv} = 2f_{ct} \approx 0.2f'_c$<br>$Tube\ Steel\ Shear\ Strength: \ f_{yv} = \frac{F_{yt}}{\sqrt{3}} \approx 0.6F_{yt}$<br>$\theta = A_{st}F_{yt}/A_c f'_c$ |
| Xu, C. et al. (2009) | • Specimens: 35 total - 30 made with end caps and 27 made with self-stressing concrete<br>• Geometry: Dia. of 140 to 165.5 mm (5.5 to 6.5 in.)<br>• Parameters: $a/D$, $D/t$, and self-stressing concrete<br>• Testing: 3 point bending with monotonic transverse load | <br>Xu et al. (2009) | $V_0 = V_{0(Xiao)}\,(1 + \Phi)$<br>$\Phi = -0.55 + 0.55\sqrt{1 + 0.7\theta} - 0.1\theta$<br>$\theta = A_{st}F_{yt}/A_c f'_c$ |

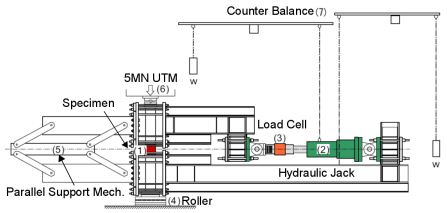
Continued on next page

Table 2.1 – Continued from previous page

| Researcher | Program Description | Setup | Proposed Equation |
|---|---|---|---|
| Qian, J. et al. (2007) | • Specimens: 35 total, all with end caps<br>• Geometry: Dia. of 194 mm (7.64 in.)<br>• Parameters: $a/D$ and $P/P_o$<br>• Testing: 3 point bending with monotonic transverse load | <br><br><br>Qian et al. (2007) | **For $< \mathbf{a/D} < \mathbf{0.5}$ and $\mathbf{P/(F_{yt}A_{st} + f'_cA_c)} \leq \mathbf{0.4}$ :**<br>$V_n = \frac{1.6}{a/D+0.3} f_{ct}A_c + \left[0.3 - \left(0.6 - \frac{1+a^2}{2}\right) a/D\right] F_{yt}A_{st} + 0.05\frac{P}{a/D}$<br>**For $\mathbf{a/D} \geq \mathbf{0.5}$ and $\mathbf{P/(F_{yt}A_{st} + f'_cA_c)} \leq \mathbf{0.4}$ :**<br>$V_n = 2.0 f_{ct}A_c + \frac{1+a^2}{8a/D} F_{yt}A_{st} + 0.1P$<br>**For $\mathbf{0 < a/D < 0.5}$ and $\mathbf{P/(F_{yt}A_{st} + f'_cA_c)} > \mathbf{0.4}$ :**<br>$V_n = \frac{1.6}{a/D+0.3} f_{ct}A_c + \left[0.3 - \left(0.6 - \frac{1+a^2}{2}\right) a/D\right] F_{yt}A_{st} + 0.02\frac{F_{yt}A_{st} + f'_cA_c}{a/D}$<br>**For $\mathbf{a/D} \geq \mathbf{0.5}$ and $\mathbf{P/(F_{yt}A_{st} + f'_cA_c)} > \mathbf{0.4}$ :**<br>$V_n = 2.0 f_{ct}A_c + \frac{1+a^2}{8a/D} F_{yt}A_{st} + 0.04(F_{yt}A_{st} + f'_cA_c)$<br>$where: f_{ct} = 0.395 f_{cu}^{0.55};\ a = \frac{D}{D-t};$<br>$and\ P = axial\ force$ |

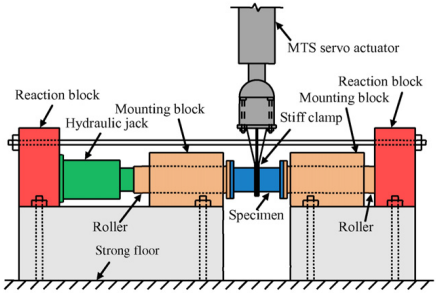
Continued on next page

Table 2.1 – Continued from previous page

| Researcher | Program Description | Setup | Proposed Equation |
|---|---|---|---|
| Nakahara, H. et al. (2012) | • Specimens: 5 total, all with end caps<br>• Geometry: Dia. of 165 to 166 mm (6.5 in.) and $a/D = 0.5$<br>• Parameters: $f'_c$ and $P/P_o$<br>• Testing: Double-curvature with cyclic transverse load | <br>Nakahara and Tokuda (2012) | **Using American Institue of Japan (2008):**<br>$V_n = V_{st} + V_c$<br>**For the tube steel:**<br>$When\ 3P_s + 2\pi\bar{a}_s V_{st} \leq P_{s0},$<br>$V_{st} = \frac{P_{s0}}{\pi}$<br>$When\ 3P_s + 2\pi\bar{a}_s V_{st} \geq P_{s0} \geq 2\pi\bar{a}_s V_{st},$<br>$\pi^2\left\{1+\bar{a}_s^2\right\}V_{st}^2 + \pi\bar{a}_s(3P_s - P_{s0})V_{st} - \frac{3}{2}P_s P_{s0} + \frac{9}{4}P_s^2 - 34P_{s0}^2 = 0$<br>$When\ 2\pi\bar{a}_s V_{st} \geq P_{s0},$<br>$\pi^2\left\{1+4\bar{a}_s^2\right\}V_{st}^2 - 4\pi\bar{a}_s V_{st} P_{s0} + \frac{9}{4}P_s^2 = 0$<br>$Where:\ \bar{a}_s = a/D;\ P_{s0} = A_{st}F_{yt};$<br>$and\ P_s = \ axial\ force\ of\ tube$<br>**For the concrete fill:**<br>$P_c = r_1^2(\theta - \sin\theta\cos\theta)f'_c$<br>$V_c = \frac{1}{3\bar{a}_c}r_1^2\sin^3\theta f'_c$<br>$Where:\ r_1 = D_c/2;\ \theta = \cos^{-1}\left(\frac{r_1 - x_n}{r_1}\right);\ \bar{a}_c = a/D_c$<br>$P_c = \ axial\ force\ of\ inner\ concrete;$<br>$and\ D_c = \ diameter\ of\ concrete\ fill$ |

Continued on next page

Table 2.1 – Continued from previous page

| Researcher | Program Description | Setup | Proposed Equation |
|---|---|---|---|
| Ye, Y. et al. (2016) | • Specimens: 38 total, both circular and square cross-sections, all with end caps<br>• Geometry: Dia./side length of 120 mm (4.72 in.)<br>• Parameters: $a/D$, $A_{st}/A_c$, $f'_c$, and $P/P_o$<br>• Testing: Double-curvature with two shear spans and monotonic transverse load | <br>Ye et al. (2016) | **Using DBJ/T13-51-2010:**<br>$When\ \frac{P}{P_0} \geq 2\eta_0\sqrt[2.4]{1-\left(\frac{V}{V_0}\right)^2},$<br>$\left(\frac{P}{P_0}+a\frac{M}{M_n}\right)^{2.4}+\left(\frac{V}{V_0}\right)^2=1$<br>$When\ \frac{P}{P_0} < 2\eta_0\sqrt[2.4]{1-\left(\frac{V}{V_0}\right)^2},$<br>$\left[-b\left(\frac{P}{P_0}\right)^2-c\left(\frac{P}{P_0}\right)+\frac{M}{M_u}\right]^{2.4}+\left(\frac{V}{V_u}\right)^2=1$<br>$where:\ a=1-2\eta_0;\ b=\frac{1-\zeta_0}{\eta_0^2};\ c=\frac{2(\zeta_0-1)}{\eta_0};\ \xi=\alpha_s\frac{F_{yt}}{f_{ck}};$<br>$f_{ck}=0.67f_{cu};\ M_n=\ flexural\ strength\ of\ CFST;$<br>$V_0=\ pure\ shear\ strength\ =\gamma_v A_{sc}\tau_{sc}$<br>**For circular CFSTs:** $\zeta_0=1+0.18\xi^{-1.15}$<br>$\eta_0=\begin{cases}0.5-0.245\xi & \xi\leq 0.4\\ 0.1+0.14\xi^{-0.84} & \xi>0.4\end{cases}$<br>$\gamma_v=0.97+0.2\ln\xi;\ \tau_{sc}=\left(0.422+0.313\alpha_s^{2.33}\right)\xi^{0.134}f_{sc};$<br>$f_{sc}=(1.14+1.02\xi)f_{ck}$<br>**For square CFSTs:** $\zeta_0=1+0.14\xi^{-1.3}$<br>$\eta_0=\begin{cases}0.5-0.318\xi & \xi\leq 0.4\\ 0.1+0.13\xi^{-0.81} & \xi>0.4\end{cases}$<br>$\gamma_v=0.954+0.162\ln\xi;\ \tau_{sc}=\left(0.455+0.313\alpha_s^{2.33}\right)\xi^{0.25}f_{sc};$<br>$f_{sc}=(1.18+0.85\xi)f_{ck}$<br>$^*Note\ that\ these\ are\ limited\ to\ cases\ with:$<br>$\alpha_s=0.04-0.2;\ F_{yt}=235-420\ MPa\ (34-61\ ksi);$<br>$f_{cu}=30-90\ MPa\ (4.4-13\ ksi);\ D/t=10-120$ |

### *2.3.2 Previous Research Results and Conclusions*

For each of the experimental programs presented in Table F.2, a summary of specimens tested, test results, and conclusions is given here. The researchers themselves only report experimental shear force values, and no reflection specimen moment. So, for comparison purposes in later discussions and to assess plastic development, a moment, $M_{ed}$, is estimated here and normalized against $M_{PSDM}$. Because the moment was not directly evaluated by the researchers, and discussions of moment arm not described, the $M_{ed}$ values are estimated with the reported shear force and a moment arm designated as the center-to-center distance between load and support points for Xiao, Qian, and Xu. Nakahara's moment arm was estimated as the clear span between fixed points and Ye's the center of the load application surface to face of fixed support.

*Xiao, Cai, Chen, and Xu (2012)*

Xiao et al. (2012) largely studied CFST specimens for shear capacity, ductility, and damage modes. Of the fifty-eight specimens, the authors reported fifty-one shear failures, two flexural failures, two flexure-shear failures, and three weld failures at the end cap. A summary of these results is found in Table 2.2. Note that all specimens in this program were made with end caps.

Table 2.2: Summary of Specimens and Results (Xiao et al., 2012)

| Specimen | a (in.) | $a/D$ | t (in.) | $D/t$ | $F_{ytm}$ (ksi) | $f'_{cm}$ (ksi) | $P/P_0$ | $V_{ed}$ (kips) | $M_{ed}/M_{PSDM}$ | Reported Failure Mode |
|---|---|---|---|---|---|---|---|---|---|---|
| X1 | 2.52 | 0.4 | 0.217 | 29.1 | 54.7 | 3.76 | 0 | 221 | 1.70 | shear |
| X2 | 2.52 | 0.4 | 0.217 | 29.1 | 54.7 | 4.70 | 0 | 211 | 1.60 | shear |
| X3 | 2.52 | 0.4 | 0.217 | 29.1 | 54.7 | 4.28 | 0 | 209 | 1.59 | shear |
| X4 | 2.61 | 0.4 | 0.173 | 37.7 | 50.0 | 3.76 | 0 | 169 | 1.62 | shear |
| X5 | 2.61 | 0.4 | 0.173 | 37.7 | 50.0 | 4.70 | 0 | 174 | 1.64 | shear |
| X6 | 2.61 | 0.4 | 0.173 | 37.7 | 50.0 | 4.28 | 0 | 168 | 1.59 | shear |
| X7 | 2.60 | 0.4 | 0.118 | 55.0 | 59.2 | 3.76 | 0 | 115 | 1.32 | shear |
| X8 | 2.60 | 0.4 | 0.118 | 55.0 | 59.2 | 4.70 | 0 | 123 | 1.40 | shear |
| X9 | 2.60 | 0.4 | 0.118 | 55.0 | 59.2 | 4.28 | 0 | 118 | 1.35 | shear |

Continued on next page

Table 2.2 – Continued from previous page

| Specimen | a (in.) | $a/D$ | t (in.) | $D/t$ | $F_{ytm}$ (ksi) | $f'_{cm}$ (ksi) | $P/P_0$ | $V_{ed}$ (kips) | $M_{ed}/M_{PSDM}$ | Reported Failure Mode |
|---|---|---|---|---|---|---|---|---|---|---|
| X10 | 2.52 | 0.4 | 0.217 | 29.1 | 54.7 | 3.76 | 0.32 | 228 | 1.78 | shear |
| X11 | 2.52 | 0.4 | 0.217 | 29.1 | 54.7 | 4.70 | 0.32 | 218 | 1.62 | shear |
| X12 | 2.52 | 0.4 | 0.217 | 29.1 | 54.7 | 4.28 | 0.31 | 230 | 1.74 | shear |
| X13 | 2.61 | 0.4 | 0.173 | 37.7 | 50.0 | 3.76 | 0.32 | 195 | 1.80 | shear |
| X14 | 2.61 | 0.4 | 0.173 | 37.7 | 50.0 | 4.70 | 0.31 | 183 | 1.60 | shear |
| X15 | 2.61 | 0.4 | 0.173 | 37.7 | 50.0 | 4.28 | 0.31 | 190 | 1.70 | shear |
| X16 | 2.60 | 0.4 | 0.118 | 55.0 | 59.2 | 3.76 | 0.31 | 141 | 1.52 | shear |
| X17 | 2.60 | 0.4 | 0.118 | 55.0 | 59.2 | 4.70 | 0.29 | 133 | 1.34 | shear |
| X18 | 2.60 | 0.4 | 0.118 | 55.0 | 59.2 | 4.28 | 0.29 | 133 | 1.37 | shear |
| X19 | 2.52 | 0.4 | 0.217 | 29.1 | 54.7 | 3.76 | 0.65 | 198 | 2.36 | shear |
| X20 | 2.52 | 0.4 | 0.217 | 29.1 | 54.7 | 4.70 | 0.63 | 234 | 2.53 | shear |
| X21 | 2.61 | 0.4 | 0.173 | 37.7 | 50.0 | 3.76 | 0.64 | 184 | 2.46 | shear |
| X22 | 2.61 | 0.4 | 0.173 | 37.7 | 50.0 | 4.70 | 0.61 | 204 | 2.42 | shear |
| X23 | 2.60 | 0.4 | 0.118 | 55.0 | 59.2 | 3.76 | 0.62 | 144 | 2.10 | shear |
| X24 | 2.60 | 0.4 | 0.118 | 55.0 | 59.2 | 4.70 | 0.58 | 153 | 1.92 | shear |
| X25 | 0.88 | 0.14 | 0.217 | 29.1 | 54.7 | 3.76 | 0 | 170 | 0.73 | weld |
| X26 | 0.88 | 0.14 | 0.217 | 29.1 | 54.7 | 4.70 | 0 | 174 | 0.73 | weld |
| X27 | 0.88 | 0.14 | 0.217 | 29.1 | 54.7 | 4.28 | 0 | 169 | 0.72 | weld |
| X28 | 0.88 | 0.14 | 0.217 | 29.1 | 54.7 | 4.28 | 0 | 289 | 1.23 | shear |
| X29 | 0.91 | 0.14 | 0.173 | 37.7 | 50.0 | 4.28 | 0 | 225 | 1.18 | shear |
| X30 | 0.91 | 0.14 | 0.118 | 55.0 | 59.2 | 4.28 | 0 | 155 | 0.98 | shear |
| X31 | 0.91 | 0.14 | 0.173 | 37.7 | 50.0 | 3.76 | 0 | 220 | 1.17 | shear |
| X32 | 0.91 | 0.14 | 0.173 | 37.7 | 50.0 | 4.70 | 0 | 220 | 1.15 | shear |
| X33 | 0.91 | 0.14 | 0.173 | 37.7 | 50.0 | 4.28 | 0 | 212 | 1.11 | shear |
| X34 | 0.91 | 0.14 | 0.118 | 55.0 | 59.2 | 3.76 | 0 | 154 | 0.99 | shear |
| X35 | 0.91 | 0.14 | 0.118 | 55.0 | 59.2 | 4.70 | 0 | 157 | 0.98 | shear |
| X36 | 0.91 | 0.14 | 0.118 | 55.0 | 59.2 | 4.28 | 0 | 169 | 1.07 | shear |
| X37 | 0.88 | 0.14 | 0.217 | 29.1 | 54.7 | 3.76 | 0.32 | 327 | 1.42 | shear |
| X38 | 0.88 | 0.14 | 0.217 | 29.1 | 54.7 | 4.70 | 0.32 | 328 | 1.36 | shear |
| X39 | 0.88 | 0.14 | 0.217 | 29.1 | 54.7 | 4.28 | 0.31 | 337 | 1.42 | shear |
| X40 | 0.91 | 0.14 | 0.173 | 37.7 | 50.0 | 3.76 | 0.32 | 280 | 1.43 | shear |
| X41 | 0.91 | 0.14 | 0.173 | 37.7 | 50.0 | 4.70 | 0.31 | 284 | 1.38 | shear |
| X42 | 0.91 | 0.14 | 0.173 | 37.7 | 50.0 | 4.28 | 0.31 | 281 | 1.39 | shear |
| X43 | 0.91 | 0.14 | 0.118 | 55.0 | 59.2 | 3.76 | 0.31 | 216 | 1.28 | shear |
| X44 | 0.91 | 0.14 | 0.118 | 55.0 | 59.2 | 4.70 | 0.29 | 205 | 1.15 | shear |
| X45 | 0.91 | 0.14 | 0.118 | 55.0 | 59.2 | 4.28 | 0.29 | 214 | 1.23 | shear |
| X46 | 0.88 | 0.14 | 0.217 | 29.1 | 54.7 | 3.76 | 0.65 | 336 | 2.24 | shear |
| X47 | 0.88 | 0.14 | 0.217 | 29.1 | 54.7 | 4.70 | 0.63 | 405 | 2.44 | shear |
| X48 | 0.88 | 0.14 | 0.217 | 29.1 | 54.7 | 4.28 | 0.63 | 384 | 2.36 | shear |
| X49 | 0.91 | 0.14 | 0.173 | 37.7 | 50.0 | 3.76 | 0.64 | 333 | 2.46 | shear |
| X50 | 0.91 | 0.14 | 0.173 | 37.7 | 50.0 | 4.70 | 0.61 | 323 | 2.11 | shear |

Continued on next page

Table 2.2 – Continued from previous page

| Specimen | a (in.) | $a/D$ | t (in.) | $D/t$ | $F_{ytm}$ (ksi) | $f'_{cm}$ (ksi) | $P/P_0$ | $V_{ed}$ (kips) | $M_{ed}/M_{PSDM}$ | Reported Failure Mode |
|---|---|---|---|---|---|---|---|---|---|---|
| X51 | 0.91 | 0.14 | 0.173 | 37.7 | 50.0 | 4.28 | 0.61 | 233 | 1.56 | shear |
| X52 | 0.91 | 0.14 | 0.118 | 55.0 | 59.2 | 3.76 | 0.62 | 240 | 1.93 | shear |
| X53 | 0.91 | 0.14 | 0.118 | 55.0 | 59.2 | 4.70 | 0.58 | 222 | 1.54 | shear |
| X54 | 0.91 | 0.14 | 0.118 | 55.0 | 59.2 | 4.28 | 0.58 | 233 | 1.70 | shear |
| X55 | 3.17 | 0.5 | 0.256 | 24.8 | 64.5 | 2.92 | 0 | 206 | 1.38 | flexure-shear |
| X56 | 6.34 | 1.0 | 0.256 | 24.8 | 64.5 | 2.92 | 0 | 137 | 1.59 | flexure |
| X57 | 3.25 | 0.5 | 0.161 | 40.2 | 55.8 | 2.92 | 0 | 129 | 1.43 | flexure-shear |
| X58 | 6.50 | 1.0 | 0.161 | 40.2 | 55.8 | 2.92 | 0 | 82 | 1.58 | flexure |

Xiao, et. al made the following observations:

- CFSTs with $a/D$ ratios of 0.14 to 0.4 failed in a ductile manner with large shear deformations, specimens with an $a/D$ of 0.14 displayed direct shear failure, and specimens having an $a/D$ of 0.4 displayed diagonal compression failure.
- CFSTs with $a/D$ ratios greater than or equal to 0.5 failed in flexure, with specimens having $a/D$ of 0.5 exhibiting some shearing behaviors.
- Test results showed that shear capacity decreases with increasing $a/D$.
- The presence of end caps and the effectiveness of their weld attachment greatly influenced the CFST specimen behaviors.
- The shear strength of CFSTs increased with increasing axial load.
- An equation for the shear capacity of CFSTs with and without axial load was proposed.

*Xu, Haixiao, and Chengkui (2009)*

Xu et al. (2009) focused their research on the effectiveness of reducing shrinkage, and therefore maintaining composite action, with the use of expansive concrete fill in CFSTS under three-point transverse loading. The authors reported twenty-nine shear failures and six flexural failures. Table 2.3 provides specimen details and results.

Table 2.3: Summary of Specimens and Results (Xu et al., 2009)

| Specimen | a (in.) | $a/D$ | t (in.) | $D/t$ | $F_{ytm}$ (ksi) | $f'_{cm}$ (ksi) | Radial Self-Stress (ksi) | End Cap | $V_{ed}$ (kips) | $M_{ed}/M_{PSDM}$ | Reported Failure Mode |
|---|---|---|---|---|---|---|---|---|---|---|---|
| Xu1 | 0.65 | 0.1 | 0.145 | 45.0 | 52.8 | 6.49 | 0.812 | yes | 104 | 0.74 | shear |
| Xu2 | 1.30 | 0.2 | 0.145 | 45.0 | 52.8 | 6.49 | 0.812 | yes | 97 | 0.91 | shear |
| Xu3 | 1.95 | 0.3 | 0.145 | 45.0 | 52.8 | 6.49 | 0.812 | yes | 89 | 1.03 | shear |
| Xu4 | 3.26 | 0.5 | 0.145 | 45.0 | 52.8 | 6.49 | 0.812 | yes | 69 | 1.09 | flexure |
| Xu5 | 6.52 | 1 | 0.145 | 45.0 | 52.8 | 6.49 | 0.812 | yes | 53 | 1.41 | flexure |
| Xu6 | 0.65 | 0.1 | 0.145 | 45.0 | 52.8 | 6.18 | 0.885 | yes | 109 | 0.78 | shear |
| Xu7 | 1.30 | 0.2 | 0.145 | 45.0 | 52.8 | 6.18 | 0.885 | yes | 91 | 0.85 | shear |
| Xu8 | 1.95 | 0.3 | 0.145 | 45.0 | 52.8 | 6.18 | 0.885 | yes | 84 | 0.97 | shear |
| Xu9 | 3.26 | 0.5 | 0.145 | 45.0 | 52.8 | 6.18 | 0.885 | yes | 76 | 1.20 | flexure |
| Xu10 | 6.52 | 1 | 0.145 | 45.0 | 52.8 | 6.18 | 0.885 | yes | 57 | 1.54 | flexure |
| Xu11 | 0.65 | 0.1 | 0.145 | 45.0 | 52.8 | 7.21 | 0.986 | yes | 109 | 0.77 | shear |
| Xu12 | 1.30 | 0.2 | 0.145 | 45.0 | 52.8 | 7.21 | 0.986 | yes | 100 | 0.92 | shear |
| Xu13 | 1.95 | 0.3 | 0.145 | 45.0 | 52.8 | 7.21 | 0.986 | yes | 94 | 1.07 | shear |
| Xu14 | 3.26 | 0.5 | 0.145 | 45.0 | 52.8 | 7.21 | 0.986 | yes | 69 | 1.09 | flexure |
| Xu15 | 4.56 | 0.7 | 0.145 | 45.0 | 52.8 | 7.21 | 0.986 | yes | 62 | 1.25 | flexure |
| Xu16 | 0.65 | 0.1 | 0.145 | 45.0 | 52.8 | 6.10 | 0 | yes | 93 | 0.67 | shear |
| Xu17 | 1.30 | 0.2 | 0.145 | 45.0 | 52.8 | 6.10 | 0 | yes | 83 | 0.78 | shear |
| Xu18 | 1.95 | 0.3 | 0.145 | 45.0 | 52.8 | 6.10 | 0 | yes | 80 | 0.92 | shear |
| Xu19 | 3.26 | 0.5 | 0.145 | 45.0 | 52.8 | 6.10 | 0 | yes | 68 | 1.08 | flexure |
| Xu20 | 6.52 | 1 | 0.145 | 45.0 | 52.8 | 6.10 | 0 | yes | 52 | 1.38 | flexure |
| Xu21 | 0.65 | 0.1 | 0.145 | 45.0 | 52.8 | 6.18 | 0.682 | no | 100 | 0.72 | shear |
| Xu22 | 1.30 | 0.2 | 0.145 | 45.0 | 52.8 | 6.18 | 0.682 | no | 88 | 0.82 | shear |
| Xu23 | 1.95 | 0.3 | 0.145 | 45.0 | 52.8 | 6.18 | 0.682 | no | 82 | 0.95 | shear |
| Xu24 | 0.65 | 0.1 | 0.145 | 45.0 | 52.8 | 7.21 | 0.841 | no | 110 | 0.78 | shear |
| Xu25 | 1.30 | 0.2 | 0.145 | 45.0 | 52.8 | 7.21 | 0.841 | no | 92 | 0.85 | shear |
| Xu26 | 0.65 | 0.1 | 0.145 | 45.0 | 52.8 | 6.10 | 0.841 | no | 88 | 0.63 | shear |
| Xu27 | 1.30 | 0.2 | 0.145 | 45.0 | 52.8 | 6.10 | 0.841 | no | 79 | 0.74 | shear |
| Xu28 | 1.95 | 0.3 | 0.145 | 45.0 | 52.8 | 6.10 | 0.841 | no | 75 | 0.87 | shear |
| Xu29 | 0.65 | 0.1 | 0.117 | 55.9 | 53.8 | 6.49 | 0.682 | yes | 107 | 0.68 | shear |
| Xu30 | 1.30 | 0.2 | 0.117 | 55.9 | 53.8 | 6.49 | 0.682 | yes | 99 | 0.83 | shear |
| Xu31 | 1.95 | 0.3 | 0.117 | 55.9 | 53.8 | 6.49 | 0.682 | yes | 91 | 0.95 | shear |
| Xu32 | 3.26 | 0.5 | 0.117 | 55.9 | 53.8 | 6.49 | 0.682 | yes | 78 | 1.15 | flexure |
| Xu33 | 0.65 | 0.1 | 0.117 | 55.9 | 53.8 | 7.21 | 0.754 | yes | 111 | 0.69 | shear |
| Xu34 | 1.30 | 0.2 | 0.117 | 55.9 | 53.8 | 7.21 | 0.754 | yes | 94 | 0.78 | shear |
| Xu35 | 1.95 | 0.3 | 0.117 | 55.9 | 53.8 | 7.21 | 0.754 | yes | 88 | 0.91 | shear |

Xu, et. al made the following observations:

- CFSTs with $a/D$ ratios less than 0.5 failed in shear by diagonal tension failure of the steel tube.
- CFSTs with $a/D$ ratios ranging from 0.5 to 1.0 failed in flexure.
- Shear resistance and plastic deformation of specimens with end caps were larger than comparable specimens without.

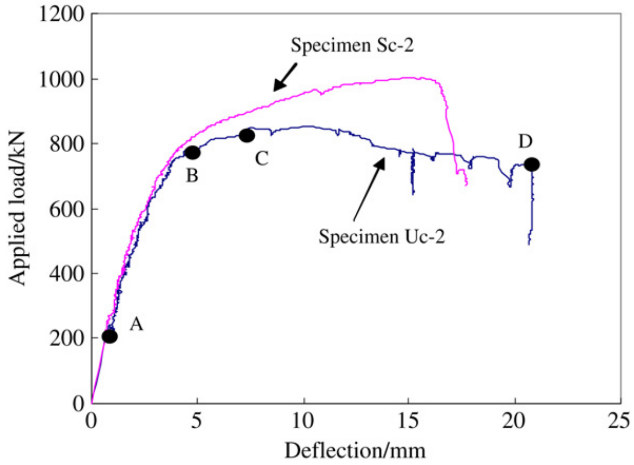



Figure 2.4: Effect of End Caps on CFST Specimen Behavior (Xu et al., 2009)

- With all other parameters kept constant, specimens with self-stressing concrete fill had a higher shear capacity when compared to normal concrete fill; however, this difference lessened with increasing $a/D$.
- Slippage between the concrete fill and steel tube resulted in a decreased shear resistance.
- Conventional approaches to shear capacity as defined for reinforced concrete are inappropriate for CFST members.
- An expression for the determination of shear capacity of self-stressing CFSTs was proposed.

*Qian, Cui, and Fang (2007)*

Qian et al. (2007) studied the shear span to depth ratio, concrete strength, axial force ratio, and tube wall thickness under three-point bending. The researchers reported twenty-nine shear failures, two flexural failures, and four flexure-shear failures. Table 2.4 summarizes the research results. Note that all specimens in this program were made with end caps.

Table 2.4: Summary of Specimens and Results (Qian et al., 2007)

| Specimen | a (in.) | $a/D$ | t (in.) | $D/t$ | $F_{ytm}$ (ksi) | $f'_{cm}$ (ksi) | $P/P_0$ | $V_{ed}$ (kips) | $M_{ed}/M_{PSDM}$ | Reported Failure Mode |
|---|---|---|---|---|---|---|---|---|---|---|
| Q1 | 0.76 | 0.10 | 0.217 | 35.3 | 47.9 | 5.9 | 0 | 286 | 1.60 | shear |
| Q2 | 0.76 | 0.10 | 0.295 | 25.9 | 61.2 | 5.9 | 0 | 395 | 1.36 | shear |
| Q3 | 0.76 | 0.10 | 0.217 | 35.3 | 47.9 | 5.9 | 0.43 | 375 | 2.00 | shear |
| Q4 | 0.76 | 0.10 | 0.295 | 25.9 | 61.2 | 5.9 | 0.46 | 498 | 1.88 | shear |
| Q5 | 0.76 | 0.10 | 0.217 | 35.3 | 47.9 | 5.9 | 0.72 | 439 | 3.74 | shear |
| Q6 | 0.76 | 0.10 | 0.295 | 25.9 | 61.2 | 5.9 | 0.77 | 559 | 4.13 | shear |
| Q7 | 1.15 | 0.15 | 0.217 | 35.3 | 47.9 | 5.9 | 0 | 283 | 1.75 | shear |
| Q8 | 1.15 | 0.15 | 0.295 | 25.9 | 61.2 | 5.9 | 0 | 373 | 1.41 | shear |
| Q9 | 0.76 | 0.10 | 0.217 | 35.3 | 47.9 | 8.1 | 0 | 289 | 1.58 | shear |
| Q10 | 0.76 | 0.10 | 0.295 | 25.9 | 61.2 | 8.1 | 0 | 387 | 1.30 | shear |
| Q11 | 0.76 | 0.10 | 0.217 | 35.3 | 47.9 | 8.1 | 0.41 | 378 | 1.80 | shear |
| Q12 | 0.76 | 0.10 | 0.295 | 25.9 | 61.2 | 8.1 | 0.45 | 528 | 1.81 | shear |
| Q13 | 0.76 | 0.10 | 0.217 | 35.3 | 47.9 | 8.1 | 0.69 | 458 | 3.14 | shear |
| Q14 | 0.76 | 0.10 | 0.295 | 25.9 | 61.2 | 8.1 | 0.30 | 463 | 1.46 | shear |
| Q15 | 1.15 | 0.15 | 0.217 | 35.3 | 47.9 | 8.1 | 0 | 272 | 1.64 | shear |
| Q16 | 1.15 | 0.15 | 0.295 | 25.9 | 61.2 | 8.1 | 0 | 372 | 1.38 | shear |
| Q17 | 2.29 | 0.30 | 0.295 | 25.9 | 61.2 | 8.1 | 0 | 289 | 1.37 | shear |
| Q18 | 2.29 | 0.30 | 0.295 | 25.9 | 61.2 | 8.1 | 0.45 | 398 | 1.93 | shear |
| Q19 | 2.29 | 0.30 | 0.217 | 35.3 | 47.9 | 8.1 | 0.69 | 336 | 3.25 | shear |
| Q20 | 3.82 | 0.50 | 0.295 | 25.9 | 61.2 | 8.1 | 0 | 64 * | 0.39 * | flexure |
| Q21 | 3.82 | 0.50 | 0.295 | 25.9 | 61.2 | 8.1 | 0.45 | 376 | 2.36 | shear |
| Q22 | 3.82 | 0.50 | 0.217 | 35.3 | 47.9 | 8.1 | 0.69 | 263 | 3.29 | shear |
| Q23 | 5.73 | 0.75 | 0.295 | 25.9 | 61.2 | 8.1 | 0 | 220 | 1.72 | flexure |
| Q24 | 5.73 | 0.75 | 0.295 | 25.9 | 61.2 | 8.1 | 0.45 | 271 | 2.17 | flex-shear |
| Q25 | 5.73 | 0.75 | 0.217 | 35.3 | 47.9 | 8.1 | 0.69 | 230 | 3.69 | flex-shear |
| Q26 | 7.64 | 1.00 | 0.295 | 25.9 | 61.2 | 8.1 | 0.45 | 226 | 2.21 | flex-shear |
| Q27 | 7.64 | 1.00 | 0.217 | 35.3 | 47.9 | 8.1 | 0.69 | 225 | 4.40 | flex-shear |
| Q28 | 0.76 | 0.10 | 0.217 | 35.3 | 47.9 | 9.8 | 0 | 281 | 1.51 | shear |
| Q29 | 0.76 | 0.10 | 0.295 | 25.9 | 61.2 | 9.8 | 0 | 391 | 1.29 | shear |
| Q30 | 0.76 | 0.10 | 0.217 | 35.3 | 47.9 | 9.8 | 0.40 | 409 | 1.80 | shear |
| Q31 | 0.76 | 0.10 | 0.295 | 25.9 | 61.2 | 9.8 | 0.44 | 528 | 1.70 | shear |
| Q32 | 0.76 | 0.10 | 0.217 | 35.3 | 47.9 | 9.8 | 0.67 | 501 | 3.02 | shear |
| Q33 | 0.76 | 0.10 | 0.295 | 25.9 | 61.2 | 9.8 | 0.29 | 464 | 1.39 | shear |
| Q34 | 1.15 | 0.15 | 0.217 | 35.3 | 47.9 | 9.8 | 0 | 277 | 1.64 | shear |
| Q35 | 1.15 | 0.15 | 0.295 | 25.9 | 61.2 | 9.8 | 0 | 326 | 1.19 | shear |

* Possible mistake in original reporting.

Qian, et. al made the following observations:

- CFSTs have large deformation capacities.
- When axial load was present, CFSTs with $a/D$ less than or equal to 0.5 failed in shear and CFSTs with $a/D$ greater that 0.5 failed in "shear-bending."
- When no axial load was applied, CFSTs with $a/D$ equal to or greater than 0.5 failed in bending, whereas specimens with $a/D$ less than 0.5 failed in shear.
- For specimens with $a/D$ less than 0.5, the contribution of the concrete fill to the shear resistance of CFSTs increased with decreasing shear span to depth ratio.

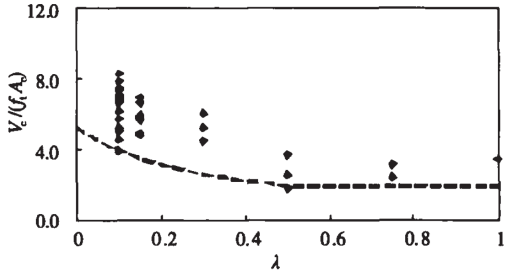



Figure 2.5: $V_c/(f_{ct}A_c)$ vs. $a/D$ (or $\lambda$) (Qian et al., 2007)

- Test results showed an increase in shear loading with smaller $D/t$ ratios.

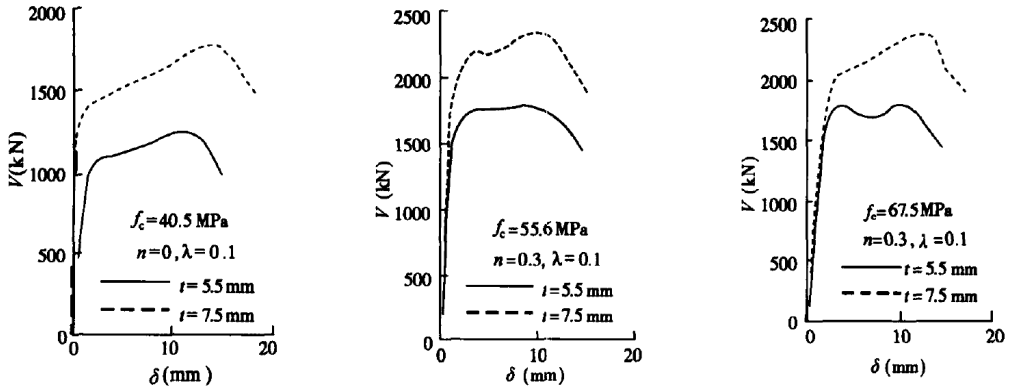



Figure 2.6: Shear Force vs. Deflection Behaviors of CFST Specimens with Varying $D/t$ and Concrete Strength (Qian et al., 2007)

- The shear strength of CFSTs was dependent upon the $a/D$ ratio.
- Shear resistance of CFSTs increased with increasing axial load.
- An equation for the determination of CFST shear capacity was proposed.

*Nakahara and Tokuda (2012)*

Unlike the other researchers already discussed in this section, Nakahara and Tokuda (2012) used a double-curvature setup with cyclic loading to investigate the shear strength and deformation behaviors of CFSTs. Only five specimens were tested and all were reported to have yielded significantly in shear before flexural yielding was observed. Nonetheless, all specimens were desginated as shear failures. Table 2.5 summarizes these five specimens and their resulting capacities.

Table 2.5: Summary of Specimens and Results (Nakahara and Tokuda, 2012)

| Specimen | a (in.) | $a/D$ | t (in.) | $D/t$ | $F_{ytm}$ (ksi) | $f'_{cm}$ (ksi) | $P/P_0$ | $V_{ed}$ (kips) | $M_{ed}/M_{PSDM}$ | Reported Failure Mode |
|---|---|---|---|---|---|---|---|---|---|---|
| N1 | 3.27 | 0.5 | 0.193 | 34.0 | 77.5 | 9.34 | 0 | 154 | 0.72 | shear |
| N2 | 3.27 | 0.5 | 0.193 | 34.0 | 77.5 | 9.34 | 0.3 | 158 | 0.67 | shear |
| N3 | 3.25 | 0.5 | 0.197 | 34.0 | 78.6 | 7.03 | 0.1 | 152 | 0.68 | shear |
| N4 | 3.25 | 0.5 | 0.197 | 34.0 | 78.6 | 7.03 | 0.2 | 155 | 0.68 | shear |
| N5 | 3.25 | 0.5 | 0.197 | 34.0 | 78.6 | 7.03 | 0.4 | 144 | 0.68 | shear |

Nakahara, et. al made the following observations:

- All CFST specimens, all having $a/D$ equal to 0.5, yielded in shear before flexure.
- The specimens increased in shear resistance after shear yielding occurred in the steel tube, reaching a maximum at a drift of 0.02 *radians*, without severe deterioration in force, before the test was stopped.
- The hysteretic behavior of short CFSTs was found to be sufficient for use as damping devices in seismic regions.
- An evaluation of the provision by the American Institue of Japan (2008) for the CFST shear calculation were found to be "safe" when compared to the experimental data.

*Ye, Han, Tao, and Guo (2016)*

Ye et al. (2016) tested CFST specimens with a similar setup to Nakahara and Tokuda (2012), having ends restrained from rotation and translation, but a stiff clamp was placed at midpsan where the actuator applied a displacement monotonically. This then results in a setup with two clear spans between load points. The researchers studied both circular and square CFSTs. For the purpose of relation to the current program, only the results from the circular specimens are included here. Ye et al. (2016) reported sixteen shear failures and four flexural failures, from the twenty circular CFSTs. Table 2.6 summarizes these specimens and results.

Table 2.6: Summary of Specimens and Results (Ye et al., 2016)

| Specimen | a (in.) | $a/D$ | t (in.) | $D/t$ | $F_{ytm}$ (ksi) | $f'_{cm}$ (ksi) | $P/P_0$ | $V_{ed}$ (kips) | $M_{ed}/M_{PSDM}$ | Reported Failure Mode |
|---|---|---|---|---|---|---|---|---|---|---|
| Y1 | 0.71 | 0.15 | 0.079 | 60 | 49.1 | 3.70 | 0 | 54 | 1.11 | shear |
| Y2 | 0.71 | 0.15 | 0.079 | 60 | 49.1 | 3.70 | 0 | 54 | 1.11 | shear |
| Y3 | 0.71 | 0.15 | 0.079 | 60 | 49.1 | 3.70 | 0.25 | 60 | 1.09 | shear |
| Y4 | 0.71 | 0.15 | 0.079 | 60 | 49.1 | 3.70 | 0.25 | 57 | 1.02 | shear |
| Y5 | 0.71 | 0.15 | 0.079 | 60 | 49.1 | 3.70 | 0.60 | 71 | 1.95 | shear |
| Y6 | 0.71 | 0.15 | 0.079 | 60 | 49.1 | 3.70 | 0.60 | 72 | 1.96 | shear |
| Y7 | 0.71 | 0.15 | 0.079 | 60 | 49.1 | 3.70 | 0.75 | 75 | 3.94 | shear |
| Y8 | 0.71 | 0.15 | 0.079 | 60 | 49.1 | 3.70 | 0.75 | 71 | 3.76 | shear |
| Y9 | 0.35 | 0.075 | 0.079 | 60 | 49.1 | 6.66 | 0.50 | 104 | 1.89 | shear |
| Y10 | 0.35 | 0.075 | 0.079 | 60 | 49.1 | 3.70 | 0.50 | 97 | 1.78 | shear |
| Y11 | 0.71 | 0.15 | 0.079 | 60 | 49.1 | 0.00 | 0.50 | 65 | 1.43 | shear |
| Y12 | 0.71 | 0.15 | 0.079 | 60 | 49.1 | 0.00 | 0.50 | 64 | 1.42 | shear |
| Y13 | 2.36 | 0.5 | 0.079 | 60 | 49.1 | 0.00 | 0.50 | 39 | 1.59 | flexure |
| Y14 | 2.36 | 0.5 | 0.079 | 60 | 49.1 | 0.00 | 0.50 | 44 | 1.76 | flexure |
| Y15 | 3.54 | 0.75 | 0.079 | 60 | 49.1 | 0.00 | 0.50 | 39 | 2.10 | flexure |
| Y16 | 3.54 | 0.75 | 0.079 | 60 | 49.1 | 0.00 | 0.50 | 37 | 1.99 | flexure |
| Y17 | 0.71 | 0.15 | 0.079 | 60 | 49.1 | 0.00 | 0.35 | 79 | 1.21 | shear |
| Y18 | 0.71 | 0.15 | 0.079 | 60 | 49.1 | 0.00 | 0.35 | 76 | 1.15 | shear |
| Y19 | 0.71 | 0.15 | 0.118 | 40 | 60.3 | 0.00 | 0.38 | 88 | 1.09 | shear |
| Y20 | 0.71 | 0.15 | 0.118 | 40 | 60.3 | 0.00 | 0.38 | 88 | 1.09 | shear |

Ye, et. al made the following observations:

- CFSTs with $a/D$ less than 0.5 failed in shear.
- CFSTs with $a/D$ greater than or equal to 0.5 failed in flexure.
- Smaller shear spans and higher axial load ratios, concrete strength, steel yield strength, and steel ratio ($A_{st}/A_c$) resulted in increased shear capacity. The increase in strength was nearly linear with increasing $P/P_0$, and with increasing $a/D$, the strength decreased more gradually.
- An assessment of Chinese code provisions (DBJ/T13-51-2010) demonstrated reasonable accuracy when compared to the experimental results.

### *2.3.3 Comparison of Previous Research to Current Shear Provisions*

The experimental shear capacities for each of the reported shear failures without axial load or expansive concrete is compared here to the current design provisions in order to assess their validity. For evaluation, the experimental shear capacities are normalized by the respective design method nominal values. These results are shown in Tables 2.7 through 2.9. AISC Method 3 is excluded since the absence of shear reinforcement makes this equivalent to Method 1. It is clear from these reports that the current design expressions are quite conservative and essentially inaccurate.

Table 2.7: Results using AISC Method 1, without Axial Load or Expansive Concrete

| Research Program | $V_{ed}/V_{n(AISC1)}$ | | | | | | |
|---|---|---|---|---|---|---|---|
| | No. Tests | Mean | Median | Max | Min | Std. Dev. | COV |
| Xiao | 18 | 3.56 | 3.51 | 4.34 | 2.73 | 0.54 | 0.15 |
| Xu | 3 | 2.20 | 2.15 | 2.40 | 2.06 | 0.18 | 0.08 |
| Qian | 13 | 3.35 | 3.16 | 3.99 | 2.31 | 0.56 | 0.17 |
| Nakahara | 1 | 1.73 | 1.73 | 1.73 | 1.73 | N/A | N/A |
| Ye | 2 | 3.20 | 3.20 | 3.22 | 3.19 | 0.019 | 0.0059 |
| All Specimens | 37 | 3.30 | 3.22 | 4.34 | 1.73 | 0.67 | 0.20 |

Table 2.8: Results using AISC Method 2, without Axial Load or Expansive Concrete

| Research Program | $V_{ed}/V_{n(AISC2)}$ | | | | | | |
|---|---|---|---|---|---|---|---|
| | No. Tests | Mean | Median | Max | Min | Std. Dev. | COV |
| Xiao | 18 | 48.1 | 44.2 | 81.7 | 29.2 | 14.0 | 0.29 |
| Xu | 3 | 28.5 | 27.8 | 31.1 | 26.7 | 2.3 | 0.08 |
| Qian | 13 | 46.7 | 45.3 | 66.1 | 34.3 | 10.2 | 0.22 |
| Nakahara | 1 | 26.8 | 26.8 | 26.8 | 26.8 | N/A | N/A |
| Ye | 2 | 27.2 | 27.2 | 27.3 | 27.1 | 0.16 | 0.0059 |
| All Specimens | 37 | 44.3 | 42.2 | 81.7 | 26.7 | 13.50 | 0.30 |

Table 2.9: Results using WSDOT Method (prior to 2016 BDM), without Axial Load or Expansive Concrete

| Research Program | $V_{ed}/V_{n(Method\ 4)}$ | | | | | | |
|---|---|---|---|---|---|---|---|
| | No. Tests | Mean | Median | Max | Min | Std. Dev. | COV |
| Xiao | 18 | 3.42 | 3.37 | 4.18 | 2.61 | 0.52 | 0.15 |
| Xu | 3 | 2.12 | 2.07 | 2.31 | 1.99 | 0.17 | 0.08 |
| Qian | 13 | 3.22 | 3.09 | 3.80 | 2.24 | 0.51 | 0.16 |
| Nakahara | 1 | 1.67 | 1.67 | 1.67 | 1.67 | N/A | N/A |
| Ye | 2 | 3.02 | 3.02 | 3.03 | 3.01 | 0.018 | 0.0059 |
| All Specimens | 37 | 3.18 | 3.11 | 4.18 | 1.67 | 0.64 | 0.20 |

As it stands, the WSDOT approach to calculating shear resistance is the most precise, even being an average of less than one-third of the measured resistance and having a coefficient of variation of 0.20. AISC Method 1 is close behind WSDOT though. The results with AISC Method 2 are extremely conservative with the predicted capacity less than half of the average experimental values, because AISC Method 2 heavily relies on the concrete fill contribution. However, there are concerns with the applicability of this data.

Most researchers defined failure mode primarily by the specimens' shear span to depth ratio. Furthermore, some researchers did not clearly define their interpretation of the shear span length, $a$, with their experimental setup. In theory, the shear span is the distance be-

tween the load point and support point. In actuality, the true location of force concentration onto a specimen is difficult to determine, because load application is spread over an area and can continuously change through the test, particularly when large rotations occur. Furthermore, the spans required to induce shear failure in these tests are small, and therefore, even small variations in true span length greatly affect behaviors and make conclusions based solely on this value futile.

Ultimately though, many of the reported shear capacities may actually be controlled by flexural resistance. The measured shear resistances then are not actually full capacities, but rather either corresponding shear values to ultimate flexural resistance or combined flexure-shear behavior. Additionally, the data with axial load and expansive concrete are not included in this analysis, as they are not included in the provisional calculations. Both of these components increase the observed shear resistance and therefore would be underestimated even more significantly. Taking these circumstances into account, the predictive models are even more conservative than noted in the tables.

### *2.3.4 Assessment of Experimental Specimens and Setups*

Thorough evaluation of the experimental specimens and setups of the prior experiments were performed so that this research study could improve upon past studies. Some uncertainties with the setups, largely shear span and the combination of flexure and shear behaviors, have already been noted and were considered in the design of this program, accordingly. In addition to those concerns though, the specimen compositions of the programs were also examined. All previous experiments presented in this section utilized steel end caps on the CFST specimens. These caps limit the slippage between the concrete fill and the steel tube and, ultimately, are expected to increase the CFST's resistance. Xu et al. (2009) provides support for this conclusion (Figure 2.4). The reliability of the weld strength on the CFST behavior was also noted, sometimes resulting in failure of the specimen at the end plate weld rather than in the CFST itself. Therefore, determination of their influence with this data is uncertain and conclusions on composite behaviors can not be made. For these reasons, no

end caps were to be used in the current experimental program.

Another concern with the prior studies' specimens is the short overhang length provided beyond support points. A large contribution to the CFSTs' capacity is the strength provided by the bond between the steel tube and concrete fill. For this to develop, a minimum length is required. This was not explicitly examined by the prior experimenters and, therefore, is assessed in the present program.

Lastly, it was noted that the five researchers tested small-scale specimens of about six inches in diameter. Because size effects often can have influence on member behaviors, the current program tested larger-scale specimens with diameters more than three times this (20 $in.$). Additionally, the prior research suggests that with the increase in diameter, $D$, the shear resistance will increase by $D^2$. Based on this and preliminary finite element analyses of larger CFSTs, the load demands on the system needed to induce failure of specimens this size were expected to increase by a magnitude of ten compared to the prior researchers. This creates more complications in the designing of the experimental apparatus. Considering the large demands then, a double-curvature apparatus like that used by Nakahara not only requires less force, but also better control of invoking shear in the specimen. However, a double-curvature design calls for the construction of a large, complex mechanism in order to apply such high shear forces, while restraining the specimen against rotation. This approach would become rather expensive and so a simpler scheme, more similar to that of Xian, Xu, and Qian, was more attainable. Nevertheless, a simpler setup though comes with difficulties in establishing definitive shear span lengths and developing appropriate moment diagrams with truly pinned conditions that do not induce additional forces into the specimen. All of these aspects need to be recognized when analyzing the data collected with these previous programs and when looking to develop a new experimental program.

## 2.4 Previous Analytical Modeling of CFSTs

### 2.4.1 Summary of Available Analytical Programs

As seen with the experimental work, little analytical modeling of CFSTs in shear has been performed. Ignoring the difficulty in modeling concrete materials, the complex shearing actions of the composite action in CFSTs is an inherently difficult problem to solve by non-linear finite element analysis. Nevertheless, success has been found by previous researchers in simulating CFSTs. Their efforts are summarized here by researcher and objective, as they relate to the goals of the present program.

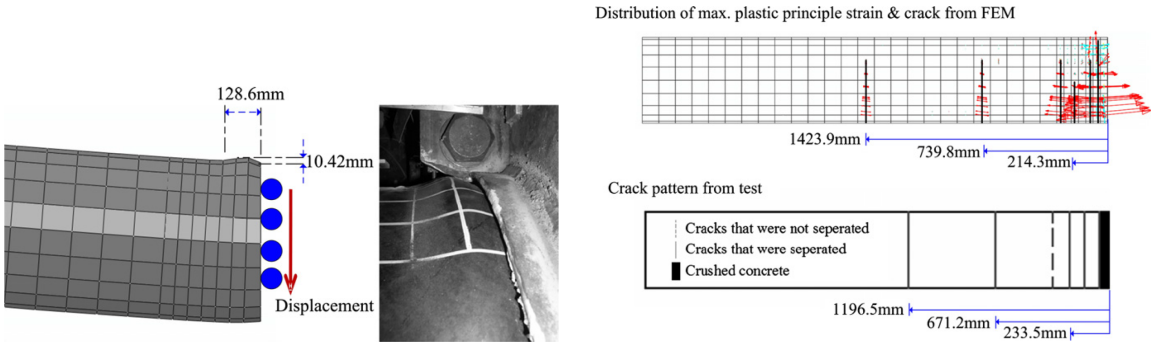
### 2.4.2 Bending and Combined Loading of Circular CFSTs - Moon et al. (2012, 2013)

Moon et al. (2012) developed a finite element model in the program ABAQUS (Dassault Systemes Simulia Corp.) for the simulation of the bending behavior of circular CFSTs, validated against experimental research performed by Thody (2006). Thody (2006) tested large-scale CFSTs with a three-point bending apparatus to observe flexural behavior. The analytical study was created to supplement the experimental data with simulated parametric studies.

In the developed simulation, the concrete fill and steel tube were modeled as separate parts, with 8-node solid elements (C3D8R) and 4-node shell elements (S4R), respectively. Then, the tube steel and concrete fill were connected by GAP elements that utilized a friction coefficient to define transverse behavior at the two materials' interfaces. A friction coefficient of 0.47 was calibrated in this study with experimental slip data. In the normal direction, the surfaces were restricted from penetrating at their interface while applying a compressive stress, but not permitting tensile stress development upon separation.

The compressive stresses of the GAP elements were found to provide the necessary confinement and composite action of CFST members without requiring an explicit confined concrete material model. So, a uniaxial stress-strain relationship was defined as part of the concrete damaged plasticity (CDP) model provided in ABAQUS. The CDP model requires

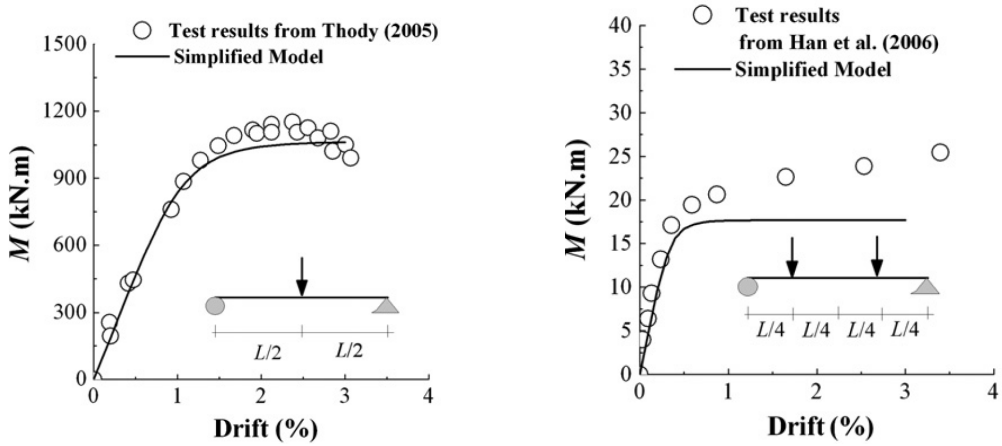
the definition of five parameters, detailed later in this document. In Moon et al. (2012), the authors focused discussion on the calibration of the dilation angle parameter, $\psi$, as it pertains to the confinement effect in the CFST specimen, concluding that a value of 20° was appropriate. The steel was simulated with a trilinear stress-strain behavior. Lastly, symmetry was utilized along the CFST's cross-section at the central point load location, where an imposed displacement was applied. The model was verified by demonstrating observed local buckling and concrete crack patterns (Figure 2.7), and closely predicting moment-drift relationships seen in the experiments by Thody (2006) and Han et al. (2006) (Figure 2.8).




(a) Local Behaviors of Tube Steel

(b) Cracking of Concrete Fill

Figure 2.7: Validation of Model by Moon et al. (2012) with Simulated and Observed Local Behaviors




(a) Using Thody (2006) Data (b) Using Han et al. (2006) Data

Figure 2.8: Validation of Model by Moon et al. (2012) with Moment vs. Drift Relationships

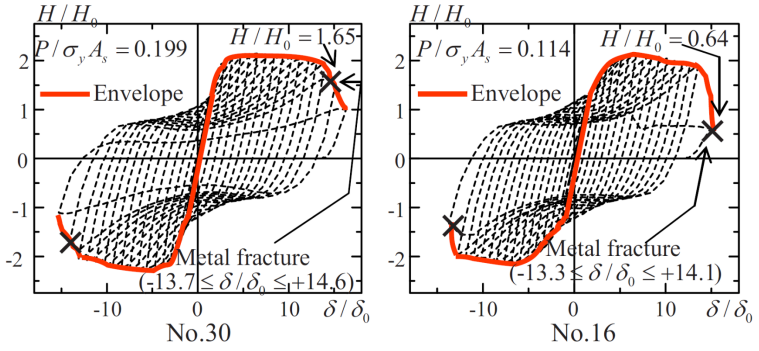
Moon used this model to perform parameter studies in order to define the effects of $D/t$ and $F_{yt}/f'_c$ on flexural response. The authors concluded that $F_{yt}/f'_c$ improved the moment strength of CFST members while delaying the initiation of local buckling. The $D/t$ ratio though did not significantly affect bending behavior. The same base model was then used in Moon et al. (2013) for the evaluation of design provisions for CFSTs with and without internal reinforcement under combined loading. The reinforcement was modeled with truss elements constrained to the movement of the surrounding concrete elements with the "EMBEDED" property. The model proved to again be effective at predicting local behaviors in the tube steel and concrete, and moment drift relationships observed by multiple experimental programs. This study concluded that the plastic stress distribution method did not sufficiently represent global buckling effects. Therefore, an adaptation to the material P-M interaction curve was proposed to account for stability.

### *2.4.3 Cyclic Behavior of Circular Steel Columns with In-Filled Concrete - Goto et al. (2010)*

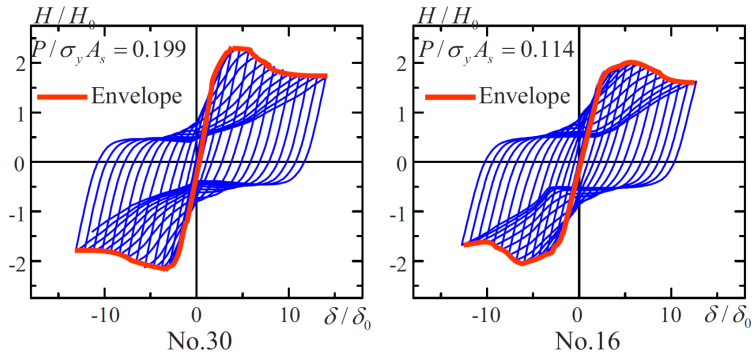
The analytical research program by Goto et al. (2010) proposed a finite element model in ABAQUS that accurately simulated cyclic local buckling of the steel tube, nonlinear concrete fill behavior, and the interface condition between the concrete fill and steel tube of experimental research by the Public Work Research Institute (1997-2000). These experiments were performed on one-third scale elevated highway bridge piers with a fixed base. An axial compressive load was held constant while an alternating lateral displacement was applied quasistatically to the top of the CFST cantilever.

In the proposed model, the researchers simulated the CFST with two parts: a steel tube using 4-node shell elements (S4R) and a concrete fill using 8-node solid elements (C3D8R). For the interface action, a surface contact was defined with "Hard Contact" normal pressure and a coulomb friction coefficient, $\mu$, of 0.2 in the tangential direction. The material model of the tube steel was calibrated using a three-surface cyclic plasticity model. For the concrete fill, the CDP model provided by ABAQUS was used, with the dilation angle, $\psi$, defined as 38°. The compressive behavior showed to be sufficient in the model; however, the tension behavior in the CDP model did not properly demonstrate the crack opening and closing action of the concrete fill with load reversals in the experiment. Therefore, a predefined discrete crack surface was modeled at a location similar to the experimental cracking surface. With this modeling technique, the pinching behavior of the hysteretic curve was captured, as shown in Figure 2.9.

While the simulation successfully captured load magnitude and pinching, it did not accurately predict the occurrence of steel tube fracture ('×' in figures) or the subtle post-peak softening observed in the experiment. Nevertheless, the researchers concluded that the model accurately represented the cyclic action of CFSTs, by showing tensile and compressive reversal in the tube and continued stress increase in the concrete fill beyond its compressive strength, as permitted by the tube confinement.




(a) Experiments




(b) Simulations

Figure 2.9: Validation of Model by Goto et al. (2010) with Hysteretic Behaviors

### *2.4.4 Finite Element Modeling of CFSTs Subjected to Constant Axial Compression and Shear Loads - Han et al. (2008)*

The analyses presented by Han et al. (2008) were performed using the ABAQUS software so that a simple model of the interaction between axial load, moment, and shear in CFSTs could be developed. The finite element models used in this study were based on those developed in a previous program that looked at pure and combined torsion (Han et al., 2007b,a). Both the tube steel and concrete fill of the CFST were modeled with 8-node brick elements (C3D8R) and their interface with a surface-based interaction using a normal "Hard Contact" pressure and coulomb friction coefficient in the tangential direction. The steel material used was a bilinear, elastic-plastic model with a hardening modulus of $0.01E_s$. The concrete material was modeled using the concrete damaged plasticity option with a confined concrete relationship developed by the authors (Han et al., 2007b).

The simulation used a cantilever setup, with the base of the CFST column fixed and both axial and lateral load being applied to the top surface. However, the experimental programs used to validate this model did not use these boundary conditions. The model was compared to four experimental programs (Tomii and Sakino, 1979; Ichinohe et al., 1991; Xiao et al., 2012; Xu et al., 2009). All of these experiments used small scale specimens with small $D/t$ ratios, end caps, and a combination of square and circular cross-sections. Three of the researchers tested their specimens under three-point bending. The last (Ichinohe et al., 1991) used a double cantilever setup. Nonetheless, the analyses were validated against shear, moment, deflection, and rotation from these experiments. Figure 2.10 illustrates the accuracy achieved using shear vs. deflection behaviors from Xiao et al. (2012) and Xu et al. (2009).

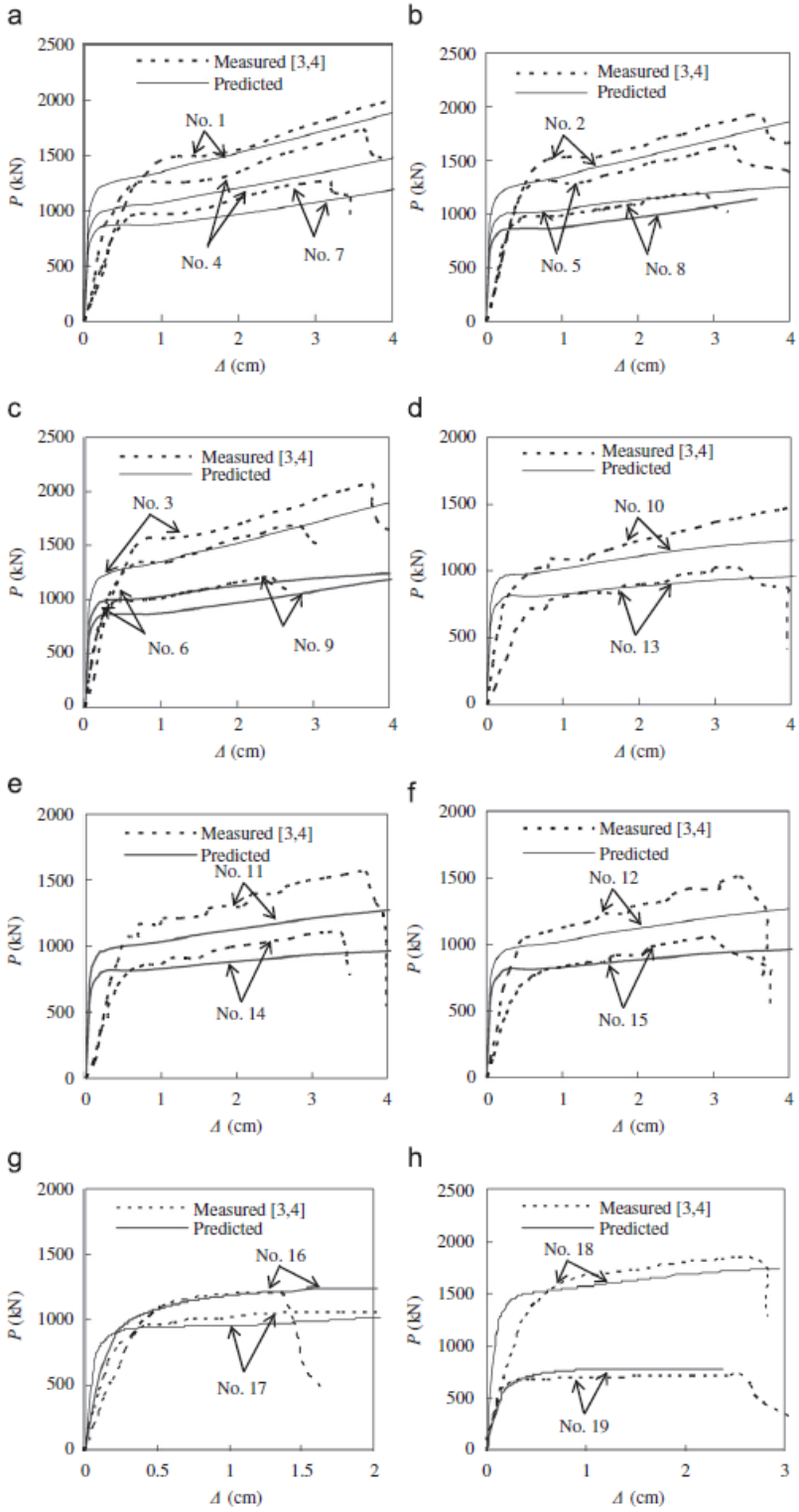



Figure 2.10: Validation of Model by Han et al. (2008) with Select Experimental Data Sets

# Chapter 3

# EXPERIMENTAL PROGRAM SUMMARY

## *3.1 Introduction*

The experimental program was developed to investigate the shear capacity of CFSTs and RCFSTs, and the impact of various parameters on this resistance. This chapter summarizes the testing procedure, specimen matrix, and conclusions from the experiments. For further details, see Maki (2015).

## *3.2 Experimental Setup and Procedure*

A four-point loading configuration was used in this testing plan because it simplified maximum moment determination of the specimen, which was crucial in distinguishing shear from bending-controlled failures, and was far less expensive than a double-curvature apparatus. Additionally, large bearing stresses with the large-scale specimens were lessened with the use of four-point over three-point loading. The four-point setup also isolated flexural and shear damage to separate regions of the specimen. For example, flexural buckling and concrete cracking would occur within the pure moment region, leaving the concrete in the shear spans confined and undisturbed by flexural action. Figures 3.1 and 3.2 illustrate the final apparatus, with detailed drawings for the rig provided in Appendix B.

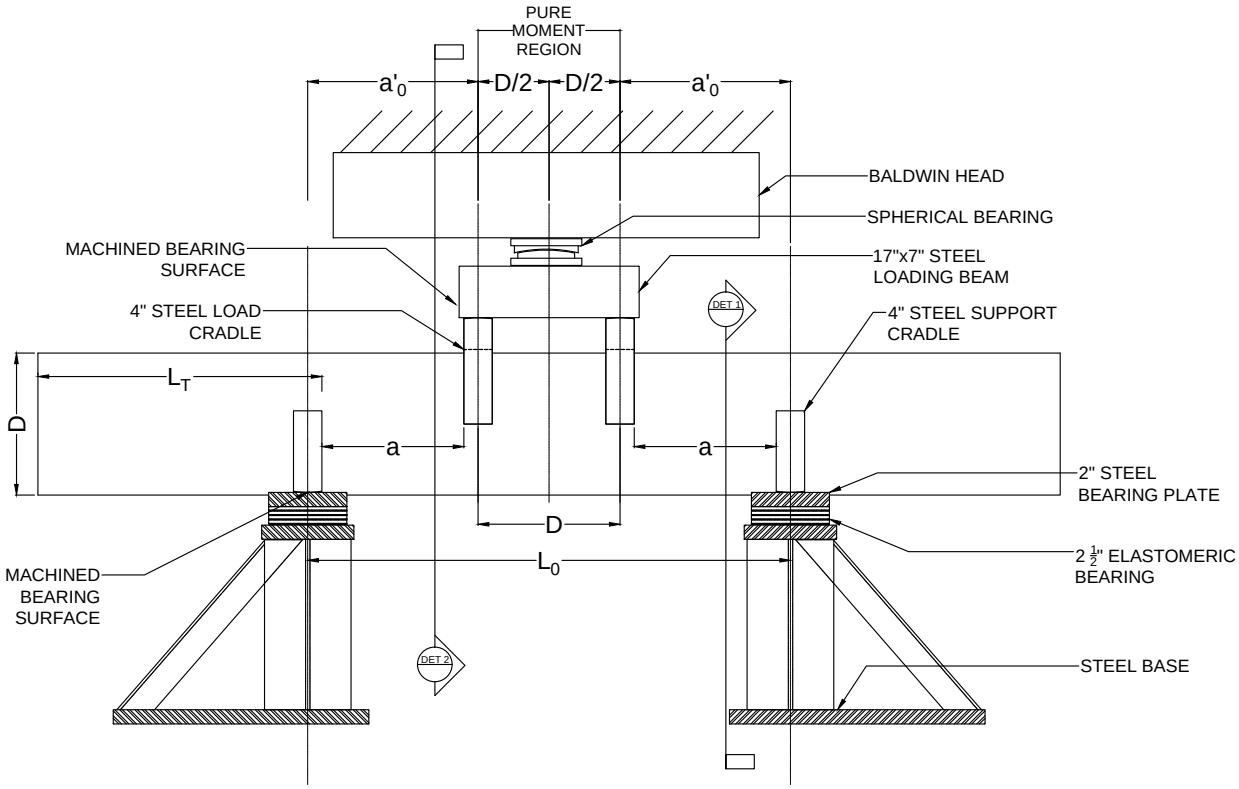


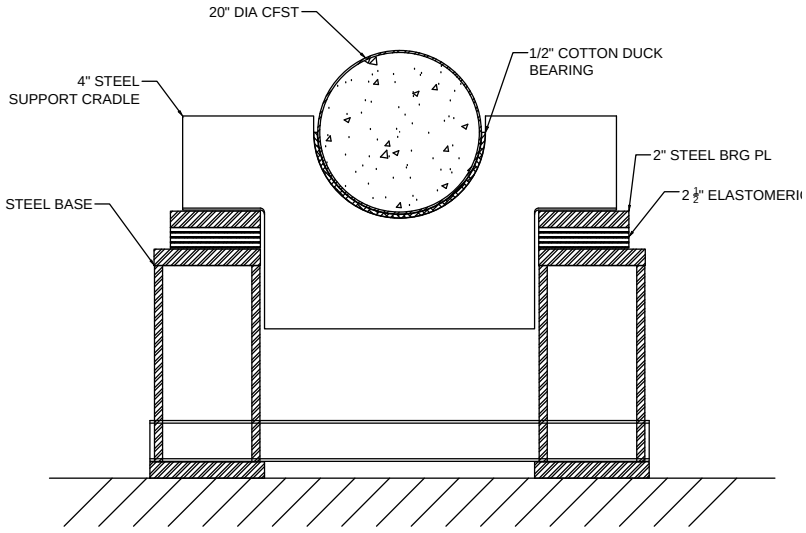

Figure 3.1: Schematic of Experimental Apparatus

A number of dimensions used for specimen design are shown in Figure 3.1. They are defined as follows:

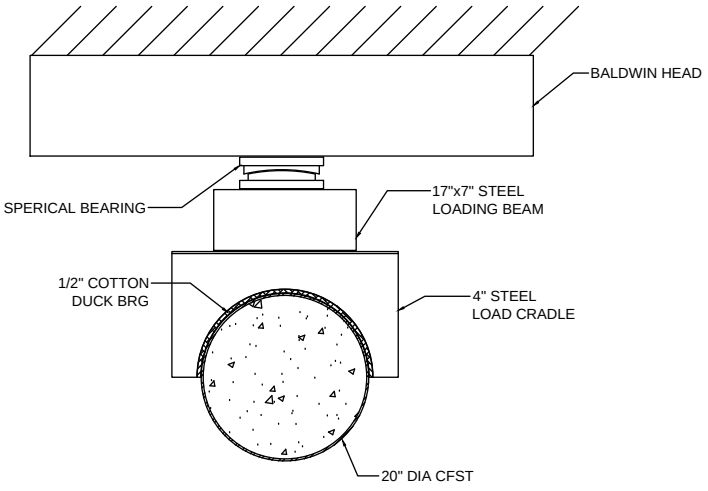
- $a$ is the clear shear span
- $a_0'$ is the initial center-to-center distance from the support cradle to load cradle
- $D$ is the outer diameter of the CFST specimen
- $L_0$ is the initial center-to-center span length
- $L_T$ is the overhang/tail length

Bishop (2009) concluded that the mean flexural capacity of various experiments on CFSTs was 123% of the plastic moment as determined by the plastic distribution method, $M_{PSDM}$. In theory then, specimens that fail by bending reach approximately $1.25M_{PSDM}$, while shear controlled specimens fail at a smaller moment. Therefore, the apparatus was designed for a shear force demand corresponding to the development of $1.25M_{PSDM}$ of the CFSTs being tested and a moment arm as defined by $a_0'$. These design values are shown in Table 3.4.

In addition to force magnitudes for setup design purposes, the preliminary ABAQUS analyses showed that large specimen rotations, significant strains at the extreme tension side of the steel tube, and flexural buckling at the top of the tube in the pure moment region were expected in these tests. Therefore, the setup was also designed to accommodate these deformation behaviors. To permit rotations of load and support cradles due to specimen rotations, a radius was cut along their bearing surfaces. Elastomeric bearings were utilized under the support cradles to accept the large lateral forces and deformations. Lastly, cotton duck bearing pads were inserted between the cradles and CFST specimen contact points to distribute bearing stresses and limit local damage to the specimen. These are illustrated in Figure 3.2 and 3.3.




(a) Apparatus Support Detail




(b) Apparatus Load Detail

Figure 3.2: Experimental Apparatus Details

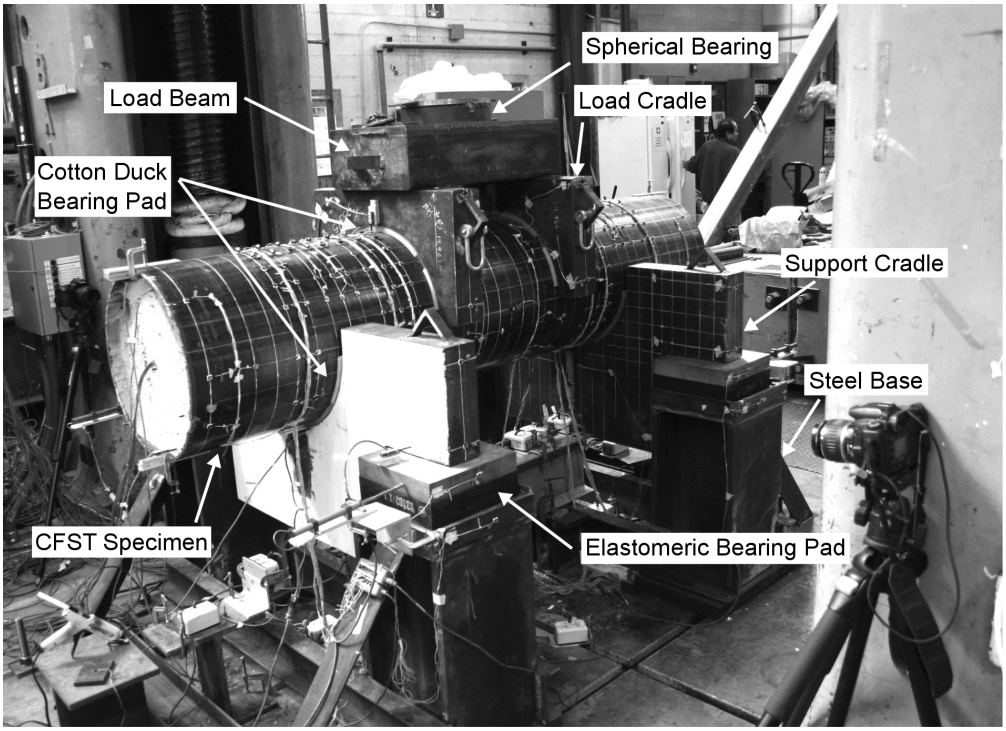


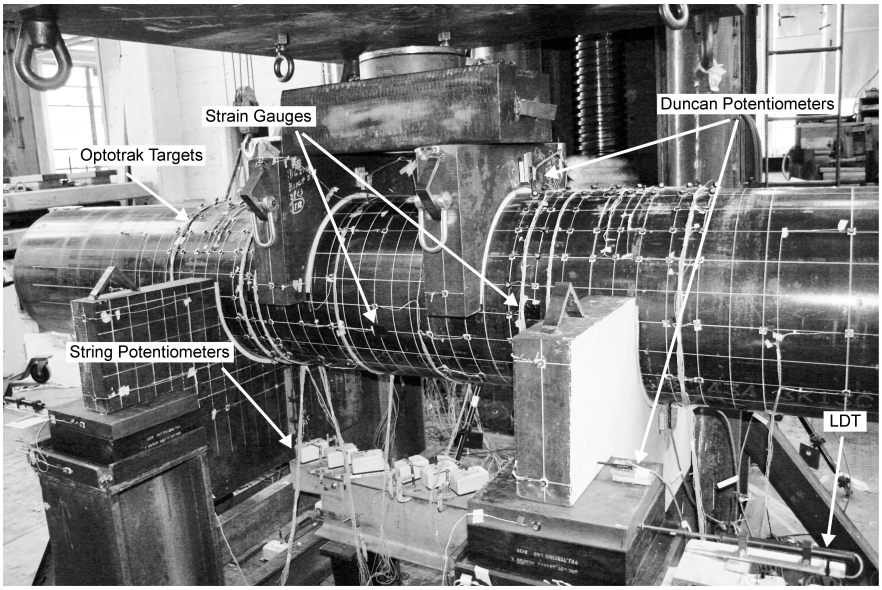

Figure 3.3: In-Place Experimental Apparatus

The tests were conducted using the 2.4-million pound Baldwin hydraulic testing machine in the structures laboratory at the University of Washington ("Baldwin Head" in Figure 3.1). The Baldwin machine is calibrated annually using AWST-traceable load cells and can be operated under both displacement and load controls. A combination of these was used to load the CFST specimens. Load control was used starting with 5 *kip* increments up to 40 *kips* load, followed by 10 *kip* increments up to 80 *kips*, and 20 *kip* increments until significant non-linearity in force-displacement behavior was observed. At this point, displacement control was used at a rate of 0.002 $in./sec$ until failure occurred.

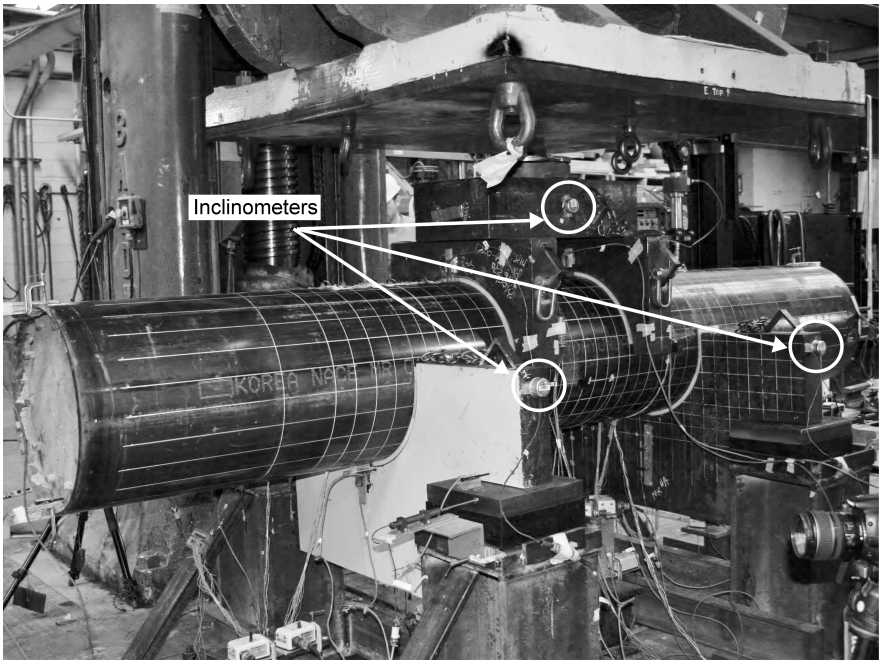
Extensive instrumentation was used on both the specimen and the apparatus to capture all deformations of the system, as shown in Figure 3.4. These included:

- *TML strain gauges* - single element and three-element rosettes directly applied to the steel tube in critical regions

- *Geokon vibrating wire gauges* - embedded in the concrete fill of select specimens
- *Linear displacement transducers (LDT)* - used at various locations to capture displacements of the specimen and setup
- *String Potentiometers* - used at various locations to capture larger displacements of the specimen and setup
- *Duncan linear potentiometers* - used at various locations to capture small displacements of the specimen and setup
- *Inclinometers* - attached directly to support cradles and load beam to measure setup rotations
- *NDI Optotrak Certus system* - LED targets are placed directly on the west side of the steel tube in a grid layout; their movements are captured by two cameras positioned outside the testing area




(a) West Side Instrumentation




(b) East Side Instrumentation

Figure 3.4: Typical Experiment Instrumentation

The exact locations and data collected from these instruments are reported in detail in Maki (2015). However, this thesis focuses on the data collected by the Optotrak system and, thus, is explained further here. A grid was drawn on each specimen to help visualize deformation patterns and provide discrete points for the placement of the Optotrak targets. The grid was spaced about 2.5 to 1 *in.* in the critical shear span area so that large inelastic strains and deflection behaviors of the setup and specimen could be estimated. The locations of the targets varied slightly among the specimens with different shear spans, as illustrated in Figures 3.5 through 3.8.

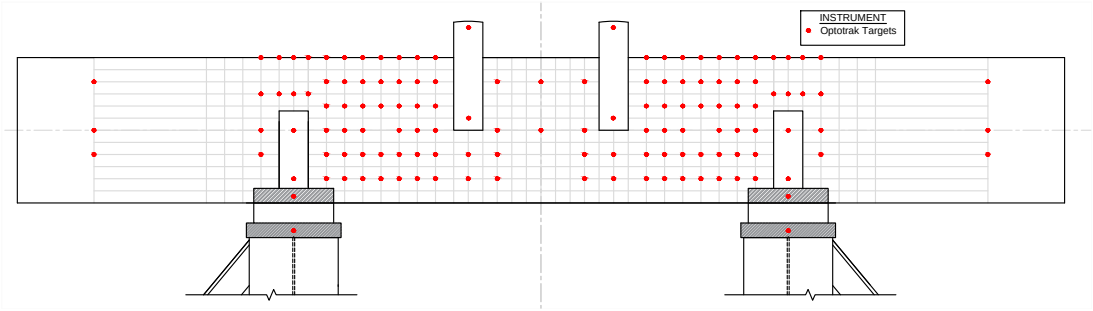



Figure 3.5: Optotrak Layout for $a/D = 1.0$

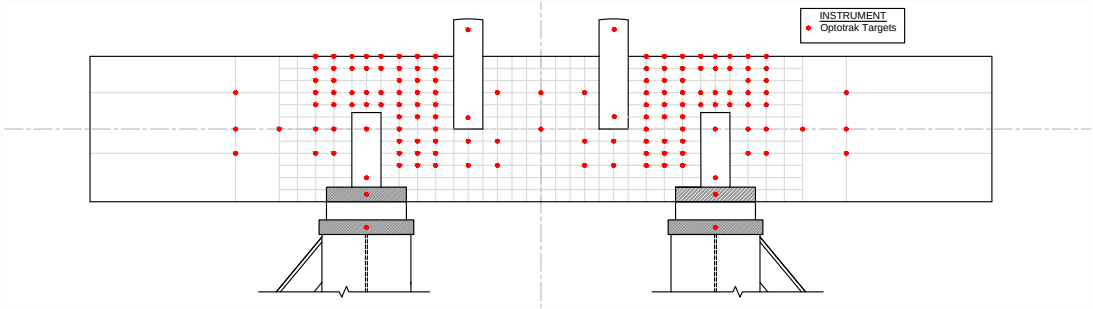



Figure 3.6: Optotrak Layout for $a/D = 0.5$

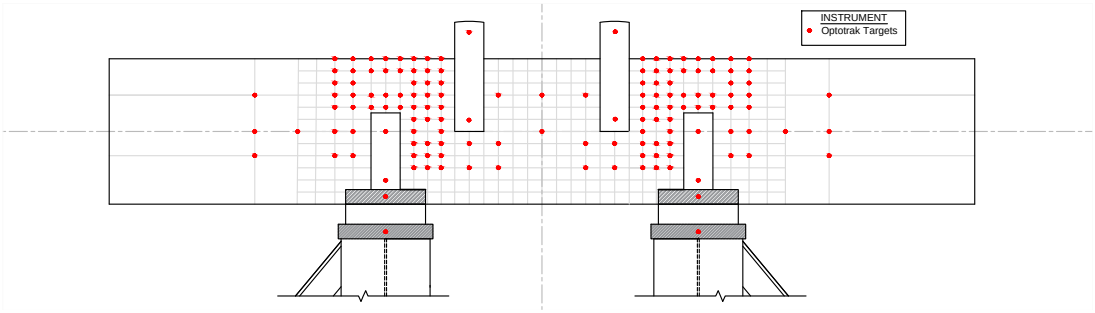



Figure 3.7: Optotrak Layout for $a/D = 0.375$

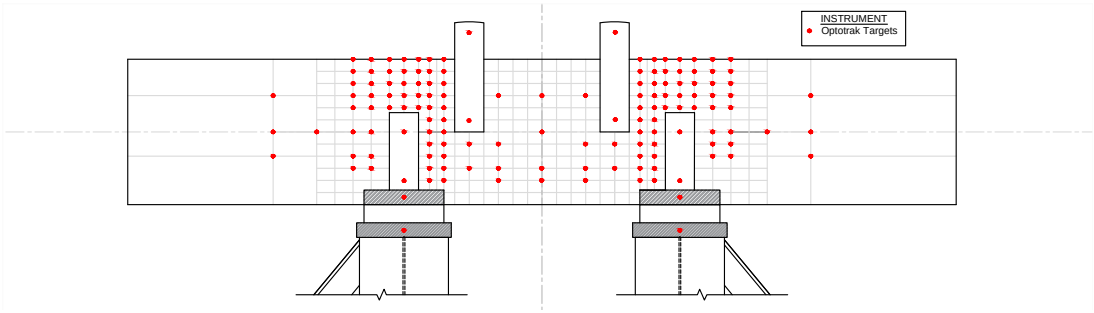



Figure 3.8: Optotrak Layout for $a/D = 0.25$

## *3.3 Test Matrix*

### *3.3.1 Specimens*

Twenty-one specimens were tested under the four-point loading described. They were prepared without special cleaning of the tube interface or special curing processes, unless noted as part of the testing program study. The steel tubes were first cut to length with an oxygen-acetylene cutting torch and placed vertically so that concrete could be pumped through a hose at the top. They were then left to cure with wet burlap covering the exposed top for at least 28 days. Table 3.1 summarizes the specimens made for the test matrix in the experimental program. All CFSTs had outer diameters, $D$, of 20 *in.*, but varied otherwise to address the following relevant parameters:

1. Shear span to depth ratio, $a/D$: 1.0, 0.5 , 0.375, and 0.25
2. Length beyond support/tail length, $L_T$: $2D$, $D$, $5/8 \cdot D$, and $D/2$
3. Tube diameter to wall thickness ratio, $D/t$: 80 and 53.3
4. Prescribed concrete strength, $f'_c$: 12, 6, 2.5, and 0 $ksi$ (where 0 indicates the presence of gravel in place of concrete fill in the shear span)
5. Interface condition between tube steel and concrete fill: clean, greased, and muddied
6. Tube type: spiral and straight-seam
7. Internal Reinforcement, $\rho_{int}$: 0, 1, and 2%
8. Axial load ratio, $P/P_0$: 0 and 8.5% of the CFST's nominal axial capacity

Table 3.1: Test Matrix

| Specimen | $a/D$ | t (in) | a (in) | D/t | $F_{yt}$ (ksi) [2] | $f'_c$ (ksi) | $P/P_0$ | $L_T$ (in.) | $\rho_{int}$ | Interface [3] |
|---|---|---|---|---|---|---|---|---|---|---|
| 10 [1] | 0.375 | 0.25 | 7.5 | 80 | 42 | 6.0 | 0 | 2D | 0 % | Clean |
| 1 | 1.0 | 0.25 | 20 | 80 | 42 | 6.0 | 0 | 2D | 0 % | Clean |
| 2 | 0.5 | 0.25 | 10 | 80 | 42 | 6.0 | 0 | 2D | 0 % | Clean |
| 3 | | 0.25 | 10 | 80 | 42 | 6.0 | 0 | D/2 | 0 % | Clean |
| 4 | | 0.25 | 10 | 80 | 42 | 6.0 | 0 | D | 0 % | Clean |
| 5 | | 0.25 | 10 | 80 | 42 | 6.0 | 0 | 2D | 0 % | Muddy |
| 6 | | 0.25 | 10 | 80 | 70 | 6.0 | 0 | 2D | 0 % | Spiral |
| 9 | | 0.25 | 10 | 80 | 42 | 6.0 | 0 | 2D | 0 % | Greased |
| 12 | | 0.25 | 10 | 80 | 42 | 6.0 | 0 | 2D | 1.13 % | Clean |
| 17 | | 0.25 | 10 | 80 | 42 | 12 | 0 | 2D | 0 % | Clean |
| 18 | | 0.375 | 10 | 53.3 | 42 | 12 | 0 | 2D | 0 % | Clean |
| 19 | | 0.375 | 10 | 53.3 | 42 | 12 | 0 | 2D | 1.07 % | Clean |
| 7 | 0.375 | 0.25 | 7.5 | 80 | 42 | 6.0 | 0 | 2D | 1.04 % | Clean |
| 8 | | 0.25 | 7.5 | 80 | 42 | 6.0 | 0 | 2D | 2.01 % | Clean |
| 11 | | 0.25 | 7.5 | 80 | 42 | 6.0 | 0 | D/2 | 0 % | Clean |
| 13 | | 0.25 | 7.5 | 80 | 42 | 6.0 | 0.085 | D/2 | 0 % | Clean |
| 16 | | 0.25 | 7.5 | 80 | 42 | 12 | 0 | 2D | 0 % | Clean |
| 21 | | 0.25 | 7.5 | 80 | 42 | gravel | 0 | 2D | 0 % | Clean |
| 14 | 0.25 | 0.25 | 5 | 80 | 42 | 12 | 0 | 2D | 0 % | Clean |
| 15 | | 0.25 | 5 | 80 | 42 | 12 | 0 | 5/8·D | 0 % | Clean |
| 20 | | 0.25 | 5 | 80 | 42 | 2.5 | 0 | 2D | 0 % | Clean |

[1] Specimen 10 was the baseline test in the entire series. The test parameters that differ from this specimen are highlighted.

[2] All tube steel conformed to both API 5L X42 and ASTM A53B standards, except Specimens 6 and 22 which conformed to ASTM A1011 HSLAS Gr 70 C1/C2.

[3] All specimens were constructed with straight-seam tubes unless noted otherwise.

### *3.3.2 Materials*

A summary of the measured material properties for the specimens is found in Tables 3.2 and 3.3. Twenty test specimens were constructed with straight-seam tubes that conform to API 5L X42 and ASTM A53B standards. Specimen 6 was constructed from a spirally welded tube made with ASTM A1011 HSLAS coil steel, having a greater yield strength than the straight-seamed tube, and formed with double submerged arc welding. The RCFST specimens used reinforcing bars that conformed to ASTM A615 Gr 60 standards at a minimum, with some up to ASTM A706 Gr 60, as noted in the table. The steel material properties presented were found by performing tensile tests on coupons from each 40 $ft.$ stock tube and rebar samples from each RCFST specimen, according to ASTM E8/E8M-15.

Three concrete mix designs were used in the specimens: a low strength, high strength, and mid-range strength. Each utilized normal weight aggregate and contained no designated self-consolidating or low-shrinkage characteristics. The properties presented in Table 3.2 were gathered from compression testing according to ASTM C39/C39M of standard 6 $\times$ 12 $in.$ cylinders that were prepared at each casting date and cured in a temperature and moisture-controlled room. These cylinders were tested at 7, 14, and 28 days, in addition to the day of each CFST test (i.e. reported value). The high strength concrete was specified for 12 $ksi$ 28-day strength, but tested at a much lower value. However, cores taken from a couple specimens tested at higher strengths than those reported by the prepared cylinders. The testing of these cores suggest that the compressive strength of the concrete fill for many specimens could be higher than reported by the cylinders. Nevertheless, these cores were taken at later dates than the individual CFST tests, and some of the additional strength could be attributed to this. Therefore, the prepared cylinder data is reported and used in data analyses.

Table 3.2: CFST Material Properties

| Specimen | Tube Steel | | | | Concrete Fill | | | | |
|---|---|---|---|---|---|---|---|---|---|
| | Tube ID * | $F_{yt}$ (ksi) | $F_{ytm}$ (ksi) | $F_{utm}$ (ksi) | Mix ID * | $f'_c$ (psi) | $f'_{cm}$ (psi) | $f'_{ctm}$ (psi) | Age (days) |
| 1 | SS-1 | 42 | 49.6 | 61.0 | 563375 | 6000 | 6012 | 630 | 22 |
| 2 | SS-1 | 42 | 49.6 | 61.0 | 563375 | 6000 | 6220 | 561 | 31 |
| 3 | SS-2 | 42 | 50.1 | 61.0 | 563375 | 6000 | 6655 | 554 | 45 |
| 4 | SS-2 | 42 | 50.1 | 61.0 | 563375 | 6000 | 6558 | N/A | 59 |
| 5 | SS-1 | 42 | 49.6 | 61.0 | 563375 | 6000 | 7041 | 704 | 101 |
| 6 | SW-1 | 70 | 70.8 | 83.5 | 563375 | 6000 | 7182 | 554 | 115 |
| 7 | SS-2 | 42 | 50.1 | 61.0 | 563375 | 6000 | 6447 | 704 | 50 |
| 8 | SS-3 | 42 | 53.9 | 66.1 | 563375 | 6000 | 6484 | 552 | 56 |
| 9 | SS-2 | 42 | 50.1 | 61.0 | 563375 | 6000 | 6317 | 506 | 33 |
| 10 | SS-3 | 42 | 53.9 | 66.1 | 563375 | 6000 | 6151 | 608 | 42 |
| 11 | SS-4 | 42 | 56.8 | 66.4 | 563375 | 6000 | 6609 | 645 | 47 |
| 12 | SS-3 | 42 | 53.9 | 66.1 | 563375 | 6000 | 6177 | 592 | 28 |
| 13 | SS-3 | 42 | 53.9 | 66.1 | 563375 | 6000 | 5326 | 570 | 64 |
| 14 | SS-6 | 42 | 55.4 | 71.3 | 880378X | 12000 | 8596 | 694 | 41 |
| 15 | SS-6 | 42 | 55.4 | 71.3 | 880378X | 12000 | 8792 | 796 | 47 |
| 16 | SS-4 | 42 | 56.8 | 66.4 | 880378X | 12000 | 8609 | 737 | 34 |
| 17 | SS-6 | 42 | 55.4 | 71.3 | 880378X | 12000 | 9450 | 753 | 50 |
| 18 | SS-5 | 42 | 57.2 | 70.2 | 880378X | 12000 | 8641 | 760 | 54 |
| 19 | SS-5 | 42 | 57.2 | 70.2 | 880378X | 12000 | 9131 | 706 | 56 |
| 20 | SS-4 | 42 | 56.8 | 66.4 | 3051 | 2500 | 2787 | 347 | 37 |
| 21 | SS-4 | 42 | 56.8 | 66.4 | N/A | N/A | N/A | N/A | N/A |

* See Maki (2015) for tube tensile test data and detailed concrete mix designs.

Table 3.3: CFST Reinforcing Bar Material Properties

| Specimen | Reinforcing Steel | | | | |
|---|---|---|---|---|---|
| | Bar Size | ASTM Spec | $F_{yrl}$ (ksi) | $F_{yrlm}$ (ksi) | $F_{urlm}$ (ksi) |
| 7 | No. 5 | A615 | 60 | 72.3 | 107.8 |
| 8 | No. 7 | A706 | 60 | 68.4 | 96.7 |
| 12 | No. 5 | A615 | 60 | 71.5 | 107.6 |
| 19 | No. 5 | A706 | 60 | 68.5 | 98.4 |

## 3.4 Results

### *3.4.1 Specimen Failure*

CFST specimen failure was determined in the experiments by a significant drop in resistance occurring with the formation of a significant tube tear. For RCFSTs, failure was noted when the tube tore and at least two layers of tensile reinforcing steel ruptured, resulting in a significant drop in resistance. After failure, the specimens were removed from the test apparatus and the steel tube was cut away from the concrete so that damage of the concrete fill could be closely examined. Numerous photos were taken before, during, and after testing. The photos, visual observations, and the data collected were used to evaluate the experiments.

The undeformed clear shear span length, $a$, was used to define the initial $a/D$ ratio. However, the load and support forces are applied over a width of 4 $in.$, so that the true distance between load points can vary significantly with specimen rotation. Additionally, the total span, $L$, and the shear spans, $a'_{north}$ and $a'_{south}$, were not constant throughout each test, as a result of the large plastic deformations, the short shear spans, and the vertical location of the support cradle's bearing surface (i.e. not at the plastic neutral axis, which is important for flexure determination). This is illustrated by Figure 3.9. Consequently, the total span and shear span lengths were measured using Optotrak targets. They start at initial lengths, $L_0$ and $a'_0$, and are measured at each time step of the Optotrak system during the test. This procedure is described in Appendix C for the specimens analyzed in Chapter 4, other data interpretation was completed in Maki (2015) and is used in this document.

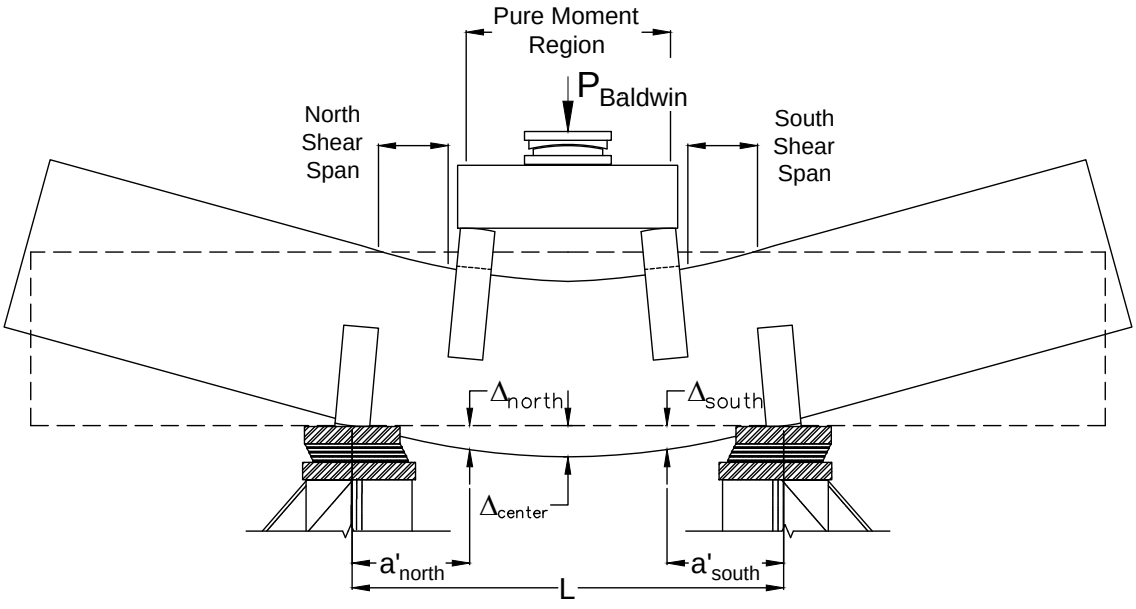



Figure 3.9: Deformed Geometry of Experimental Apparatus

Even a small change in length can be big relative to the short spans in this testing program, and this change in length is directly proportional to changes the bending moment that often dictates failure. For this reason, $a'$ values are considered more accurate for experimental moment and shear calculation purposes, $M_{exp}$ and $V_{exp}$, but less accurate in determining shear angle with shear controlled specimens due to cradle restraints here (see Figure 3.10).

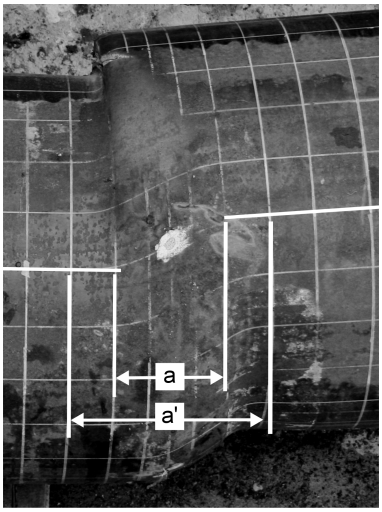



Figure 3.10: Shear Span Deformation

Furthermore, because the Baldwin load was applied to a spherical bearing at the center of of the specimen span, the applied load was intended to be divided equally between the two load cradles. However, despite the attempts made to ensure symmetry, differential movements occurred as a result of nonuniform yielding of the north and south spans. Therefore, the experimental shears and moments at the midspan, north span, and south span were adjusted according the the following expressions, with $P_{Baldwin}$ as the total force applied by the Baldwin UTM, in order to estimate the true internal forces of the specimen.

$$V_{north} = \frac{P_{Baldwin}}{2L}(L - a'_{north} + a'_{south}) \tag{3.1}$$

$$V_{south} = \frac{P_{Baldwin}}{2L}(L - a'_{south} + a'_{north}) \tag{3.2}$$

$$V_{center} = \frac{P_{Baldwin}}{2L}(a'_{south} - a'_{north}) \tag{3.3}$$

$$M_{north} = V_{north} \times a'_{north} \tag{3.4}$$

$$M_{south} = V_{south} \times a'_{south} \tag{3.5}$$

$$M_{center} = \frac{M_{north} + M_{south}}{2} \tag{3.6}$$

The concluded experimental shear value, $V_{exp}$, was taken as the larger, maximum value of $V_{north}$ and $V_{south}$ as calculated above, noting that the larger value represented the side that showed more shear deformations. The reported moment was most often $M_{center}$. However, when shear became more evident, the three moment values began to differ more significantly, and so the moment value corresponding to the side of failure was concluded as $M_{exp}$.

Additionally, because the experimental moment and shear values, $M_{exp}$ and $V_{exp}$ values, require detailed analysis of $a'_{north}$ and $a'_{south}$, a relatively uncertain value, for their determination, a simpler and more conservative method of reporting moment and shear values is also provided, where the applied Baldwin load was assumed to be distributed evenly to both supports and the moment arm was the known initial distance between load points with the full cradle contact area considered, $a'_0$. These are summarized by Equations 3.7 and 3.8.

$$V_{ed} = \frac{P_{Baldwin}}{2} \tag{3.7}$$

$$M_{ed} = V_{ed} \times a'_0 \tag{3.8}$$

A summary of values determined with these two methods is given in Table 3.4. In addition to simplicity, the use of the "experimentally determined" values allows for better comparison to previous studies where more detailed determination of the shear span was not available or reported. Nevertheless, the experimental values, $M_{exp}$ and $V_{exp}$, are provided to demonstrate the reliability and conservatism in using $M_{ed}$ and $V_{ed}$ to define shear and moment capacities in the analyses of this thesis. They are not used in any conclusions beyond this point.

Table 3.4: Moment and Shear Test Results

| Specimen | $a/D$ | Primary Study Parameter | $M_{PSDM}$ (k-in) | $V_{1.25MPSDM}$ (kips) | $M_{exp}$ (k-in) | $V_{exp}$ (kips) | $M_{ed}$ (k-in) | $V_{ed}$ (kips) |
|---|---|---|---|---|---|---|---|---|
| 1 | 1.0 | baseline | 6069 | 316 | 7893 [1] | 322 [1] | 7728 | 322.0 |
| 2 | 0.5 | baseline | 6085 | 543 | 8099 [1] | 550.8 [1] | 7686 | 549.0 |
| 3 | | $L_T = D/2$ | 6174 | 551 | 8111 | 552.0 | 7693 | 549.5 |
| 4 | | $L_T = D$ | 6167 | 551 | 8035 | 543.0 | 7595 | 542.5 |
| 5 | | muddied | 6143 | 549 | 8124 | 556.0 | 7756 | 554.0 |
| 6 | | spiral weld | 8533 | 762 | 11665 | 779.0 | 10864 | 776.0 |
| 9 | | greased | 6149 | 549 | 6528 | 442.0 | 6139 | 438.5 |
| 12 | | $\rho_{int} = 1.13\%$ | 8019 | 716 | 9679 | 651.0 | 9044 | 646.0 |
| 17 | | $f'_c$ | 6958 | 621 | 8056 [1] | 549.3 [1] | 7623 | 544.5 |
| 18 | | $D/t = 53.3$ | 10165 | 908 | 12444 | 832.0 | 11550 | 825.0 |
| | | $f'_c$ | | | | | | |
| 19 | | $\rho_{int} = 1.07\%$ | 11434 | 1021 | 13816 | 952.0 | 13230 | 945.0 |
| | | $D/t = 53.3$ | | | | | | |
| | | $f'_c$ | | | | | | |
| 10 | 0.375 | baseline | 6564 | 713 | 8159 [1] | 668.9 [1] | 7590 | 660.0 |
| 11 | | $L_T = D/2$ | 6926 | 753 | 7024 | 600.0 | 6889 | 599.0 |
| 7 | | $\rho_{int} = 1.04\%$ | 7524 | 818 | 8807 | 705.0 | 8102 | 704.5 |
| 8 | | $\rho_{int} = 2.01\%$ | 9016 | 980 | 9239 | 802.0 | 8947 | 778.0 |
| 13 | | $P/P_0 = 8.5\%$ | 7362 | 800 | 8270 | 710.0 | 8148 | 708.5 |
| | | $L_T = D/2$ | | | | | | |
| 16 | | $f'_c$ | 7069 | 769 | 9204 [1] | 759.2 [1] | 8746 | 760.5 |
| 21 | | gravel | 5539 | 602 | 5211 | 449.0 | 5164 | 449.0 |
| 14 | 0.25 | baseline | 6910 | 960 | 7678 [3] | 874.9 [3] | 7434 [3] | 788.4 [3] |
| 15 | | $L_T = 5/8 \cdot D$ [2] | 6922 | 961 | 7164 | 796.0 | 7164 | 796.0 |
| 20 | | $f'_c$ | 6451 | 896 | 6838 | 712.0 | 6404 | 711.5 |

[1] Some of these values may vary from Maki (2015), as they have been re-analyzed with slight variation in $a'$ determination. Only specimens that are modeled in Chapter 4 are adjusted here. See Appendix C.

[2] As part of the test matrix, the tail length for Specimen 15 was designated as $D/2$, but the actual length was $5/8 \cdot D$.

[3] The reported values correspond to the secondary peak shown in Figures 3.24 and 3.23, rather than the absolute maximum as it appears some sort of erroneous behavior may be observed here.

### *3.4.2 Failure Mode Characteristics*

Based on previous experimental research, the average moment capacity of CFSTs is 1.25 times the moment capacity predicted by the PSDM, $M_{PSDM}$. Therefore, it is expected that on average CFSTs would fail by shear when $V_{exp} \cdot a' < 1.25 M_{PSDM}$, and by bending when $V_{exp} \cdot a' > 1.25 M_{PSDM}$. However, there is uncertainty in this calculation for these experiments because $a'$ was not known with precision and 1.25 is only a mean value that includes statistical scatter. Therefore, it was not surprising to find that the results in this program differ from these remarks a bit. Additionally, there exists a region of behavior between definitive flexural and shear control, having characteristics of both. This observation does not suggest that the expected shear capacity will be reduced by bending moment, but that there is some uncertainty of response sequence here.

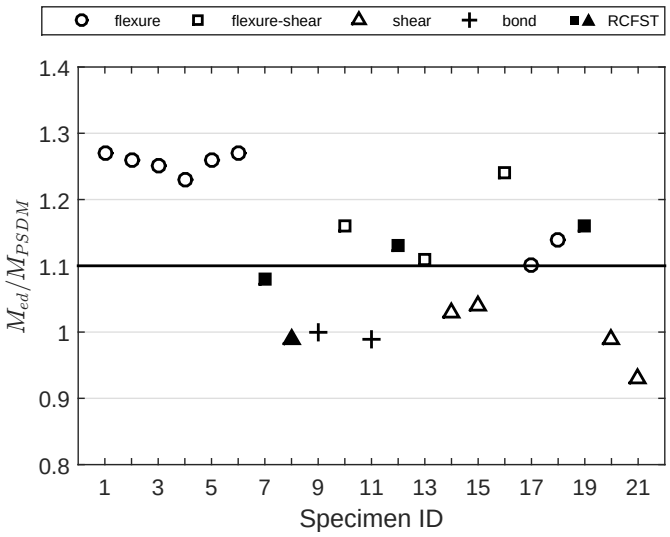
A last state of behavior seen in this study was bond slip failure. The parameters of tail length, $L_T$, and interface condition were included in the test matrix for direct influence on bond strength development. Slip at the steel-concrete interface was measured for all specimens so that assessment of the full development of bond at the tail could be evaluated. In the end, if the bond stress and tail length were not adequate to develop composite behavior, the full moment and shear capacity potential of the composite members could not be reached, resulting in decreased resistance.

Equations 3.1 through 3.8 were used to estimate the shear and bending moment responses of the CFST specimens. Trends including these, tube tearing, visual strain distribution of the steel tube, and final state concrete fill crack patterns were then established, and based on these, a set of criteria was developed to identify the four different failure modes: 1) flexural failure, 2) shear failure, 3) flexure-shear interaction, and 4) bond slip failure. By this evaluation, eight specimens fail in flexure, five specimens fail by shear, six specimens showed evidence of flexure-shear interaction, and two specimens displayed bond slip failure (clearly identified by severe slip). Table 3.5 summarizes this evaluation.

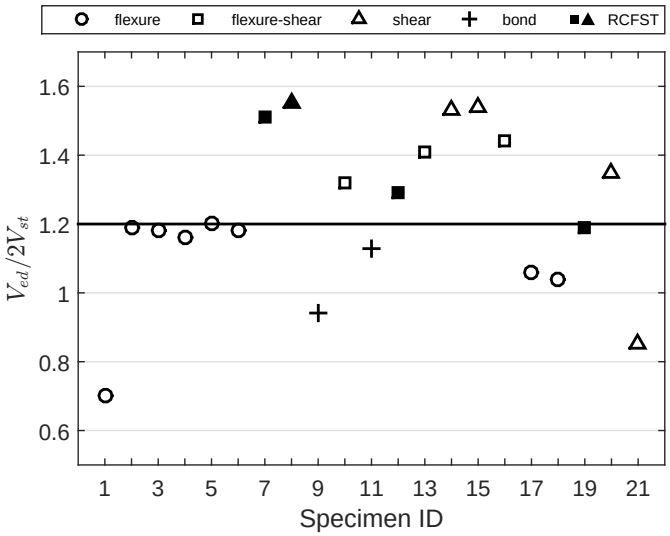
As part of this assessment, it was noted that shear failure modes could be approximated to

occur when an $M_{ed}/M_{PSDM}$ less than 1.10 was developed and sufficient bond stress provided, as shown in Figure 3.11a. From this criterion though, Specimen 7 should also be considered shear-controlled, but notable flexural deformations found during testing put this into the interaction category. Additionally, Maki (2015) found that a good approximation of the steel contribution could be $2V_{st}$, with $V_{st}$ as defined by WSDOT, 2012 and ASIC, 2010, based on the values obtained from Specimen 21 (gravel filled, see Section 3.4.3.4). Recognizing this, it can be found that when $V_{ed}/2V_{st}$ is less than 1.20, and adequate bond development is provided, flexurally dominant behavior is likely, with the potential of flexure-shear interaction behaviors to be present (Figure 3.11b). Specimen 21 was not part of this conclusion, as it was not considered a true CFST, having a shear span filled with gravel.

The following passages discuss the primary characteristics of each failure mode, including force-deflection responses of select specimens using a combination of data by Maki (2015) and that completed for this thesis, i.e. those analyzed in Chapter 4. A description of the procedures used for data filtering is provided in both the former document and in Appendix C. Furthermore, each of the moment and shear behavior plots provided in this section use a normalized deflection, $\Delta/a_0'$, and note the observed limits of $1.1M_{PSDM}$ and $1.2V_{st}$ discussed with a dotted line where notable.




(a) Normalized Moment




(b) Normalized Shear

Figure 3.11: Failure Mode Results

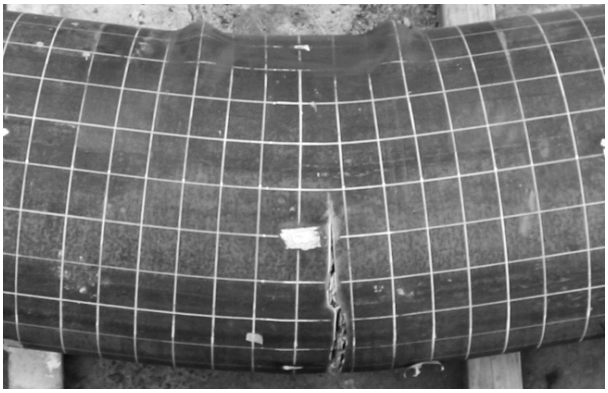
Table 3.5: Specimen Failure Mode Classification

| Failure Mode | Specimen | $a/D$ | Inclined Tear | Visible Flex. Def. | $M_{exp}/M_{PSDM}$ | $V_{exp}/2V_{st}$ | $M_{ed}/M_{PSDM}$ | $V_{ed}/2V_{st}$ | $Max\ Slip/L_T$ |
|---|---|---|---|---|---|---|---|---|---|
| Flexure | 1 | 1.0 | No | Yes | 1.29 | 0.70 | 1.27 | 0.70 | 0.06 % |
| | 2 | 0.5 | No | Yes | 1.31 | 1.19 | 1.26 | 1.19 | 0.04 % |
| | 3 | 0.5 | No | Yes | 1.31 | 1.18 | 1.25 | 1.18 | 0.44 % |
| | 4 | 0.5 | No | Yes | 1.30 | 1.16 | 1.23 | 1.16 | 0.13 % |
| | 5 | 0.5 | No | Yes | 1.32 | 1.20 | 1.26 | 1.20 | 0.06 % |
| | 6 | 0.5 | No | Yes | 1.37 | 1.18 | 1.27 | 1.18 | 0.02 % |
| | 17 | 0.5 | No | Yes | 1.16 | 1.06 | 1.10 | 1.06 | 0.03 % |
| | 18 | 0.5 | No | Yes | 1.22 | 1.05 | 1.14 | 1.04 | 0.03 % |
| Flex-Shear | 7 | 0.375 | Yes | Yes | 1.17 | 1.51 | 1.08 | 1.51 | 1.46 % |
| | 10 | 0.375 | Yes | Yes | 1.11 | 1.33 | 1.16 | 1.32 | 1.71 % |
| | 12 | 0.5 | Yes | Yes | 1.21 | 1.30 | 1.13 | 1.29 | 0.07 % |
| | 13 | 0.375 | N/A | Yes | 1.12 | 1.41 | 1.11 | 1.41 | 1.07 % |
| | 16 | 0.375 | Yes | Yes | 1.27 | 1.44 | 1.24 | 1.44 | 0.22 % |
| | 19 | 0.5 | Yes | Yes | 1.21 | 1.20 | 1.16 | 1.19 | 0.08 % |
| Shear | 8 | 0.375 | Yes | No | 1.02 | 1.60 | 0.99 | 1.55 | 0.55 % |
| | 14 | 0.25 | Yes | No | 1.21 | 1.70 | 1.03 | 1.53 | 0.18 % |
| | 15 | 0.25 | Yes | No | 1.04 | 1.54 | 1.04 | 1.54 | 3.23 % |
| | 20 | 0.25 | Yes | No | 1.06 | 1.35 | 0.99 | 1.35 | 0.43 % |
| | 21 | 0.375 | Yes | No | 0.94 | 0.85 | 0.93 | 0.85 | 0.11 % |
| Bond | 9 | 0.5 | No | Yes | 1.06 | 0.95 | 1.00 | 0.94 | 10.0 % |
| | 11 | 0.375 | Yes | No | 1.01 | 1.13 | 0.99 | 1.13 | 7.29 % |

#### *3.4.2.1 Flexural Failure in CFST*

The predominant characteristics of flexural failures in CFSTs include:

- Flexural buckling of the tube steel due to compressive flexural stresses, and rupture of steel tube due to tensile bending stresses within the pure moment region, as seen in Figure 3.12a.
- Plane section appear to remain approximately plane throughout the specimen, with no apparent shear strain deformation in the shear spans.
- The tube tears in a vertical direction within the pure moment region.
- Dense, transverse flexural cracking in the midspan region of the concrete fill as shown in Figure 3.12b.
- Minor to no diagonal cracking of the concrete fill in the shear spans, as demonstrated in Figure 3.12c.
- A moment-displacement response with a long, smooth plateau and sudden loss of resistance once the tube steel ruptures due to bending action. See Figures 3.14, 3.17, and 3.20.
- $M_{ed}/M_{PSDM}$ approximately greater than or equal to 1.10 and $V_{ed}/2Vs$ less than 1.20; however, not exclusively.
- Shear resistance values insufficient to induce significant shear deformations. See Figures 3.13, 3.16, and 3.19.



(a) Steel compression buckling and tensile tearing




(b) Flexural cracking of concrete fill in pure moment region




(c) Limited diagonal cracking of concrete fill in shear span

Figure 3.12: Characteristics of Flexural Failure Mode in CFSTs (as demonstrated by Specimen 17)

A few representative flexurally-controlled specimens are summarized here. These specimens are also used for analytical study in Chapter 4, so their detailed behaviors may be referenced in those discussions.

*Specimen 17 ($a/D = 0.5$, $L_T = 40$ in., $D/t = 80$, $\rho = 0\%$, $f'_c = 9450$ psi, clean interface)*
Specimen 17 had a prescribed 28-day concrete strength of $12,000$ $psi$, twice that of Specimen 2 (baseline specimen for $a/D = 0.5$), but had a measured concrete strength of 9.45 $ksi$. It achieved a moment of $1.10M_{PSDM}$ and shear of $1.06(2V_{st})$, curiously, both smaller forces than Specimen 2 with a smaller concrete strength of 6.22 $ksi$. This more limited force with the higher strength was only seen with these flexurally-dominated specimens, and may be a result of the more brittle behavior of higher strength concretes that impacts flexural compressive response. The tube steel tore just 2 $in$. south of the centerline after significant flexural deformations formed, including compression buckling of the tube in the pure moment region. The concrete showed crack patterns as described in the above summary. These deformations were shown in Figure 3.12 and the complete moment and shear-deflection responses are given in Figures 3.13 and 3.14.

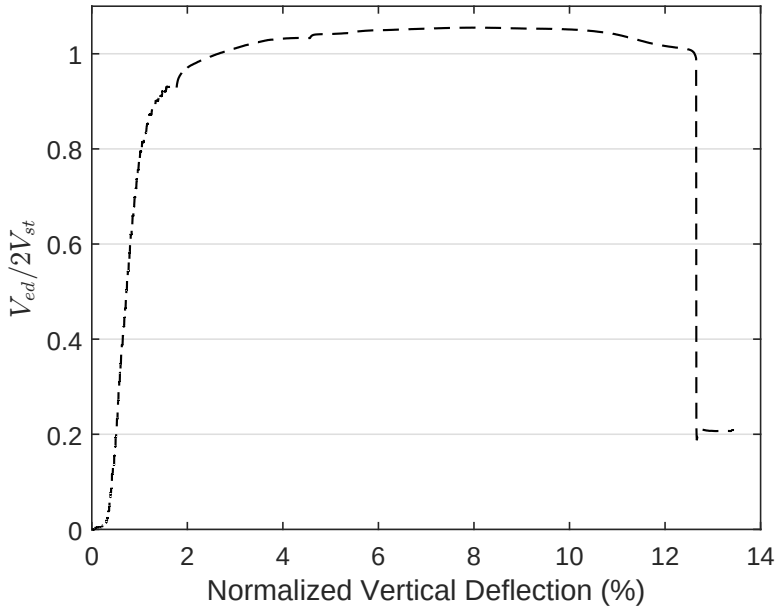



Figure 3.13: Specimen 17 Normalized Shear vs. Vertical Deflection Behavior

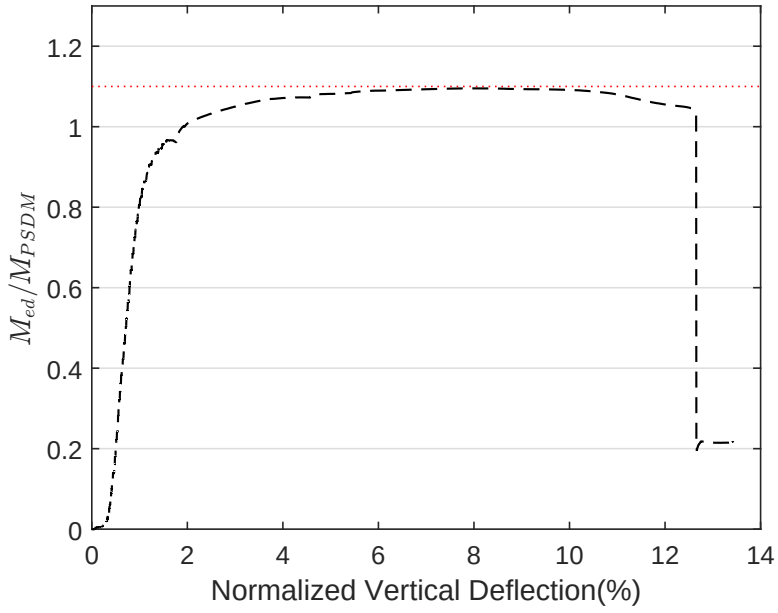
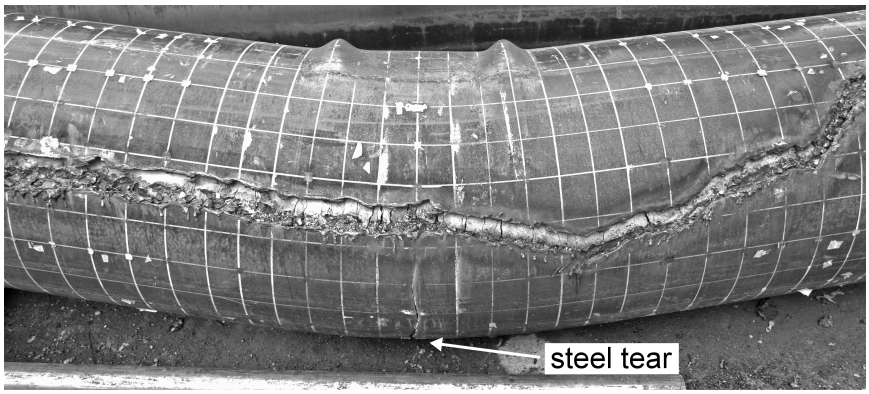


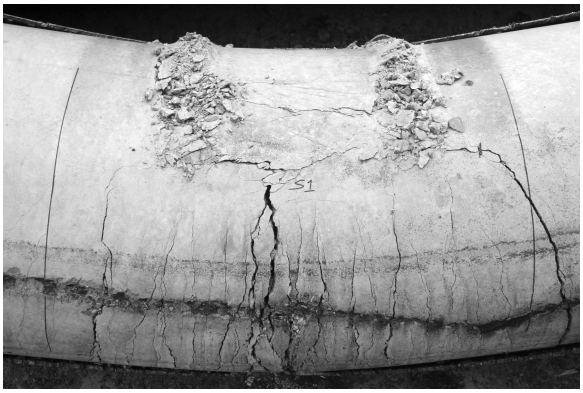

Figure 3.14: Specimen 17 Normalized Moment vs. Vertical Deflection Behavior

*Specimen 1 ($a/D = 1.0$, $L_T = 40$ in., $D/t = 80$, $\rho = 0\%$, $f'_c = 9450$ psi, clean interface)*

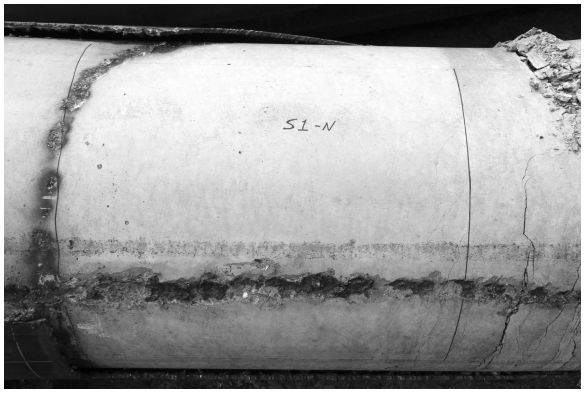
Specimen 1 was the only CFST specimen with a shear span to depth ratio of 1.0 and, hence, the only definitively planned flexural failure. The specimen failed after peaking at $1.27M_{PSDM}$ in moment and $0.70(2V_{st})$ in shear and tearing in the midspan region. The vertical tear in the tube occurred at the centerline of the specimen after flexural compressive buckling and tensile yielding formed. As described for specimens of this type, extensive flexural cracking and no diagonal shear cracking was found in the concrete fill. Figures 3.15 through 3.17shows these behaviors and the force-deflection relations observed.




(a) Deformed state of steel tube




(b) Flexural cracking of concrete fill in pure moment region




(c) No diagonal cracking of concrete fill in shear span

Figure 3.15: Specimen 1 Photos

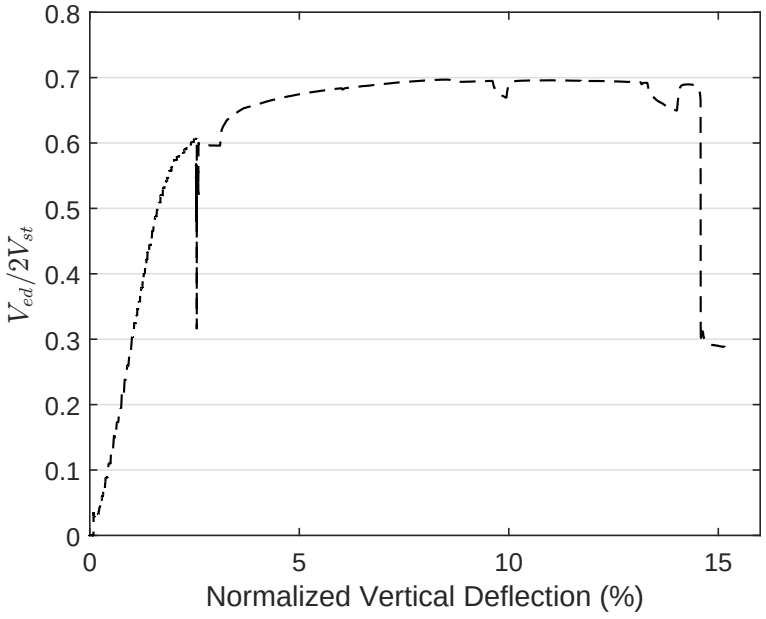



Figure 3.16: Specimen 1 Normalized Shear vs. Vertical Deflection Behavior

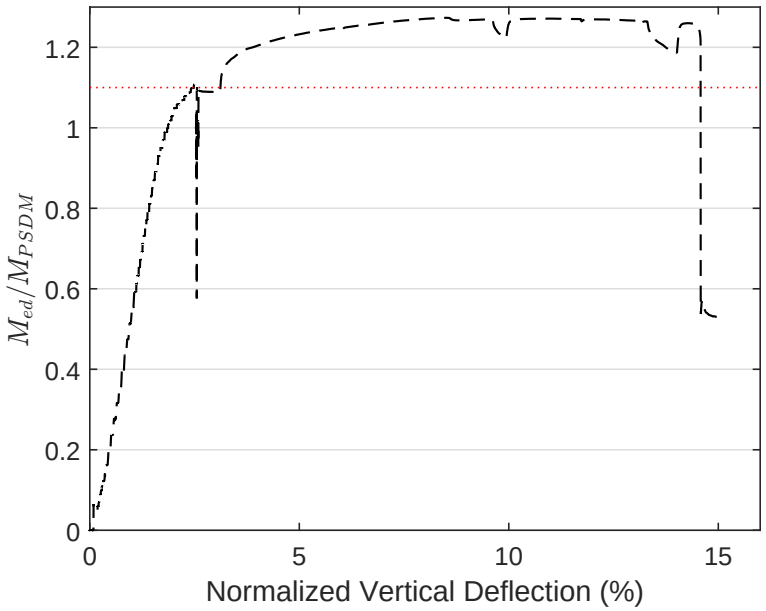
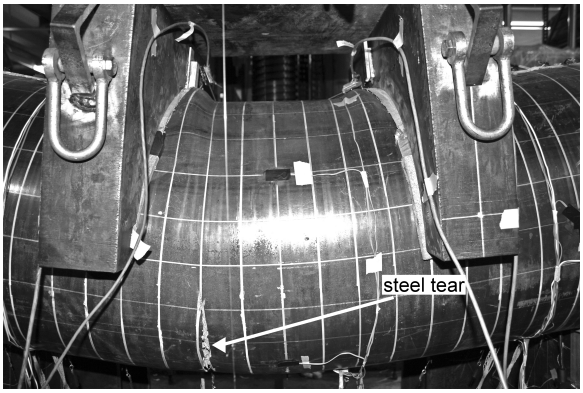
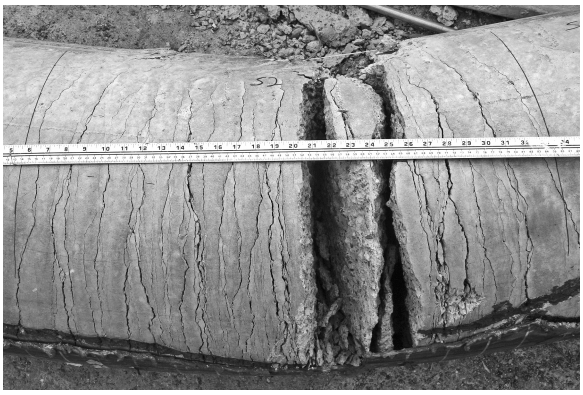



Figure 3.17: Specimen 1 Normalized Moment vs. Vertical Deflection Behavior

*Specimen 2 ($a/D = 0.5$, $L_T = 40$ in., $D/t = 80$, $\rho = 0\%$, $f'_c = 6220$ psi, clean interface)*
Specimen 2 was the baseline specimen for $a/D = 0.5$. The specimen achieved $1.26M_{PSDM}$ in moment and $1.19(2V_{st})$ in shear. The tube tore vertically in flexural tension 4 *in.* south of the centerline, with evident flexural deformations that included compressive buckling at the top of the tube (more prominently on the south side). Limited diagonal cracking was present in the shear spans and dense flexural cracking was found in the midspan region. These behaviors and force-deflection responses are shown in Figures 3.18 through 3.20.




(a) Deformed state of steel tube



(b) Flexural cracking of concrete fill in pure moment region



(c) Limited diagonal cracking of concrete fill in shear span

Figure 3.18: Specimen 2 Photos

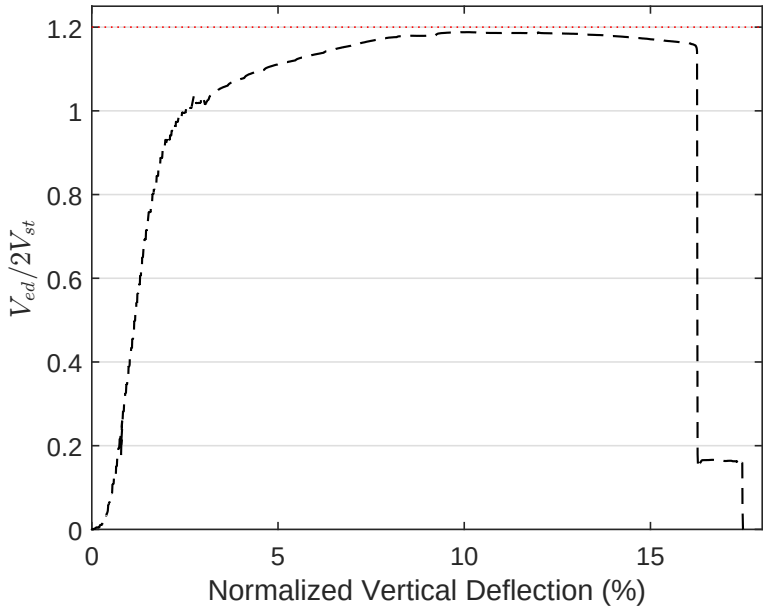



Figure 3.19: Specimen 2 Normalized Shear vs. Vertical Deflection Behavior

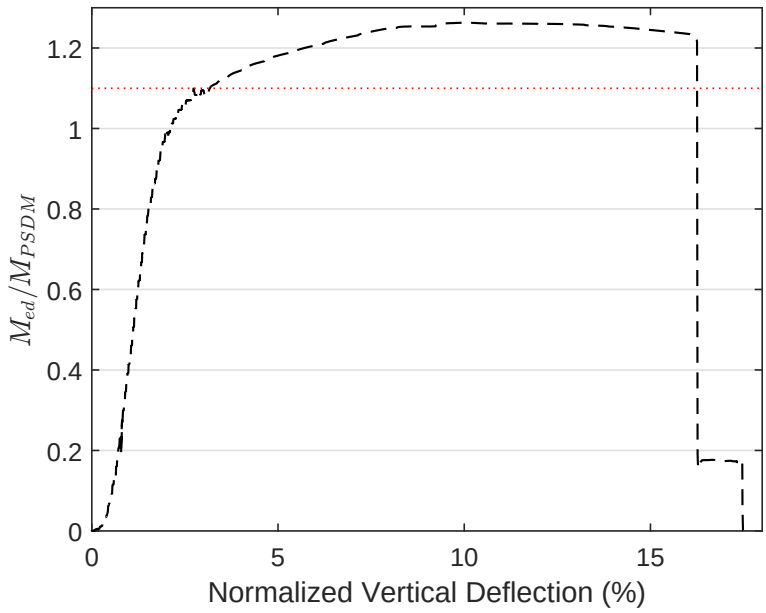
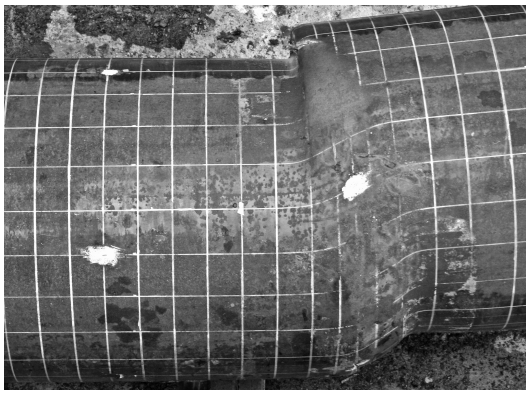



Figure 3.20: Specimen 2 Normalized Moment vs. Vertical Deflection Behavior

#### *3.4.2.2 Shear Failure in CFST*

The predominant characteristics of shear failures in CFSTs include:

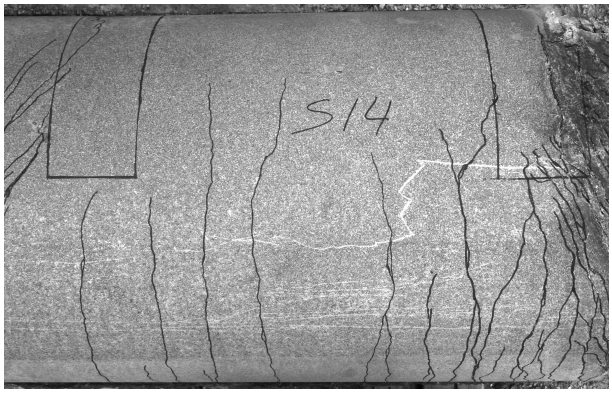
- Evident shear straining and inclined tearing of the steel tube in at least one shear span. See Figure 3.21a and b.
- No visible flexural deformation of the steel tube, including flexural buckling, in the pure moment region (Figure 3.21a).
- Relatively minor flexural cracking in the concrete fill, as seen in Figure 3.21c.
- Extensive diagonal cracking in the concrete fill in the shear spans. See Figure 3.21d.
- $M_{ed}/M_{PSDM}$ less than 1.10.



(a) Evidence of shear yielding strain in shear span



(b) Inclined steel tube tear in shear zone*




(c) Minimal flexural cracking of concrete fill in pure moment region




(d) Extensive diagonal cracking of concrete fill in shear span

Figure 3.21: Characteristics of Shear Failure Mode in CFSTs (as demonstrated by Specimen 14 and *Specimen 8)

*Specimen 14 ($a/D = 0.25$, $L_T = 40$ in., $D/t = 80$, $\rho = 0\%$, $f'_c = 8596$ psi, clean interface)*

A good representative specimen of this failure mode was Specimen 14, the baseline specimen for $a/D = 0.25$. Photos of this specimen's behaviors are already given in Figure 3.21. Specimen 14 reached a moment and shear force magnitude of $1.03M_{PSDM}$ and $1.53(2V_{st})$, respectively. The complete moment and shear-displacement relationships are shown in Figures 3.23 and 3.24. In addition to the general observations for shear specimens, an inclined tear formed in the north shear span at the bottom of the tube and at the top against the north load cradle (Figure 3.22). The latter likely being a product of localized forces from the boundary condition here. Visible shear yielding was observed in the tube and dense diagonal cracking in the concrete fill of the north shear span. There was also a notable amount of diagonal cracking of the concrete fill in the south shear span, with limited flexural cracking in the midspan region.

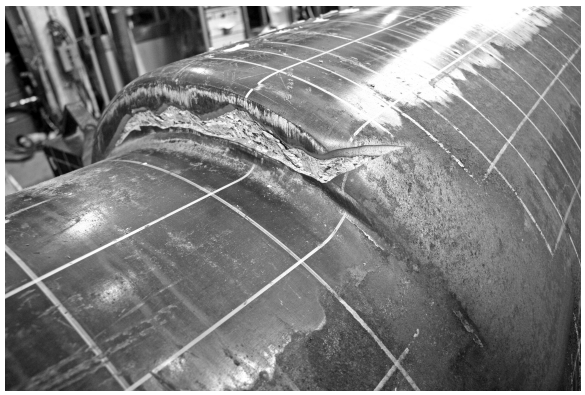


Figure 3.22: Specimen 14 Tear in Top of Steel Tube

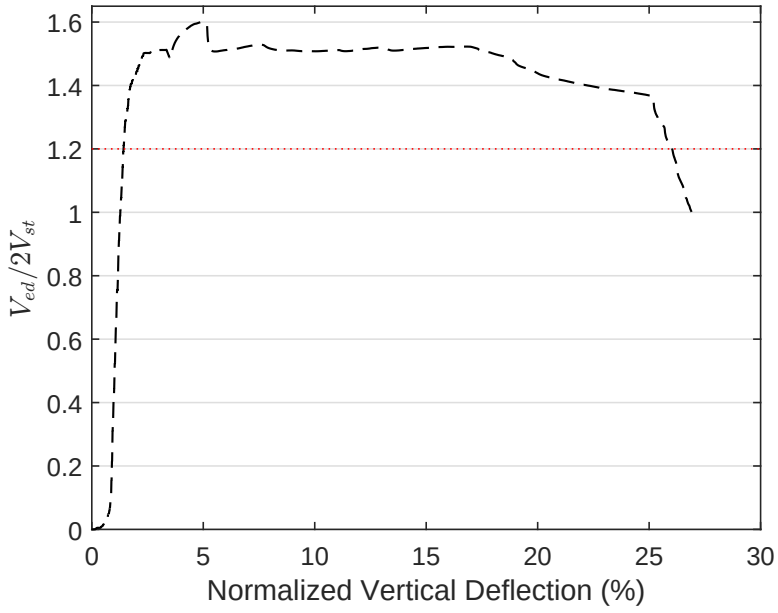



Figure 3.23: Specimen 14 Normalized Shear vs. Vertical Deflection Behavior

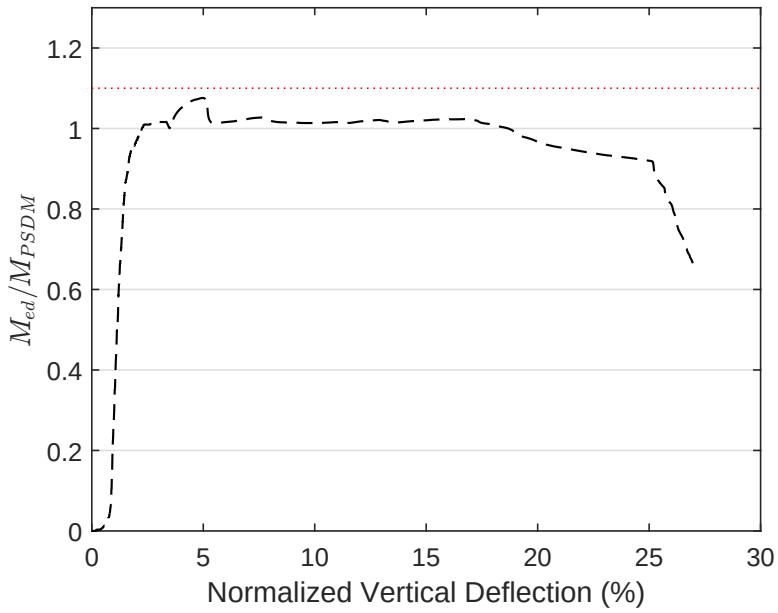
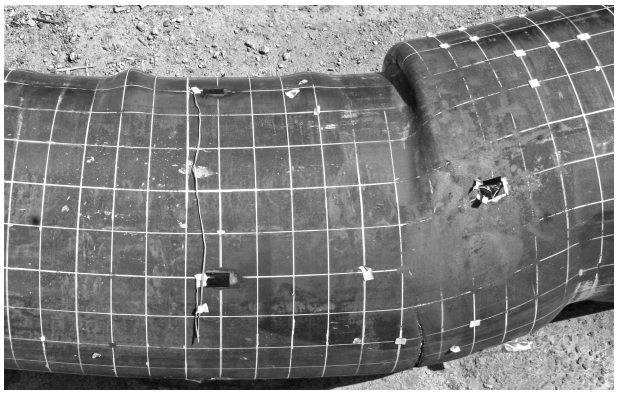



Figure 3.24: Specimen 14 Normalized Moment vs. Vertical Deflection Behavior

### *3.4.2.3 Flexure-Shear Interaction in CFST*

The observed flexure-shear behavior found in several of the specimens showed a combination of the above characteristics for flexure and shear controlled failures. The predominant characteristics of flexure-shear interaction in CFSTs include:

- Flexural buckling and flexural deformations in the pure moment region, coupled with shear deformation in at least one shear span, as shown in Figure 3.25a.
- Steel tube tear located under the load cradle of one side and set at a small incline.
- Substantial flexural cracking in the midspan, in addition to dense diagonal cracking in at least one shear span. See Figures 3.25b and c.



(a) Evidence of both flexural and shear deformations in steel tube




(b) Flexural cracking of concrete fill in pure moment region




(c) Diagonal cracking of concrete fill in shear span

Figure 3.25: Characteristics of Flexure-Shear Behavior in CFSTs (as demonstrated by Specimen 10)

Specimens 10 and 16 demonstrate these aspects well. They are presented in more detail here as they are evaluated again through finite element analysis in Chapter 4.

*Specimen 10 ($a/D = 0.375$, $L_T = 40$ in., $D/t = 80$, $\rho = 0\%$, $f'_c = 6151$ psi, clean interface)*
Specimen 10 was the baseline specimen for the $a/D = 0.375$ series. It's deformations were shown in Figure 3.25. In addition to those behaviors though, the specimen was observed to resist $1.16M_{PSDM}$ and $1.32(2V_{st})$ in moment and shear, respectively. The steel tube tore at the bottom approximately 15.5 *in.* south of the midspan, after significant flexural and shear deformations occurred. Both the north and south shear spans showed shear yielding deformations in the steel tube and clear diagonal shear cracking in the concrete fill, more severely in the south span. The tube steel buckled in compression on the north and south sides of the pure moment region. The concrete in this region also showed flexural crack patterns.

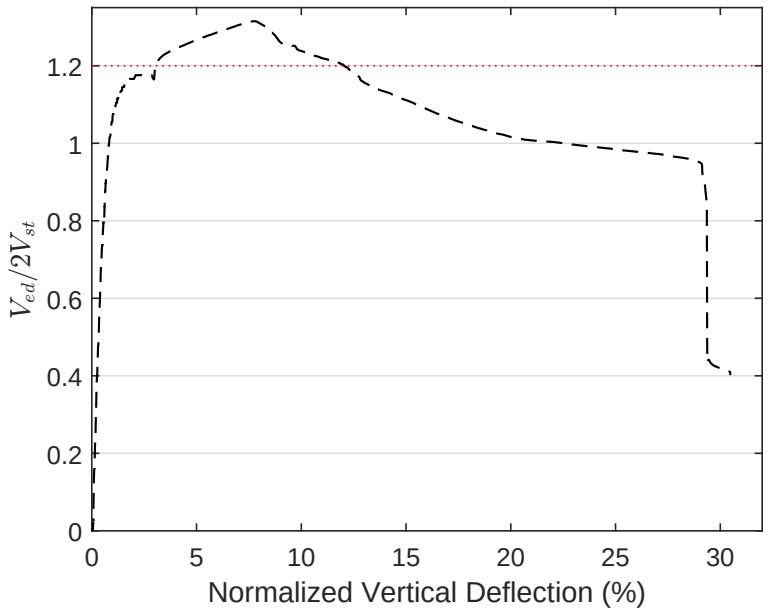



Figure 3.26: Specimen 10 Normalized Shear vs. Vertical Deflection Behavior

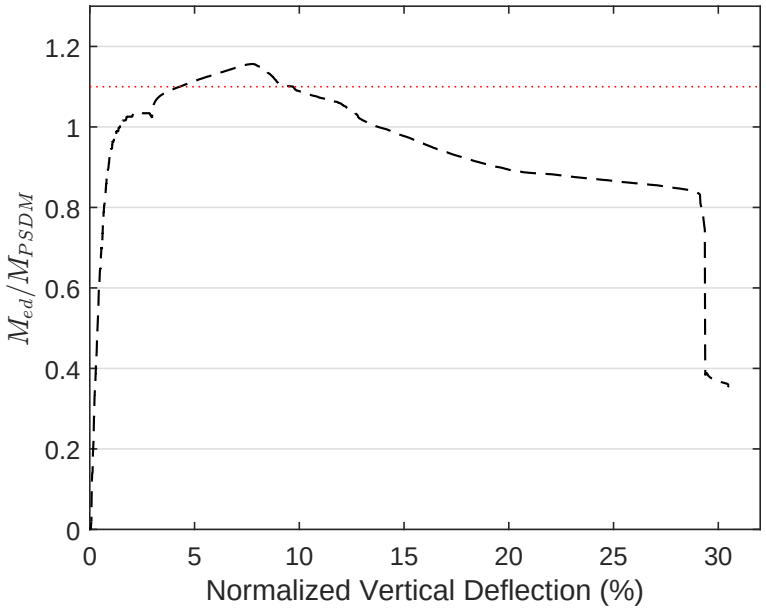
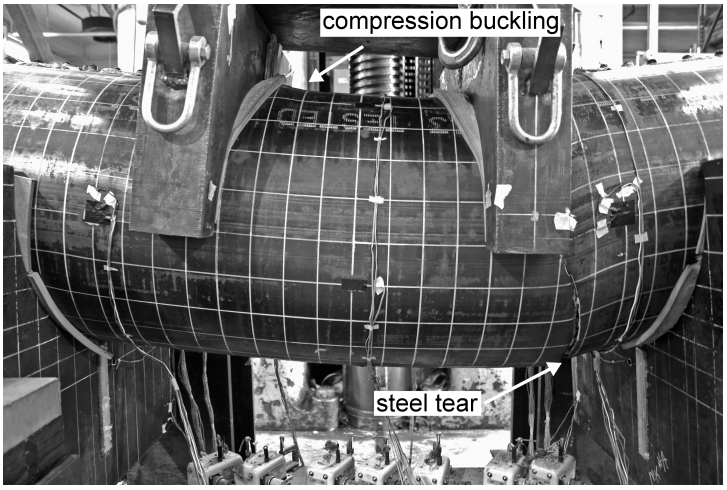
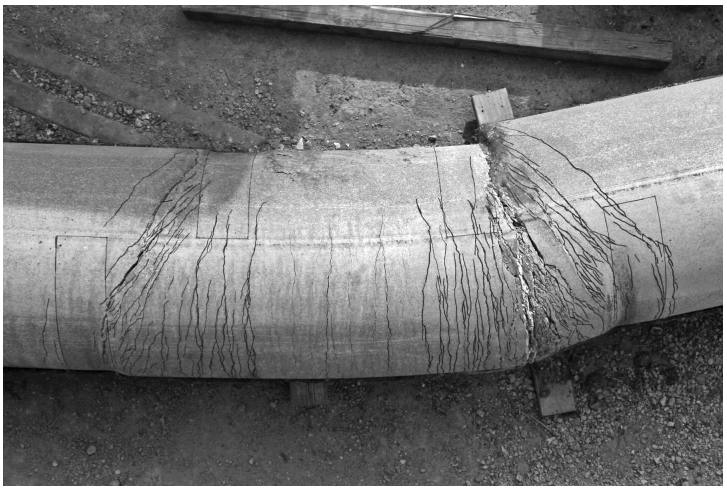



Figure 3.27: Specimen 10 Normalized Moment vs. Vertical Deflection Behavior

*Specimen 16 ($a/D = 0.375$, $L_T = 40$ in., $D/t = 80$, $\rho = 0\%$, $f'_c = 8609$ psi, clean interface)*
Specimen 16 had a prescribed concrete strength twice that of the baseline $a/D = 0.375$ specimen, Specimen 10, but was only reported to reach approximately 1.4 times the baseline $f'_c$. This CFST reached a moment 1.24 times $M_{PSDM}$ and a shear 1.44 times $2V_{st}$, both magnitudes being greater than the smaller concrete strength specimen. Similar to Specimen 10, the tube steel tore at an incline 14 *in.* north of the midspan with both evident shear and flexural yielding present in the shear spans and pure moment region, respectively. More severe shear yielding and diagonal cracking of the concrete fill were found in the north span, but still notable on the south side. In the pure moment region, visible flexural cracking of the fill and small compressive buckling at the top of the tube, more notable on the south side, were observed. These behaviors and complete force-deflection responses are provided in Figures 3.28 through 3.30.




(a) Deformed steel tube



(b) Cracking of concrete fill

Figure 3.28: Specimen 16 Photos

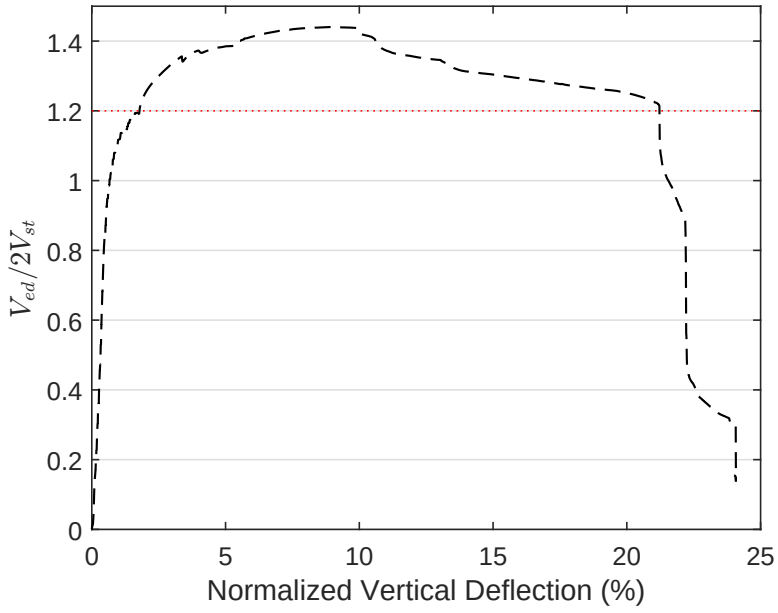



Figure 3.29: Specimen 16 Normalized Shear vs. Vertical Deflection Behavior

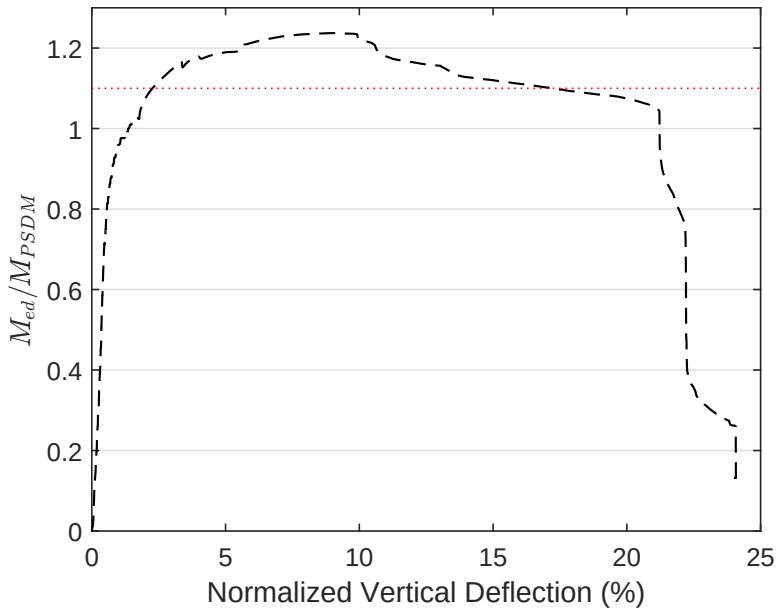
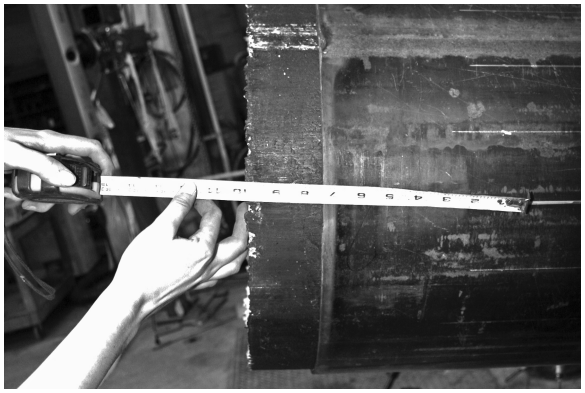



Figure 3.30: Specimen 16 Normalized Moment vs. Vertical Deflection Behavior

#### *3.4.2.4 Significant Bond Slip in CFST*

CFSTs are composite members, which require stress continuity at the different material interfaces to transfer forces most effectively, and if this bond is compromised, the materials no longer act together, but instead as separate entities. As such, they lose their load carrying capacity potentials, no longer failing directly by shear or flexure, but rather through bond slip. The predominant characteristics of significant bond slip behavior in CFSTs include:

- Significant slip and relative displacements between the concrete fill and the steel tube, as shown in Figures 3.31a and b.
- With extreme loss of bond, large concrete blocks separate within the tube, showing limited concrete cracking, and rigid body movements develop (Figure 3.31c). With more gradual loss of bond, rigid bodies develop more slowly so that previous bond action is evident with distributed cracking in the concrete fill present, but in a more concentrated form (Figure 3.31d).
- A loss of shear and moment carrying capacity in the CFST due to the lack of composite behavior.
- Moment and shear displacement behaviors that show a drop in resistance after reaching peak load at small deflections (Figures 3.33, 3.34, 3.36, and 3.37.



(a) Relative slip between steel tube and concrete fill (Specimen 9)



(b) Relative displacement between steel tube and concrete fill (Specimen 11)



(c) Rigid body action (Specimen 9)



(d) Rigid body formation (Specimen 11)

Figure 3.31: Characteristics of Bond Slip Behavior in CFSTs

In the experiments, the bond between the steel tube and concrete fill was lost in two ways: 1) directly through the application of grease at the steel tube to concrete interface (Specimen 9), and 2) indirectly by the lack of development length provided with a short tail length, $L_T$ (Specimen 11).

*Specimen 9 ($a/D = 0.5$, $L_T = 40$ in., $D/t = 80$, $\rho = 0\%$, $f'_c = 6317$ psi, clean interface)*
Specimen 9 differed from its respective baseline $a/D = 0.5$ specimen, Specimen 2, because its steel-concrete interface was coated with grease. This CFST reached a moment magnitude equal to $1.00M_{PSDM}$ and shear force magnitude of $0.94(2V_{st})$,. Ultimately, it failed with flexure-shear characteristics present, but the flexural behaviors more prevalent: vertical tube tear in the midspan region, flexural compression buckling, and shear deformations (Figure 3.32). However, its behavior was truly controlled by the lack of composite action. It did developed the CFST's full plastic capacity, but with reduced bond stress, the ultimate shear and moment forces were 20% smaller than with Specimen 2. Figures 3.33 and 3.34 show these results. The concrete fill also showed significant rigid body displacements, with up to 4 *in.* of slip through the south tail (Figure 3.31a). These rigid bodies formed from large concentrated cracks in the fill, contrasting the wide distribution of cracks found in most CFST specimens (Figure 3.31c).

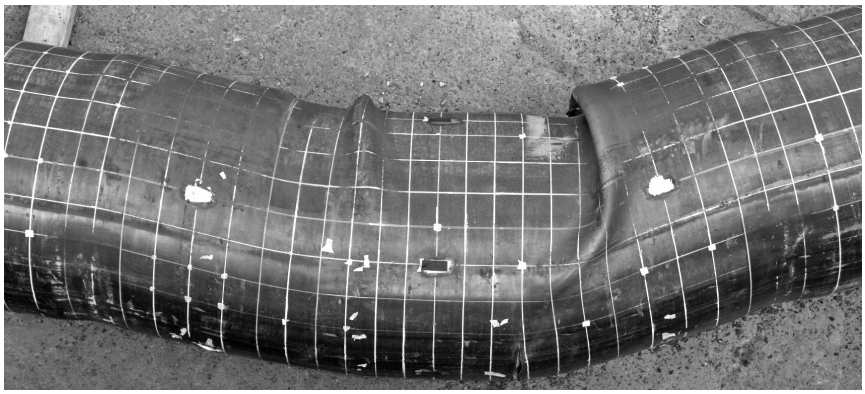


Figure 3.32: Specimen 9 Deformed State of Steel Tube

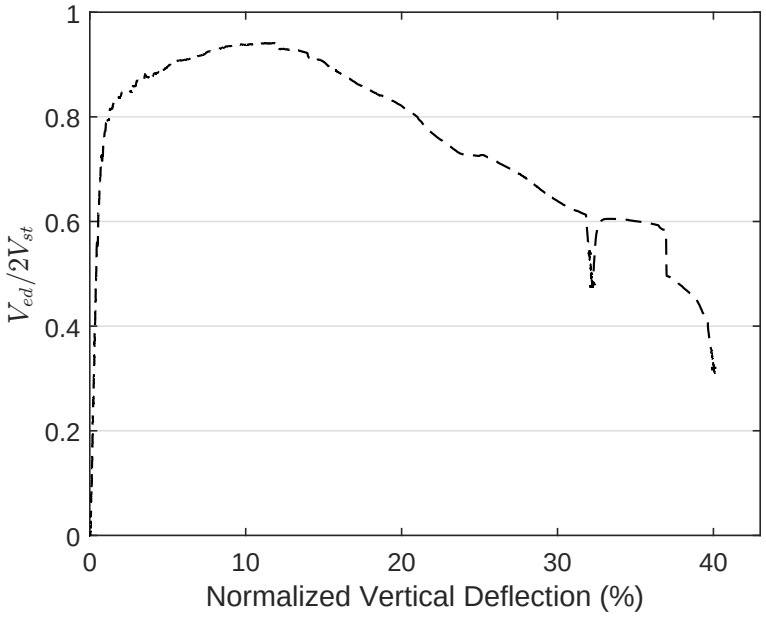



Figure 3.33: Specimen 9 Normalized Shear vs. Vertical Deflection Behavior

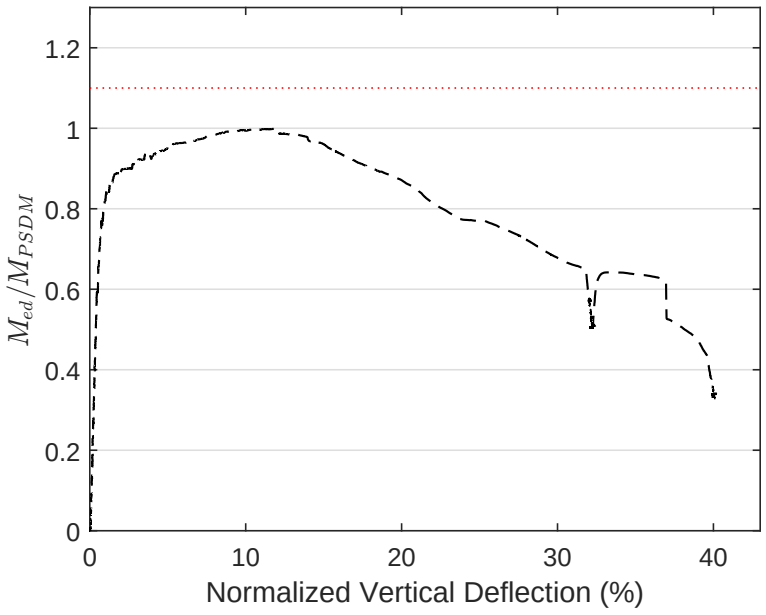
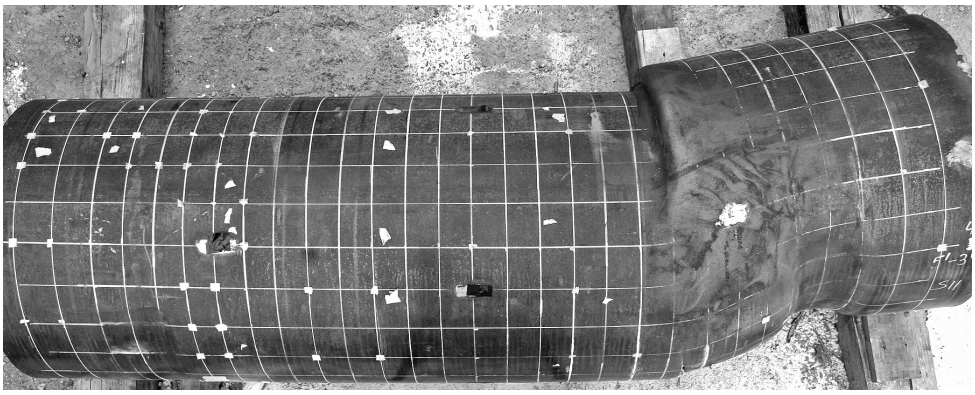
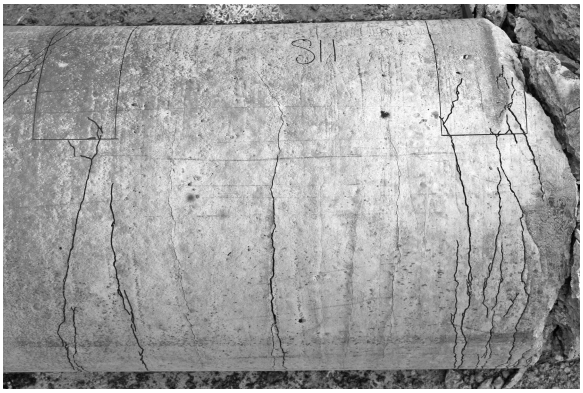



Figure 3.34: Specimen 9 Normalized Moment vs. Vertical Deflection Behavior

*Specimen 11 ($a/D = 0.375$, $L_T = 10$ in., $D/t = 80$, $\rho = 0\%$, $f'_c = 6609$ psi, clean interface)*
Specimen 11 had short tail length, $L_T = 10$ *in*, compared to Specimen 10, the baseline specimen for $a/D = 0.375$. The specimen failed with shear dominant deformation characteristics, but was significantly influenced by the lack of an effective bond stress transfer mechanism resulting from insufficient development length at the tail. With this inadequacy, the specimen only achieved $0.99M_{PSDM}$ and $1.13(2V_{st})$, both approximately 15% less than their long tail length counterpart, as shown in Figures 3.36 and 3.37. The final tube tear was inclined just inside the south shear span, close to the load cradle (Figure 3.35a). The midspan concrete showed very limited flexural cracking (Figure 3.35b) and, while the north end showed diagonal cracking only in a concentrated location (Figure 3.31d), the south end showed extensive diagonal cracking (Figure 3.35c) and severe movement of the remaining concrete block at the tail (Figure 3.31b).



(a) Deformed state of steel tube




(b) Flexural cracking of concrete fill




(c) Diagonal cracking of concrete fill in shear span

Figure 3.35: Specimen 11 Photos

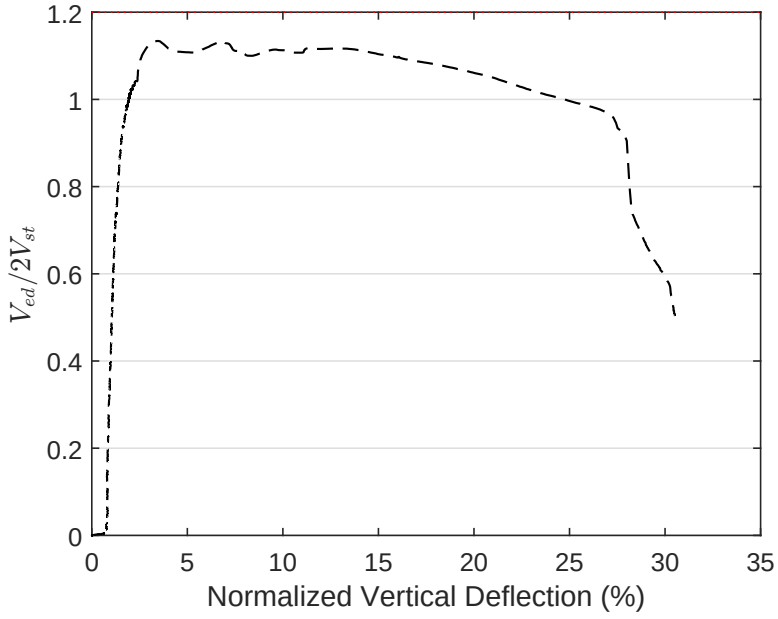



Figure 3.36: Specimen 11 Normalized Shear vs. Vertical Deflection Behavior

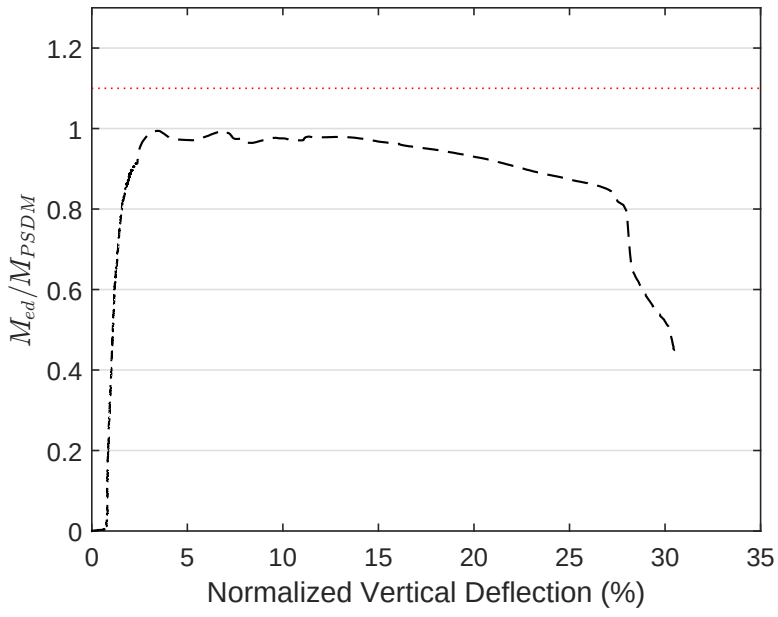



Figure 3.37: Specimen 11 Normalized Moment vs. Vertical Deflection Behavior

### *3.4.3 Additional Specimens of Interest*

A total of twenty-one tests were performed in the experimental program, and while several of these specimens have already been described in detail, some additional specimens represent parameters and resulting behaviors of particular interest. Therefore, they are explicitly presented here:

- Specimen 5 - CFST with muddy interface condition
- Specimen 12 - RCFST
- Specimen 13 - CFST with axial load
- Specimen 21 - Steel tube with gravel fill

#### *3.4.3.1 Specimen 5 - CFST with muddy interface*

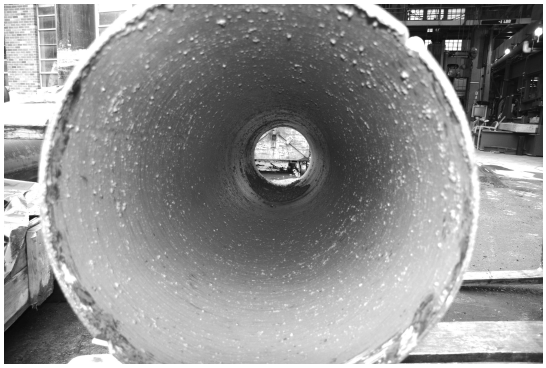
Specimen 5 was similar to Specimen 2 (baseline specimen for $a/D = 0.5$), with a tail length of 40 *in.*, straight-seam tube, and no internal reinforcement. However, Specimen 5 had a muddied steel-concrete interface. The goal of this test was to assess the potential damage to the composite behavior from surface contamination that could be expected in the field with a pile or drilled shaft. To create this condition, dirt and a relatively well-graded aggregate mix was put into the hollow cut steel tube that was set at an incline on rollers. The dirt was then wetted as the tube was rotated about its axis in the rollers until a well-coated surface was achieved. This procedure is shown in Figures 3.38a and b.

The specimen reached moment and shear force magnitudes of $1.26M_{PSDM}$ and $1.20(2V_{st})$. The complete moment and shear-displacement behaviors are shown in Figures 3.39 and 3.40. Although the inelastic deformation potential was reduced, Specimen 5 demonstrated slightly larger, but nearly equivalent, resistance in moment and shear compared to the clean interface specimen. The CFST failed in flexure with a vertical tube tear just off the specimen centerline and predominant flexural deformations and compressive buckling in the pure moment region. No shear deformation of the steel tube was apparent in the shear spans. Additionally, dense flexural cracking was found in the midspan, with limited diagonal cracking in the shear spans.

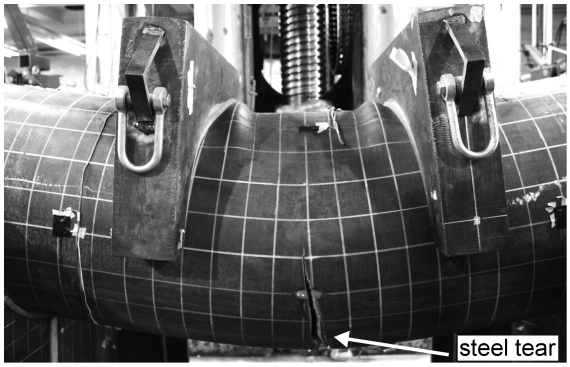
The deformations described are shown in Figures 3.38c through f.



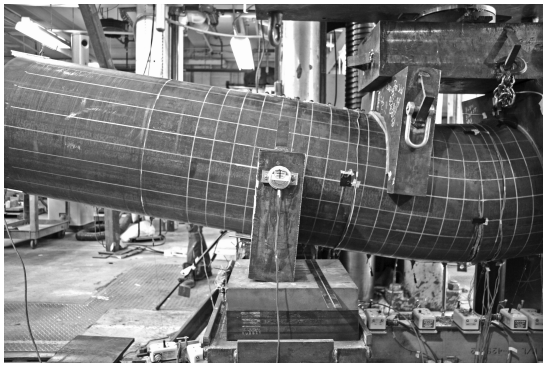
(a) Application of muddy interface condition



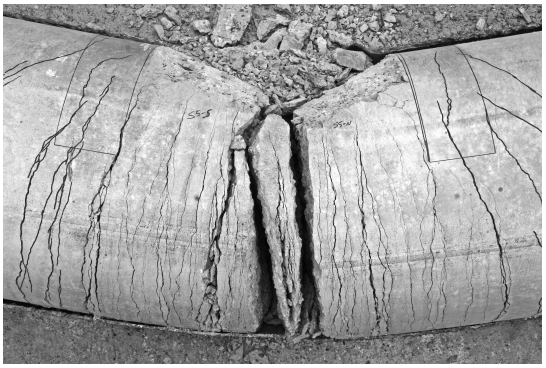
(b) Final muddied tube surface



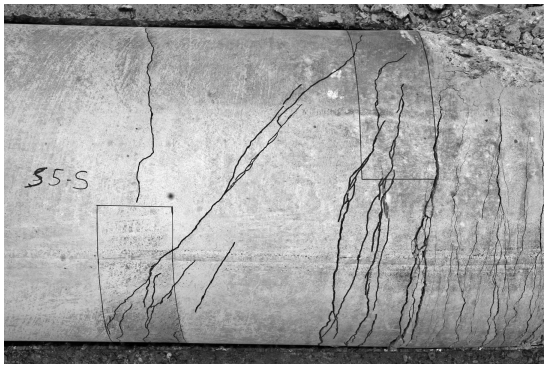

(c) Deformed steel tube



(d) Deformed steel tube



(e) Extensive flexural cracking of concrete fill




(f) Limited diagonal cracking of concrete fill in shear span

Figure 3.38: Specimen 5 Photos

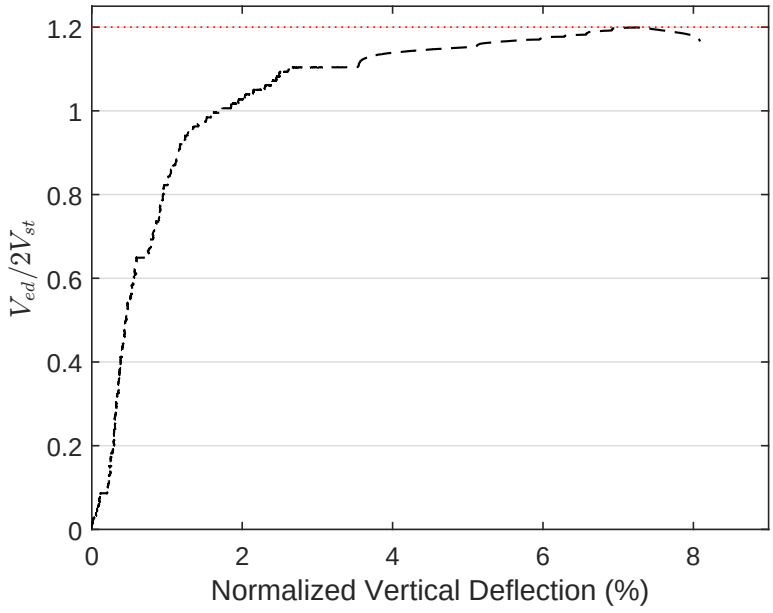



Figure 3.39: Specimen 5 Normalized Shear vs. Vertical Deflection Behavior

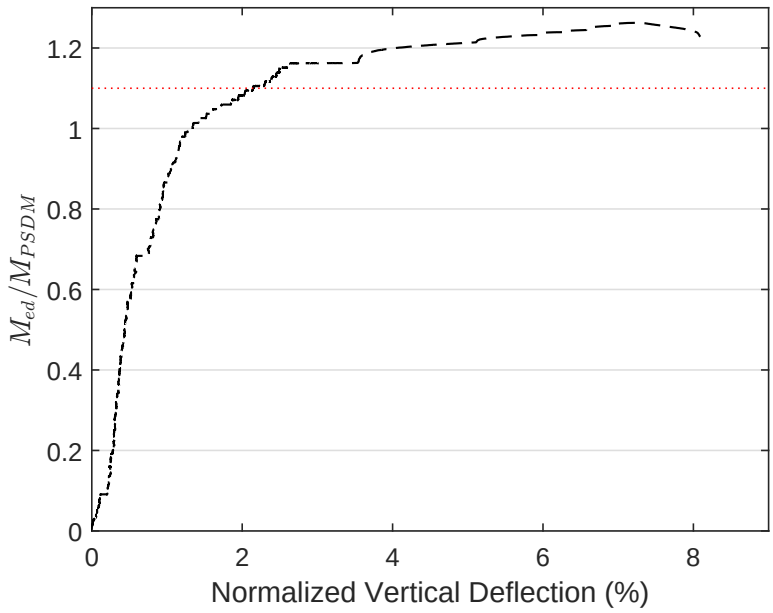



Figure 3.40: Specimen 5 Normalized Moment vs. Vertical Deflection Behavior

#### *3.4.3.2 Specimen 12 - RCFST*

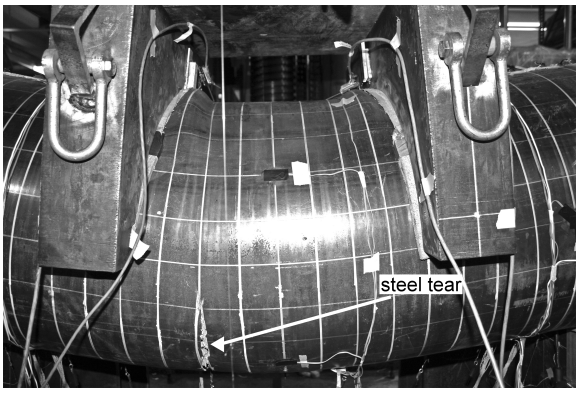
Specimen 12 was an internally reinforced variation of Specimen 2 (baseline specimen for $a/D = 0.5$), with a clean interface, tail length of 40 *in.*, straight-seam tube, and $\sim 1.1\%$ internal reinforcement. The amount of reinforcement used, 11-No. 5 bars, was considered a practical value for RCFSTs based on discussions with practicing engineers. To construct the RCFTS specimens, free-standing reinforcement cages were built with minimal transverse hoops placed outside critical shear and bending stress regions, and plywood holsters at each end to maintain their distribution. The hoops were only used for cage stability during construction and not section strengthening. The cage was then inserted into the upright tube using a crane prior to casting of the concrete fill, as shown in Figure 3.41.



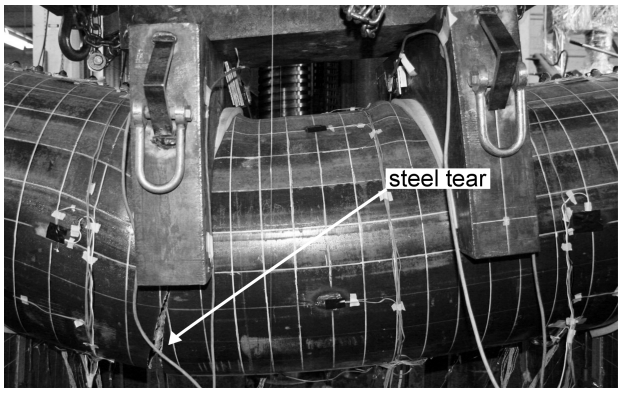
Figure 3.41: Placement of reinforcement steel cage in RCFST prior to casting

The specimen achieved $1.21M_{PSDM}$ and $1.30(2V_{st})$, as shown in Figures 3.43 and 3.44. With the total steel area increased by 22%, the flexural and shear resistance of Specimen 12 were both 17.7% higher than its CFST counterpart. Because the reinforcing steel was approximately 34% stronger than the tube itself, the reinforcement was less efficient than the steel tube in terms of strengthening the RCFST. At failure, the tube tore at an incline approximately 11 *in.* south of the midspan, just inside the shear span, after significant flexural and shear deformations occurred. The shear deformations were focused in the south span. Extensive cracking of the concrete fill was seen throughout the midspan and shear

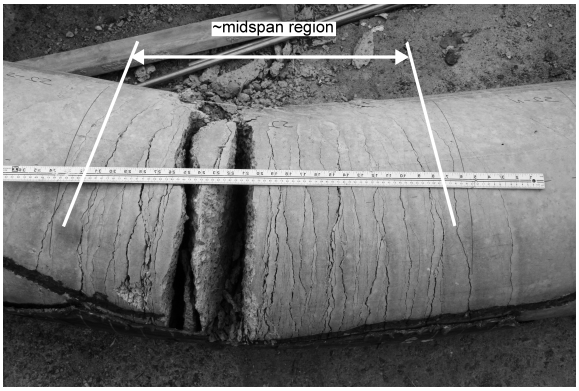
spans of the specimen due to the distribution of force by the reinforcement. More significant cracking was found in the south shear span though, and slight compressive tube buckling was seen in the midspan at the top of the tube. These deformations noted all are indicative of flexural-shear interaction. Specimen 2, the CFST counterpart of Specimen 12 on the other hand was a clearly controlled by bending behaviors, with no shear yielding on the steel tube and only extensive flexural cracking of the concrete fill. These are compared directly in Figure 3.42. This suggests that the inclusion of reinforcement permits more significant shear yielding, possibly because the shear capacity is not being strengthened as significantly as it is moment.



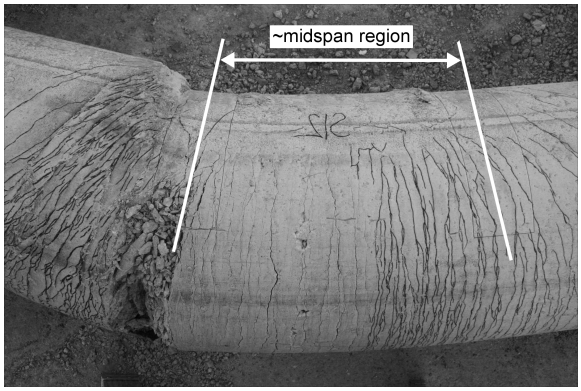

(a)




(b)




(c) Specimen 2




(d) Specimen 12

Figure 3.42: RCFST (Specimen 12) vs. CFST (Specimen 2) Photos

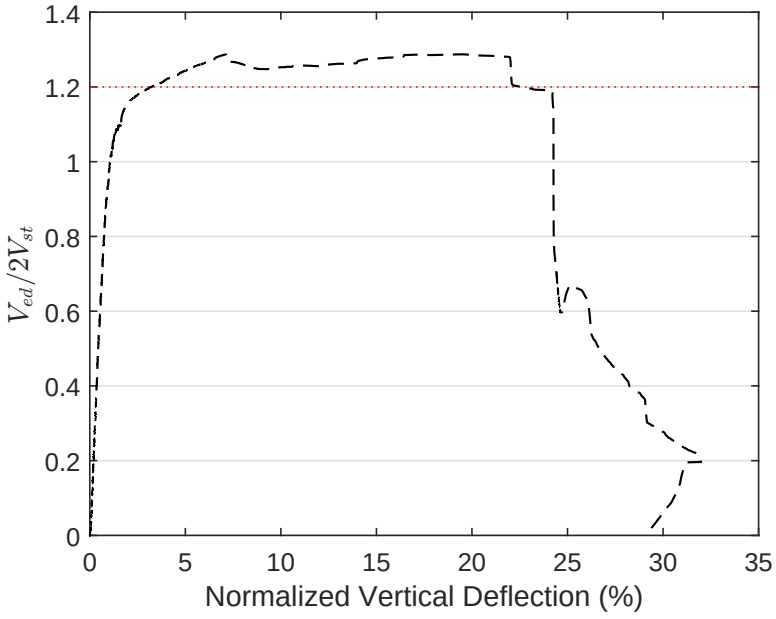



Figure 3.43: Specimen 12 Normalized Shear vs. Vertical Deflection Behavior

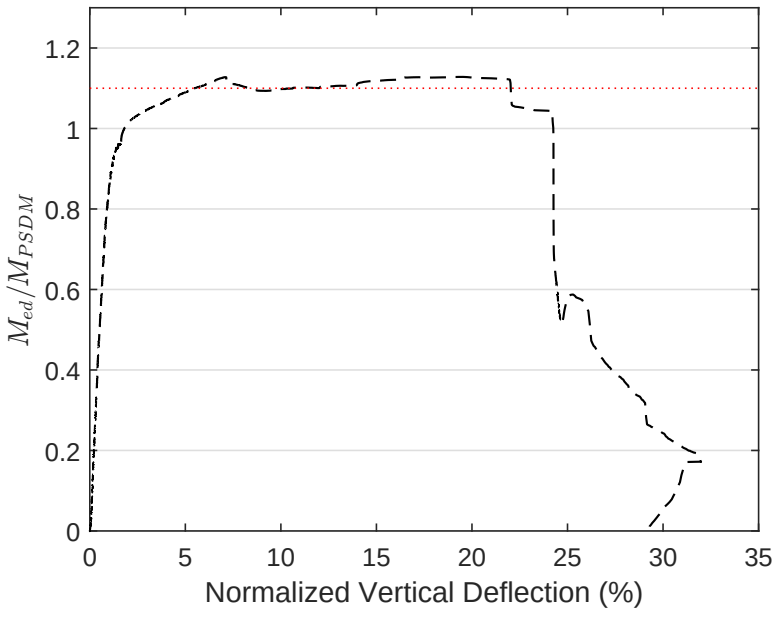
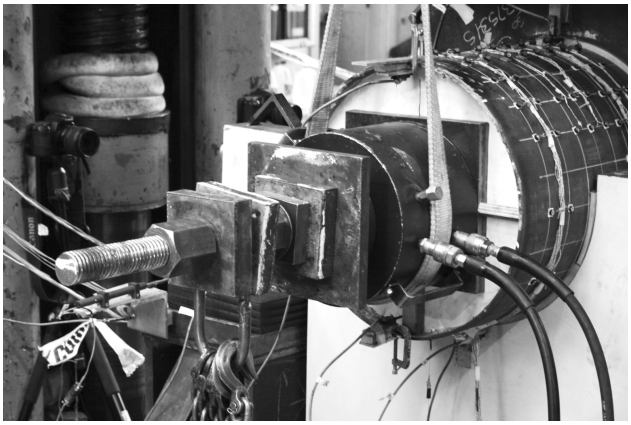



Figure 3.44: Specimen 12 Normalized Moment vs. Vertical Deflection Behavior

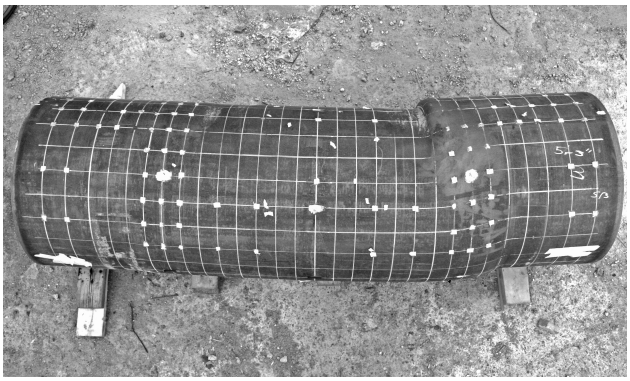
#### *3.4.3.3 Specimen 13 - CFST with axial load*

Specimen 13 was similar to Specimen 11, the short tail specimen with a shear span to depth ratio of 0.375, having a clean interface, tail length of 10 *in.*, straight-seam tube, and no internal reinforcement. However, Specimen 13 had an axial load applied to it that represented 8.5% of the CFST's compression capacity, $P_0$ (Equation 2.3). The axial load was applied manually to the concrete fill using a center-hole hydraulic ram, fit onto a large diameter Williams rod, and secured in place with a series of steel plates and nuts for added safety. This is shown in Figure 3.45a.

The load was maintained within $+/-3\%$ of the target until reaching $1.10M_{PSDM}$ at which point the load dropped by 78% of the target load, and became difficult to control manually. Additionally, pressure was released four times throughout testing while attempting to maintain constant load, which accounts for some of the sawtooth pattern in the response plots (Figures 3.46 and 3.47). At about 11.2% vertical deflection ($\sim 1.0M_{PSDM}$), the axial load was completely released and the transverse load continued. At peak, the specimen reached $1.11M_{PSDM}$ and $1.41(2V_{st})$ and later failed with predominantly flexure-shear interaction behaviors. This shows some increase in capacity from the axial load, but further data is required to quantify it. The tube was not taken to a displacement to cause tearing though, as the test was stopped to avoid damage to the Williams rod. Nevertheless, substantial shear yielding was evident in the south span, more minor in the north span, and less severe flexural deformations in the midspan. In the concrete fill, extensive diagonal cracking was found in both spans, and moderate flexural cracking in the pure moment region. Additionally, minor evidence of flexural buckling in the steel tube began to appear near the end of the experiment. Figure 3.45 shows these behaviors.



(a) Deformed state of steel tube



(b) Deformed steel tube



(c) Crack patterns in concrete fill

Figure 3.45: Specimen 13 Photos

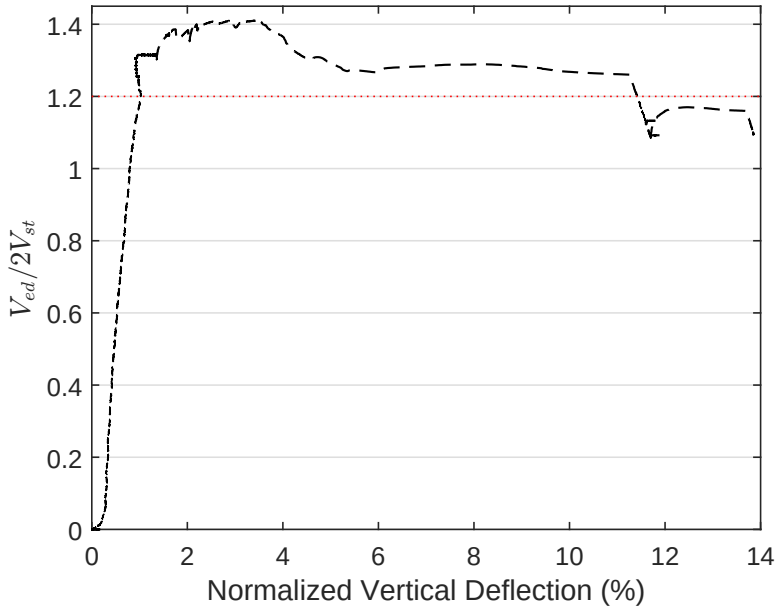



Figure 3.46: Specimen 13 Normalized Shear vs. Vertical Deflection Behavior

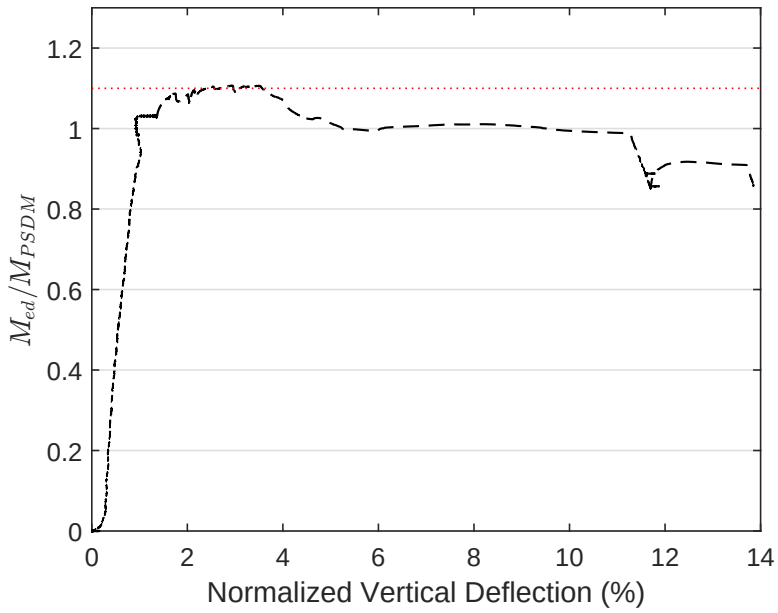
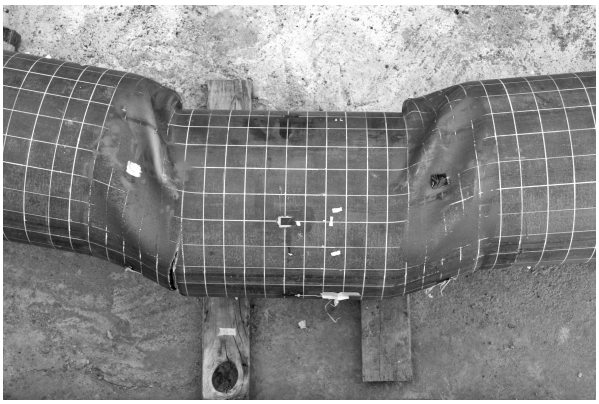



Figure 3.47: Specimen 13 Normalized Moment vs. Vertical Deflection Behavior

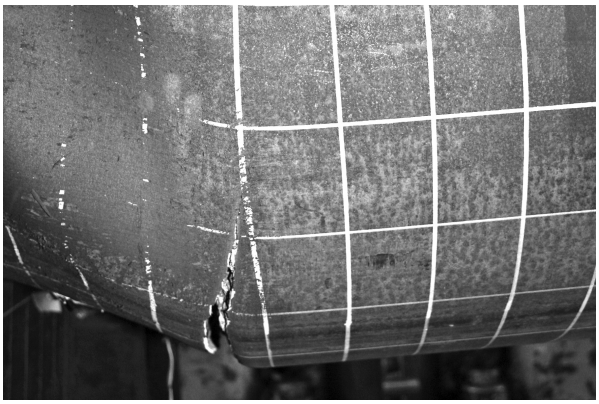
#### *3.4.3.4 Specimen 21 - Steel tube with gravel fill*

Specimen 21 was constructed with gravel in the shear spans, in place of concrete, so that the individual contributions of the concrete and steel tube to the shear resistance of CFSTs could be estimated. Because it was constructed in this manner, this specimen cannot be considered a CFST, as it isolates the contribution of the steel tube. Nevertheless, it is compared to calculated CFST properties for consistency in the experimental program.

Specimen 21 was similar to Specimen 10 (baseline specimen for $a/D = 0.375$), with a clean interface, tail length of 40 *in.*, straight-seam tube, and no internal reinforcement. Before failing in shear, the specimen reached moment and shear magnitudes of $0.93M_{PSDM}$ and $0.85(2V_{st})$, respectively. Figures 3.49 and 3.50 show the complete behaviors. The tube tore just south of the midspan concrete block, in the gravel region, with substantial shear deformations visible in both shear spans. Around $0.5M_{PSDM}$ and $0.45(2V_{st})$, shear buckling initiated with the development of tension-field action that provided increased shear resistance. That is, the gravel in the shear spans was able to restrain against typical shear yielding and buckling seen with a CFST, but did not provide enough stiffness to maintain a circular cross-section like normal concrete would. Lastly, no visible flexural buckling was found in the pure moment region and very minimal cracking observed in throughout the specimen. Figure 3.48 shows these deformations.



(a) Deformed steel tube



(b) Steel tube tear



(c) Gravel deformation and crack patterns in concrete fill



(d) Gravel deformation

Figure 3.48: Specimen 21 Photos

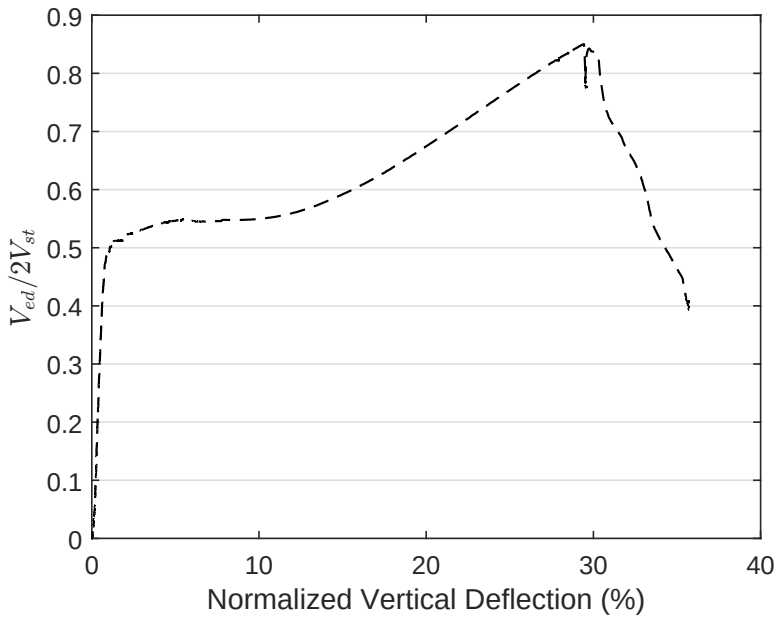



Figure 3.49: Specimen 21 Normalized Shear vs. Vertical Deflection Behavior

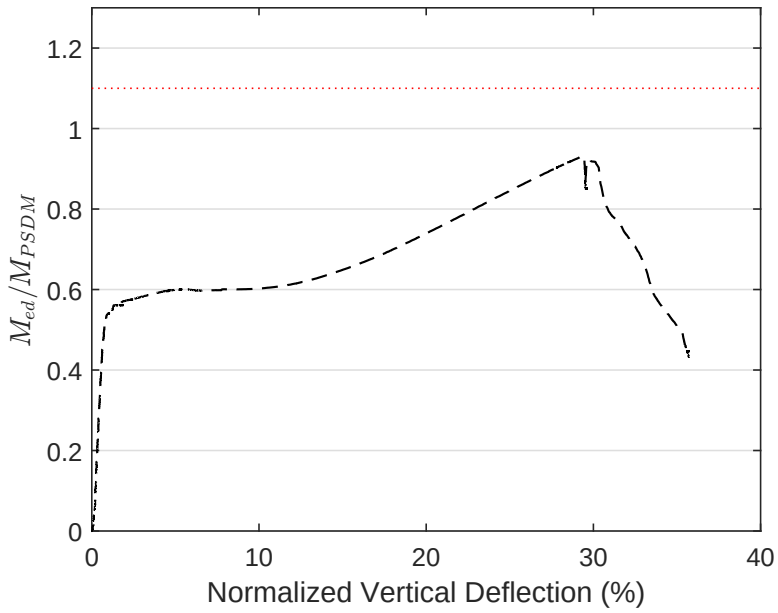



Figure 3.50: Specimen 21 Normalized Moment vs. Vertical Deflection Behavior

## *3.5 Parameter Influence*

This section focuses on the overall influence of various parameters on the shear capacity and behavior of CFSTs for the development of recommendations to current design capacity expressions. Variables part of the test matrix that are not discussed either did not prove to impact behavior significantly or their sample size too small to make distinct conclusions. Nonetheless, some of these parameters will be studied numerically in Chapter 4.

### *3.5.1 Composite Action due to Tail Length, $L_T$, and Steel-Concrete Interface Condition*

Previous research has concluded that the composite action of CFSTs provide a substantial increase in strength and stiffness over that achieved by steel or reinforced concrete elements of the same size and geometry (Roeder et al., 2009). To achieve composite action, shear stress must be transferred between the steel and concrete. In order to develop the full composite resistance then, both sufficient length beyond the maximum moment, like a reinforcing bar embedded in concrete, and appropriate interior tube surface conditions must be provided.

Prior research (Section 2.3) did not studied the impact of these parameters. In fact, much of the previous research was done using specimens end caps, which did not allow differential movement of the steel tube and concrete fill. Therefore, these specimens should develop full composite action for all cases by theory. However, this does not reflect actual boundary conditions in practice. This experimental program used the parameters tail length, $L_T$, and interface condition to simulate field conditions and investigate the required length to develop full composite action and effect of potential contact surface contamination.

Table 3.6 shows the specimens with varying tail lengths and interface conditions. Most specimens had a tail length equal to two times to diameter of the tube, $2D$, which consistently assured full composite behavior unless affected by interface conditions. Five specimens had shorter tail lengths, $D$, $D/2$, and $5/8 \cdot D$. The shaded specimens in the table can be directly compared to highlight the effect of interface condition, with Specimen 9 essentially representing the case where no bond transfer exists and Specimen 5 mimicking potential con-

tamination when placing piles or shafts on site. Furthermore, often CFSTs are constructed with spirally welded tubes such the the weld bead left creates the opportunity for additional mechanical bond to develop. All of the interface specimens shaded have a shear span to depth ratio of 0.5, and were therefore expected to act in flexure with the resulting shear force being determined by flexural capacity.

Table 3.6: Composite Action Series Specimen Summary

| Specimen | $a/D$ | $P/P_0$ | $L_T$ | Max Slip (in.) | $Max\ Slip/\ L_T$ | Interface | $M_{ed}/\ M_{PSDM}$ | $V_{ed}/\ 2V_{st}$ | Failure Mode |
|---|---|---|---|---|---|---|---|---|---|
| 2 | 0.5 | 0% | 2D | 0.018 | 0.045 % | clean | 1.26 | 0.70 | flexure |
| 3 | | | D/2 | 0.044 | 0.44 % | clean | 1.25 | 1.18 | flexure |
| 4 | | | D | 0.026 | 0.13 % | clean | 1.23 | 1.16 | flexure |
| 5 | | | 2D | 0.022 | 0.055 % | muddy | 1.26 | 1.20 | flexure |
| 6 | | | 2D | 0.007 | 0.02 % | spiral [2] | 1.27 | 1.18 | flexure |
| 9 | | | 2D | 4.00 | 10.00 % | greased | 1.00 | 0.94 | bond |
| 10 | 0.375 | 0% | 2D | 0.683 | 1.71 % | clean | 1.16 | 1.32 | flex-shear |
| 11 | | | D/2 | 0.926 | 9.26 % | clean | 0.99 | 1.13 | bond |
| 13 [3] | | 8.5% | D/2 | 0.107 | 1.07 % | clean | 1.11 | 1.41 | flex-shear |
| 14 | 0.25 | 0% | 2D | 0.070 | 0.18 % | clean | 1.03 | 1.53 | shear |
| 15 | | | 5/8·D | 0.404 | 3.23 % | clean | 1.04 | 1.54 | shear |

[1] Shaded rows note directly comparable specimens in the interface condition series.
[2] Specimen 6 was made with a spirally welded tube and clean interface.
[3] Specimen 13 had an applied axial load that may have enhanced the bond transfer mechanism, in spite of its short tail length.

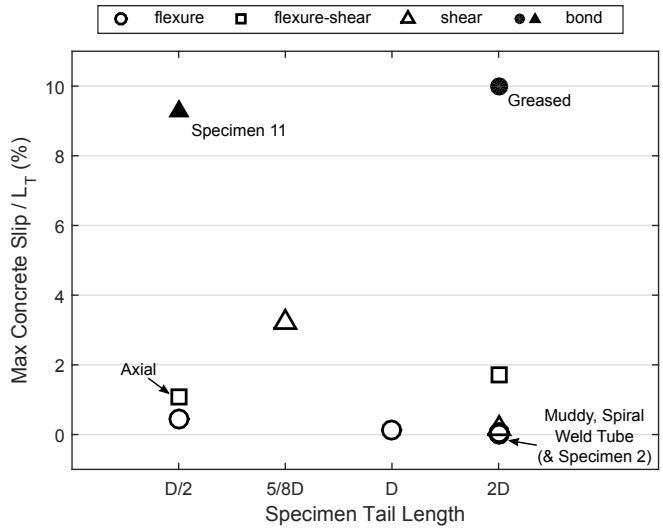
The relative slip between the steel tube and concrete fill was measured at the north and south free ends of all specimens using Duncan linear potentiometers. The maximum values are presented in the table and in Figure 3.51a for the current specimens of interest. The normalized moment values as they vary with tail length for these specimens are then provided in Figure 3.51b. Two specimens in the research program failed due to severe loss of bond. These exhibited large slip values that correspond to significant loss of moment, and therefore shear, resistance. Nevertheless, full plastic capacity was developed. Specimen 9

had a greased interface, so large slip is expected; however, Specimen 11 simply had a normal interface, but short tail length, nominally identical to Specimens 10 and 13, pointing to the issue of friction and binding action development through tail length. Other CFST specimens with short tail lengths though did not show this same extreme slip behavior, but did show to drop in capacity.

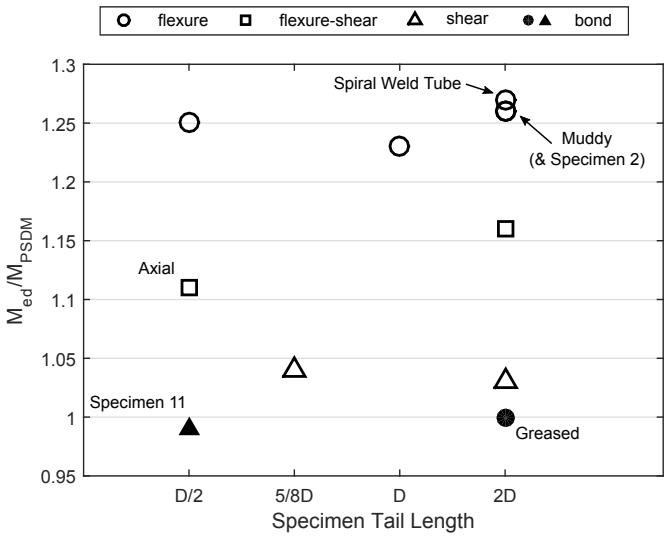
In the end, the shorter tail length provides less length for the horizontal shear transfer and allows for more distortion of the cross-section through prying action near the tube's free end. Hence, it is recommended that a minimum tail length of one times the diameter of the tube, $D$, be provided before the CFST is expected to develop its full plastic capacity, as defined by the plastic stress distribution method, $M_{PSDM}$, but more data is required to relate this to development length directly.

Additionally, when slip is restrained, the capacity of the CFST was shown to be larger. This happens with the spirally welded tube and extra friction from the muddied interface. Consequently, it can be said that some contamination may actually improve resistance capacity of CFSTs.

Lastly, resulting failure mode was observed to be related to observed slip values. That is, more slip was seen in tests where shear yielding became more evident. Therefore, shear resistance was shown to not only be affected by its capacity, but also by bond.




(a) Normalized Maximum Slip vs. Tail Length




(b) Normalized Moment vs. Tail Length

Figure 3.51: Composite Action Specimens Comparisons

### *3.5.2 Comparison of RCFST and CFST, $\rho_{int}$*

Data for RCFST behavior in shear was not found in previous experimental programs. In the UW testing program, four RCFSTs were tested. The properties of these and comparable CFSTs are given in Table 3.7. The steel reinforcement used has a larger yield strength than the steel tube, $F_{yrl} = 67\ ksi$ and $F_{yt} = 50\ ksi$, so when comparing the increase in steel area, it should be noted that a given cross-sectional area of reinforcement was effectively about 34% stronger, with strength estimated as $F_y \cdot A$, than an equivalent area of tube steel.

Table 3.7: RCFST Series Specimen Summary

| Specimen | $a/D$ | D/t | $\rho_{int}$ | $A_{srl}/\ A_{st}$ | $M_{ed}/$ $M_{PSDM}$ | $V_{ed}/$ $2V_{st}$ | Failure Mode |
|---|---|---|---|---|---|---|---|
| 2 | 0.5 | 80 | 0 % | 0 % | 1.26 | 0.70 | flexure |
| 12 | | | 1.13 % | 22.0 % | 1.13 | 1.29 | flex-shear |
| 19 [a] | | 53.3 | 1.07 % | 13.4 % | 1.16 | 1.19 | flex-shear |
| 10 | 0.375 | 80 | 0 % | 0 % | 1.16 | 1.32 | flex-shear |
| 7 | | | 1.04 % | 20.0 % | 1.08 | 1.51 | flex-shear |
| 8 | | | 2.01 % | 38.7 % | 0.99 | 1.55 | shear |

[a] Specimen 19 had a higher concrete strength ($f'_c = 9.13\ ksi$) compared to the remaining specimens listed ($f'_c = 6.15$ to $6.48\ ksi$).

Looking at the selected specimens, Specimen 12 had 22% more steel due to internal longitudinal reinforcement compared to Specimen 2 and, as such, experiences an 18% increase in moment and shear, respectively. Specimens 7 and 8 showed an increase in moment of 7% and 18% compared to Specimen 10, with 20% and 38% increased steel area from reinforcement. In both cases, this increase in capacity was not directly proportional to the increase strength that their full area would provide. Specimen 21 though, showed that the steel tube provided resistance nearly equivalent to its full area. The increase in capacity from the internal reinforcement clearly was not as efficient as additional steel tube are would have been, even having a greater yield strength than the tube.

In addition to providing more steel area though, the restraint in crack opening provided by the reinforcement in the concrete fill of the shear spans inherently increased the RCFST shear capacity. On the other hand, the introduction of reinforcement also resulted in increased shear deformations, that begins to limit flexural strength. This is illustrated with the change in failure mode from flexure to flexure-shear interaction noted with the $a/D = 0.5$ RCFSTs, and flexure-shear to shear with $a/D = 0.375$ RCFSTs. There is a distinct change in force transfer with these specimens. Ultimately though, the reinforcement adds to the capacity of the specimens by resisting shear through catenary action, as opposed to flexure, due to the large deflections, which can create these differences in observed behaviors. It is also possible that the increase in shear deformations simply comes from the fact that flexure was being better reinforced by the internal bars, than shear action was.

### *3.5.3 Effect of Concrete Strength, $f'_c$*

Concrete provides strength to CFSTs in shear as a function of its compressive strength, $f'_c$, cross-sectional area, and deformation restraint of the steel tube. The contribution of $f'_c$ is studied here with the three different specified concrete strengths used in this program. Additionally, Specimen 21 was filled with gravel in its shear spans, and was considered to represent concrete with very little compressive strength in these locations, providing a fourth variation of this parameter. Table 3.8 summarizes the properties of the specimens to be used for evaluating the influence of concrete strength on shear resistance.

Although the sample size provided here is small, the results clearly show that the steel tube provides the majority of the composite shear resistance. Significant buckling formed in Specimen 21 through tension-field action because the gravel did not develop any shear and could not fully restrain the tube from this deformation, like a severely damaged concrete fill might. In spite of this, it achieved a large shear resistance in addition to nearly reaching its full plastic moment capacity. Furthermore, comparing the other specimens in each $a/D$ category, it was demonstrated that even a significant increase in compressive strength of the concrete fill resulted in only a small increase in shear force.

Table 3.8: Concrete Strength Series Specimen Summary

| Specimen | $a/D$ | D/t | $f'_c$ (ksi) | $f'_{cm}$ (ksi) | $M_{ed}/M_{PSDM}$ | $V_{ed}/2V_{st}$ | Failure Mode |
|---|---|---|---|---|---|---|---|
| 2 | 0.5 | 80 | 6.0 | 6.22 | 1.26 | 1.19 | flexure |
| 17 | | 53.5 | 12.0 | 9.45 | 1.10 | 1.06 | flexure |
| 10 | 0.375 | 80 | 6.0 | 6.15 | 1.16 | 1.32 | flex-shear |
| 16 | | | 12.0 | 8.61 | 1.24 | 1.44 | flex-shear |
| 21 | | | gravel | gravel | 0.93 | 0.85 | shear |
| 14 | 0.25 | 80 | 12.0 | 8.60 | 1.03 | 1.53 | shear |
| 20 | | | 2.5 | 2.79 | 0.99 | 1.35 | shear |

### *3.5.4 Shear Span to Depth Ratio, $a/D$*

It has been noted that the shear span to depth ratio cannot be practically determined through the experimental program, so it is difficult to make firm conclusions on this matter. Nevertheless, trends similar to previous research conclusions can be observed. Noting the specimens in Table 3.9, it is clear that $a/D$ does have a heavy influence on failure mode, not to be confused with an effect on strength of the section. That is, tests that resulted in flexure or flexure-shear failures never saw the shear strength magnitude of the section, and specimens with relatively smaller $a/D$ ratios exhibited increasingly shear-like deformations.

Four shear span to depth ratios were tested in this program: 1, 0.5, 0.375, and 0.25 (using the undeformed clear span definition of $a$). From the results of this experimental study, CFSTs with a shear span to depth ratio of 1.0 and 0.25 definitively failed in flexure and shear, respectively. The specimens with ratios of 0.5 and 0.375 were not as easily defined though, largely due to the uncertainty of true shear span at failure and resulting combinations of flexure and shear deformations found. Furthermore, when introducing other factors such as internal reinforcement, the $a/D$ ratios possibly attributed to a given failure mode can change, as noted in Section 3.5.2. These factors then make results more difficult to relate to discrete shear span values.

Table 3.9: Shear Span to Depth Ratio Series Specimen Summary

| Specimen | $a/D$ | Failure Mode | $f'_c$ (ksi) | $f'_{cm}$ (ksi) | $M_{ed}/M_{PSDM}$ | $V_{ed}/2V_{st}$ |
|---|---|---|---|---|---|---|
| 1 | 1 | Flexure | 6.0 | 6.01 | 1.27 | 0.70 |
| 2 | 0.5 | Flexure | 6.0 | 6.22 | 1.26 | 1.19 |
| 17 | | Flexure | 12.0 | 9.45 | 1.10 | 1.06 |
| 10 | 0.375 | Flex-Shear | 6.0 | 6.15 | 1.16 | 1.32 |
| 16 | | Flex-Shear | 12.0 | 8.61 | 1.24 | 1.44 |
| 21 | | Shear | gravel | gravel | 0.93 | 0.85 |
| 14 | 0.25 | Shear | 12.0 | 8.60 | 1.03 | 1.53 |
| 20 | | Shear | 2.5 | 2.79 | 0.99 | 1.13 |

# Chapter 4

# ANALYTICAL MODEL

## *4.1 Introduction*

Nonlinear finite element models were developed in the ABAQUS (version 6.14) computer program, produced by the Dassault Systemes Simulia Corp, and relevant parameter studies were performed (Chapter 5) to extend the experimental results. Six specimens from the experimental program were analyzed to develop a validated model for this process. The details of the modeled specimens are shown in Table 4.1 and their experimental behaviors described in Section 3.4.1. The specimens were selected to look at different failure modes in this setup as impacted by the $a/D$ ratio and $f'_c$, with other parameters kept relatively constant, including: $D = 20\ in.$, $t = 0.25\ in.$, $F_{yt} \approx 50\ ksi$, $P/P_0 = 0\%$, $\rho_{int} = 0\%$, $L_T = 2D$, straight-seam tube, and clean interface condition.

Table 4.1: Summary of Specimens used for Analytical Model Validation

| $a/D$ | Specimen | $F_{ytm}$ (ksi) | $f'_{cm}$(ksi) | $V_{exp}$ (kips) | $V_{ed}$ (kips) | $M_{ed}/M_{PSDM}$ | Failure Mode |
|---|---|---|---|---|---|---|---|
| 1.0 | 1 | 49.6 | 6.012 | 322.0 | 322.0 | 1.27 | Flexure |
| 0.5 | 17 | 55.4 | 9.450 | 549.3 | 544.5 | 1.10 | Flexure |
| | 2 | 49.6 | 6.220 | 550.8 | 549.0 | 1.26 | Flexure |
| 0.375 | 16 | 56.8 | 8.609 | 759.2 | 760.5 | 1.24 | Flex-Shear |
| | 10 | 53.9 | 6.151 | 668.9 | 660.0 | 1.16 | Flex-Shear |
| 0.250 | 14 | 55.4 | 8.596 | 874.9 | 788.4 | 1.03 | Shear |

The description of the process to creating the validated model is divided into two sections. Section 4.2, Model Description, presents the base model, developed using Specimens 17 and 16. The model was then validated using the remaining specimens, Specimens 1, 2, 10, and 14, as presented in Section 4.3.

## 4.2 Model Description

The ABAQUS simulation was initially created with modeling recommendations based on previous research (Moon et al., 2012, 2013). The following sections describe the final proposals made in this program for the development of shear critical CFST simulations and the influence of various modeling parameters on this behavior. A basic model was first created that was able to mimic flexurally controlled experiments well, but further refinement was required to better capture the influence of the boundary conditions on the shear force magnitude of the CFSTs. Both of these steps and their motivations are detailed here.

### *4.2.1 Base Model*

A typical base model is shown in Figure 4.1. For the test setup, the load cradle, support cradle, cotton duck bearing pads, and elastomeric bearing with steel top plate were included, with dimensions as shown in the Appendix B. The following sections describe the details in this model including the general problem solving approach, development of the CFST specimen, and the modeled setup interactions.

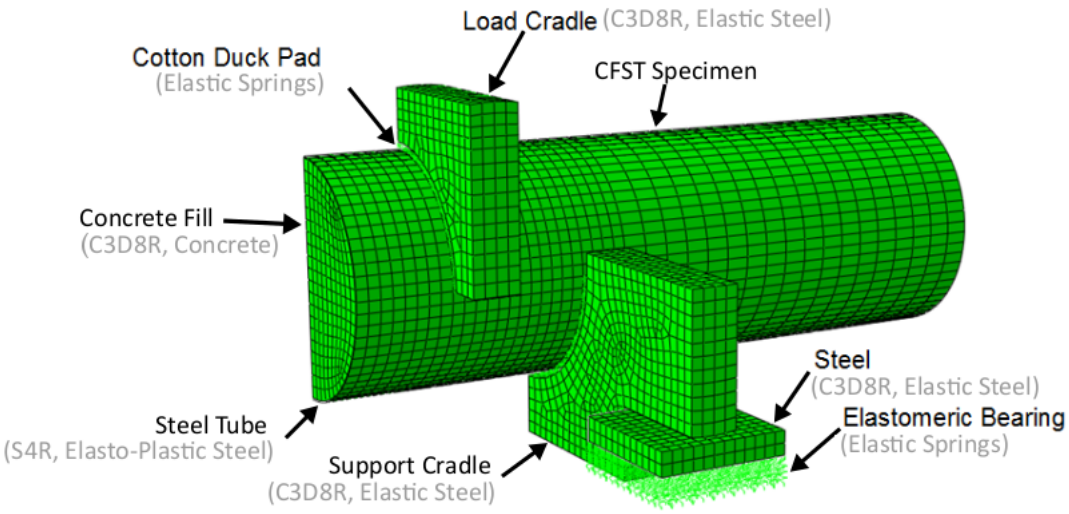



Figure 4.1: Typical ABAQUS Base Model

#### *4.2.1.1 General Approach to Problem*

An ABAQUS/Standard model was created for this application using a static displacement-controlled load step. The ABAQUS/Standard option uses implicit solution algorithms that are ideal for static and slow dynamic problems. This analysis method uses Newton-Raphson schemes to enforce equilibrium after each step of the nonlinear analysis, which can be computationally demanding. So, ideal symmetry of the system was utilized, such that one-quarter of the actual specimen and setup were modeled, as seen in Figure 4.1. Along the longitudinal axis of the specimen and at the system mid-span, "XSYMM" and "ZSYMM" restraints were applied, respectively. These ABAQUS restraints are defined with zero displacements in the named direction and zero rotations about the other remaining axes.

#### *4.2.1.2 CFST*

The CFST specimen was created in ABAQUS with two independent parts, a solid concrete fill and a shell steel tube, with individual mesh, material, and element properties. The independent parts' properties were detailed separately and then assembled together using a "surface-to-surface" contact definition.

*Mesh Refinement*

The component under study in this simulation was the CFST specimen, so concern with accuracy of stress and deformation predictions due to mesh distribution was only made here, and the remaining setup parts were meshed so that nodes aligned at contact surfaces and relatively good distribution seen. For the CFST specimen, refinement was focused in regions of high stress, including the constant moment region and shear span of the CFST, with aspect ratios of the elements close to 1.0 in these critical areas. An evaluation of appropriate element sizes was completed, and once reaching reaction force magnitudes that remained approximately constant with further refinement, while maintaining reasonable computational demands, a final mesh was chosen. The final mesh is shown in the figures of this chap-

ter, with the primary elements of focus in the midspan and shear span being approximately $1\ in. \times 1\ in. \times 1\ in.$. Taking this down further saw a change in maximum load of less than 1%, but resulted in a significant increase in computation time. The models went from running between 2 and 3 hours to over 2 days, using 4 CPUs and a total of approximately 5 gigabytes of RAM. So, both the steel tube and concrete fill were meshed with the element distribution described, and made so that nodes at their contact surface aligned closely.

*Tube Steel*

The steel tube was modeled using shell elements, with reduced integration schemes (S4R). Shell element formulations tend to converge easier than a solid element when bending stresses are high from large displacements or curved surfaces. Additionally, transverse shear strains are neglected with these elements, therefore avoiding shear locking issues.

For the tube material properties, a trilinear stress-strain relationship, including Von Mises yield function and isotropic hardening, was used. The elastic behavior was specified with an elastic modulus of $29,000\ ksi$ and poisson's ratio of 0.3. The nonlinear stress-strain relationship was defined by Moon et al. (2012), as shown in Figure 4.2. The material strength values, $F_{yt}$ and $F_{ut}$, in this relationship were then based on the measured steel coupon data for the respective specimens shown in Table 3.2. As an example, the resulting material relationship used for Specimen 17 is shown in Figure 4.3.

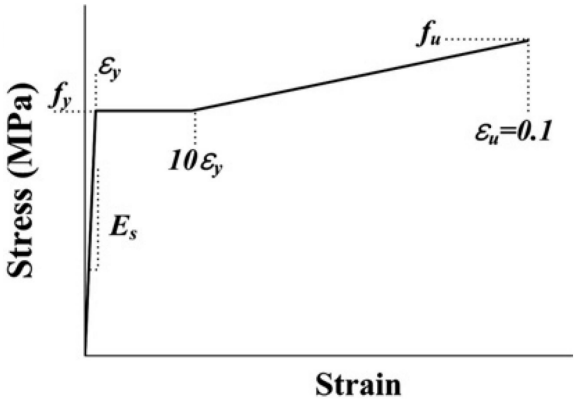



Figure 4.2: Tube Steel Stress vs. Strain Relationship by Moon et al. (2012)

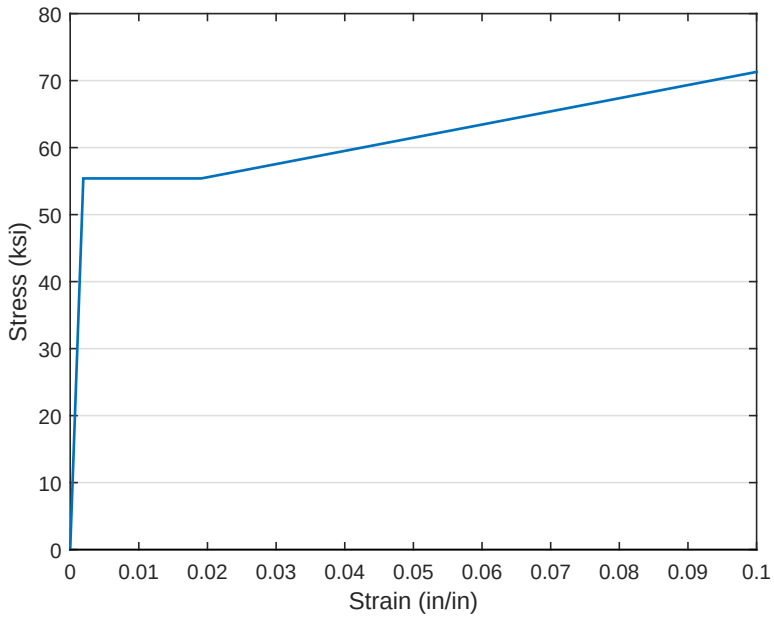



Figure 4.3: Base ABAQUS Model Tube Steel Stress vs. Strain Relationship (Specimen 17, $a/D = 0.5$)

*Concrete Fill*

The concrete fill of the CFST was made with solid 3D quadratic elements with reduced integration (C3D8R), having a nonlinear material definition. In general, concrete's response to stress can be considered brittle and often variable, even when part of the same mixing batch. In compression, it displays a relatively subtle decrease in strength after reaching its peak stress. Once reaching peak stress in tension, at $f_{ct}$ equal to 10% of $f'_c$, the load drops significantly due to tensile cracking. The elastic modulus of concrete was defined by ACI, 2011, $E_c = 57,000\sqrt{f'_c}\,(psi)$, and the poisson's ratio used is 0.2. For the uniaxial stress-strain relationship, confinement of the concrete was not directly accounted for in the base model, although it is clear that CFST members benefit from the increased strength of concrete under these conditions. The nonlinear compressive response was defined by Equation 4.1, with $R_\epsilon$ and $R_\sigma$ equal to 4 (Hu and Schnobrich, 1989).

$$f_c = \frac{E_c}{1 + (R + R_E - 2)(\epsilon_c/\epsilon_c') - (2R - 1)(\epsilon_c/\epsilon_c')^2 + R(\epsilon/\epsilon_c')^3} \tag{4.1a}$$

$$where: \; R_E = \frac{E_c \epsilon_c'}{f_c'} \tag{4.1b}$$

$$R = \frac{R_E(R_\sigma - 1)}{(R_\epsilon - 1)^2} - \frac{1}{R_\epsilon} \tag{4.1c}$$

Under tension, the post-peak behavior was estimated with a relatively soft slope, rather than dropping to zero, to avoid numerical issues. The resulting uniaxial stress-strain response used is shown in Figure 4.4, using Specimen 17 as an example.

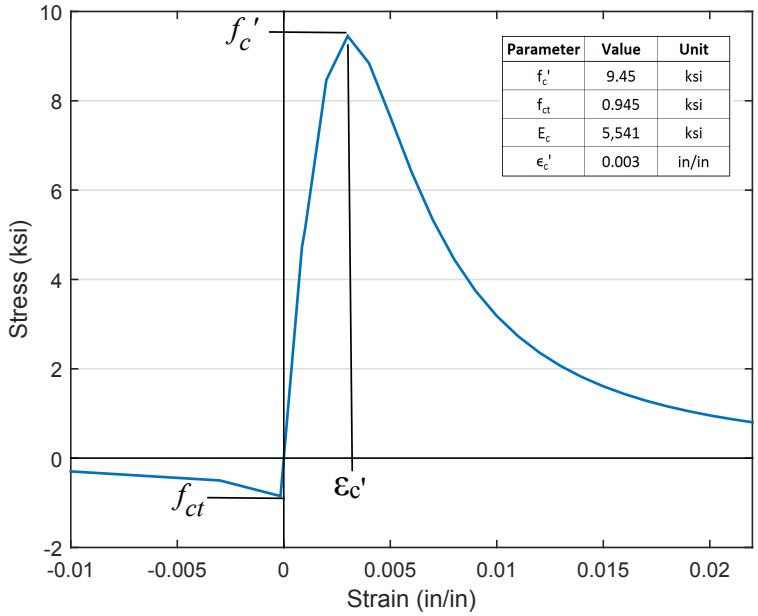
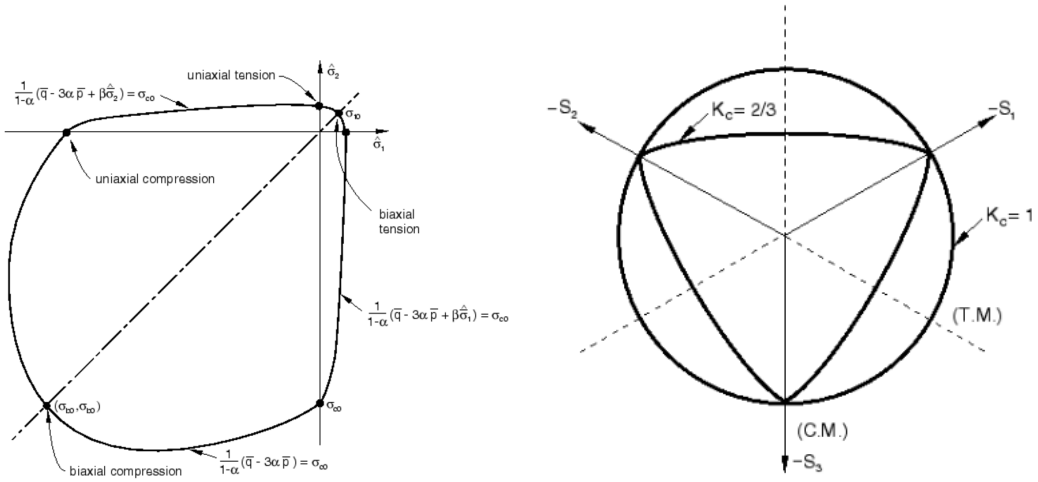



Figure 4.4: Concrete Uniaxial Stress vs. Strain Behavior (Specimen 17, $a/D = 0.5$)

For the remaining material behavior definitions, the Concrete Damaged Plasticity model in ABAQUS was used. The discrete crack model and flow rules of this material model has shown to provide good results for modeling CFSTs in flexure (Moon et al., 2012, 2013) and, therefore, was justified for this application. This model requires five parameters to define the complete performance of concrete in the numerical analysis: $f_{bo}/f_{co}$, $K_c$, dilation angle, eccentricity, and a viscosity parameter. These are all described in detail in Dassault Systemes Simulia Corp. (613) documentation and should be used as a supplement for details not provided here.

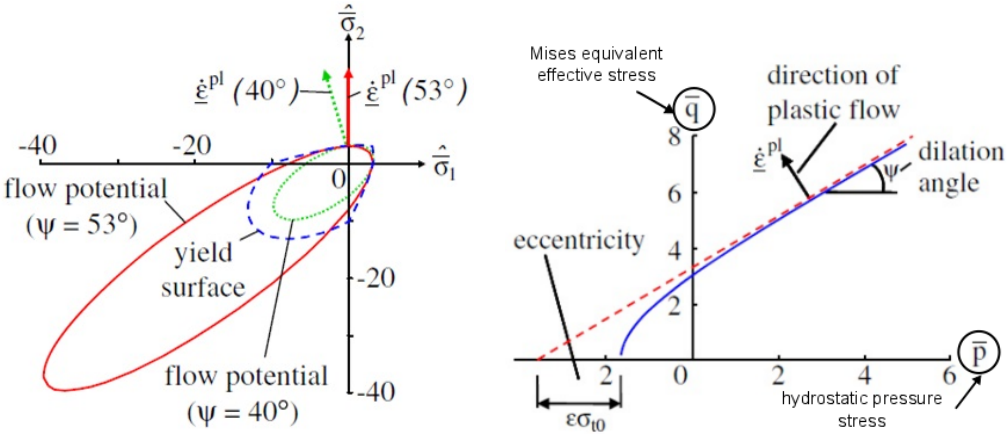
To create the yield function two criterion are defined, $f_{bo}/f_{co}$ and $K_c$. Figure 4.5 illustrates the use of these parameters in the yield function. The variable $f_{bo}/f_{co}$ defines the ratio of the strength of concrete in the biaxial state to the strength in the uniaxial state. Figure 4.5a shows that if this value were to continue to increase, the yield surface would become less circular in the 2D plane, changing the sensitivity of yielding to varying stress states. The parameter $K_c$ defines the ratio of the second stress invariant on the tensile meridian to that on the compressive meridian. Figure 4.5b shows how this parameter shapes the yield surface in three dimensions as the stresses in the material get larger. As this approaches 1.0, the surface becomes more circular.




(a) Yield surface in 2D stress state (b) Yield surface in deviatoric plane

Figure 4.5: Concrete Damaged Plasticity Parameter Influence on Yield Function (Dassault Systemes Simulia Corp., 613)

The flow rule of the material is dictated by its dilation angle and the eccentricity, or flow potential. Figure 4.6 demonstrates the effects of these parameters. The dilation angle defines the inclination of the yield surface and direction of plastic flow. The eccentricity is the ratio of tensile strength to the compressive strength of the concrete, as defined by the uniaxial behavior described above. As shown in Figure 4.6a, with larger dilation angles, the flow surfaces increases in the two dimensional plane of stress. Then, as the eccentricity of a material increases, the flow potential becomes more curved and the dilation angle increases more rapidly as confining pressure decreases (Dassault Systemes Simulia Corp., 613). This can be seen in Figure 4.6b. Finally, the viscosity parameter is used by ABAQUS for the visco-plastic regularization of the concrete constitutive equations by adjusting the relaxation time of the viscoplastic system. A default value of zero is defined by ABAQUS, but by increasing this value slightly to 0.001, convergence is better achieved without sacrificing accuracy. A summary of the CDP parameters used is given in Table 4.2.




(a) Flow potential and yield surface relationship

(b) Non-associative flow potential as related to dilation angle

Figure 4.6: Concrete Damaged Plasticity Parameter Influence on Flow Rule

Table 4.2: Concrete Damaged Plasticity Parameters

| $f_{bo}/f_{co}$ | $K_c$ | Dilation Angle | Eccentricty | Viscosity Parameter |
|---|---|---|---|---|
| 1.12 [1] | 0.666 [2] | 20 ° [1] | 0.1 | 0.001 |

[1] Values recommended by Moon et al. (2012).
[2] ABAQUS default value.

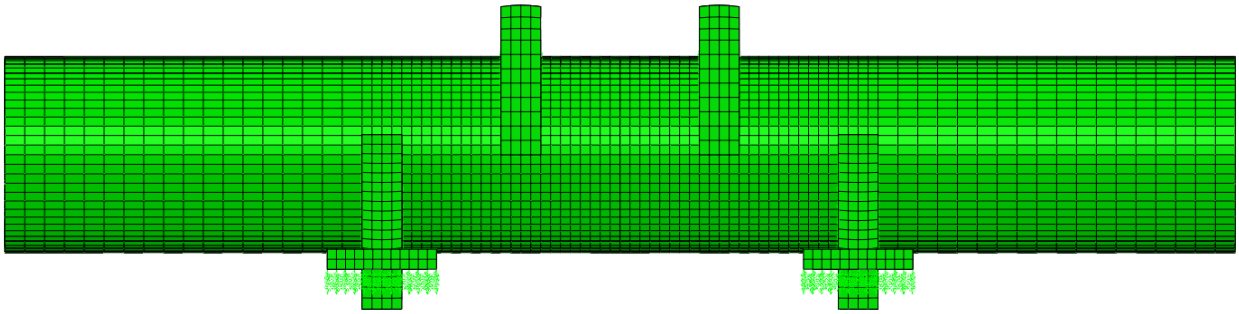
*Interface*

To achieve the appropriate CFST response to load, bond stress between the steel tube and concrete fill is required to develop composite behaviors through significant binding action forming from large local contact stresses and large deformations. In ABAQUS, this bond stress was modeled as a surface-to-surface interaction between the interfaces of the tube steel and concrete fill parts to form the CFST. A "Hard Contact" pressure in the normal direction was defined here that prevents the two surfaces from penetrating, but not restricting their separation. In the tangential direction, a coulomb friction coefficient was used. Moon

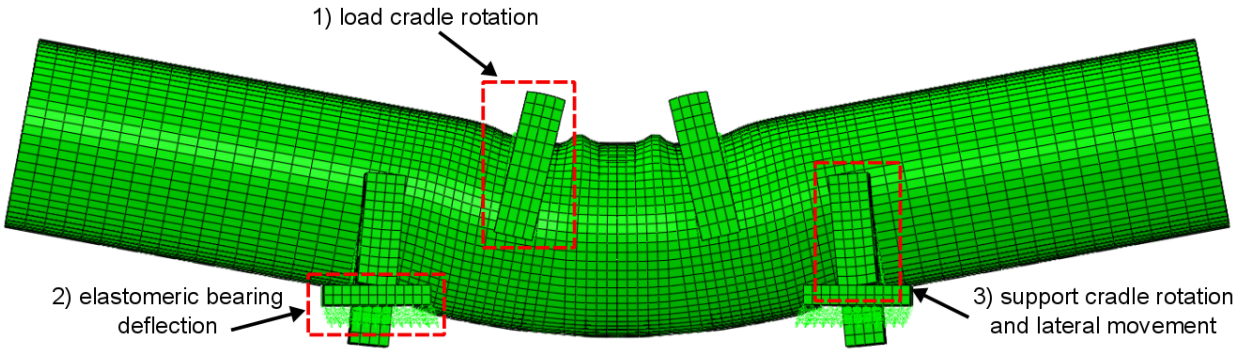
et al. (2012) showed that, for a spirally welded tube, a coulomb coefficient of friction, $\mu$, of 0.47 worked well. A smaller, 0.37, was found to be better for this application after several iterations, because straight seamed steel tubes were used in this experimental program that allowed for more slip between the two materials compared to spirally welded tubes.

#### *4.2.1.3 Test Setup*

The test setup in these experiments reacts, displaces, and deforms, which affects the force transfer through and displaced shape of the CFST specimen. The reactions of this setup include: 1) load cradle rotation, 2) support cradle rotation and lateral movement, 3) elastomeric bearing deflections, and 4) the cotton duck bearing pad deformations. All of these parts together compose the simulation's boundary conditions, and so the model was built with the aim of capturing the responses of the setup components appropriately with the procedures outlined in the following passages. Figure 4.7 highlights these deformations.



(a) Undeformed Setup



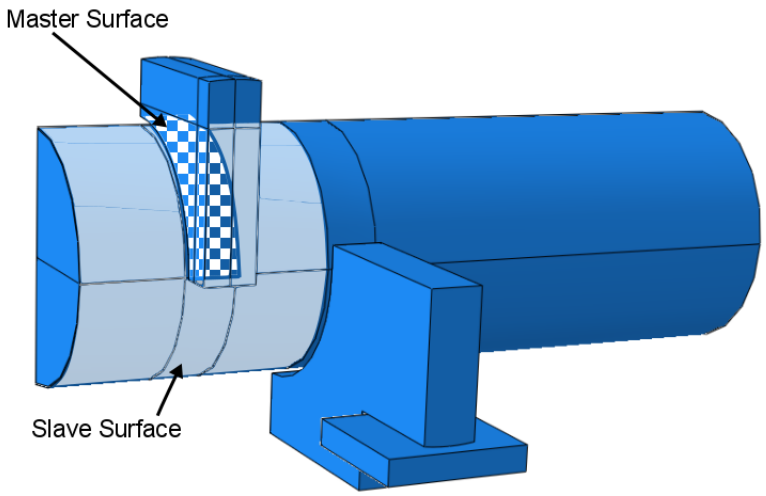

(b) Deformed Setup

Figure 4.7: Simulated Test Setup Movement

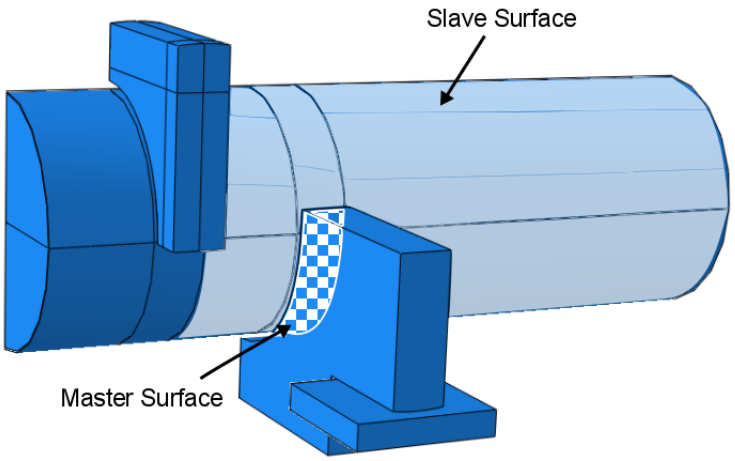
* Note that the cotton duck is not visible here and that the 'mirror' effect was used to create this image, as only one-quarter of the test is actually modeled.

*Load and Support Cradles*

The load and support cradles were composed of solid 3D quadratic elements (C3D8R) and dimensioned as detailed in the experimental design. However, the support was cradle was not modeled with its full vertical depth under the CFST cradle surface to save computational costs. Both were given elastic steel material properties with an elastic modulus, $E_s$, of $29,000\ ksi$ and a poisson's ratio of 0.3. When adding these parts to the assembled model, it was necessary to define the interaction of the outer tube surface of the CFST and cradles where they could potentially come into contact during the analysis. Figure 4.8 illustrates these locations. A surface-to-surface interaction with "Hard Contact" normal pressures and a tangential Mohr-Coulomb frictional relationship was defined, with a frictional coefficient, $\mu$, of 0.6, as typical with steel-to-steel contact.




(a) Load Cradle to Outer Tube Steel




(b) Support Cradle to Outer Tube Steel

Figure 4.8: Cradle to CFST Tube Surfaces for ABAQUS Interaction Definition

At the load cradle, it was important in the model to capture the rotation so that the angle of the force into the specimen could be achieved. Therefore, the load was applied as an imposed displacement, distributed along the centerline of the cradle enabling it to rotate as the system dictates without any additional restraints. This is illustrated in Figure 4.9.

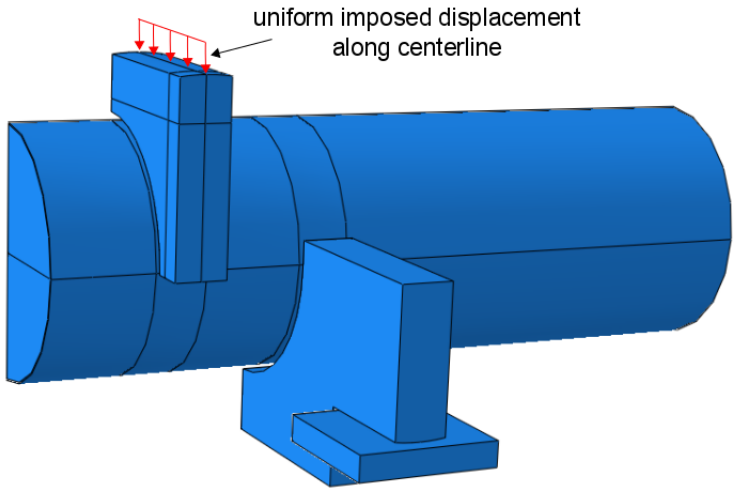



Figure 4.9: Loading Procedure in ABAQUS Model

The support cradle had two primary experimental deformation characteristics: 1) rotation with the specimen as it deflected, and 2) lateral sliding along the top plate of the elastomeric bearing. A curved radius was machined onto the cradles at the load beam and elastomeric bearing top plate bearing points to allow for free rotation (refer to Figure 3.1). This same radius was provided in the model so that this rotation was achieved in the same manner. Once reaching a the full rotation provided by the machined radius, then the support cradle began to slide. This sliding behavior was simulated with the surface-to-surface interaction where the curved support surface and elastomeric bearing top plate come into contact, as shown in Figure 4.10. This was defined with a "Hard Contact" pressure in the normal direction and a coefficient of friction, $\mu$, of 0.6 in the tangential direction.

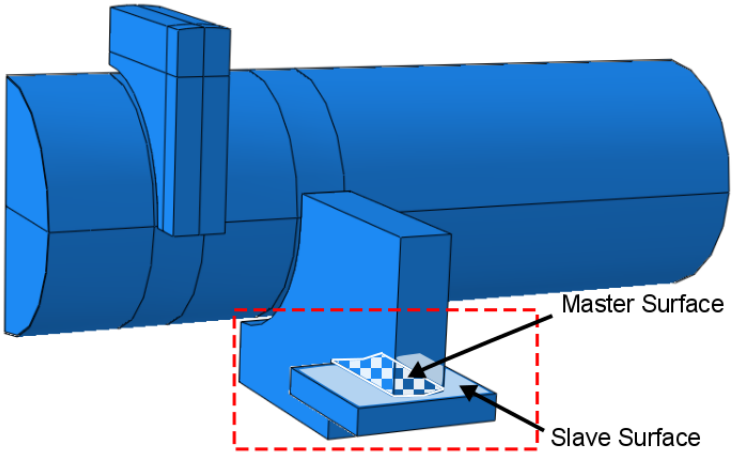



Figure 4.10: Support Cradle Sliding Surface in ABAQUS Model

*Elastomeric Bearing and Cotton Duck Bearing Pads*

As part of the experimental test setup design, elastomeric bearings and cotton duck bearing pads are put into the system at points of large stress concentrations to soften contacts with the CFST and base supports. These two objects are designed to be very nonlinear in behavior and so a unique modeling approach for them was required. In this simulation, both were modeled with elastic springs in a truss configuration, as seen in Figure 4.11, allowing for different compressive and shear stiffness definitions in the vertical and lateral directions. A summary of the spring stiffnesses used for these parts is given in Table 4.3.

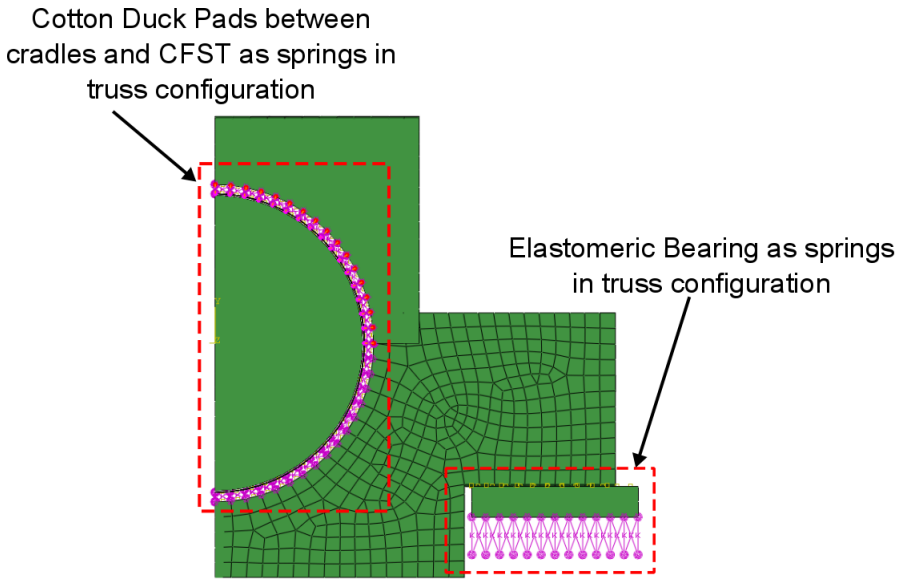



Figure 4.11: Elastomeric Bearing and Cotton Duck Pads in ABAQUS Model

Table 4.3: Elastomeric Bearing and Cotton Duck Spring Stiffnesses ($kips/in.$) in ABAQUS

| Part | Spring Type | |
|---|---|---|
| | Normal/Vertical | Diagonal |
| Elastomeric Bearing | 19 | 10 |
| Cotton Duck Bearing Pad | 41.9 | 15 |

The elastomeric bearing springs spanned a distance equal to the bearing thickness ($2.5\ in.$) between the bottom of the steel top plate and fixed reference points in space. It was from these fixed nodes that the vertical force reactions are summed and multiplied by two in order to obtain the magnitude of the shear force in the final simulation. The steel top plate was made of 3D solid elements (C3D8R) with an elastic steel material ($E_s = 29,000\ ksi$ and $\nu = 0.3$). The elastomeric bearing springs were given stiffnesses of 19 and 10 $kips/in.$, in the vertical and diagonal springs, respectively. These values were selected after a parameter study investigated values between 5 to 19 $kips/in.$, with values based on estimation of previous research (Roeder et al., 1987) and axial compression tests performed on the bearings used in

the testing program. When appropriate displacement of the bearing in vertical and lateral directions was observed, along with consistent model stability through the analysis, the stiffness values were finalized.

The cotton duck springs spanned approximately 0.5 *in.* between adjacent mesh nodes of the cradle surfaces and the CFST tube steel, with shell nodes located mid-depth of the tube thickness. The springs were arranged normal to the tube surface and diagonally, forming the truss system. Previous studies by Lehman et al. (2003) estimated the elastic modulus of similar cotton duck pads to be around 30 *ksi*. However, because this aspect was modeled with one-directional springs stiffness properties of, 41.9 and 15 *kips/in.* in the normal and diagonal directions, were selected after a parameter study was performed that looked at stiffness ranging from 10 to 41.9 *kips/in.*. The final values were chosen when accurate predictions of local CFST deformation behaviors were achieved in the model. When distributed over the bearing area, the total stiffness of the vertical springs was approximately 30 *ksi* though.

#### *4.2.1.4 Base Model Results*

*Simulation of Flexural Response*

The predicted behavior using the above modeling techniques was good for specimens controlled by flexure. The maximum shear force magnitude found in the simulation for Specimen 17 ($a/D = 0.5$ model) underestimated that found in the experiment, as defined by $V_{ed}$, by only 0.68% (Table 4.4). Additionally, the model accurately simulated the elastic stiffness, as shown in Figure 4.12.

Table 4.4: Base Model Maximum Shear Force Results for Flexurally Dominated Specimen (Specimen 17, $a/D = 0.5$)

| Max Shear Force | | Units |
|---|---|---|
| $V_{ed}$ | 544.3 | kips |
| $V_{pr}$ | 540.6 | kips |
| Error | 0.68 | % |

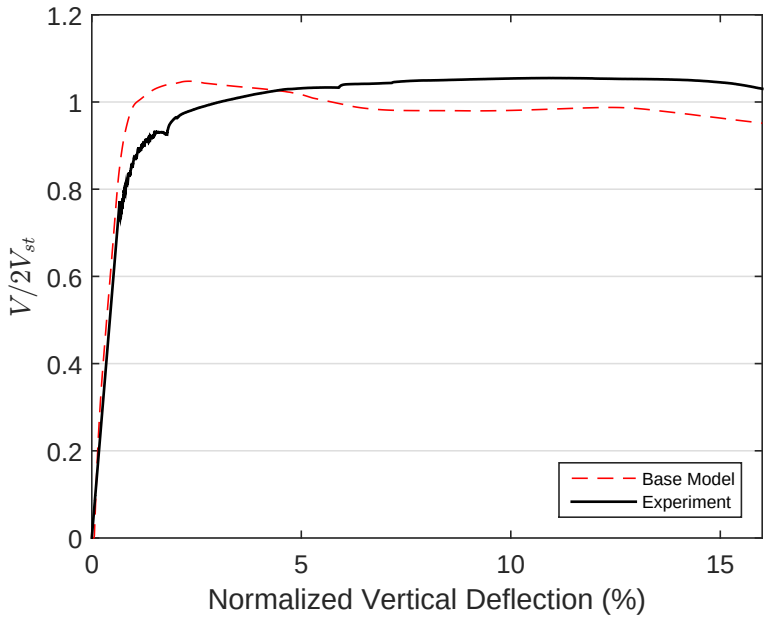
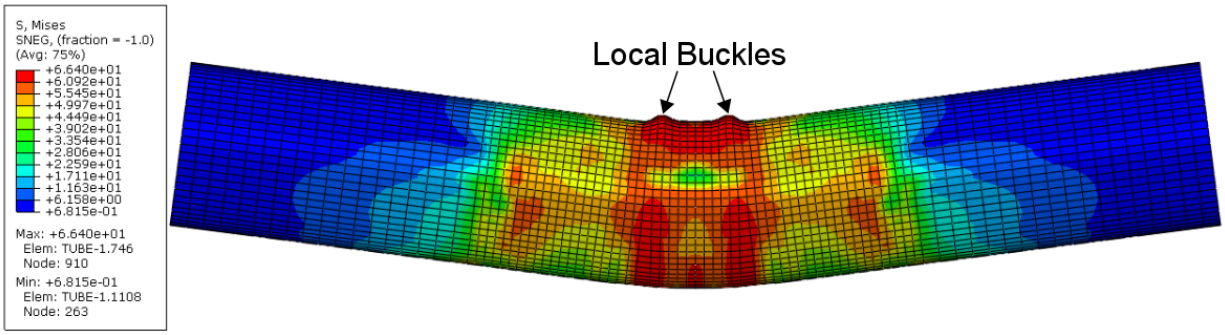
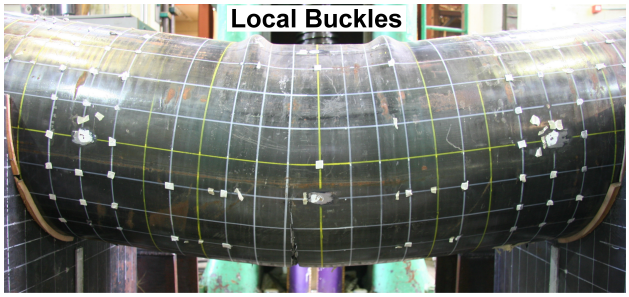



Figure 4.12: Measured, $V_{ed}$, and Predicted Normalized Normalized Shear vs. Vertical Deflection for Flexurally Dominated Specimen using Base Model (Specimen 17, $a/D = 0.5$)

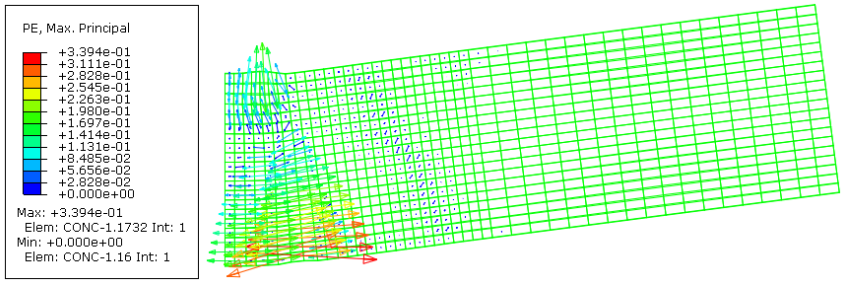
The local deformations observed in the experiment were also accurately simulated. Figure 4.13a and b shows the tube steel yielding distribution and local buckling. Note that the mirror effect was used for visualization in Figure 4.13a. The simulation did not include both symmetric halves shown here. Additionally, Figure 4.13c and d shows a comparison of concrete cracking patterns in the model compared to the experimental specimen. This is estimated by visualizing cracks that run perpendicular to the outward facing arrows that represent the maximum principal strains in the concrete. The resulting patterns are generally quite similar with dense tensile cracking in the pure moment region, concrete crushing in compression due to flexure, and minimal diagonal cracking in the shear span.




(a) Predicted von mises stresses and deformation of tube steel




(b) Observed deformations of tube steel




(c) Predicted maximum principal concrete strains at CFST centerline (cracks can be estimated perpendicular to arrows)




(d) Observed cracking patterns of concrete fill

Figure 4.13: Observed and Simulated Local Behaviors of Flexurally Dominated Specimen using Base Model (Specimen 17, $a/D = 0.5$)

*Simulation of Shear Response*

The base model was not capable of simulating shear yielding response appropriately. Table 4.5 and Figure 4.14 show that the maximum predicted shear force in the model underestimated that measured in the experiment by 26% for Specimen 16 ($a/D = 0.375$ model). It was found that with continued modifications to the parameters discussed as part of the base model development, the prediction remained to be confined at this low maximum force because strain hardening after yielding onset was not being captured in the model. However, the local deformations in the base model for Specimen 16 were simulated as observed in the test (Figure 4.15).

Table 4.5: Base Model Maximum Shear Force Results for Shear Yielding Specimen Specimen (Specimen 16, $a/D = 0.375$)

| Max Shear Force | | Units |
|---|---|---|
| $V_{ed}$ | 760.6 | kips |
| $V_{pr}$ | 561.2 | kips |
| Error | 26.2 | % |

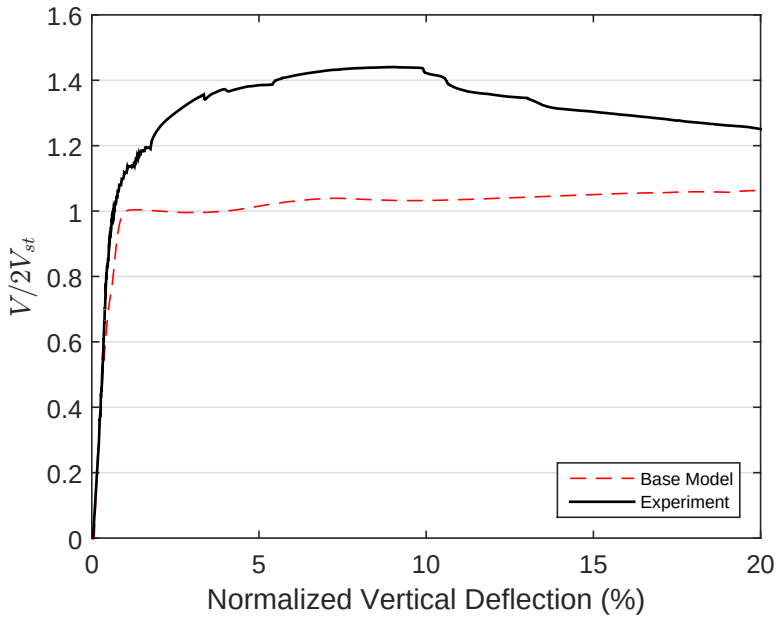
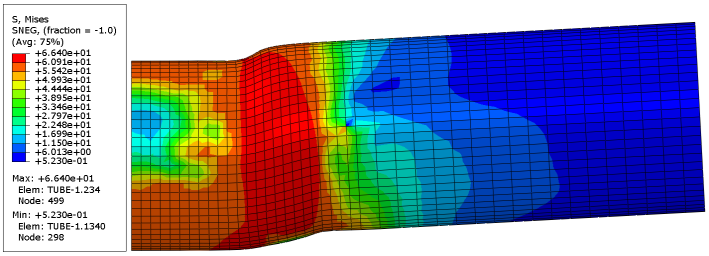
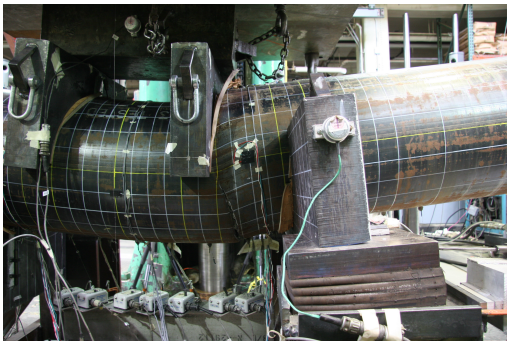


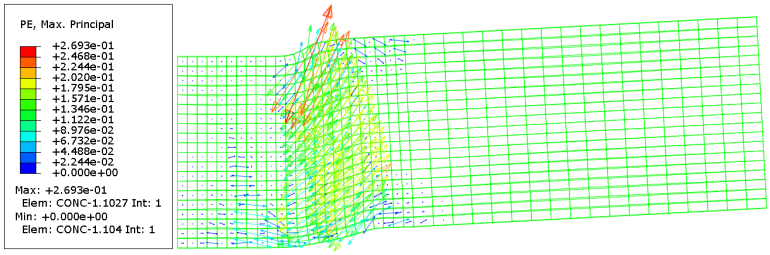

Figure 4.14: Measured, $V_{ed}$, and Predicted Normalized Shear vs. Vertical Deflection for Shear Yielding Specimen using Base Model (Specimen 16, $a/D = 0.375$)




(a) Predicted von mises stresses and deformation of tube steel



(b) Observed deformations of tube steel




(c) Predicted maximum principal concrete strains at CFST centerline (cracks can be estimated perpendicular to arrows)




(d) Observed cracking patterns of concrete fill

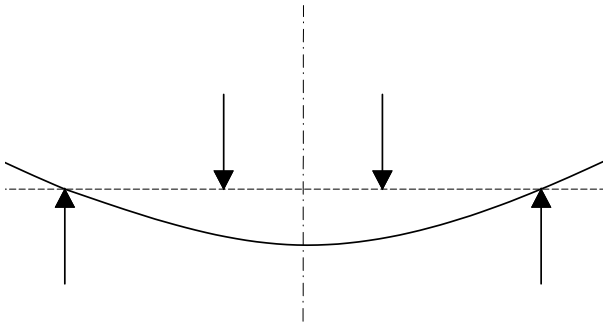
Figure 4.15: Observed and Simulated Local Behaviors of Shear Yielding Specimen using Base Model (Specimen 16, $a/D = 0.375$)

### *4.2.2 Modeling Issues*

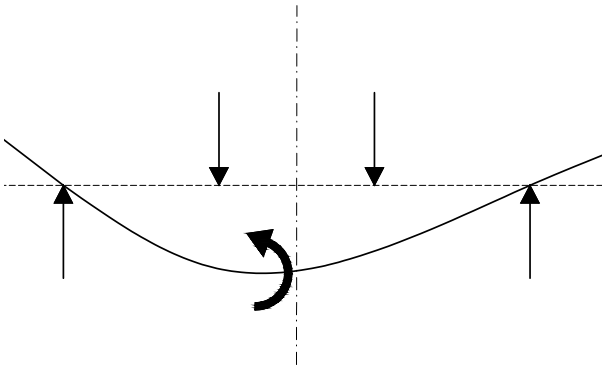
Although explicit attempts to capture the performance of both the setup and specimen were made with the base model, the results of the shear-dominated specimen demonstrated that there exists physical behaviors in the experiments that the analytical program is not capable of predicting. Three complex differences between the model and the experiments are: 1) non-symmetric experimental behaviors, 2) large deformations of the CFST member, and 3) significant nonlinearity in the test setup.

*Symmetry*

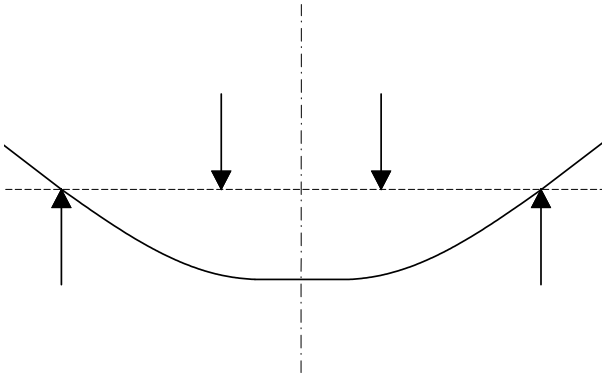
While the models assume symmetry, there was actually an inherent imbalance in the experiments that caused one side of the specimen to fail in shear before the other. This could have been an issue with the setup geometry, concrete imperfection, or some other intractable variable. Consequently, in the tests, an additional moment was felt internally by the specimen, applied near midspan, that caused it to reach a higher shear at a given displacement value, had it failed symmetrically in shear, as illustrated in Figure 4.16. Ultimately, this conflict between simulation and experimentation results in a difference in deflections and force magnitude.



(a) Flexural Specimen: Experimental and Simulated



(b) Shear Specimen: Experimental



(c) Shear Specimen: Simulated

Figure 4.16: Illustration of Symmetry Issue in Analytical Models

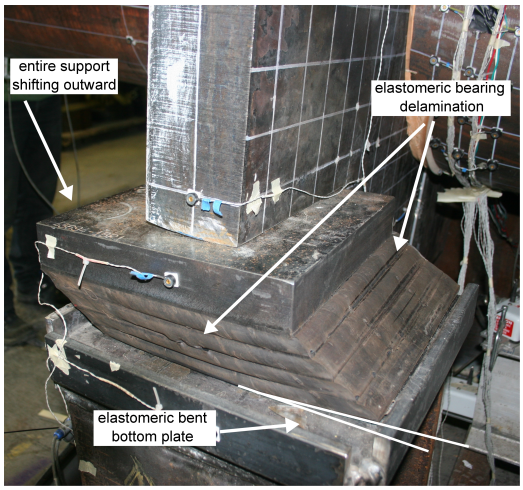
*Large CFST Deformations*

In order to induce shear controlled behaviors into the CFST specimens, significant local and global deformations are required, resulting in evident shear yielding in the steel tube and extensive cracking in the concrete fill, as shown in Chapter 3. The reaction of the steel tube material's yield surface in shear to these high stresses can be difficult to mimic with the classic plasticity model and Von Mises criterion in ABAQUS. Furthermore, in models where high strains are present, numerical convergence becomes more difficult, particularly with concrete models, and although the CDP material model accounts for discrete cracks, it was not capable of accurately opening cracks and advancing displacement behaviors as seen in the tests.

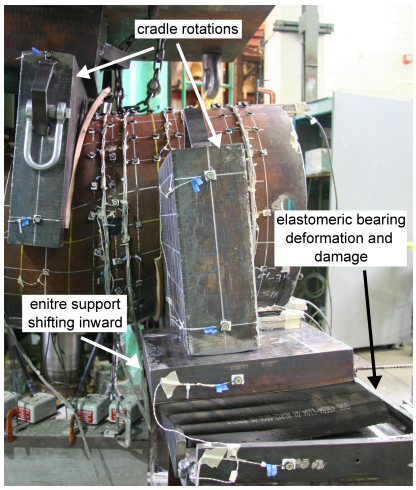
*Significant Setup Nonlinearity*

The experimental testing apparatus was designed with the intent of creating a truly pinned support condition, that did not cause unwanted additional restraints and forces in the specimen, so that pure moment and shear responses could be observed. In doing so, the rotating support cradles, elastomeric bearing, and cotton duck introduced to the system varying nonlinear effects that are difficult to analytically predict. Additionally, the substantial demands put onto the system in the testing program pushed these nonlinear components to extreme deformations (Figure 4.17) that sometimes induced ancillary movements. These individual behaviors were discussed briefly in Chapter 3, but are reiterated here more explicitly to demonstrate their highly unpredictable performance.

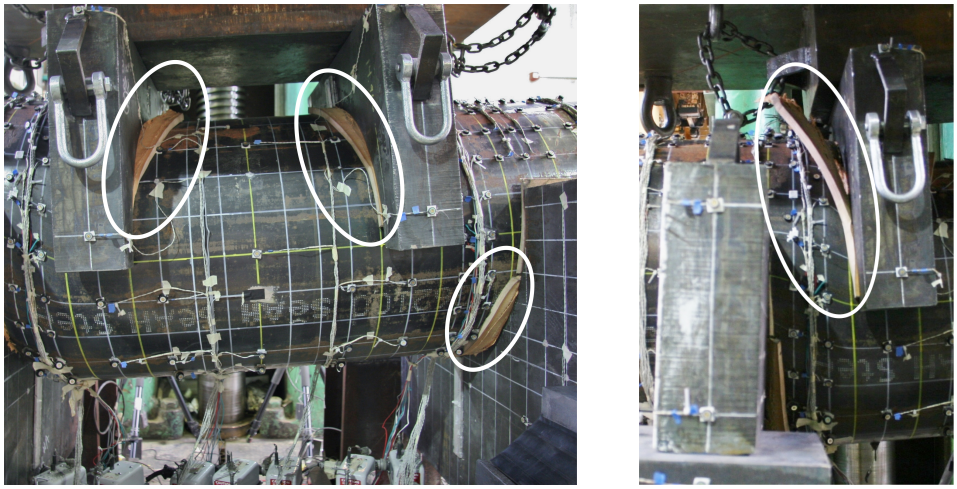
First, early on in testing, the cotton duck bearing pads were essentially lost from severe compression and damage. For the remainder of the test, the direction of rotations and displacements of the support cradles and elastomeric bearings could be either toward or away from the specimen midspan, based the resulting failure mode, sometimes changing directions during testing. Then, when the lateral demands on the elastomeric bearings became extreme, they began to delaminate and eventually rubber layers split from the steel layers. Around this same deformation limit, the support cradles reached their full rotation capacity and would slide horizontally across the top surface of the elastomeric bearing.




(a) Extreme outward elastomeric bearing deformation (Specimen 8)




(b) Significant support displacements (Specimen 11)



(c) Typical cotton duck bearing pad deformations (Specimen 14)

Figure 4.17: Experiment Nonlinear Setup Deformations

### *4.2.3 Refined Base Model*

Given the modeling constraints described in the previous section, the base model was further refined, using Specimen 16 to start, with the goal of optimizing maximum shear force prediction, while maintaining initial elastic stiffness behaviors, because deflections could not be captured in the simulations. To do this, four techniques were introduced sequentially to make the final validated model, each either improving material contribution or mimicking the test setup arrangement at peak load in the experiments:

1. Large strain material definitions
2. Remove cotton duck bearing pad springs
3. Replace support setup, including support cradle and elastomeric bearing, with series of springs
4. Confined concrete uniaxial stress-strain model

A comparison of predicted maximum shear with the base model and refined base model is given in Table 4.6. Figure 4.18 compares the experimental and predicted force-deflection behaviors with the refined base model improvements.

Table 4.6: Refined Base Model Maximum Shear Force Results for Shear Yielding Specimen (Specimen 16, $a/D = 0.375$)

| Model | $V_{pr}$ (kips) | % Error |
|---|---|---|
| Base Model | 583.5 | 23.3 % |
| Refined Base Model | 655.6 | 13.8 % |

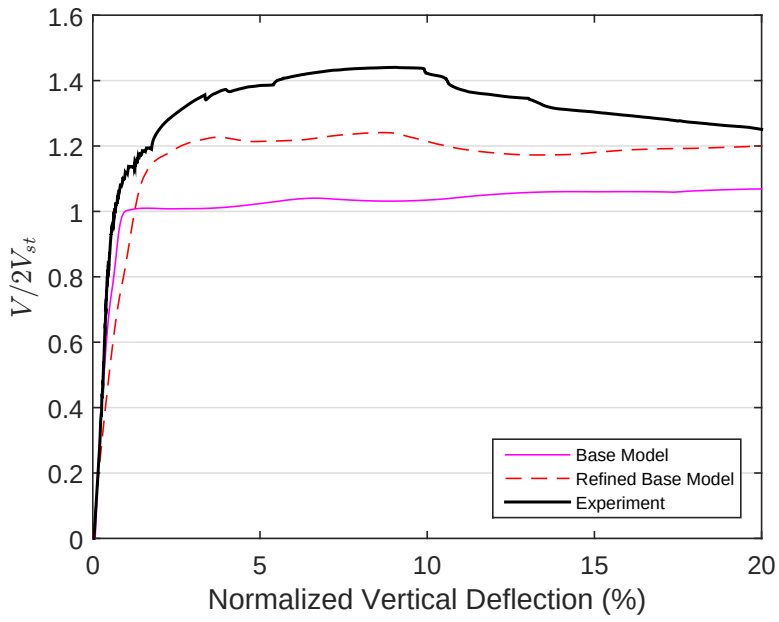



Figure 4.18: Measured and Predicted Normalized Shear vs. Vertical Deflection for Shear Yielding Specimen using Refined Base Model (Specimen 16, $a/D = 0.375$)

The resulting model achieved both reasonable elastic stiffness estimation and predicted maximum shear force magnitude. Explicit explanations of the methods used to implement these techniques is discussed in the following passages, along with motivations and direct results from each step.

#### *4.2.3.1 Large Strain Approach*

Although the deformations with the flexure and shear-controlled specimens were similar, the shear-dominated models saw significantly higher strains, therefore finite material definitions better represented these behaviors. So, while retaining the base model stress-strain relationships, Cauchy stress and logarithmic strains were derived from Equations 4.2 and 4.3 for both concrete and tube steel material models. Furthermore, the concrete elastic modulus was defined by the EuroCode, $E_c = 10,000(f'_c + 8)^{0.33}$ $(MPa)$, as justified by studies from Hanneson (2010). This definition resulted in more strain hardening of the system and better

prediction of shear resistance, with 16.6% error.

$$\sigma = \sigma_{eng}(1 + \epsilon_{eng}) \tag{4.2}$$

$$\epsilon_{pl} = ln(1 + \epsilon_{eng}) - \frac{\sigma_{eng}}{E_w} \tag{4.3}$$

#### *4.2.3.2 Remove Cotton Duck Bearing Pads*

The cotton duck bearing pad springs were removed from the model so that the cradles bear directly onto the tube steel. By removing these springs altogether, the shear force increased in the model to be within 12% of the experimental value. Because the maximum shear value obtained in the final refined model had 13.8% error, one could conclude that the model was sufficient after removing the cotton duck and further adjustments were not necessary. However, this refinement technique also resulted in a severe loss in initial stiffness (Figure 4.19). This result could have be expected though because, as noted previously, the cotton duck was really only effective early on in the tests. By the time maximum shear force was reached, the cotton duck pad had become so severely damaged, it had no impact on the system reaction. Consequently, the model need not include this component when considering ultimate shear force, but further steps were needed to better capture the elastic behavior of the CFST.

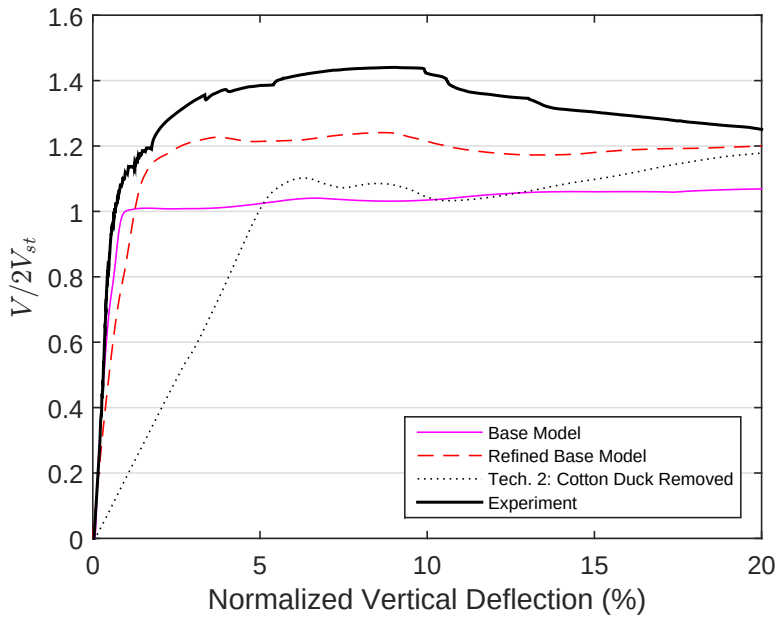


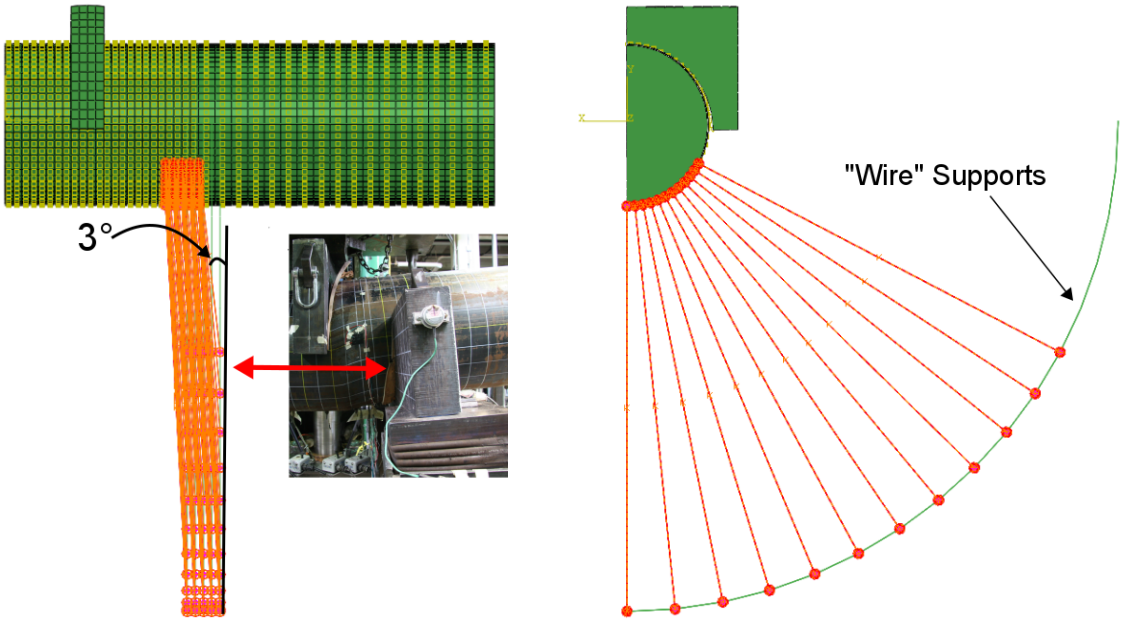

Figure 4.19: Measured and Predicted Normalized Shear vs. Vertical Deflection for Shear Yielding Specimen with Cotton Duck Removal (Specimen 16, $a/D = 0.375$ ABAQUS model)

#### *4.2.3.3 Replace Support Setup with Springs*

Following the removal of the cotton duck springs, the approach to modeling the experimental support system, including the support cradle and elastomeric bearing, was replaced with springs, having a stiffness of 100 *kips/in.* and set at an angle of 3°, as illustrated in Figure 4.20. This simulation was able to both retrieve the lost initial stiffness and maintain a shear load within 17.8% of the measured response.

The angle of 3° was used to replicate the angle of the support cradle at peak load for specimens showing significant shear yielding, like Specimen 16. This approach focuses on the support reaction at the point of peak resistance and removes the reliability of the model to capture the exact movement of the support setup throughout the simulation. The springs connect to nodes on the steel tube and then out to nodes on elastic wires that provide support to the system in the x, y, and z directions. The vertical reactions here are summed

and multiplied by two in order to determine the shear force in the simulation. Furthermore, the collection of springs cover a surface area 4 *in.* wide by approximately 1/3 of the tube circumference to simulate the bearing area of the tube to cradle at maximum load.




(a) Side View (b) End View

Figure 4.20: Illustration of the Final Model Boundary Conditions

#### *4.2.3.4 Concrete Confinement*

The final adjustment to the model was the implementation of a confined concrete uniaxial stress-strain model. While evaluating different salient techniques to use in the refined base model, a pressure of 1 *ksi* was applied normally to the concrete in the radial direction and at the free end surface. This resulted in an increase in shear resistance of the model within 6.2% of the experimental response, suggesting that the inherent increase in concrete strength of the fill due to the tube confinement was not being predicted. Therefore, the explicit application of a confined concrete material model was used.

Analytical research performed by Han et al. (2007b) gave the model defined by Equation 4.4. In these equations, the variable $f_{ck}$ is equivalent to $0.67f_{cu}$ for normal concrete, with $f_{cu}$ being the concrete's cube strength. Because only cylinder strength was obtained in the experimental program though, $f_{cu}$ was set to $1.25f'_c$ (ECS, 2013). Using these values, the stress-strain behavior was defined by the parameters, $y = \sigma/\sigma_0$ and $x = x = \epsilon/\epsilon_0$, and the confinement adjustment provided by the factor $\xi = \frac{A_{st}F_{yt}}{A_c f_{ck}} = \alpha\frac{F_{yt}}{f_{ck}}$. The resulting material relationship used in the final model is shown in Figure 4.21.

$$y = \begin{cases} 2x - x^2 & x \leq 1 \\ \frac{x}{\beta_0(x-1)^\eta + x} & x \geq 1 \end{cases} \tag{4.4a}$$

$$\begin{aligned} where: \quad E_c = 4730\sqrt{f'_c}\ \ (MPa); \quad \sigma_0 = f'_c\ (N/mm^2); \\ \epsilon_0 = \epsilon_c + 800\xi^{0.2} \times\ 10^{-6}; \quad \epsilon_c = (1300 + 12.5f'_c)\ \times\ 10^{-6} \end{aligned} \tag{4.4b}$$

$$\eta = \begin{cases} 2 & \text{(circular CFST)} \\ 1.6 + 1.5x & \text{(square CFST)} \end{cases} \tag{4.4c}$$

$$\beta_0 = \begin{cases} 0.5(2.36\ \times\ 10^{-5})^{[0.25+(\xi-0.5)^7]}(f'_c)^{0.5} \geq 0.12 & \text{(circular CFST)} \\ \frac{(f'_c)^{0.1}}{1.2\sqrt{1+\xi}} & \text{(square CFST)} \end{cases} \tag{4.4d}$$

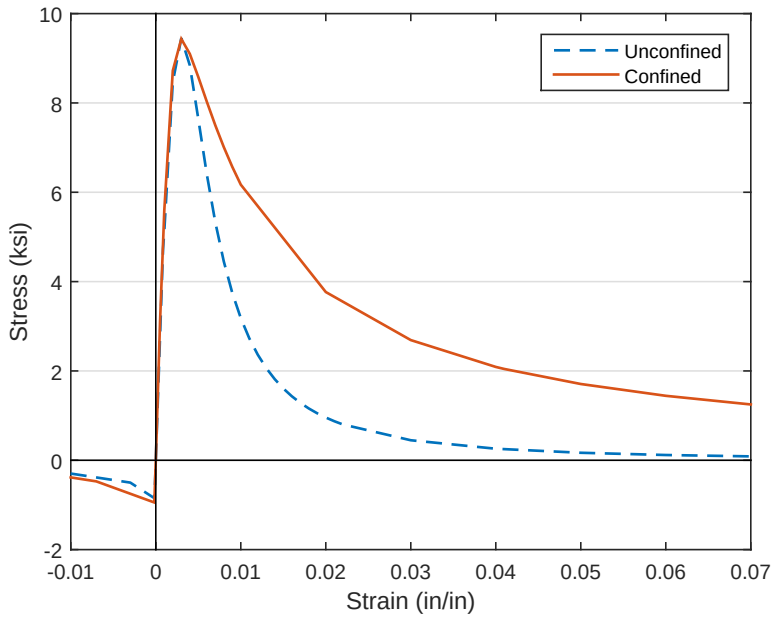



Figure 4.21: Concrete Stress vs. Strain Behavior (Specimen 17, $a/D = 0.5$ model)

This final iteration of the refined base model resulted in a maximum shear that underestimated the observed shear force by 13.8% while maintaining initial stiffness and local deformations very similar to Figure 4.15.

#### *4.2.3.5 Refined Base Model Summary*

The success demonstrated by these modifications to the base model conclude that: 1) the estimation of displacement past yield is complicated by the significant nonlinear responses of the cotton duck, elastomeric bearing, and load cradles; 2) the boundary conditions have a significant influence on the force transfer through the CFST and predicted maximum load; and 3) the concrete was not being accurately confined solely with the interface definition in the base model and improvement in concrete material modeling is needed for CFST application. A likely reason the approaches to simulating the experimental behaviors in the refined model more appropriately reflected shear resistance and local behaviors was that the various uncertainties and deformations from the experimental setup have been condensed

into fewer distinct properties, namely angle and spring stiffness of the support. Additionally, the concrete fill was able to contribute more to the CFST performance with the confined material definition.

A summary of the components and their respective simulation techniques in the final model is as follows (* signifies updates from the base model):

*CFST Specimen*

1. Steel Tube
    - Shell elements, with reduced integration schemes (S4R)
    - Material: $E_s = 29,000\ ksi$, $\nu = 0.3$; trilinear stress-strain relationship (Moon et al., 2012) using steel coupon data for $F_{yt}$ and $F_{ut}$ and; * Cauchy stress-logarithmic strain definitions
2. Concrete Fill
    - Solid 3D quadratic elements, with reduced integration (C3D8R)
    - Material: $E_c = 4730\sqrt{f'_c}\ \ (MPa)$, $\nu = 0.2$; Concrete Damaged Plasticity model with the parameters shown in Table 4.2; * confined compressive uniaxial stress-strain relationship (Han et al., 2007b) with $f'_c$ from cylinder data and the tensile relationship presented in Section 4.2.1.2
3. Interface
    - Surface-to-Surface contact interaction between tube and concrete fill interfaces
        - Normal behavior: "Hard Contact" pressure-overclosure with "penalty" constraint enforcement method
        - Tangential behavior: Penalty friction formulation with a frictional coefficient, $\mu$, of 0.37
        - Geometric properties: "Out-of-plane surface thickness or cross-sectional area" of 1

*Test Setup*

1. Load Cradle * without Cotton Duck Bearing Pad
    - Solid 3D quadratic elements, with reduced integration (C3D8R)
    - Material: Elastic steel with $E_s = 29,000\ ksi$ and $\nu = 0.3$
    - Surface-to-Surface contact interaction between cradle and outer tube surfaces
        - Normal behavior: "Hard Contact" pressure-overclosure with "penalty" constraint enforcement method
        - Tangential behavior: Penalty friction formulation with a frictional coefficient, $\mu$, of 0.6
        - Geometric properties: "Out-of-plane surface thickness or cross-sectional area" of 1
    - Load applied as imposed displacement, distributed along the centerline of the cradle
2. * Support
    - Springs as shown in Figure 4.20 with stiffness, $k = 100\ kips/in.$, positioned at an angle of 3°

## *4.3 Model Validation*

Using the techniques in the refined base model, simulations of the specimens listed in Table 4.1 were created and validated using maximum experimental shear force magnitudes. A summary of the simulated values compared to the experiments is found in Table 4.7, with the average absolute error being approximately 8%. A positive value in the table reflects underestimation and a negative value, overestimation. Furthermore, the term $V_{ed}$ is being used for comparison because it is a better reflection of the symmetry being simulated.

It is clear from this data that larger errors are found with the intermediate shear span ratios of 0.5 and 0.375, where, in the experiments, varying failure modes were observed.

This could be reflective of many things, including uncertainty with the true shear span length at peak load in the models and tests, and the flexure-shear interaction behavior seen in the experiments that can't be replicated clearly through simulation. Han et al. (2008) noted similar issues with obtaining the same failure modes as experiments at a given $a/D$ ratio. Han required much smaller $a/D$ ratios than his experiments reported, in order to achieve shear failure. Similarly, the results here do not represent the appropriate failure mode. It is also worth noting that the average absolute error and individual error with the more shear-like specimens, 10 and 14, are quite small and the majority of the analytical models under-predicted the shear resistance compared to the already conservative estimate of $V_{ed}$. Therefore, this model is used for further parametric study of shear response, where the conclusions are considered both conservative, and reasonably accurate considering the validation here. Additional results from the validated models are given Appendix D.

Table 4.7: Summary of Error in Predicted Ultimate Shear Resistance

| $a/D$ | Specimen | Failure Mode | $V_{ed}$ (kips) | $V_{pr}$ (kips) | $\%Error_{ed}$ |
|---|---|---|---|---|---|
| 1 | S1 | Flexure | 322.0 | 327.9 | -1.83 % |
| 0.5 | S17 | Flexure | 544.5 | 624.8 | -14.7 % |
| | S2 | Flexure | 549.0 | 496.0 | 9.65 % |
| 0.375 | S16 | Flex-Shear | 760.5 | 655.6 | 13.8 % |
| | S10 | Flex-Shear | 660.0 | 628.1 | 4.83 % |
| 0.25 | S14 | Shear | 788.4* | 764.7 | 3.01 % |

* $V_{ed}$ corresponds to the peak shown in Figure D.1f by the dotted line.

# Chapter 5

# PARAMETER STUDIES

## *5.1 Introduction*

Utilizing the refined base model in ABAQUS, the influence of the following parameters on the shear strength of CFSTs were investigated:

- Axial Load Ratio, $P/P_0$
- Tube Diameter to Thickness Ratio, $D/t$
- Concrete Strength, $f'_c$
- Tube Steel Yield Strength, $F_{yt}$
- Internal Reinforcement Ratio, $\rho_{int}$

All models had a diameter of 20 *in.*, a long tail length, $L_T$, of $2D$, to ensure full composite action, and either $a/D$ of 0.375 or 0.25, since only these saw shear failure in the experiments. Additionally, all steel tubes were assumed to be straight seamed with a clean interface between the steel tube and concrete fill, as these conditions were used to develop the interface condition in the validated models.

It is understood that the shear capacity of CFSTs is a combination of three components' material and geometric properties, steel tube, internal reinforcement, and concrete fill, with some relationship reflecting their relative contributions to total resistance. Using measured material properties, the experiments suggest that $2V_{st}$, with $V_{st} = 0.6F_{yt}(0.5A_{st})$, and $V_{srl}$, with $V_{srl} = 0.6F_{yrl}(0.5A_{srl})$, can be estimates for the steel tube and internal reinforcement

contributions. The concrete fill though has yet to be explicitly quantified. In terms of nominal capacity then, shear resistance is defined as:

$$V_n = 2V_{st} + V_{srl} + \eta V_c \tag{5.1}$$

with the concrete contribution estimated as $\eta \cdot 0.0316 A_c \sqrt{f'_c}$ (in ksi), and $\eta$ calculated as:

$$\eta = \frac{V_{pr} - 2V_{st} - V_{srl}}{0.0316 A_c \sqrt{f'_c}}$$
$$(f'_c \; is \; in \; ksi \; units) \tag{5.2a}$$

$$where: \;\; V_{st} = 0.6 F_{yt} (0.5 A_{st}) \tag{5.2b}$$
$$V_{srl} = 0.6 F_{yrl} (0.5 A_{srl}) \tag{5.2c}$$

### *5.2 Axial Load Ratio,* $P/P_0$

CFSTs are typically used for piers or deep pile foundations in bridges and, therefore, resist axial load, in addition to flexure and shear. Axial compression can increase the shear strength contribution of the concrete, but tends to also have negative effects due to stability issues. Since only one test examined the impact of axial load, parameter studies were used to evaluate this effect further.

Axial load was applied to the CFST in the simulations as a uniform pressure on the tail surface of the concrete fill and line load on the steel tube edge, since the shell element application does not explicitly model a finite thickness (Figure 5.1). When distributing the line load over the tube thickness, the pressure was equivalent to the pressure applied to the concrete surface. The base CFST, summarized in Table 5.1, was analyzed with the following axial load ratios, $P/P_0$ ($P_0$ defined by Equation 2.3): **0**%, **5**%, **8.5**%, **10**%, **15**%, **20**%, **30**%, **40**%, and **50**%.

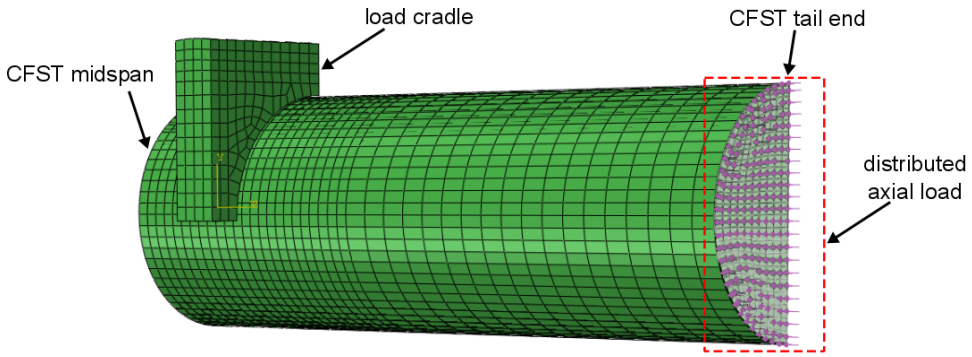



Figure 5.1: Application of Axial Load in ABAQUS Simulations

Table 5.1: Base CFST Properties in Axial Load Parameter Study

| $D$ (in.) | D/t | $F_{yt}$ (ksi) | $f'_c$ (ksi) | $L_T$ | $\rho_{int}$ |
|---|---|---|---|---|---|
| 20 | 80 | 56.8 | 8.6 | 2D | 0 % |

Moment values were taken from the ABAQUS simulations using free-body cuts along the cross-section, approximately 1 *in.* apart, so that a complete diagram could be formed, as shown in Figure 5.2. This section presents the moment in two locations, on the midspan and shear span sides of the load cradle. This is done only here to demonstrate that the moment varies through the thickness of the cradles similarly with changes in load. However, it is understood that the controlling moment was that on the midspan side and so, only this value is represented in the following studies of this chapter. The results for the axial load study are provided in the following figures.

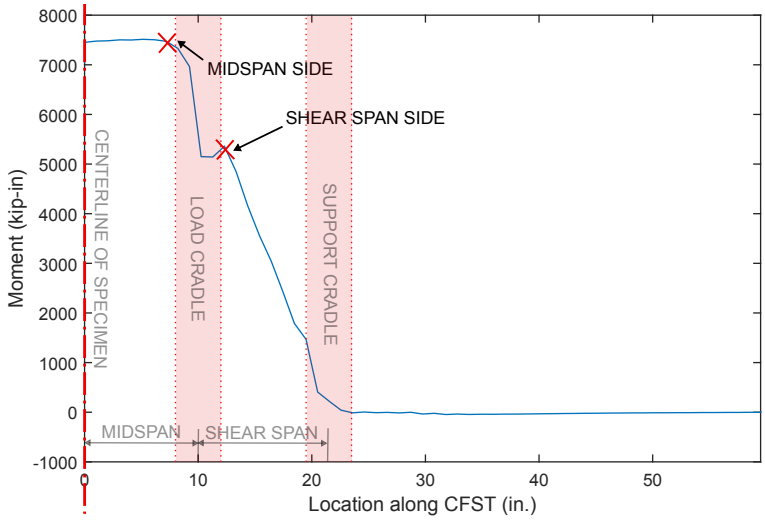



Figure 5.2: Illustration of Predicted Moment, $M_{pr}$, for Following Figures ($a/D = 0.375$)

Furthermore, all provided moment values are normalized by their respective plastic capacities, $M_{PSDM}$, although it is known that this method of calculation becomes less accurate with higher axial loads, which may explain some of the trends displayed at significant loads. Nevertheless, conclusions on general behaviors, particularly at the lower axial load ratios typically seen in practice, are accurate.

Figure 5.3 shows the variation of predicted maximum moment with axial load for models with $a/D = 0.375$ and 0.25. All moment values of this CFST design fell below $1.1M_{PSDM}$ and varied little with increasing axial load, suggesting shear-dominated behavior. Additionally, the simulations with a shear span to depth ratio of 0.25 all predict smaller moments than those with a ratio of 0.375, as the moment arm is smaller here.

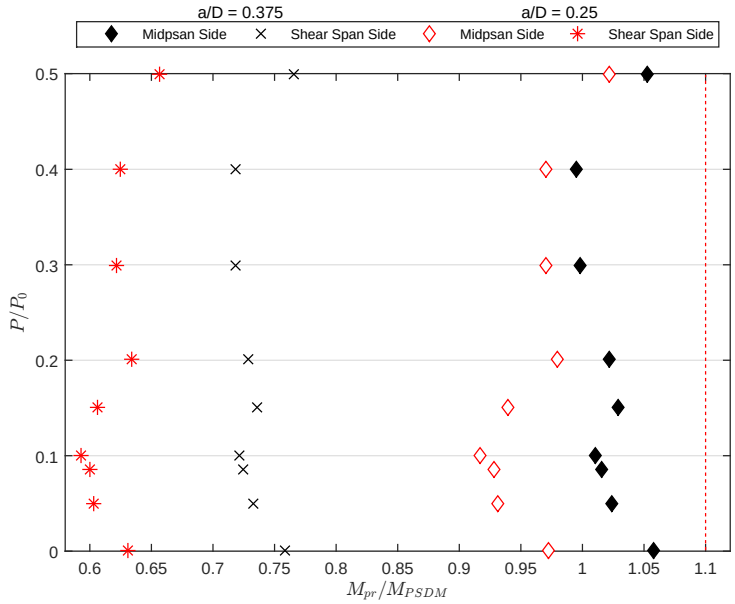



Figure 5.3: Variation of Axial Load Ratio vs. Normalized Maximum Moment

Figure 5.4 shows the shear force to increase with increasing axial load, with the rate of increase tapering off around 20% of the axial capacity. The models with $a/D$ equal to 0.25 all show a larger resistance at a given axial load ratio, suggesting a relationship exists here. However, in the experiments, models, and potential application, the shear span length cannot be practically determined and therefore, cannot be concluded on explicitly.

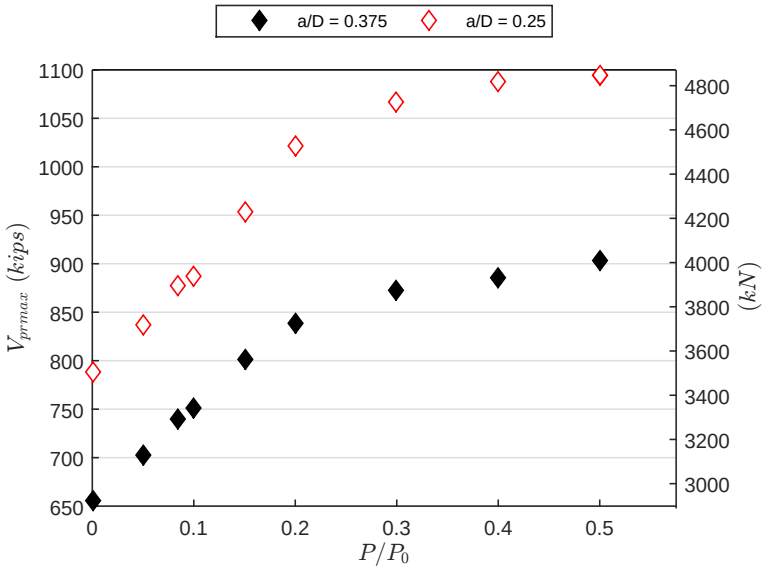



Figure 5.4: $V_{prmax}$ vs. Axial Load Ratio

Figure 5.5 shows how $\eta$ increases with axial load for this CFST. A bilinear relationship is found, with a significant decrease in slope occurring at approximately 20% axial load, like in the previous figure. For example, looking at the $a/D$ of 0.375 models, $\eta$ begins at 4.7 and increases with a slope of 33.2. Around the axial load ratio 20%, this value approaches 11 and increases with a slope now of 2.2, as shown in Figure 5.6. This bilinear trend for $\eta$ and predicted shear force is noted throughout the parameter studies.

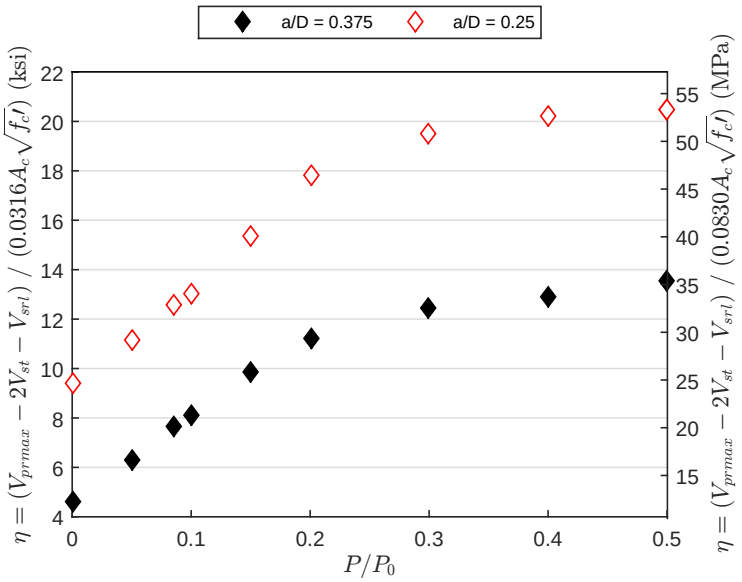



Figure 5.5: $\eta$ vs. Axial Load Ratio for Axial Load Ratio Study

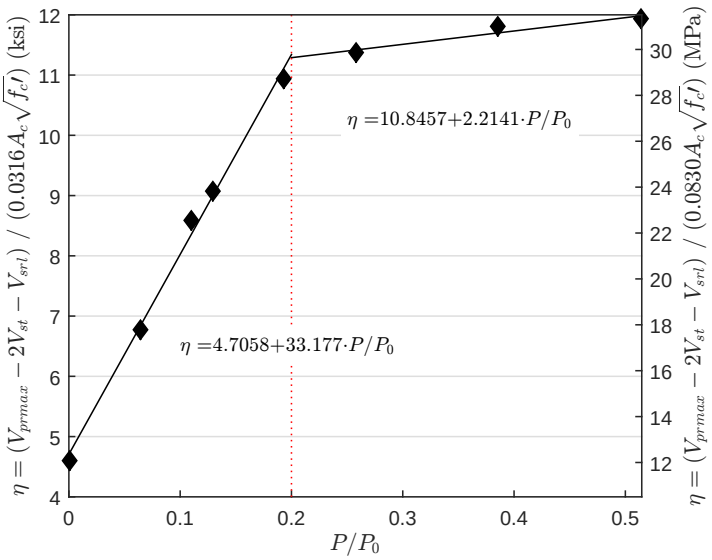



Figure 5.6: Bilinear Relationship of $\eta$ vs. Axial Load Ratio for $a/D = 0.375$ Model in Figure 5.5

### *5.3 Tube Diameter to Thickness Ratio, $D/t$*

The ratio of tube diameter to thickness, $D/t$, is used to define the slenderness of circular CFSTs. Typically, CFSTs with larger $D/t$ ratios are more susceptible to local buckling before reaching their full plastic capacity. AISC 2010 limits $D/t$ for compact sections to $0.15E_s/F_{yt}$, when primarily subjected to axial compression, and $0.09E_s/F_{yt}$ for flexure. WSDOT 2012 limits $D/t$ to $0.22E_s/F_{yt}$ for flexural loading and $0.15E_s/F_{yt}$ for axial loading. The $D/t$ ratios used in this study were:

- $D/t = 53.3 \approx 0.10E_s/F_{yt}$
- $D/t = 80 \approx 0.16E_s/F_{yt}$
- $D/t = 100 \approx 0.20E_s/F_{yt}$

Table 5.2: Base CFST Properties in D/t Parameter Study

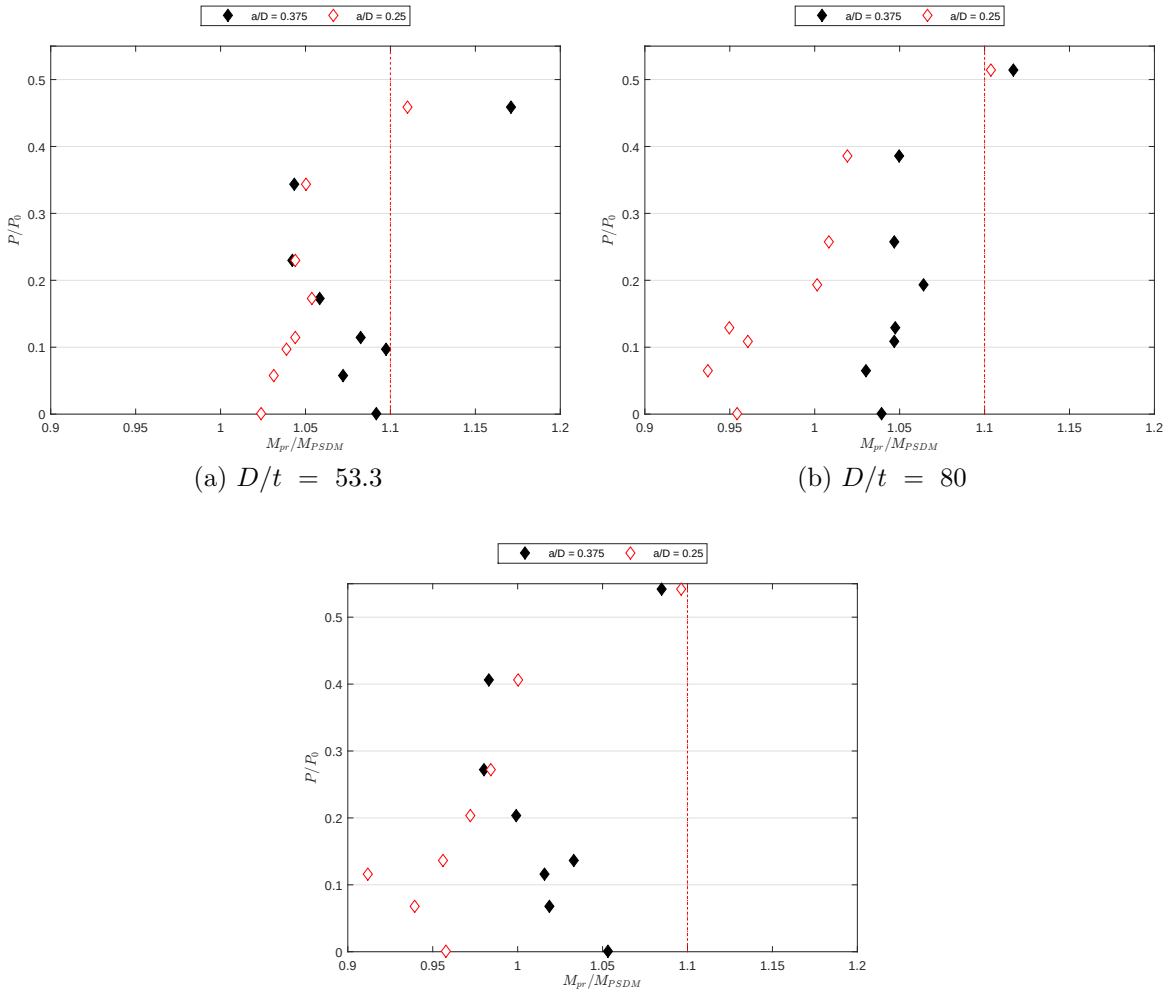
| $D$ (in.) | $F_{yt}$ (ksi) | $f'_c$ (ksi) | $L_T$ | $\rho_{int}$ |
|---|---|---|---|---|
| 20 | 56.8 | 6 | 2D | 0 % |

Figure 5.7 shows the results for moment in the models as they vary with axial load ratio for the three $D/t$ ratios. Generally, the analyses with $a/D$ of 0.375 have larger maximum moments compared to those with a ratio of 0.25, until higher axial load ratios are applied where the moments of the two models become closer in magnitude and sometimes overlap or intersect. It can also be noted at these larger axial load ratios that the relationship between moment and axial load becomes more noticeably curved, similar to a typical PM-diagram for reinforced concrete columns. These two details suggest that with increasing axial load in these models, the final behaviors are being limited by bending capacity.

Furthermore, the predicted moments show little variation with axial load. This is more reflective of the impact of $D/t$ on flexural capacity with this variation. That is, $D/t$ ratios

can restrict increases in capacity with the application of axial load because it controls the concrete area that will benefit from the axial load. With lower $D/t$ ratios, more compact sections, the amount of variation in moment capacity is more limited. Nevertheless, the models all predict moments lower than or near $1.1M_{PSDM}$ which shows some shear influence in restricting moment development, and because shear response is dependent on moment, one can conclude that the compact $D/t$ ratios limit shear development with axial load as well, which will also be seen directly in Figure 5.8.

Comparing $D/t$ ratios, there was no significant difference in maximum moment at a given axial load, 10% of $M_{PSDM}$ at the most. Moment values in the lower axial load range, about 0% to 10%, were higher for the stockier section, with $D/t$ equal to 53.3, and nearly the same for the more slender sections, with $D/t$ of 80 and 100. With the larger axial load ratios, similar trends in moment can be found among the three slenderness ratios. However, previous discussions did suggest that these models were limited by shear and did not see full capacity in bending so conclusions on observed maximum moments are not definitive. Additionally, there is no evidence in this study that local stability has reduced moment development.

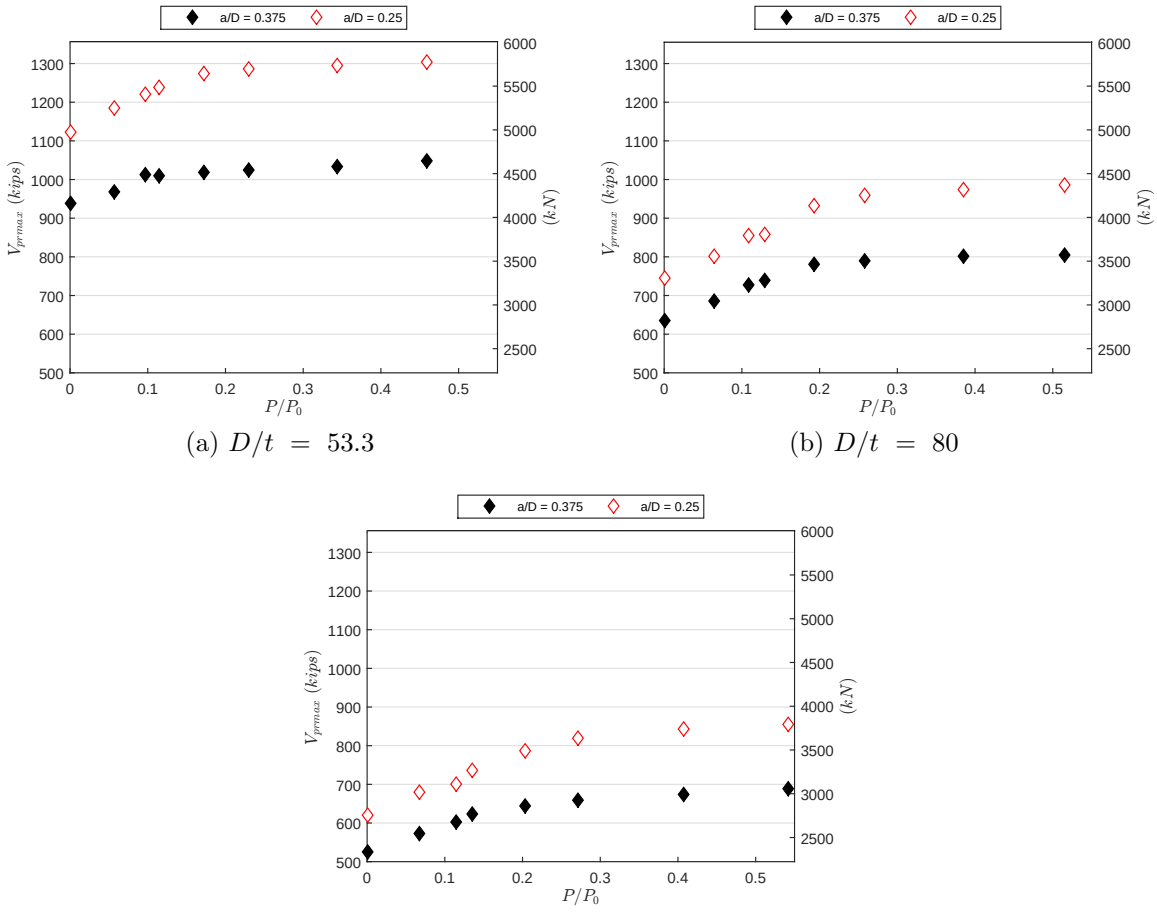



(a) $D/t = 53.3$ (b) $D/t = 80$

(c) $D/t = 100$

Figure 5.7: Variation of Axial Load Ratio vs. Normalized Maximum Moment with Different $D/t$ Ratios

The predicted maximum shear values in Figure 5.8 increase with axial load in the bilinear relationship already noted, but less significantly with the stockier section, $D/t$ of 53.3. It is also evident from the figures that the stockier the section, the greater the shear resistance. In other terms, as the ratio of steel tube to concrete cross-sectional area, $A_{st}/A_c$, increased, so did the shear resistance.




(a) $D/t$ = 53.3

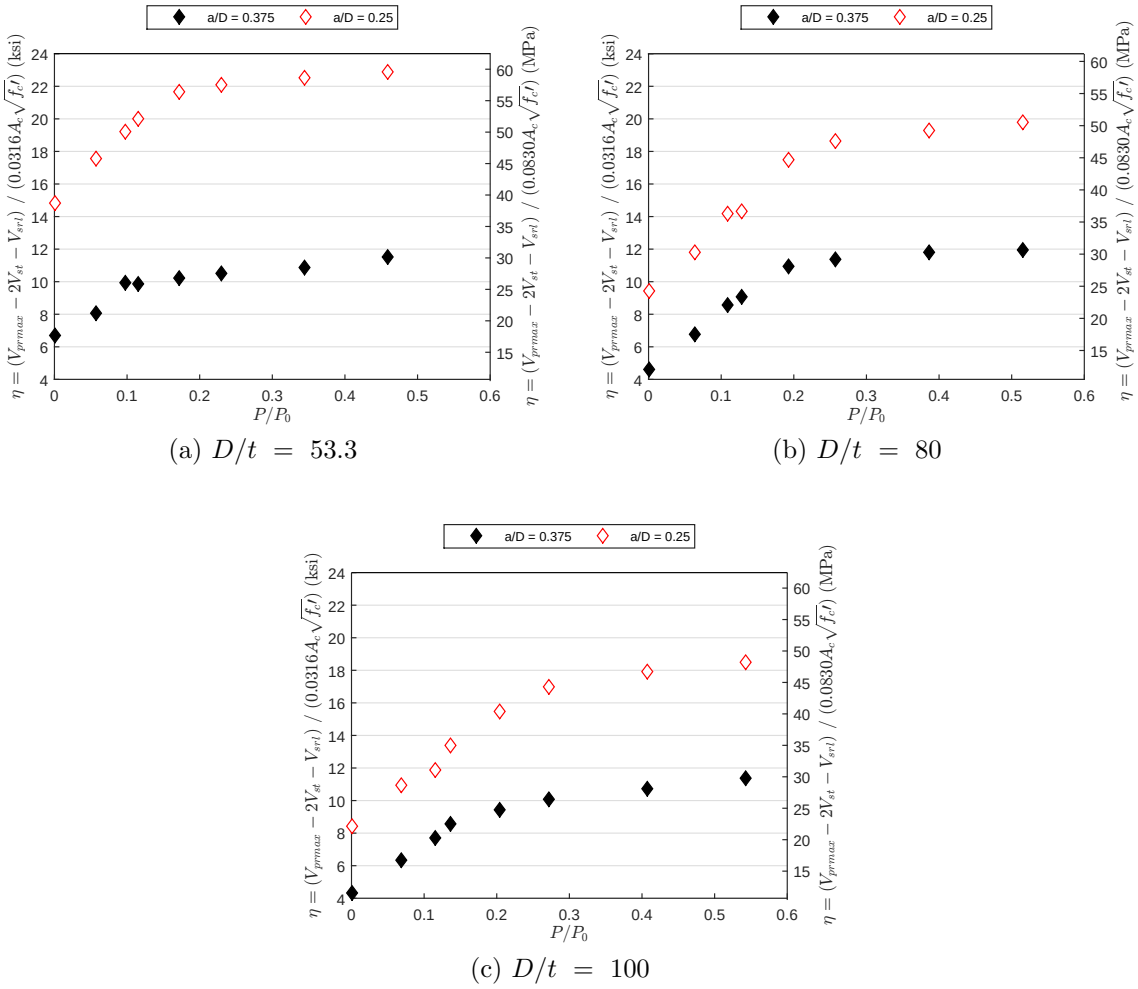
(b) $D/t$ = 80

(c) $D/t$ = 100

Figure 5.8: $V_{prmax}$ vs. Axial Load with Different $D/t$ Ratios

Figure 5.9 shows the change in concrete contribution, estimated by $\eta$, with these simulations. The contribution of the concrete is shown to be highest in the stockiest section ($D/t$ of 53.3) when the shear span to depth ratio is 0.25, and generally decreased with increasing $D/t$

in this series. While this is to be reflective of concrete presence, this difference among the varying $D/t$ models actually suggests that the steel contribution is being underestimated, making it appear that the concrete contributes more. Furthermore, the $\eta$ term remained similar at given axial load ratios across the different slenderness ratios with the larger $a/D$ ratio, where shear yielding in the tube is less prominent and the underestimation of the tube shear would not be as clear.




(a) $D/t = 53.3$ (b) $D/t = 80$

(c) $D/t = 100$

Figure 5.9: $\eta$ vs. Axial Load Ratio with Different $D/t$ Ratios

## *5.4 CFST Materials*

The cross-sectional area and strength of steel and concrete are used quantify their individual contributions to CFST resistance. The experimental results in this program have already demonstrated that the steel tube provides the majority of the shear strength of CFSTs, and the changes in material areas with the $D/t$ study have supported this. Now, looking at the material strength contributions, this distinction is made more clear.

### *5.4.1 Concrete Strength, $f'_c$*

The influence of concrete strength on the total shear resistance was studied by varying $f'_c$, while maintaining the general stress-strain relationship of the confined concrete model. Strengths of **3.0**, **6.0**, **8.6**, and **12 ksi** were analyzed. The remaining properties of the base CFST in this series are shown in Table 5.3.

Table 5.3: Base CFST Properties in $f'_c$ Parameter Study

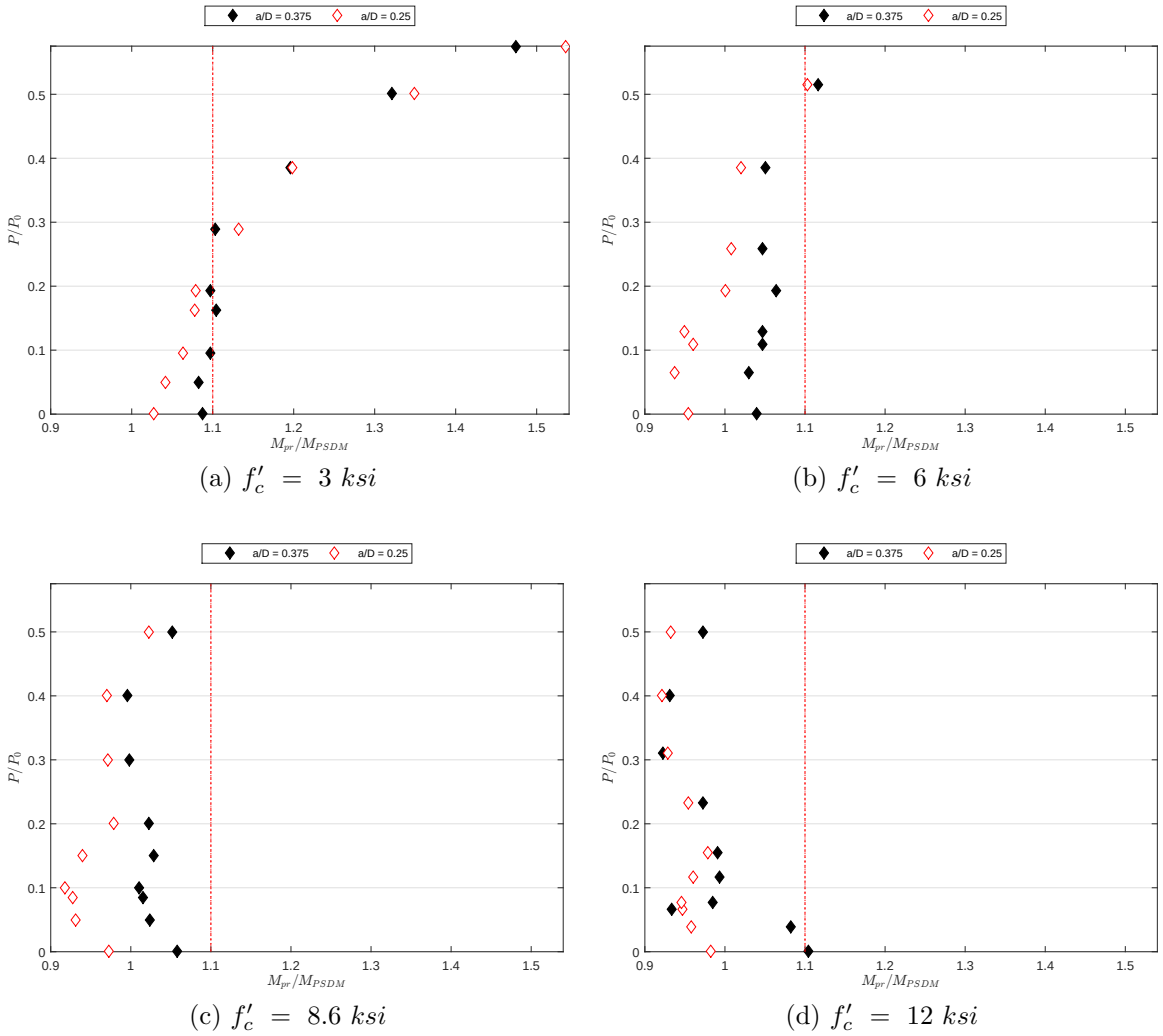
| $D$ (in.) | D/t | $F_{yt}$ (ksi) | $L_T$ | $\rho_{int}$ |
|---|---|---|---|---|
| 20 | 80 | 56.8 | 2D | 0 % |

The predicted axial-moment responses in this study are shown in Figure 5.10. A trend in the general behaviors with increasing concrete strength can be observed among these relationships. With the smallest concrete strength, 3 $ksi$, it is apparent that the CFST undergoes flexurally dominated response at larger compressive loads, with the smallest predicted midspan moment valued at, or just below, $1.1M_{PSDM}$ and an apparent increase in moment with increasing axial load. Additionally, the moment values for each $a/D$ ratio quickly converged with increasing axial load. On the other hand, there was a general decrease in strength with increasing axial load at the largest concrete strength, 12 $ksi$, after the short period of increase between 10 and 20% axial load. To explain this, one has to recall that with the plastic stress distribution method, full plasticity of the section is assumed, and

with higher concrete strengths and larger axial loads, this assumption may become less appropriate. So, part of what is being seen here is the inaccuracy with the $M_{PSDM}$ value used for normalization. Another part of this explanation would be the typical decrease in moment with large axial loads often noted in reinforced concrete column design. The combination of these results in the slightly unusual variation with the high strength concrete models. On the other hand, these models use CFSTs with a $D/t$ equal to 80, which is a bit large compared to common practice, and with large, more common tube geometry, this variation would be increasingly less significant.

Furthermore, most moment values in this series, excluding the 3 $ksi$ models, fell below $1.1M_{PSDM}$, suggesting shear-dominant action in these CFSTs. However, caution is taken with this conclusion having noted the PSDM assumptions. Nevertheless, assuming shear-controlled behaviors only makes conclusions more conservative.

Finally, if one were to fit a line to the data in a given axial load series among the concrete strengths, an increasingly vertical slope, eventually moving in the negative direction, with increasing $f'_c$ would be observed. The two middle concrete strengths show this gradual transition of slopes between the low and high $f'_c$ values, noting the shift in behavior from flexural control to shear dominance with increasingly large concrete strength.

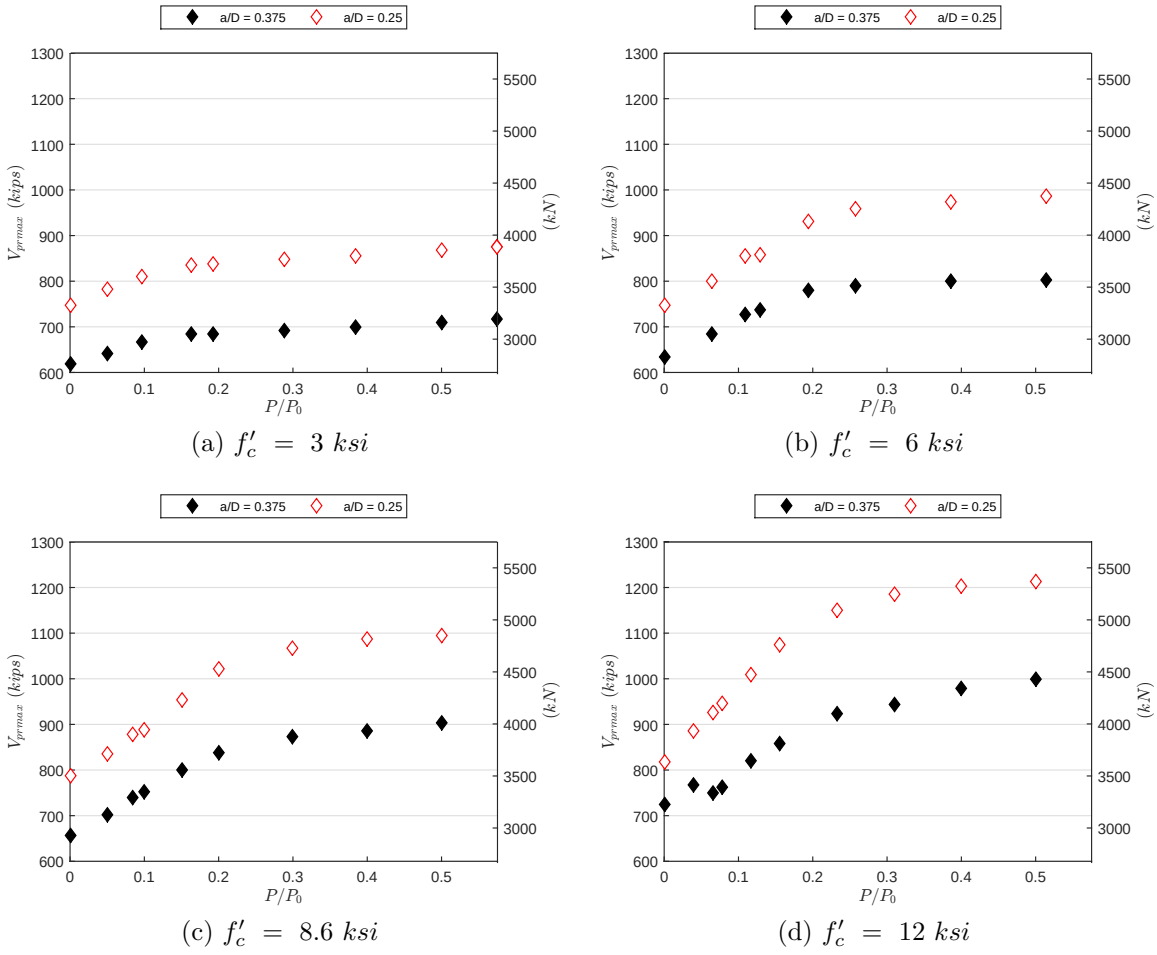



(a) $f'_c = 3\ ksi$ (b) $f'_c = 6\ ksi$

(c) $f'_c = 8.6\ ksi$ (d) $f'_c = 12\ ksi$

Figure 5.10: Variation of Axial Load Ratio vs. Normalized Maximum Moment with Different Concrete Strengths, $f'_c$

Figure 5.11 shows that maximum predicted shear did not increase significantly with each gain in concrete strength. Within a given $f'_c$ series though, it did increase with axial load as typical, but less notably at lower concrete strengths.



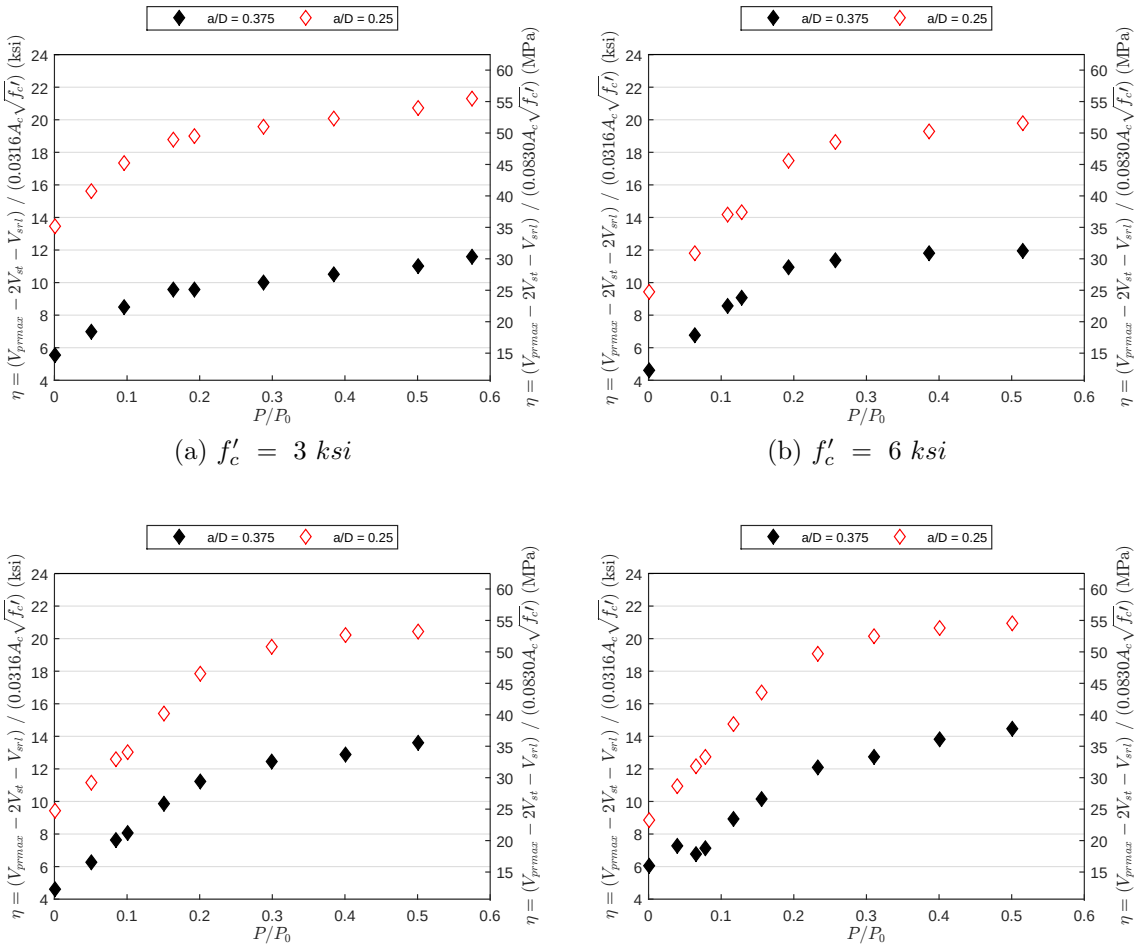

(a) $f'_c = 3\ ksi$ (b) $f'_c = 6\ ksi$

(c) $f'_c = 8.6\ ksi$ (d) $f'_c = 12\ ksi$

Figure 5.11: $V_{prmax}$ vs. Axial Load Ratio with Different Concrete Strengths, $f'_c$

As shown in Figure 5.12, the $\eta$ values in this parameter study all fell within relatively the same total range. With the mid-range concrete strengths, $\eta$ values start lower than the high strength series, 12 $ksi$, for no axial load, but do not differ much with the 12 $ksi$ models as axial load was applied, hence the drop noted in Figure 5.12d around 5% axial load. Both of these facts support the notion that the concrete fill has little influence on composite behavior

when compared to the steel tube. And although slightly higher $\eta$ values were seen in the low concrete strength series, 3 $ksi$, with $a/D$ of 0.25, this group also showed presumably flexure-controlled behavior, and conclusions on shear strength cannot be made in this case. It has also been noted that the tube influence is potentially underestimated in the calculation of $\eta$, which can give the impression of larger concrete influence.




(a) $f_c' = 3\ ksi$ (b) $f_c' = 6\ ksi$

(c) $f_c' = 8.6\ ksi$ (d) $f_c' = 12\ ksi$

Figure 5.12: $\eta$ vs. Axial Load Ratio with Different Concrete Strengths, $f_c'$

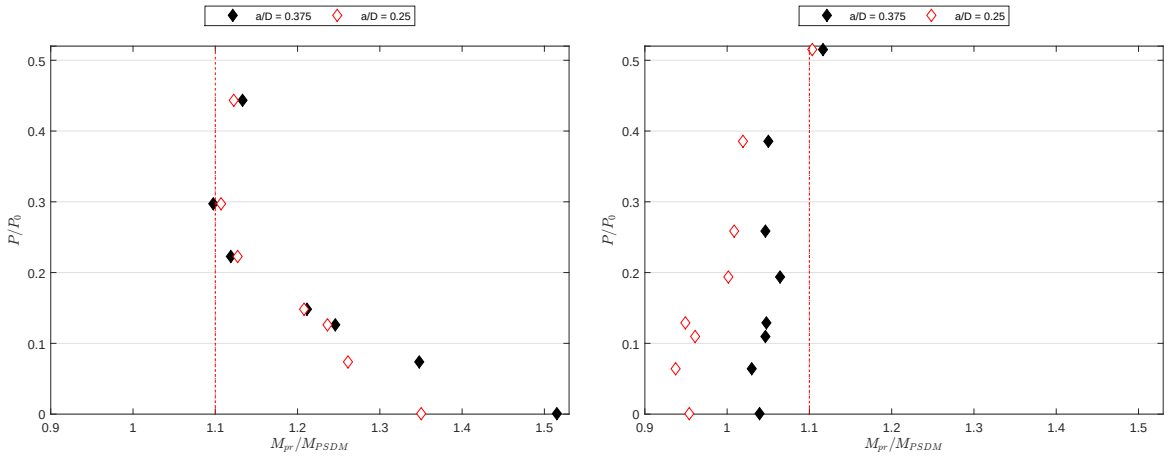
### *5.4.2 Tube Steel Yield Strength, $F_{yt}$*

The influence of the steel tube's yield strength on the CFST behaviors in these models was assessed with $F_{yt}$ values of **35**, **56.8**, and **70 ksi**, and the same trilinear stress-strain relationship in the validated models. The ultimate strength values, $F_{ut}$, for the lowest and highest designated yields were 60 and 82 $ksi$, as specified for API 5L, Gr. B and API 5L X70 tubes, respectively. The middle range strength tube used the measured yield and ultimate strengths for the API 5L X42 tubes from the experimental program, as seen in Chapter 4. The base CFST was otherwise modeled with the properties shown in Table 5.4.

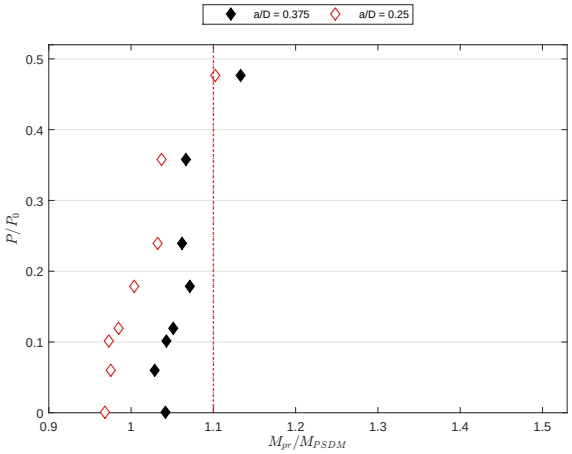
Table 5.4: Base CFST Properties in $F_{yt}$ Parameter Study

| $D$ (in.) | D/t | $f'_c$ (ksi) | $L_T$ | $\rho_{int}$ |
|---|---|---|---|---|
| 20 | 80 | 6 | 2D | 0 % |

The resulting axial-moment behaviors in these models are shown in Figure 5.13. Two distinct behaviors were noted in this data. First, the low strength tube, 35 $ksi$, shows a general decrease in moment and notably curved relationship with increasing axial load, like seen with the high strength concrete, which can also be attributed to the PSDM assumptions and typical axial-moment effects seen with reinforced concrete PM diagrams. Unlike the high strength concrete models though, all maximum moments were greater than $1.1M_{PSDM}$. This combined with the notable variation with axial load, in a distinctly curved trend, and eventual overlap in moment values between different $a/D$ ratios, conclude that this tube largely acted in flexure. However, the higher axial loads may have been increasing the CFSTs shear strength more significantly than flexure, causing the decrease in observed moment. Second, the two higher strength tubes predicted moment values less than $1.1M_{PSDM}$ and varied little with increasing axial load, suggesting their behaviors are largely controlled by shear.



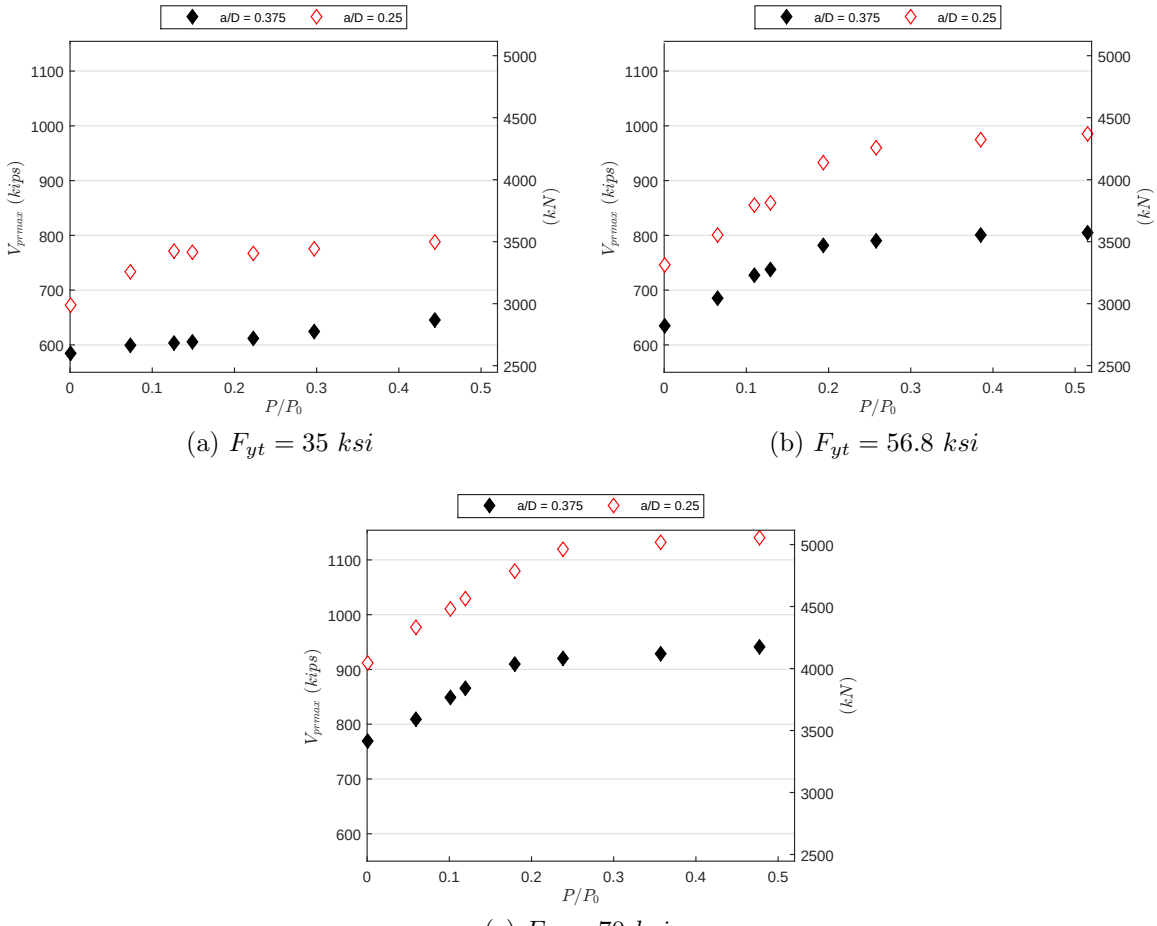

(a) $F_{yt} = 35\ ksi$ (b) $F_{yt} = 56.8\ ksi$




(c) $F_{yt} = 70\ ksi$

Figure 5.13: Variation of Axial Load Ratio vs. Normalized Maximum Moment with Different Tube Steel Strengths, $F_{yt}$

Figure 5.14 shows the increase in maximum predicted shear magnitude with increasing axial load. This gain in shear force is not as significant with the low strength steel model because the CFSTs in this series showed to be more flexural in response. Also for this reason, the 35 $ksi$ models exhibited the lowest predicted shears. The shear controlled CFSTs, $F_{yt}$ of 56.8 and 70 $ksi$, show that with greater tube strength, greater shear resistance results. Between the two tube strengths, approximately 20% more shear strength results from a 23% increase in material strength, at a given axial load. This is a more significant difference than shown with the increase in concrete strength, where doubling the strength provided just under 20% more shear resistance.



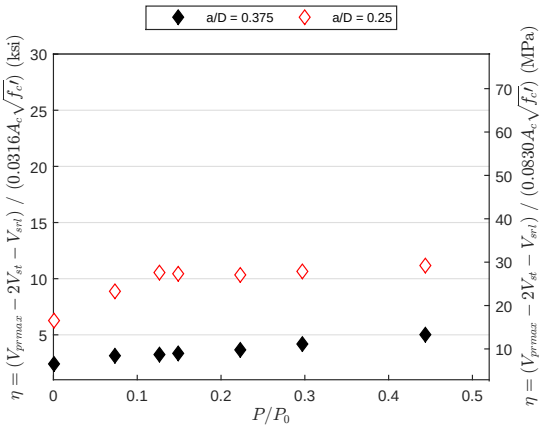

(a) $F_{yt} = 35$ $ksi$

(b) $F_{yt} = 56.8$ $ksi$

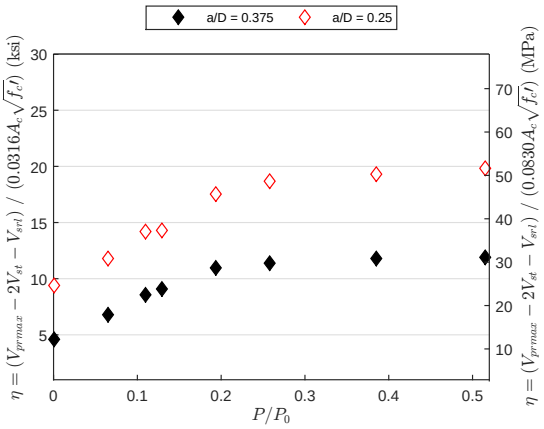
(c) $F_{yt} = 70$ $ksi$

Figure 5.14: $V_{prmax}$ vs. Axial Load Ratio with Different Tube Steel Strengths, $F_{yt}$

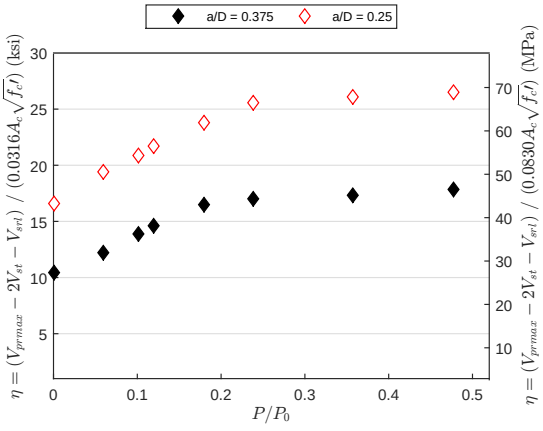
Figure 5.15 presents the trends seen for the concrete contribution factor, $\eta$. The lowest steel tube strength models, 35 $ksi$, showed an increase in $\eta$ over a smaller range than the other two models' groups, and were generally more horizontal, consistent with the higher axial load ratios where it is suspect that flexural behaviors have a larger presence. Among the two tube steel strengths where shear was observed, $\eta$ varied significantly relative to previous models. The concrete factor was greatest with the largest steel tube strength, 70 $ksi$, and decreased with tube strength. Because $\eta$ was derived to estimate the concrete contribution, these large factors would appear to contradict the notion that the concrete fill does not provide as much strength to the CFST section as the steel tube. However, because the concrete strength parameter study showed the term $\eta$ to vary little between $f'_c$ values of 3 and 12 $ksi$, again, what this may actually suggest is that the factor of 2 being used on the $V_{st}$ term is still an underestimate of the contribution of the steel tube being reinforced by the concrete fill. This has been alluded to previously, but is more easily recognized when taking in to account all previous studies.




(a) $F_{yt} = 35\ ksi$




(b) $F_{yt} = 56.8\ ksi$




(c) $F_{yt} = 70\ ksi$

Figure 5.15: $\eta$ vs. Axial Load Ratio with Different Tube Steel Strengths, $F_{yt}$

### *5.5 Internal Reinforcement Ratio,* $\rho_{int}$

Internal reinforcement is often found in CFST applications (noted as RCFSTs). However, no available prior experimental research or finite element modeling has studied this effect on CFST behavior, and only four RCFST specimens were tested in the UW program. These specimens exhibited increased shear and moment capacities, along with increased shear yielding. Further study of the effect of internal reinforcement was required, so that a larger data set could be used to quantify its effects.

In the simulation, the internal reinforcement was added as individual bars composed of truss elements (T3D2), and arranged in the concrete fill uniformly in the circumferential direction with a bar located at the top and bottom of the cross-section centerline and a clear edge space of $1\frac{3}{4}$ $in.$ The rebar material was modeled with the same trilinear elastic-plastic relationship as the tube steel, but with a designated 60 $ksi$ yield strength and 90 $ksi$ ultimate strength, as typical with Grade 60 reinforcing bar conforming to ASTM A-615 specifications. The bars were then restrained to the surrounding concrete fill's movement with the ABAQUS "EMBEDDED REGION" constraint, using default properties.

The internal reinforcement ratio, $\rho_{int}$, was varied from **1**% to **2**%. The 1% design used 10-standard No. 5 rebars, each with a cross-sectional area of 0.31 $in.^2$, and the 2% design used 10-standard No. 7 rebars, each with a cross-sectional area of 0.6 $in.^2$ Because the simulation only models half of the RCFST cross-section, only 6 bars were actually put in the model, with the top and bottom bars each given half of the designated bar area, while the others were given the full cross-sectional bar area, in order to simulate half of the total reinforcement area without losing the uniform distribution. Figure 5.16 illustrates the bar layout in the models. The remaining RCFST properties used in this study are given in Table 5.5.

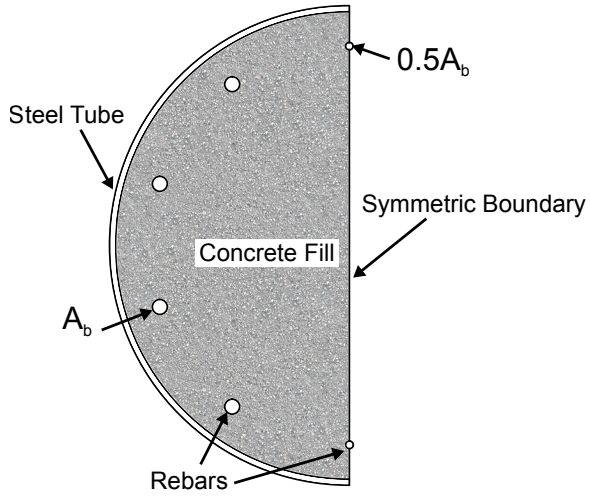


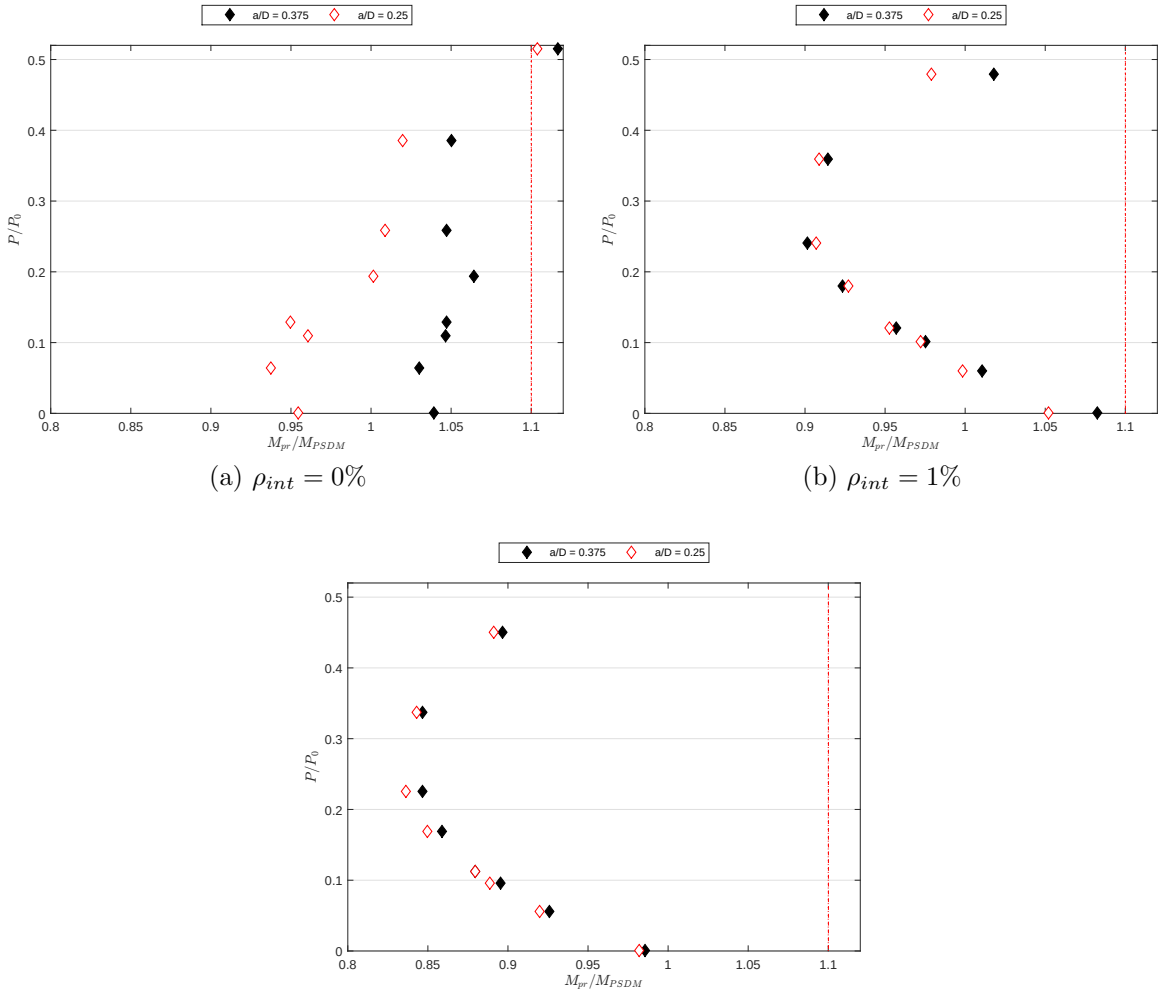

Figure 5.16: Illustration of Rebar Layout in ABAQUS Simulation

Table 5.5: Base CFST Properties in $\rho_{int}$ Parameter Study

| $D$ (in.) | D/t | $F_{yt}$ (ksi) | $f'_c$ (ksi) | $L_T$ |
|---|---|---|---|---|
| 20 | 80 | 56.8 | 6 | 2D |

Looking at the predicted normalized axial-moment relationships in Figure 5.17, there was an obvious change in overall behavior with the addition of internal reinforcement that can possibly be attributed to the catenary response of the rebars discussed with the experimental results (Section 3.5.2). The largely curved relationship shown with these two models has been noted to potentially signify the presence of more significant bending behaviors. Also noted with this trend was the converging of predicted midspan moment values for the $a/D$ of 0.375 and 0.25 models, as shown with this study. However, all of the models with reinforcement had predicted moments below $1.1M_{PSDM}$. These behaviors are consistent with the theory that the reinforcement strengthens the section in moment more efficiently than in shear, meaning shear yielding is more prevalent. Considering the flexural behaviors present though, it would appear that the response is more reflective of the flexure-shear zone where one behavior is not substantially more dominant than the other.

On the other hand, the models without internal reinforcement show a relatively small variation in moment, only reaching $1.1M_{PSDM}$ with the maximum axial load ratio of 40%. Compared to the RCFSTs though, the predicted moments are larger with the majority of axial load ratios. If not, they are smaller in the lower axial load ratios, 10% and less, where a consistent pattern is not easily observed. The CFST models appear to be largely controlled by shear behaviors.



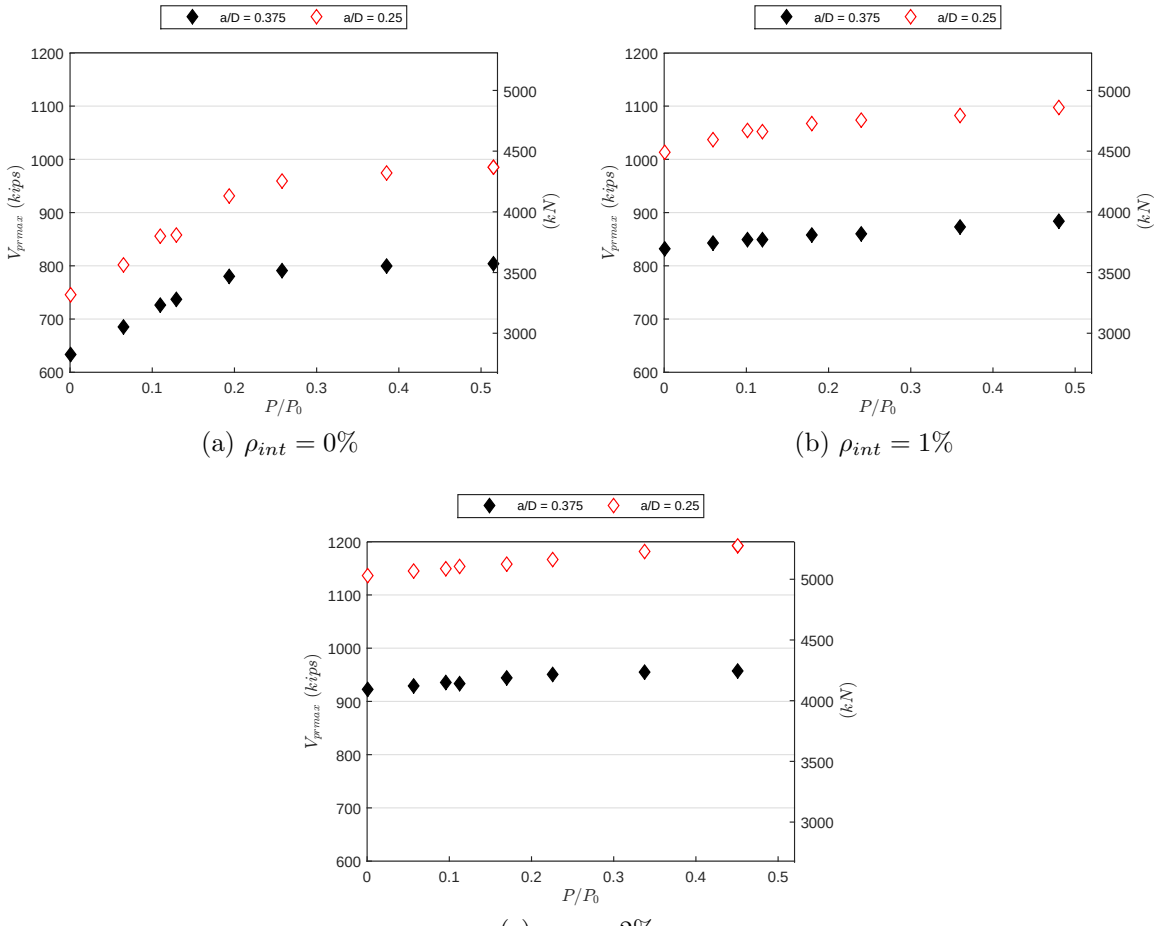

(a) $\rho_{int} = 0\%$

(b) $\rho_{int} = 1\%$

(c) $\rho_{int} = 2\%$

Figure 5.17: Variation of Axial Load Ratio vs. Normalized Maximum Moment with Different Internal Reinforcement Ratios, $\rho_{int}$

Based on the predicted maximum shear force vs. axial load relationships in Figure 6.2, the RCFSTs gain shear capacity with increasing internal reinforcement. Figure 6.2a and b show that the magnitude of shear force in the non-reinforced CFST with over 50% axial load was less than that with no axial load and 1% internal reinforcement. This would suggest that internal reinforcement could be more efficient at strengthening the concrete fill than axial load. Furthermore, the RCFSTs did not show to increase in shear resistance with axial load ratio. In general, the RCFSTs varied little in total resistance and therefore did not benefit significantly with practical axial load ratios.



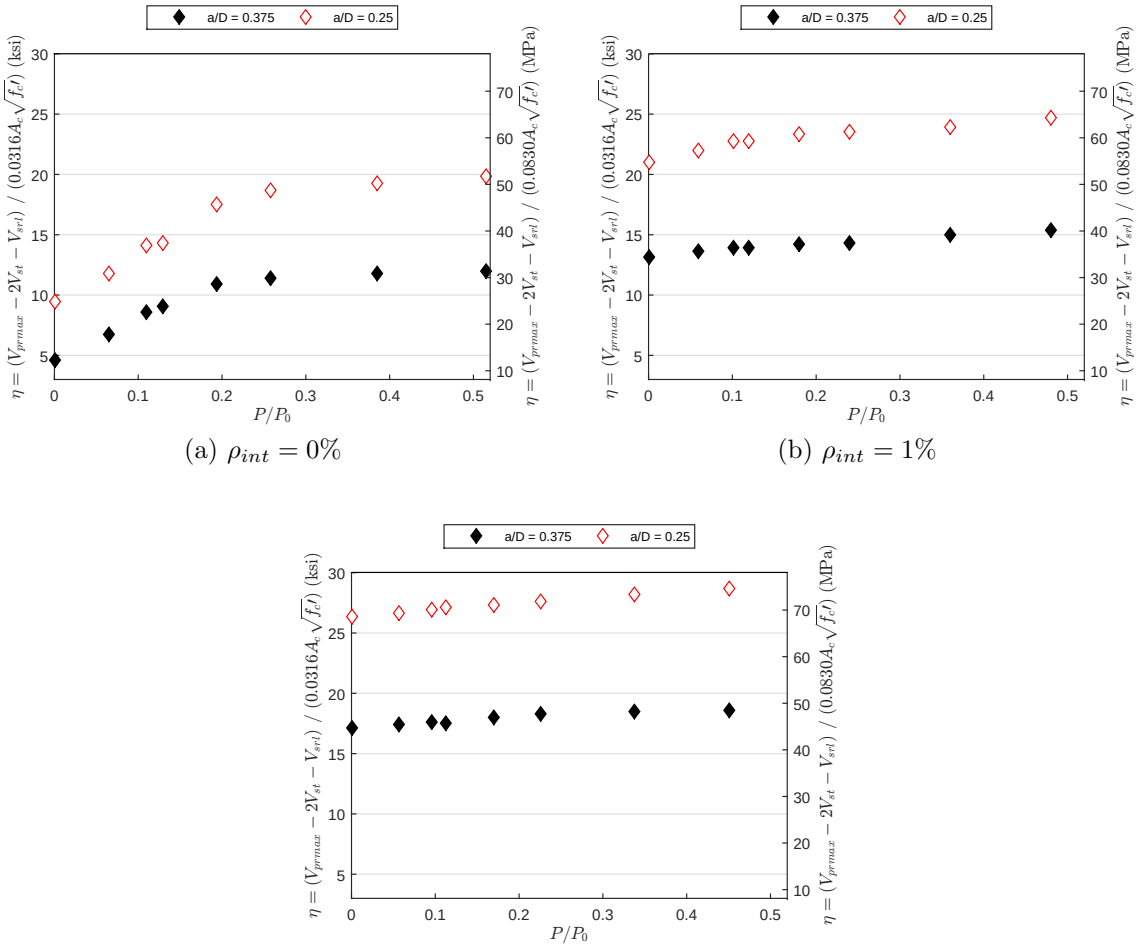

(a) $\rho_{int} = 0\%$

(b) $\rho_{int} = 1\%$

(c) $\rho_{int} = 2\%$

Figure 5.18: $V_{prmax}$ vs. Axial Load Ratio with Different Internal Reinforcement Ratios, $\rho_{int}$

Similar trends in variation of axial load are noted in Figure 5.19: little change of $\eta$ in RCFSTs with increasing axial load, large $\eta$ values with more reinforcement, and larger $\eta$ values for the 1% RCFST and no axial load than the CFST with over 50% load. Figures 6.2 and 5.19 are heavily related with this parameter study because the introduction of reinforcement allows the concrete to contribute to the resistance of the member longer by restricting large cracks from developing in the concrete as quickly. So, as $\rho_{int}$ increases, not only does that RCFST benefit in terms of moment and shear capacity from the added steel bar area, but also from the concrete crack arresting behaviors. However, that is not to overshadow the fact that the reinforcement was still not significantly influential at strengthening shear, more so in flexure, resulting in increasing shear deformations.




(a) $\rho_{int} = 0\%$

(b) $\rho_{int} = 1\%$

(c) $\rho_{int} = 2\%$

Figure 5.19: $\eta$ vs. Axial Load Ratio for CFST with Different Internal Reinforcement Ratios, $\rho_{int}$

# Chapter 6

# PROPOSED DESIGN EXPRESSION

## *6.1 Introduction*

Chapter 2 presented provisions by various design agencies for the calculation of shear capacity of CFSTs and RCFSTs. Experiments show though that these design provisions significantly underestimate this capacity, and result in unnecessary design limitations when CFSTs wrongly appear to be shear critical. Tables 6.1 through 6.3 compare prior experimental research and experiments completed in this research to various design provisions. Based on this evaluation, these provisions, again, clearly underestimate shear capacity. As a solution, this chapter provides a new expression that better represents the shear resistance of CFSTs.

Table 6.1: Results using AISC Method 1 for Reported Shear Failures, without Axial Load or Expansive Concrete, by UW and Others

| Research Program | $V_{ed}/V_{n(AISC1)}$ | | | | | | |
|---|---|---|---|---|---|---|---|
| | No. Tests | Mean | Median | Max | Min | Std. Dev. | COV |
| Xiao | 18 | 3.56 | 3.51 | 4.34 | 2.73 | 0.54 | 0.15 |
| Xu | 3 | 2.20 | 2.15 | 2.40 | 2.06 | 0.18 | 0.08 |
| Qian | 13 | 3.35 | 3.16 | 3.99 | 2.31 | 0.56 | 0.17 |
| Nakahara | 1 | 1.73 | 1.73 | 1.73 | 1.73 | 0 | 0 |
| Ye | 2 | 3.20 | 3.20 | 3.22 | 3.19 | 0.02 | 0.01 |
| UW | 5 | 2.73 | 3.06 | 3.10 | 1.70 | 0.60 | 0.22 |
| All Specimens | 42 | 3.30 | 3.22 | 4.34 | 1.70 | 0.68 | 0.21 |

Table 6.2: Results using AISC Method 2 for Reported Shear Failures, without Axial Load or Expansive Concrete, by UW and Others

| Research Program | $V_{ed}/V_{n(AISC2)}$ | | | | | | |
|---|---|---|---|---|---|---|---|
| | No. Tests | Mean | Median | Max | Min | Std. Dev. | COV |
| Xiao | 18 | 48.1 | 44.2 | 81.7 | 29.2 | 14.0 | 0.29 |
| Xu | 3 | 28.5 | 27.8 | 31.1 | 26.7 | 2.29 | 0.08 |
| Qian | 13 | 46.7 | 45.3 | 66.1 | 34.3 | 10.2 | 0.22 |
| Nakahara | 1 | 26.8 | 26.8 | 26.8 | 26.8 | 0 | 0 |
| Ye | 2 | 27.2 | 27.2 | 27.3 | 27.1 | 0.16 | 0.01 |
| UW | 4 * | 16.8 | 15.2 | 22.6 | 14.2 | 3.95 | 0.24 |
| All Specimens | 41 | 41.7 | 41.2 | 81.7 | 14.2 | 15.3 | 0.37 |

* Specimen 21 was excluded from this evaluation as the shear span is filled with gravel, instead of concrete, and this particular provision solely accounts for the concrete contribution to resistance.

Table 6.3: Results using WSDOT Method (prior to 2016 BDM) for Reported Shear Failures, without Axial Load or Expansive Concrete, by UW and Others

| Research Program | $V_{ed}/V_{n(Method\ 4)}$ | | | | | | |
|---|---|---|---|---|---|---|---|
| | No. Tests | Mean | Median | Max | Min | Std. Dev. | COV |
| Xiao | 18 | 3.42 | 3.37 | 4.18 | 2.61 | 0.52 | 0.15 |
| Xu | 3 | 2.12 | 2.07 | 2.31 | 1.99 | 0.17 | 0.08 |
| Qian | 13 | 3.22 | 3.09 | 3.80 | 2.24 | 0.51 | 0.16 |
| Nakahara | 1 | 1.67 | 1.67 | 1.67 | 1.67 | 0 | 0 |
| Ye | 2 | 3.02 | 3.02 | 3.04 | 3.01 | 0.02 | 0.01 |
| UW | 5 | 2.52 | 2.76 | 2.83 | 1.70 | 0.47 | 0.19 |
| All Specimens | 42 | 3.10 | 3.03 | 4.18 | 1.67 | 0.65 | 0.21 |

Even with the combined steel and concrete contributions in the WSDOT expression for resistance, $V_{n(Method\ 4)}$, estimation comes short of the experimental results by a large margin. The experimental and parameter study results show that the tube steel provides the majority of the shear resistance of the CFST, compared to the concrete fill. Furthermore, composite behavior has a significant impact on the shear behavior. Contributing to this behavior, the surface condition at the steel-concrete interface affects the bond stress transfer between the steel tube and concrete fill and, therefore, development of composite action. However, aside from the extreme case with the greased tube surface and very short tail length, this effect was not dramatic. Clearly, the more powerful composite benefits of the CFST are the confinement of the concrete fill provided by the tube, and the restraint of tube local buckling provided by the concrete fill. The experiments and simulations also show that internal reinforcement increases the overall shear strength of RCFSTs compared to a CFST of the same geometry, but is less efficient than the tube steel in providing shear resistance.

Considering these observations, a proposed shear expression was developed to better represent the contribution of the tube steel reinforced from local buckling, the improved behaviors of the concrete fill attributed to confinement, and the presence of longitudinal internal reinforcement. First, a limit state criterion is proposed for use in defining models and experimental specimens where shear dominates response. Then, an expression is developed using experimental results for the tube steel, and parametric study for the contribution of internal reinforcement and concrete, as it relates to axial load.

## *6.2 Equation Development Utilizing Experimental Results*

### *6.2.1 Proposed Limit State Criterion*

For the appropriate use of experimental results, only specimens that fail in shear must be used to determine shear resistance. It is evident from the experimental results that changes in loading geometry greatly affect resulting failure mode of the specimen. That is, shear force and bending moment are related through shear span, and so shear is often limited by

the flexural capacity. Therefore, experimental data from tests controlled by flexure would underestimate the shear resistance of the CFST section. Only specimens with relatively small shear span to depth ratios, 0.5, 0.375, and 0.25, were affected by shear yielding, and only specimens with the smallest ratios, 0.375 and 0.25, definitively failed in shear. Therefore, only these results should be considered in quantifying shear capacity.

Furthermore, the experimental results show no evidence that large bending moments reduce shear resistance or that large shear forces reduce flexural resistance, and since bending behaviors are more easily predicted, a bound of shear behavior related to flexural capacity is of use. Previous experimental programs concluded that, on average, measured flexural capacity is 125% of the plastic moment capacity, $M_{PSDM}$ (Bishop, 2009). Consequently, flexurally controlled failure is expected of CFSTs with measured moment greater than or equal to $1.25M_{PSDM}$, and specimens with significantly lower moments are controlled by shear. For this shear limit, a maximum moment less than $1.1M_{PSDM}$ was observed with the UW experimental data. There then exists a zone of behavior between these bounds where evidence of both flexural and shear actions are present. Specimens in this intermediate range do not clearly reflect shear of flexural resistance appropriately. Additionally, bond slip limits moment and shear responses, because composite action cannot be developed, and so specimens exhibiting large relative displacements between the steel tube and concrete fill also do not represent either flexural or shear capacities.

Considering these experimental observations, it is concluded that specimens, and analytical models, that meet the following criterion, without showing significant slipping behaviors, fail in shear, and are therefore used for the evaluation of shear capacity:

$$M_{ed/pr}/M_{PSDM} < 1.1 \tag{6.1}$$

As presented, this criterion is based on the experimentally determined $M_{ed}$ values because these are conservative estimates based on a clearly defined moment arm, the center-to-center

distances between load and reaction points (clear distance for Nakahara, 2012). However, the parameter studies show that the spans in the UW tests are actually larger than these idealized dimensions (see Figure 5.2). Prior research studies also have similar setups and so $M_{ed}$ is invariably underestimated a bit with this evaluation. Hence, the evaluation may include a few specimens influenced by flexure. Again, this circumstance simply results in a conservative shear capacity expression.

### *6.2.2 Tube Steel Contribution*

As reported by Maki (2015), Specimen 21 of the UW experimental program showed that the the steel tube with gravel fill developed a nominal shear resistance of:

$$V_n = 1.7 \cdot 0.6F_{yt}(0.5A_{st}) = 1.7V_{st} \tag{6.2}$$

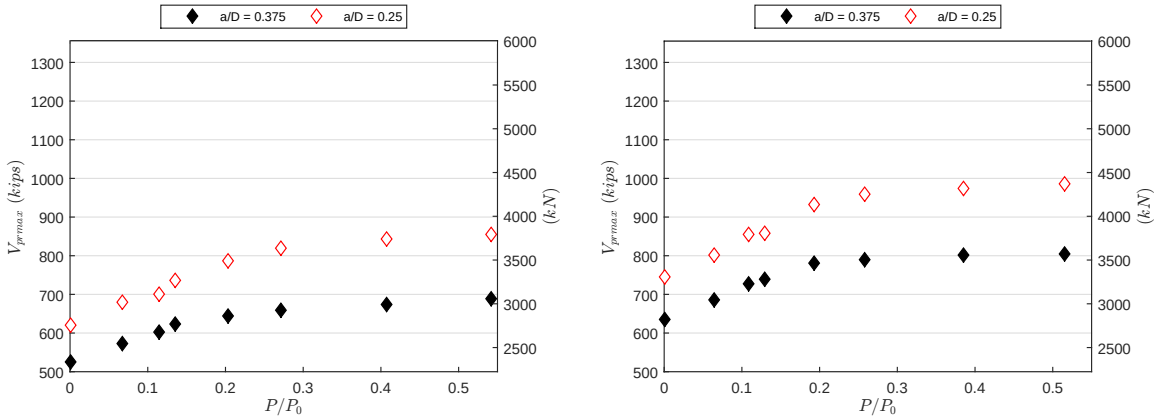
The gravel did not directly provide shear resistance in this experiment. Instead, it approximately retained the circular shape of the tube so that it developed shear buckling and diagonal tension field action. That is, this shear resistance can be considered a minimum contribution provided by the steel tube. But since the gravel was less efficient in retaining the circular shape than typical concrete fill, a steel tube contribution of $2V_{st}$ was estimated as a lower bound.

## *6.3 Equation Development Utilizing Parameter Studies*

### *6.3.1 Internal Reinforcement Contribution*

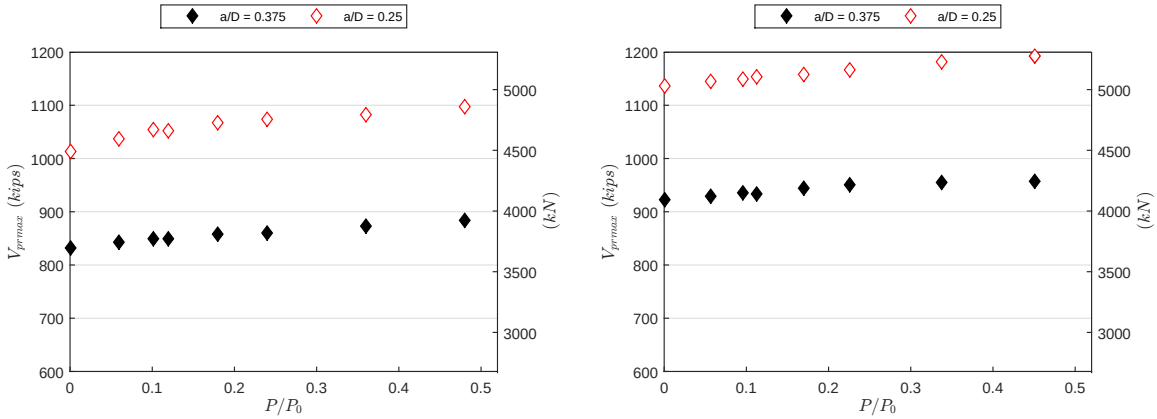
The internal reinforcement was shown to be less efficient at increasing the section's shear resistance than the steel tube, both experimentally and analytically. In the parameter studies though this was made seen more explicitly. If one recalls the results for maximum predicted shear with the $D/t$ study, it was seen that moving from a $D/t$ of 100 to 80, the total steel cross-sectional area increased by 20%. Consequently, the predicted shear at all axial load ratios increased by approximately 19%, as shown in Figure 6.1. While with the internal rein-

forcement study, the predicted shears only increased by about 12% when the reinforcement area doubled and the material strength increased by 7%.




(a) $D/t = 100$ (b) $D/t = 80$

Figure 6.1: Increase in $V_{prmax}$ with Increasing Steel Area from $D/t$ Parametric Study




(a) $\rho_{int} = 1\%$ (b) $\rho_{int} = 2\%$

Figure 6.2: Increase in $V_{prmax}$ with Increasing Internal Reinforcement Area from $\rho_{int}$ Parametric Study

So, the contribution of longitudinal reinforcement was estimated as shown in Equation 6.3, with only half the bar area being utilized. Data evaluation in the following sections review this for validity.

$$V_{srl} = 0.6F_{yrl}(0.5A_{srl}) \tag{6.3}$$

### *6.3.2 Concrete Contribution*

It was demonstrated in the parameter studies that as axial load increases, the maximum predicted shear force increases linearly until about 20% axial load, where the rate of this increase then decreases. This increase in shear resistance with axial load is typically attributed to concrete, because concrete cracking is restrained by axial load and its larger surface area allows it to take the majority of the load. Using these results, a relationship between axial load and the contribution of concrete is developed and a refined shear capacity expression formed.

Simulations of the same CFST composition that resulted in shear controlled failures, having $M_{pr} < 1.1M_{PSDM}$, and were subject to 20% axial load or less were used for evaluation. A linear least squares regression analysis was performed on these models' $\eta$-$P/P_0$ relationships, fitting a line to the data. Figure 6.3 shows an example of these fit-lines for a given CFST. Others are presented in Appendix E.

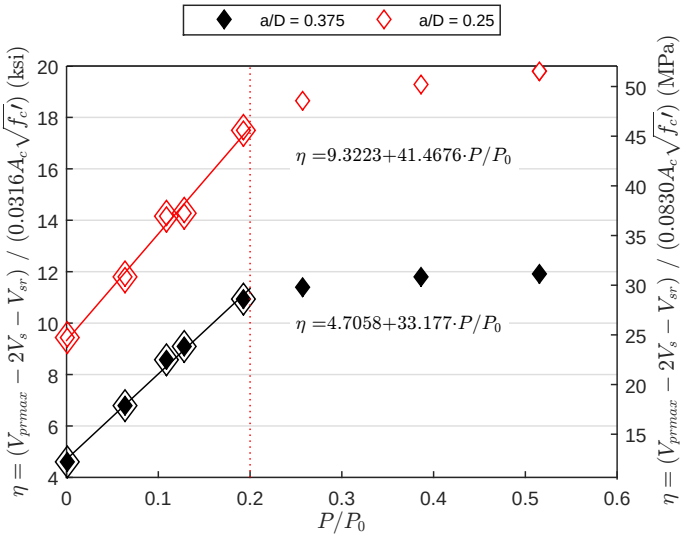



Figure 6.3: Example of Least Squares Linear Regression Fit Line using CFST having: $D/t = 80$, $f'_c = 6\ ksi$, $F_{yt} = 56.8\ ksi$, and $\rho_{int} = 0\%$

Using the relationships developed through this process, a final expression for $\eta$ is estimated, with a maximum $\eta$ of 10 set at the 20% axial load marker, where a notable decrease in the slope of the $\eta$-$P/P_0$ was observed in most models. Figure 6.4 shows that the new $\eta$ relationship better reflects the concrete contribution compared to those found in the previously discussed provisions, while remaining conservative.

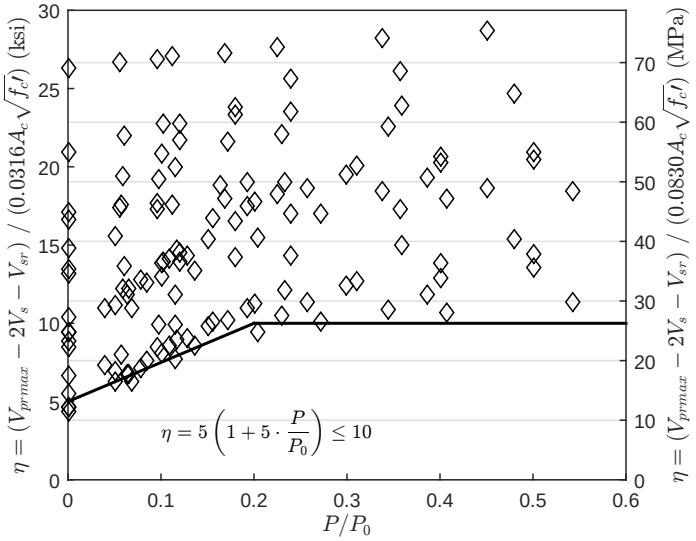



Figure 6.4: Comparison of $\eta = 5\,(1 + 5 \cdot P/P_0) \leq 10$ to Shear Controlled Models, Meeting Proposed Limit State Criterion

## *6.4 Proposed Design Expression,* $V_{n(prop)}$

Given the analyses of experimental and parametric study data, the proposed shear capacity design expression is given by Equation 6.4. The following sections compare this to available data for verification.

$$V_{n(prop)} = 2V_{st} + V_{srl} + \eta V_c \tag{6.4a}$$

$$where: \eta = 5\left(1 + 5 \cdot \frac{P}{P_0}\right) \leq 10 \tag{6.4b}$$

$$V_{st} = 0.6F_{yt}(0.5A_{st}) \tag{6.4c}$$

$$V_{srl} = 0.6F_{yrl}(0.5A_{srl}) \tag{6.4d}$$

$$V_c = 0.0316A_c\sqrt{f_c'}$$

$$(f_c' \; is \; in \; ksi \; units) \tag{6.4e}$$

### *6.4.1 Comparison of $V_{n(prop)}$ to Experimental Results*

Specimens controlled by shear, using the proposed limit state criterion, both with and without axial load are evaluated here. These specimens are given in Table 6.4. Although four specimens by Xiao met the criterion presented, this data was excluded from analysis because the researcher reported that the end plates experienced significant deformations, with some specimens designated to fail by the end plate weld, and specific specimens with these issues were not identified. With the behavior of the weld plates being so influential on the behavior of the specimens, this data was found unreliable for determining shear capacity. Nakahara also had one specimen that fell into the shear category with the proposed criterion. However, the results from this program also exhibited significant flexure-like behaviors and, therefore, was eliminated from this evaluation.

The sample size is still quite small, and the scatter relatively large, as demonstrated in Figure 6.5 and Table 6.5. The Xu data is low compared to other shear controlled specimens. It is possible that these specimens are influenced by flexural action. In fact, Xu reported the lowest specimen on the plot to be dominated by flexure. Other flexurally dominated specimens could also be mistakenly put into this analysis because of the underestimated moment arm in calculating $M_{ed}$. On the other hand, the data reported by Ye shows to be the most conservatively estimated. These specimens had large axial loads applied to them, more than typical of CFST use, where the $\eta$ value was capped, and the maximum $\eta$ value in this recommendation was based on models that allowed for relative movement between that tube steel and concrete fill. Ye's experimental program used end plates that restricted this behavior. By restricting this slippage, the composite behavior of the CFST is maintained throughout testing, allowing it to resist larger forces and therefore making the estimation with $V_{n(prop)}$ more conservative. In spite of these variations among experimental programs, the proposed design expression still shows reasonable capacity estimation with a mean $V_{ed}/V_{n(prop)}$ of 1.13 and standard deviation of 0.158.

Table 6.4: Summary of Specimens Meeting Proposed Limit State Criterion used for $V_{n(prop)}$ Analysis

| Researcher | Specimen | $a/D$ | t (in.) | $D/t$ | $F_{ytm}$ (ksi) | $f'_{cm}$ (ksi) | $P/P_0$ | $V_{ed}/2V_{st}$ | $M_{ed}/M_{PSDM}$ | $V_{ed}/V_{n(prop)}$ |
|---|---|---|---|---|---|---|---|---|---|---|
| UW | 7 [a] | 0.375 | 0.25 | 80.0 | 50.1 | 6.45 | 0 | 1.51 | 1.08 | 1.08 |
| | 8 [a] | 0.375 | 0.25 | 80.0 | 53.9 | 6.48 | 0 | 1.55 | 0.99 | 1.04 |
| | 14 | 0.25 | 0.25 | 80.0 | 55.4 | 8.60 | 0 | 1.53 | 1.03 | 1.20 |
| | 15 | 0.25 | 0.25 | 80.0 | 55.4 | 8.79 | 0 | 1.54 | 1.04 | 1.21 |
| | 20 | 0.25 | 0.25 | 80.0 | 56.8 | 2.79 | 0 | 1.35 | 0.99 | 1.17 |
| Xu | Xu16 | 0.10 | 0.145 | 38.0 | 52.8 | 4.88 | 0 | 1.20 | 0.67 | 1.10 |
| | Xu17 | 0.20 | 0.145 | 38.0 | 52.8 | 4.88 | 0 | 1.07 | 0.78 | 0.98 |
| | Xu18 | 0.30 | 0.145 | 38.0 | 52.8 | 4.88 | 0 | 1.03 | 0.92 | 0.94 |
| | Xu19 [b] | 0.50 | 0.145 | 38.0 | 52.8 | 4.88 | 0 | 0.88 | 1.08 | 0.83 |
| Ye | Y3 | 0.15 | 0.079 | 60.0 | 49.1 | 3.70 | 0.28 | 1.78 | 1.09 | 1.38 |
| | Y4 | 0.15 | 0.079 | 60.0 | 49.1 | 3.70 | 0.28 | 1.67 | 1.02 | 1.29 |
| | Y19 | 0.15 | 0.118 | 40.0 | 60.3 | 3.70 | 0.41 | 1.43 | 1.09 | 1.23 |
| | Y20 | 0.15 | 0.118 | 40.0 | 60.3 | 3.70 | 0.41 | 1.42 | 1.09 | 1.23 |

[a] Specimens 7 and 8 included internal reinforcement.
[b] Xu reported this specimen to have failed in flexure.

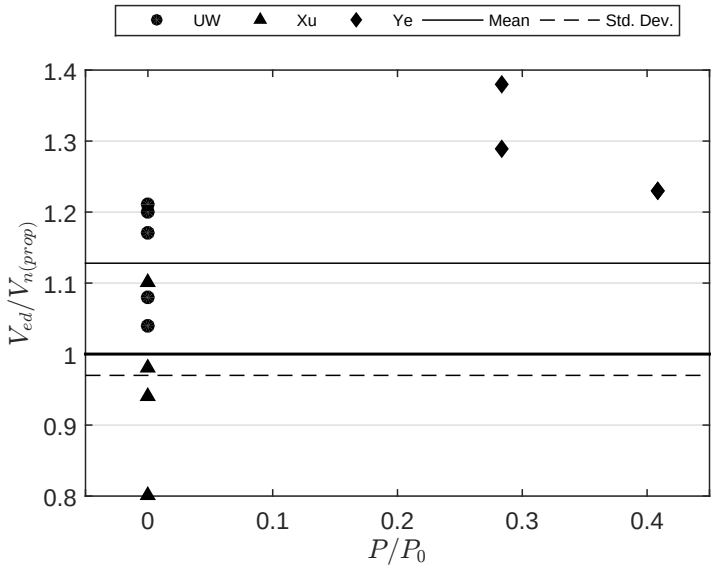



Figure 6.5: Comparison of $V_{n(prop)}$ to Experimental Results Meeting Proposed Limit State Criterion, Including Axial Load

Table 6.5: Statistical Evaluation of $V_{n(prop)}$ for Specimens Meeting Proposed Limit State Criterion, Including Axial Load

| Statistic | $V_{ed}/V_{n(prop)}$ |
|---|---|
| Count | 13 |
| Mean | 1.13 |
| Median | 1.17 |
| Min | 0.80 |
| Max | 1.38 |
| Std. Dev. | 0.158 |
| COV | 0.140 |

### *6.4.2 Comparison of $V_{n(prop)}$ to Analytical Results*

Figure 6.6 and Table 6.6 show the comparisons of $V_{n(prop)}$ to the simulations that resulted in shear-dominated response, according to the proposed limit state criterion. This evaluation shows the mean effective ratio, $V_{ed}/V_{n(prop)}$, and standard deviation to be 1.17 and 0.134. A complete list of the models and their predicted results is provided in Appendix F. Overall the expression shows to be conservative.

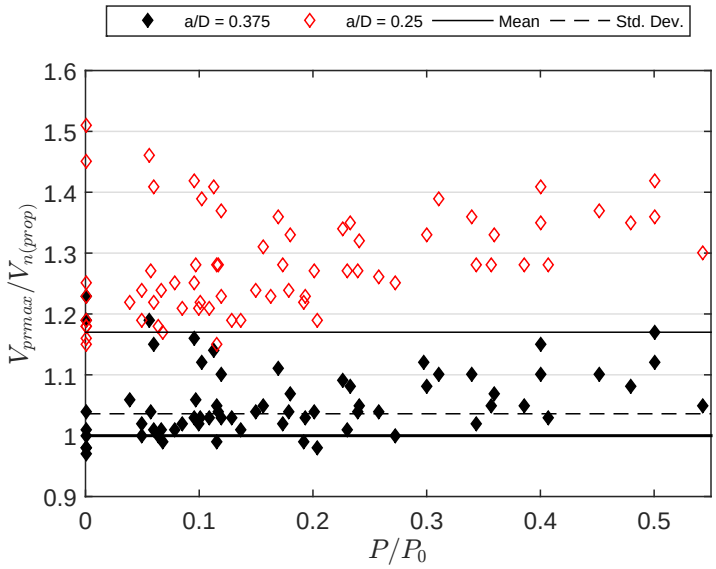



Figure 6.6: Comparison of $V_{n(prop)}$ to Shear Controlled Models, Meeting Limit State Criterion

Table 6.6: Statistical Evaluation of $V_{n(prop)}$ for Shear Controlled Models, Meeting Limit State Criterion

| Statistic | $V_{prmax}/V_{n(prop)}$ |
|---|---|
| Count | 137 |
| Mean | 1.17 |
| Median | 1.17 |
| Min | 0.97 |
| Max | 1.51 |
| Std. Dev. | 0.134 |
| COV | 0.114 |

### *6.4.3 Assessment of RCFSTs with $V_{n(prop)}$*

The longitudinal reinforcement in the proposed equation has been estimated to contribute to the total CFST capacity with only half of its total cross-sectional area being utilized. This was largely based qualitatively on experimental and parametric study data that suggested the reinforcement is less effective than the steel tube in terms of reinforcing the CFST member. Even though explicit quantitative analysis was not used in estimating this, $V_{n(prop)}$ shows to conservatively estimate the shear capacity of RCFSTs in the experiments and models meeting the proposed limit state criterion, as shown in Figure 6.7 and Table 6.7. All points are above 1.0, and the mean and standard deviation of $V_{ed/pr}/V_{n(prop)}$ are approximately 1.2 and 0.15, respectively.

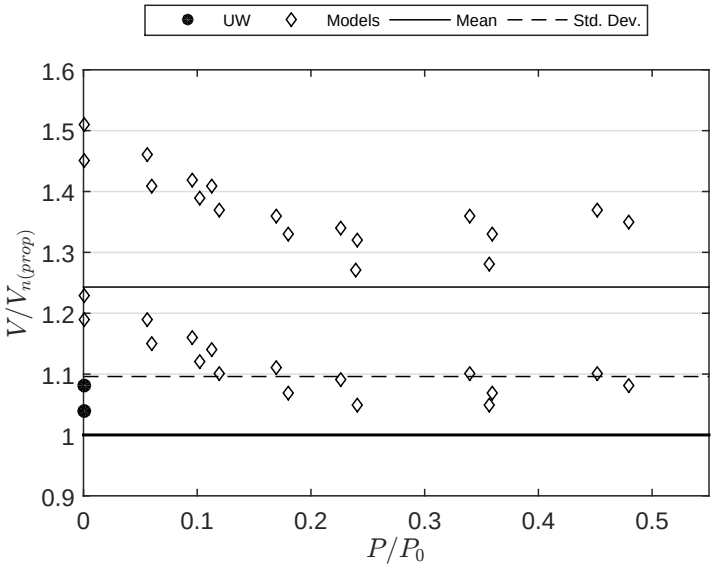



Figure 6.7: Comparison of $V_{n(prop)}$ to Experimental and Analytical RCFST Shear Specimens, Meeting Proposed Limit State Criterion

Table 6.7: Statistical Evaluation of $V_{n(prop)}$ for Experimental and Analytical RCFST Shear Specimens, Meeting Proposed Limit State Criterion

| Statistic | $V_{ed/pr}/V_{n(prop)}$ |
|---|---|
| Count | 34 |
| Mean | 1.24 |
| Median | 1.21 |
| Min | 1.04 |
| Max | 1.51 |
| Std. Dev. | 0.147 |
| COV | 0.12 |

### *6.4.4 Comparison of $V_{n(prop)}$ to All Data*

Figure 6.8 and Table 6.8 summarize the results for both experimental and analytical data that meet the proposed limit state criterion for shear. Altogether, the data demonstrates conservatism and more precise shear capacity estimation than seen with previous design expressions, with a mean effective ratio of approximately 1.2 and standard deviation of 0.14.

A few results do fall below unity in Figure 6.6 due to the incidental inclusion of flexural response from underestimated moments. Moreover, nominal capacity is being estimated here and in design application, factored loads would be analyzed and an additional resistance factor would be applied to this value, establishing further conservatism.

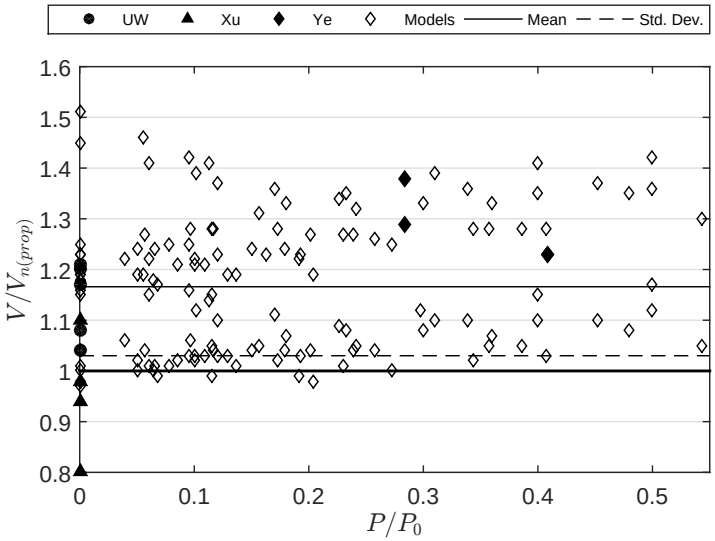



Figure 6.8: Comparison of $V_{n(prop)}$ to Experimental and Analytical Shear Specimens, Meeting Proposed Limit State Criterion

Table 6.8: Statistical Evaluation of $V_{n(prop)}$ for Experimental and Analytical Shear Specimens, Meeting Proposed Limit State Criterion

| Statistic | $V_{ed/pr}/V_{n(prop)}$ |
|---|---|
| Count | 150 |
| Mean | 1.17 |
| Median | 1.17 |
| Min | 0.80 |
| Max | 1.51 |
| Std. Dev. | 0.136 |
| COV | 0.117 |

Using the proposed equation, $V_{n(prop)}$, an evaluation of a potential resistance factor, $\phi$, that could be used for LRFD design based on Ravindra and Galambos (1978) was completed. Based on this probabilistic calculation, a $\phi$ of 0.90 would be recommended. The calculation for this is provided here, using the mean value and the coefficient of variation presented in Table 6.8, noted as $\overline{\gamma}$ and $V_P$:

$$\phi = exp(-\alpha\beta V_R) \cdot \overline{\gamma} = 0.90 \tag{6.5}$$

$$where: \; V_R = \sqrt{V_M^2 + V_F^2 + V_P^2} = 0.162$$

$$\beta = 3.0$$

$$\alpha = 0.55$$

$$\overline{\gamma} = 1.17$$

$$V_P = 0.117$$

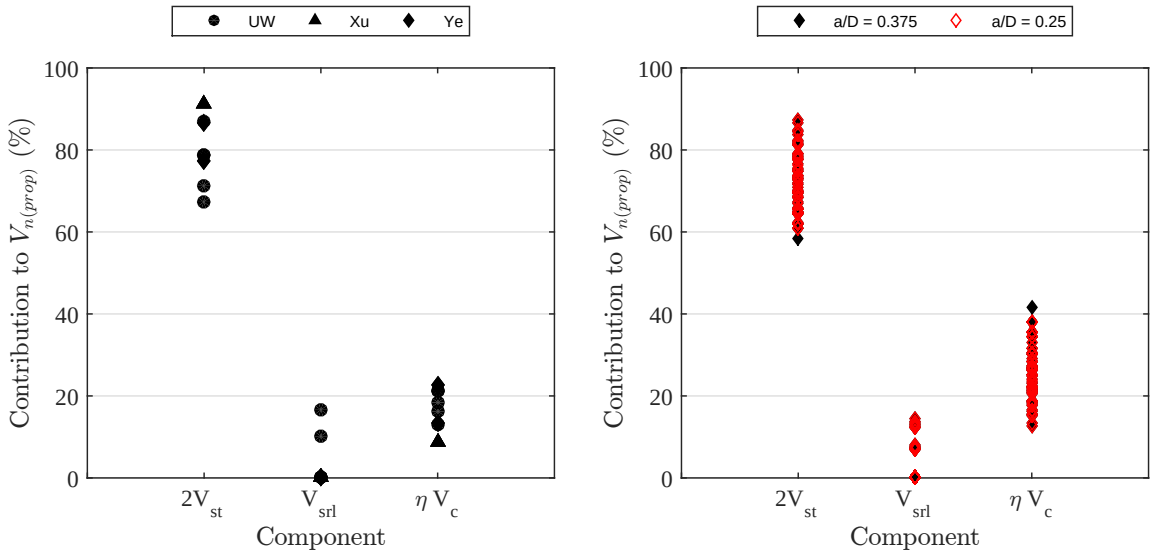
$$V_M = 0.10$$

$$V_F = 0.05$$

### *6.4.5 Summary of Component Contributions According to $V_{n(prop)}$*

For designers, it is important to make decisions that yield the most efficient solution. This comes from knowing what alterations in member design are most effective. It has been concluded throughout this document that the tube steel provides the most resistance to CFST members under shear loading. In terms of the proposed design expression, the experimental results show that on average the steel tube provides approximately 83% of the total resistance, while the concrete and reinforcement only contribute 15 and 13%, as shown in Figure 6.9a. When using the larger spectrum of material strengths, component areas, and axial load in the simulations (Figure 6.9b), the average steel tube contribution lessens to 70%, largely due to the low strength steel (35 $ksi$) and $D/t$ of 100 models. The concrete then increases

in participation to 26% due to the effect of axial load, and not the increases in $f'_c$ of some models. And finally, the reinforcement moves down to 10% contribution. With all results considered (Figure 6.10), the tube steel provides 72% of total shear resistance on average, with the concrete following with 25% average contribution, and finally, the reinforcement with 10%.




(a) *Experiments* (b) *Models*

Figure 6.9: Contribution of Tube Steel, Internal Reinforcement, and Concrete to Total Shear Resistance According to $V_{n(prop)}$

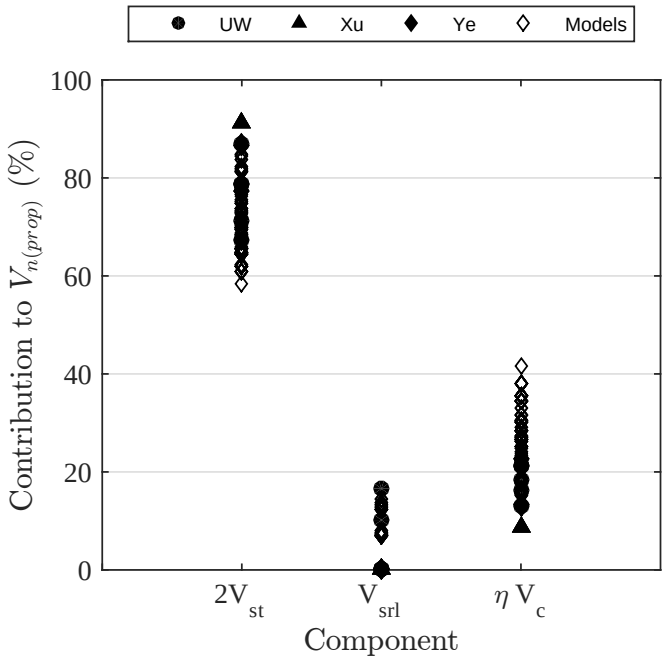



Figure 6.10: Contribution of Tube Steel, Internal Reinforcement, and Concrete to Total Shear Resistance According to $V_{n(prop)}$ using All Data

As noted, the data sets presented look at large ranges of CFST component design. However, if only parameters common to CFST and RCFST design are considered, that is, a $D/t$ of 80, $F_{yt} \approx 50\ ksi$, $f'_c \approx 6\ ksi$, and $P/P_0 \leq 0.2$, the average contributions are more commonly 70.5% from the tube, 22% from the concrete fill, and 10.7% from the internal reinforcement, as shown in Figure 6.11.

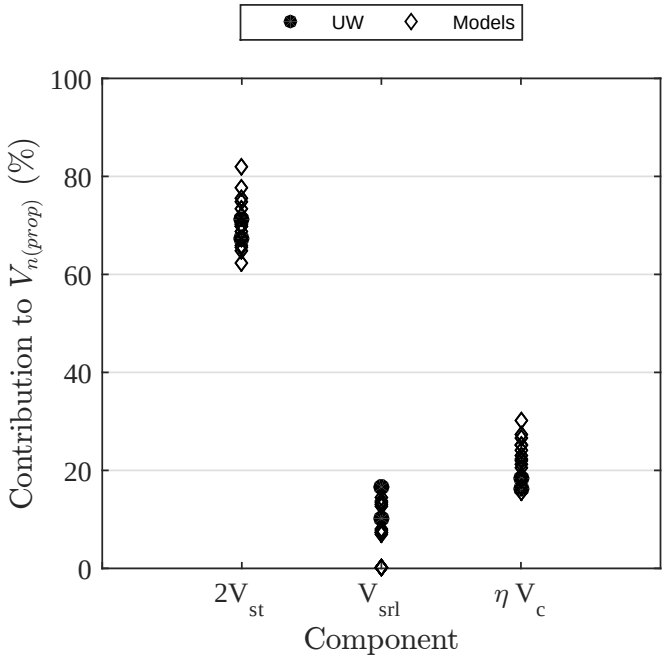



Figure 6.11: Contribution of Tube Steel, Internal Reinforcement, and Concrete to Total Shear Resistance According to $V_{n(prop)}$ using Typical CFST Design

# Chapter 7

# CONCLUSIONS AND FUTURE WORK

## *7.1 Summary*

This thesis concludes the experimental and analytical studies on the shear capacity of circular CFSTs performed at the University of Washington. The experimental program included the testing of twenty-one large diameter (20 *in.*) CFSTs, where the parameters shear span to depth ratio ($a/D$), diameter-to-thickness ratio ($D/t$), concrete compressive strength, tube type, tail length, internal reinforcement, and interface condition were varied. Using six of these specimens, models were made in ABAQUS so that peak shear resistance reasonably matching that in the experiments was achieved. Parameter studies were then performed with the developed model to expand the experimental data set by studying $a/D$, internal reinforcement, $D/t$, concrete strength, tube steel yield strength, and the effect of axial load more explicitly. With the data and conclusions from the simulations and experimental work in this program and prior research, a limit state criterion and a design expression for the shear resistance of CFSTs were proposed. This proposal, unlike the presented design provisions in Chapter 2, incorporates the benefits of axial load and the upgraded properties of the steel tube, internal reinforcement, and concrete fill that come from their interaction in a CFST and RCFST member.

## *7.2 Conclusions*

### *7.2.1 Proposed Limit State Criterion and Design Expression*

The main conclusions made in this research are summed up in the proposed shear limit state criterion and design expression (Equation 6.4), but is repeated here for clarity. In the experiments, either moment capacity limited shear development or shear capacity limited shear

development. From previous research (Bishop, 2009; Roeder et al., 2010), CFSTs on average reach 125% of their plastic capacity, $M_{PSDM}$, and this research showed that specimens developing approximately $1.2M_{PSDM}$ consistently demonstrated flexurally controlled failure. The experiments showed that shear-controlled specimens reached up to 110% of the CFSTs plastic moment capacity, $M_{PSDM}$. Any specimens that developed less than this capacity were categorized by shear failure, given sufficient tube-to-concrete bond development was provided and no significant slip was observed.

Using this as a criterion then, data from experiments and parametric study were selected and a design expression was proposed based on the following determinations. The tube steel was found to be the largest contributor to the shear resistance. The internal reinforcement increases shear resistance, but not as efficiently as the tube steel. Additionally, the two main components, the steel tube and concrete fill, have improved properties as part of a composite member than they do as separate entities: the tube is made more efficient by the deformation and local buckling restraint provided by the concrete fill and the steel tube provides superior confinement to the concrete fill, improving its participation in resisting shear. Explicit support for these conclusions are given here as they relate to the proposed design expression (Equation 7.1):

- The gravel-filled specimen (Specimen 21) achieved $1.7V_{st}$ because the gravel fill prevented severe local deformations, allowing tension-field action to control. However, concrete fill provides more deformation restraint than gravel fill and, as a result, the steel tube provides capacity equivalent to $2V_{st}$ in a CFST.

- Parameter studies showed that $V_{srl}$ is less efficient at developing shear resistance than the steel tube and its contribution is taken as half that of an equivalent steel tube area.

- Parameter studies showed that shear capacity increases with increasing axial load, up to about 20% $P/P_0$, where this increase lessens significantly. This is provided by the $\eta$ factor on the concrete fill contribution.

$$V_{n(prop)} = 2V_{st} + V_{srl} + \eta V_c \tag{7.1a}$$

$$where: \eta = 5\left(1 + 5 \cdot \frac{P}{P_0}\right) \leq 10 \tag{7.1b}$$

$$V_{st} = 0.6F_{yt}(0.5A_{st}) \tag{7.1c}$$

$$V_{srl} = 0.6F_{yrl}(0.5A_{srl}) \tag{7.1d}$$

$$V_c = 0.0316A_c\sqrt{f'_c}$$

$$(f'_c \; is \; in \; ksi \; units) \tag{7.1e}$$

The contribution factors in the new expression are greater than those in current provisional design expressions, better demonstrating the superior capacity and composition hierarchy of a CFST member. Considering typical CFST member design with this expression ($D/t$ of 80, $F_{yt} \approx 50$ $ksi$, $f'_c \approx 6$ $ksi$, and $P/P_0 \leq 0.2$), 70.5% of the total shear resistance is attributed to the tube steel, 22% to the concrete fill, and 10.7% to the internal reinforcement, based on individual averages of each component.

One conclusion from this program is not directly implemented in the proposed equation – the effect of $a/D$. Smaller $a/D$ ratios clearly increased the likelihood of shear-controlled response and the magnitude of the CFST's shear carrying capacity. However, the shear span could not be accurately determined with the test setup, because the length required to load and support the specimen, i.e. the sum of the cradle widths (8 $in.$), was longer than the nominal shear span length, $a$, required to induce shear failure. The uncertainty of shear span in design application is also an issue, particularly with soil layers in deep foundations where shear forces could potentially reach these magnitudes. Therefore, shear span was not included as part of design limits. Even without this refinement though, the proposed design expression proved to accurately estimate shear resistance with a mean $V_{ed/pr}/V_{n(prop)}$ value of 1.17 and standard deviation of 0.136. Furthermore, based on the probabilistic approach

in LRFD design and this scatter in data, the resistance factor, $\phi$, for this nominal capacity would be 0.90, demonstrating good estimation potential.

### *7.2.2 Experimental Results*

In addition to the results presented in the proposed limit state criterion and design expression, the following conclusions were made from the experimental testing of this program:

- Four failure modes were identified.

    1. Flexural Failure - Eight specimens failed due to flexure. Specimens that failed due to bending action exceeded moments greater than their plastic capacity, $M_{PSDM}$, by at least 10%, but mostly over 20%. These specimens exhibited noticeable flexural deformations, with compressive tube buckling at the top of the midspan and extensive tensile cracking at the bottom of the pure moment region where a vertical tear in the tube formed. Strain distributions also suggested that plane sections remain plane during inelastic deformation of this kind. Lastly, little to no shear deformations were visible in the tube steel or concrete fill.
    2. Shear Failure - Five specimens failed due to shear. Specimens that failed in shear did not achieve $1.1M_{PSDM}$ and demonstrated significant shear yielding in the steel tube, ultimately tearing just inside one shear span, with no evident flexural deformations present. Extensive cracking was also found in the failed shear span, with minimal cracks in the pure moment region. Finally, strain distributions were typically inconsistent with the plane sections hypothesis.
    3. Flexure-Shear Interaction - This behavior was noted as a zone between flexural and shear control where the relationship between moment and shear is not clearly defined. Evidence of both flexural and shear deformations were found in these specimens, and their ultimate shear and moment forces were, on average, found to be between the 1.2 and $1.1M_{PSDM}$ limits described. Six specimens responded in this manner.

4. Bond Slip Failure - Failure due to bond slip was found when significant slip was observed that resulted in loss of load carrying capacity. These specimens may develop smaller shear and flexural resistance than the other failure modes, and their behavior is somewhat analogous to development length failure in reinforced concrete. Two specimens were controlled by large bond slip.

- The experiments showed that the flexural and shear resistance potentials of CFSTs are dependent upon the development of composite action between the tube steel and concrete fill. Withouth it, both capacities are limited. This composite behavior was established by providing sufficient development length beyond the location of maximum moment, much like reinforcing bars in concrete design. In the experiments, a minimum of one tube diameter in tail length, $L_T$, beyond support point appeared to be sufficient, but further data was required to liken this to development length directly. Surface condition at the steel-concrete interface also influenced this development. However, extreme disturbance to this condition, such as the greased interface specimen, is not likely to be found in practice. On the other hand, the application of a muddy slur to the interface is more reflective of field conditions, and test results showed that it slightly increased the capacity of the CFST.

- Internal reinforcement provided additional load carrying capacities, but this reinforcement was less efficient than the steel tube. Additionally, more shear yielding was observed in RCFSTs compared to their CFST counterparts. This suggested that internal reinforcement bars increase both moment and shear capacity, but are less efficient at improving shear resistance.

- One specimen was loaded axially, and this specimen showed an increase in resistance as a result.

- The aspect ratio, $a/D$, had a clear influence on resulting failure mode because it is the

link between shear and moment. As the shear span decreased, the moment decreased for a given shear force, and when it became small enough, shear resistance controlled the behavior. Therefore, smaller moments and larger shear forces were seen in shear-controlled specimens at the smaller $a/D$ ratios. CFST deformations also demonstrated this shift in behavior. That is, shear-like deformations began to appear more clearly with the smallest $a/D$ ratios, 0.375 and 0.25. However, definitive values for shear span ratio, as it relates to failure mode, cannot be practically determined through experiments because the large shear demands require the spreading of load and support contact stresses over a relatively large area.

### *7.2.3 Parameter Studies*

The parameter studies confirmed the conclusions made by experimentation and introduced new results on CFST behavior. A summary of the newly developed results and further detailed validation of the experimental observations are provided here.

- Axial load increased both flexural and shear capacities, but as this load got higher, the CFST was more likely to fail by flexure, possibly because the axial load more efficiently improved shear resistance compared to bending.

- Observed shear and moment decreased with increasing $D/t$ ratios, which can be attributed to an increase in $A_{st}/A_c$.

- As $F_{yt}$ increased, so did shear resistance.

- The $\eta$ values from the $F_{yt}$ and $D/t$ studies showed significant variation within their respective test groups, while the concrete series showed little variation in $\eta$, suggesting that $\eta$ is not strongly influenced by concrete strength. Nevertheless, a small increase in capacity was noted with an increase in $f'_c$.

- The introduction of internal reinforcement increased shear resistance. However, it increased flexural resistance more, as evident by the resulting increase in shear yielding.

## *7.3 Future Work*

Although many behaviors and distinctions on the shear capacity of CFSTs have been studied in this research program, there are still aspects of behavior that need to be defined. For example, a more explicit relationship between the interaction of shear and moment could be of great value for more accurate predictions. Without this distinction, the proposed equations are still somewhat overly conservative. Furthermore, refinement in the proposed contributions of the various components might be improved. Some recommendations to future experimental and analytical work are outlined here.

### *7.3.1 Experiments*

- The parameter studies considered a larger spectrum of some previously tested parameters. It would be desirable to also increase the experimental data set so that further verification of these models and their conclusions could be made. These included larger ranges of concrete strength ($f'_c$), tube steel yield ($F_{yt}$), diameter-to-thickness ratio ($D/t$), and axial load ratio ($P/P_0$).

- As noted, composite action has a significant impact on how CFSTs carry load. Therefore, additional tests focusing on tail length, $L_T$, with varying shear spans, should be done so that more accurate recommendations for a minimum design development length can be made.

- The use of spirally welded tubes have shown improved bond stress capacity at the tube steel-concrete interface (Thody, 2006). More tests of spirally welded tubes should be completed to distinguish its effects on strength and deformation.

- The influence of internal reinforcement should be studied with additional straight-seemed and spirally-welded tube specimens, using the full range of $a/D$ ratios, to differentiate influence on moment and shear capacities.

- Strain fields could be developed with Optotrak data to highlight locations of greatest deformation and better understand the sequence of development between flexure and shear deformations. These conclusions could then be used to refine failure mode classification and, therefore, the proposed limit state criterion and design expression.

### *7.3.2 Analytical Modeling*

*Simulation Improvements*

The model validated in this program was made specific to the testing setup and procedure described in Chapter 3. This required modeling techniques specific to this testing setup in order to achieve the observed peak resistances that would not be used for other applications. Nevertheless, the simulation of the CFST specimen itself is relevant to other applications. And although the model was only validated for shear force magnitude, efforts to improve the deflection response could be made so that further parametric study and analysis of deformation behaviors could be added to the observations already made in this document. Suggestions for this improvement would be:

- A model of the full length specimen, including both shear spans and a full pure moment region, with the manual introduction of nonsymmetrical response could be made to better capture the experimental deflections. This nonsymmetrical behavior could be encouraged by precracking one of the shear spans along the diagonal strut between the load and support points, or by introducing other flaws, such as residual stress or decreased bond coefficient, $\mu$. Another option would be to intentionally model one shear span to be a bit smaller than the other, creating a single, more shear critical region to focus damage.

- More focused study with the different concrete damaged plasticity model parameters on the concrete fill response in the model would help refine concrete response.

- Continued efforts in achieving the deformation response of the setup in the current model could also be undertaken, but focus on cradle rotations as effected by surface-to-surface friction coefficients and elastomeric bearing stiffnesses is recommended. That is, the modeling of cotton duck behaviors was concluded to be unnecessary as the cotton duck was destroyed early on in the experiments. Should deflection behavior prediction be improved with these and/or other methods, validation with local behaviors and conclusions on these should be developed.

- Investigation of a new confined concrete uniaxial stress-strain model that is appropriate for CFST application would be of significant use in defining concrete behaviors in analytical models, and other applications.

*Parametric Study*

Additional models could be used to better conclude and refine the developed knowledge. In addition to the already simulated parameters, models with varying tail length ($L_T$) and interface condition to match the strength of spirally welded tubes would be desired, but more experimental data is also required to validate these.

# REFERENCES

American Association of State Highway and Transportation Officials (2016). *AASHTO LRFD Bridge Design Specifications*. Washington, D.C., 7th with 2016 interims edition.

American Concrete Institute (2011). *Buidling Code Requirements for Structural Concrete (ACI 813-11) and Commentary*. Farmington Hill, MI.

American Institue of Japan (2008). *Recommendations for Design and Construction of Concrete Filled Steel Tubular Structures*. Tokyo.

American Institue of Steel Construction (2010). *Specification for Structural Steel Buildings*. Chicago, IL.

Bishop, E. (2009). "Evaluation of the flexural resistance and stiffness models for circular concrete-filled steel tube members subjected to axial-flexural loading." M.S. thesis, University of Washington, Seattle, WA.

Dassault Systemes Simulia Corp. *ABAQUS Unified FEA Product Suite*.

Dassault Systemes Simulia Corp. (Version 6.13). *Abaqus Analysis User's Guide*.

European Committee for Standardization (2013). *BS EN 206-1 Concrete - Part 1: Specification, performance, production and conformity*. BSI, B/517/1.

Goto, Y., Kumar, G., and Kawanishi, N. (2010). "Nonlinear finite-element analysis for hysteretic behavior of thin-walled circular steel columns with in-filled concrete." *J. Str. Eng.*, 136(11), 1413–1422.

Han, L., Lu, H., Yao, G., and Liao, F. (2006). "Further study on the flexural behaviour of concrete-filled steel tubes." *J. Const. Steel Res.*, 62(6), 554–565.

Han, L., Tao, Z., and Yao, G. (2008). "Behaviour of concrete-filled steel tubular members subjected to shear and constant axial compression." *Thin-Walled Structures*, 46, 765–780.

Han, L., Yao, G., and Tao, Z. (2007a). "Behaviours of concrete-filled steel tubular members subjected to combined loading." *Thin-Walled Structures*, 45(6), 600–619.

Han, L., Yao, G., and Tao, Z. (2007b). "Performance of concrete-filled thin-walled steel tubes under pure torsion." *Thin-Walled Structures*, 45(1), 24–36.

Hanneson, G. (2010). "Mechanical properties of high-volume scm concretes." M.S. thesis, University of Washington, Seattle, WA.

Housing and Urban-Rural Development Department of Fujian Province (2010). *DBJ/T13-51-2010: Technical Specifications for Concrete-filled Steel Tubular Structures (Revised Version)*. Fuzhou, China.

Hu, H. and Schnobrich, W. (1989). "Constitutive modeling of concrete by using nonassociated plasticity." *J. Mater. Civil Eng.*, 1(4), 199–216.

Ichinohe, Y., Matsutani, T., Nakajima, M., Ueds, H., and Takada, K. (1991). "Elasto-plastic behavior of concrete filled steel circular columns." *Proc. of 3rd Intl. Conf. on Steel-Concrete Composite Structures*, Fukuoka, Japan, ASCCS, 131–136.

Lehman, D. E., Roeder, C. W., Larson, R., and Curtin, K. (2003). "Cotton duck bearing pads: Engineering evaluation and design recommendations." *Report No. WA-RD 569.1*, Washington Department of Transportation.

Maki, T. (2015). "Experimental investigation of the shear resistance of circular concrete-filled steel tubes subjected to transverse loading." M.S. thesis, University of Washington, Seattle, WA.

Moon, J., Lehman, D., Roeder, C. W., and Lee, H. (2013). "Strength of circular concrete-filled tubes with and without internal reinforcement under combined loading." *J. Str. Eng.*, 139(12).

Moon, J., Roeder, C. W., Lehman, D., and Lee, H. (2012). "Analytical modeling of bending of circular concrete-filled steel tubes." *Engineering Structures*, 42, 349–361.

Nakahara, H. and Tokuda, S. (2012). "Shearing behavior of CFT short columns." *Proc. of 10th Intl. Conf. on Advances in Steel Concrete Composite and Hybrid Structures*, Singapore, Research Publishing Services, 362–369.

Qian, J., Cui, Y., and Fang, X. (2007). "Shear strength tests of concrete filled steel tube columns." *China Civil Engineering Journal*, 40(5), 1–9.

Ravindra, M. and Galambos, T. (1978). "Load and resistance factor design for steel." *J. Str. Division*, ASCE, 104(9), 1337–1353.

Roeder, C., Lehman, D., and Bishop, E. (2010). "Strength and stiffness of circular concrete-filled tubes." *J. Struct. Eng.*, 136(12), 1545–1553.

Roeder, C., Lehman, D., and Thody, R. (2009). "Composite action in CFT components and connections." *Eng. Journal*, 46(4), 229–242.

Roeder, C. W., Stanton, J. F., and Taylor, A. W. (1987). "Performance of elastomeric bearings." *Report No. NCHRP 298*, National Cooperative Highway Research Program.

Thody, R. (2006). "Experimental investigation of the flexural properties of high-strength concrete-filled steel tubes." M.S. thesis, University of Washington, Seattle, WA.

Tomii, M. and Sakino, K. (1979). "Experimental studies on concrete filled square steel and tubular beam-columns subjected to monotonic shearing force and constant axial load." *Trans. of AIJ*, 281, 81–90.

Washington Department of Transportation (2012). *Design Memorandum: Structural Design Recommendations of CFT and RCFT for Bridge Foundation* (October).

Xiao, C., Cai, S., Chen, T., and Xu, C. (2012). "Experimental study on shear capacity of circular concrete filled steel tubes." *Steel and Composite Structures*, 13(5), 437–449.

Xu, C., Haixiao, L., and Chengkui, H. (2009). "Experimental study on shear resistance of self-stressing concrete filled circular steel tubes." *J. Const. Steel Res.*, 65, 801–807.

Ye, Y., Han, L., Tao, Z., and Guo, S. (2016). "Experimental behaviour of concrete-filled steel tubular members under lateral shear loads." *J. Const. Steel Res.*, 122, 226–237.

# Appendix A

# NOTATION LIST

## Geometry

| | |
|---|---|
| $A$ | total cross-sectional area of CFST |
| $a$ | shear span; for experimental analysis, the clear span as defined by the experimental setup (Figure 3.1) |
| $a'$ | estimated true distance between load points (Figure 3.9) |
| $a'_0$ | center-to-center distance between load and support cradles (Figure 3.1) |
| $A_b$ | individual rebar cross-sectional area |
| $A_c$ | gross cross-sectional area of concrete fill |
| $A_{srl}$ | cross-sectional area of longitudinal reinforcing steel |
| $A_{srt}$ | area of transverse shear reinforcement steel |
| $A_{st}$ | cross-sectional area of tube steel |
| $A_s$ | total cross-sectional area of steel (including tube and longitudinal reinforcement) |
| $D$ | outer diameter of CFST |
| $t$ | tube thickness |

## Material Properties

| | |
|---|---|
| $E_c$ | elastic modulus of concrete |
| $E_s$ | elastic modulus of steel |
| $f'_c$ | concrete compressive cylinder strength |
| $f_{ct}$ | concrete tensile strength |
| $f_{cu}$ | concrete cube strength |
| $F_{ut}$ | ultimate tube steel strength |
| $F_{yrl}$ | yield strength of longitudinal reinforcing steel |
| $F_{yrt}$ | yield strength of transverse reinforcing steel |
| $F_{yt}$ | yield strength of tube steel |

## Force

| | |
|---|---|
| $M$ | moment |
| $P$ | axial force |
| $P_0$ | nominal axial capacity (Equation 2.3) |
| $V$ | shear force |
| $V_c$ | shear strength of concrete fill |
| $V_n$ | nominal shear capacity of CFST |
| $V_{srl}$ | shear strength of longitudinal internal reinforcement of CFST |
| $V_{srt}$ | shear strength of transverse internal reinforcement of CFST |
| $V_{st}$ | shear strength of tube steel |

## Other

| | |
|---|---|
| $\eta$ | factor defining concrete contribution to shear (Equation 5.2) |
| $\mu$ | coefficient of friction |
| $_m$ | measured value |
| $_n$ | nominal value |
| $_{ed}$ | experimentally derived value |
| $_{exp}$ | experimental value |
| $_{pr}$ | analytically predicted value |

# Appendix B

# EXPERIMENTAL TEST RIG

All drawings provided in this Appendix were taken from Maki (2015).

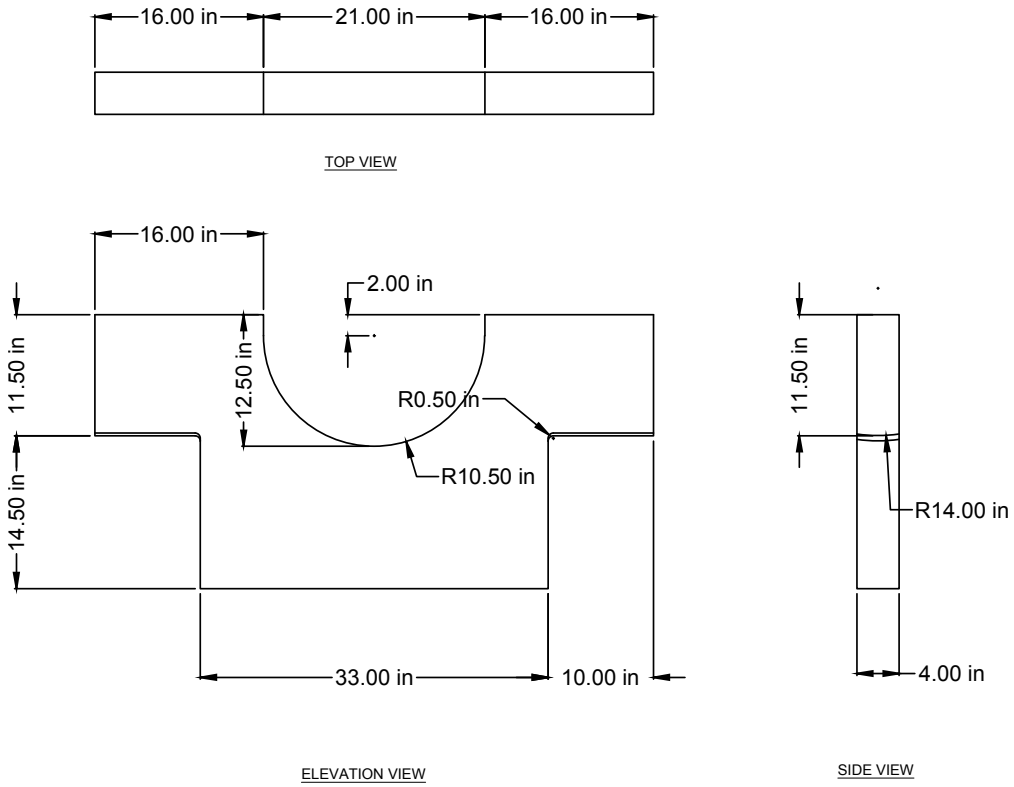



Figure B.1: Support Cradle

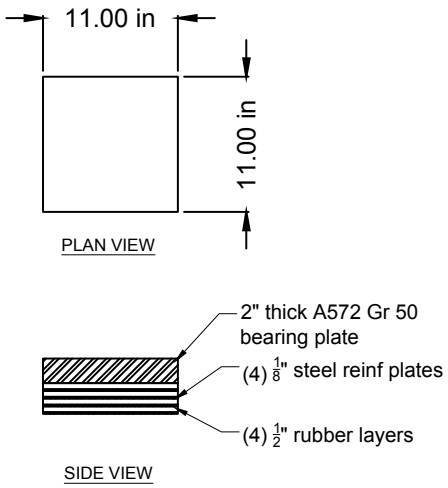



Figure B.2: Elastomeric Bearing

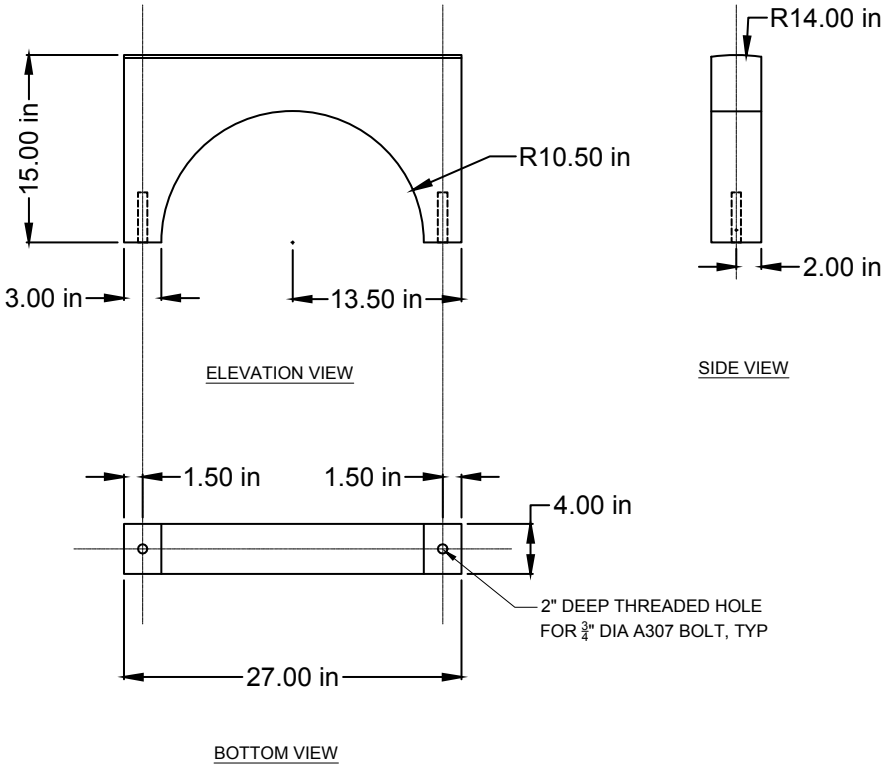



Figure B.3: Load Cradle

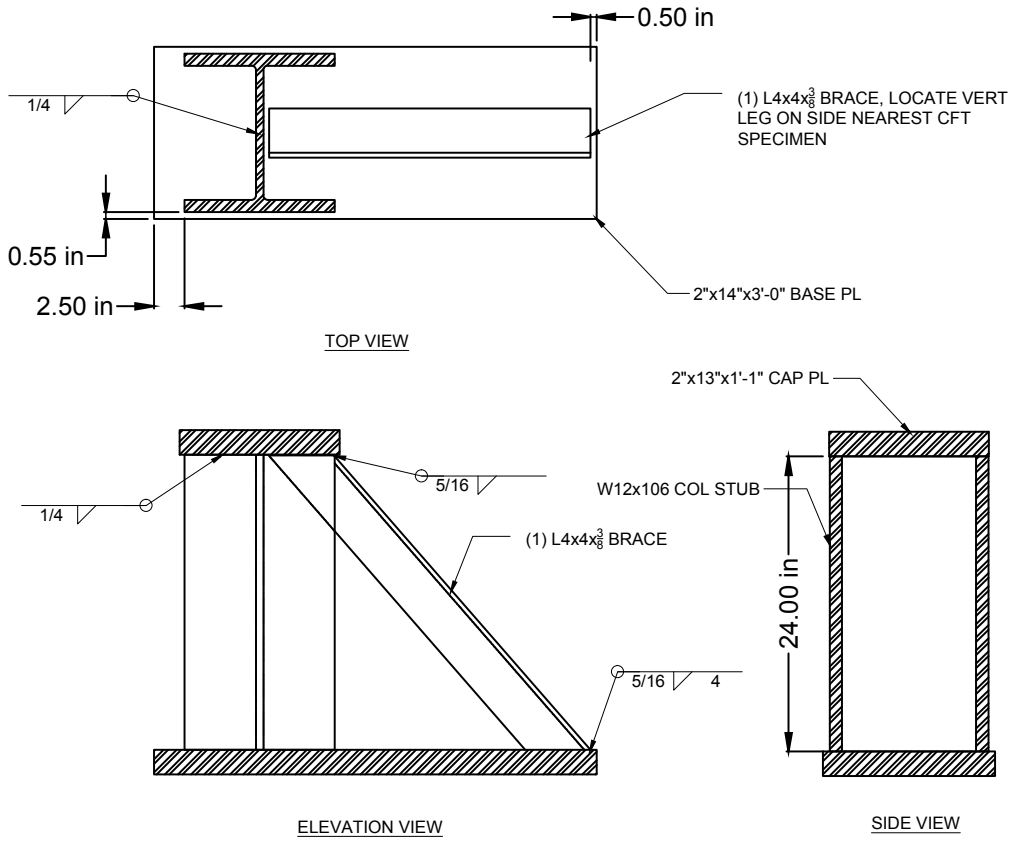



Figure B.4: Steel Base

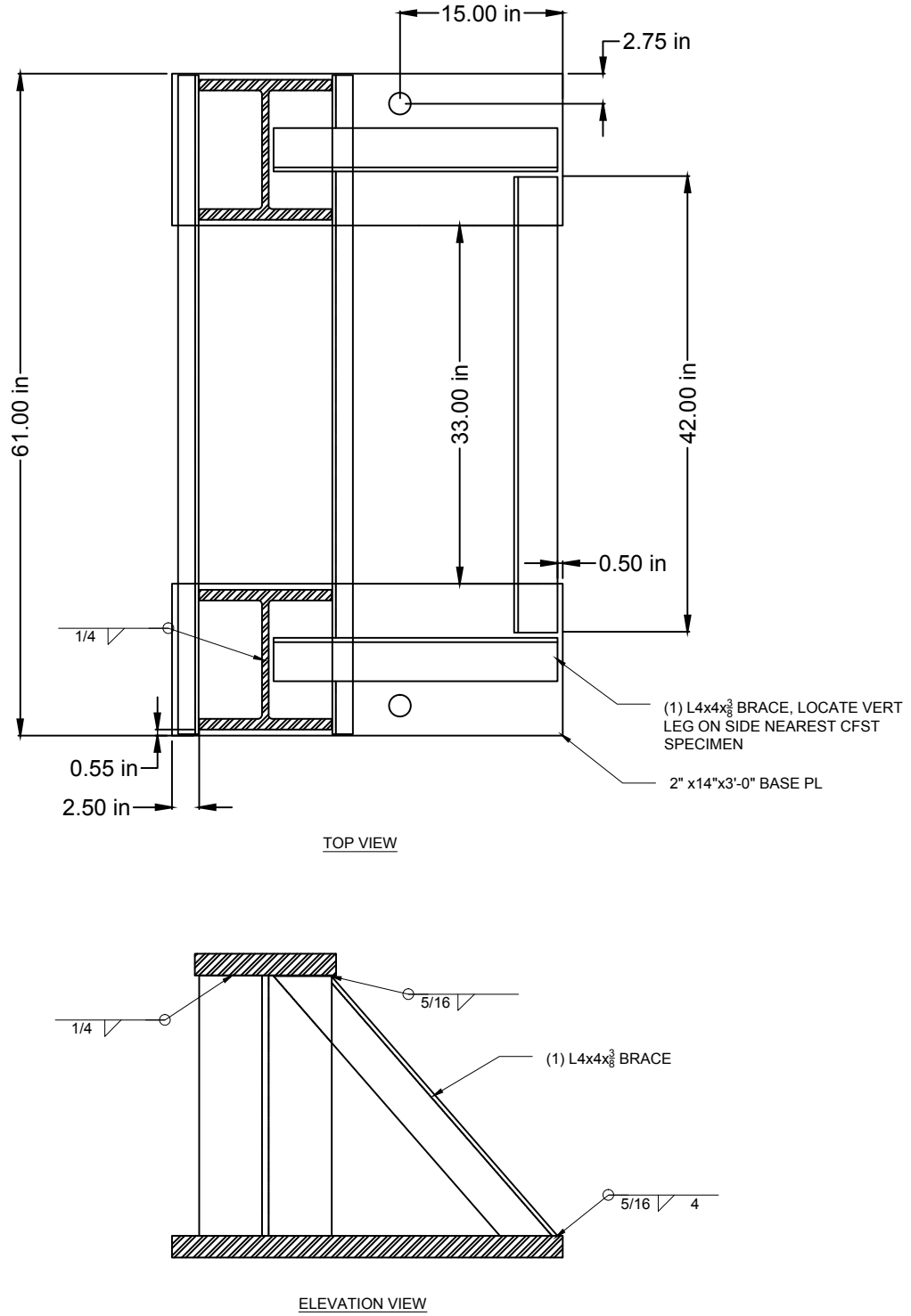



Figure B.5: Steel Base Assembly

# Appendix C

# SUPPLEMENTARY EXPERIMENTAL DATA CALCULATIONS

## *C.1 Specimen Deflection Target Locations*

Figure C.1 illustrates the available targets for presenting specimen deflections and Table C.1 shows the actual targets used based on this figure for each specimen plotted in Chapter 3. These deflections were corrected for elastomeric bearing and cotton duck deformations as described in Section C.4. Note that for flexural failure modes,the deflections taken with the north and south load targets are very similar. So, the target was chosen on the side where the central tear was shifted slightly.

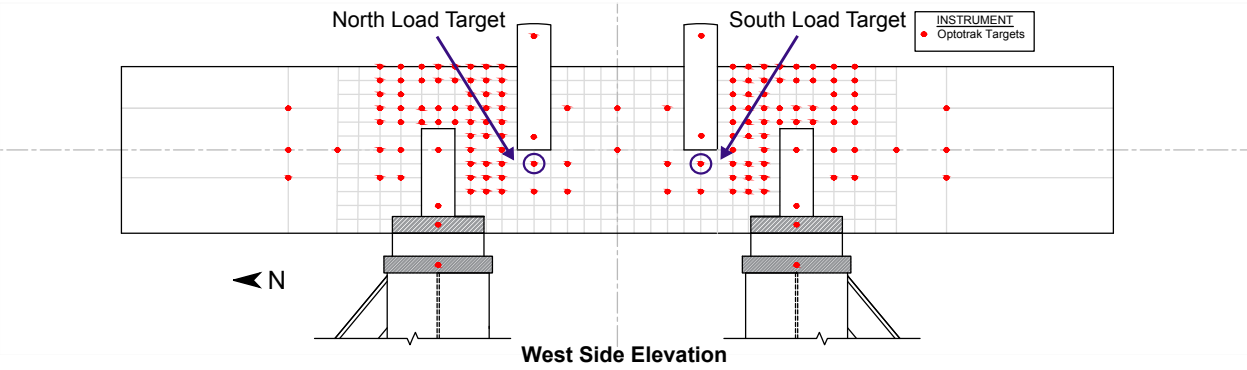



Figure C.1: Illustration of Targets used for Deflection in Force-Displacement Plots in Chapter 3 (as demonstrated by the Optotrak layout for a/D = 0.375)

Table C.1: Summary of Targets used for Force-Deflection Plots in Chapters 3, 4, and Appendix D

| Specimen | Failure Mode | Failure Side | Target Location |
|---|---|---|---|
| 1 | Flexure | N/A | N load |
| 2 | Flexure | N/A | S load |
| 5 | Flexure | N/A | N load |
| 8 | Shear | South | S load |
| 9 | Bond | South | S load |
| 10 | Flex-Shear | South | S load |
| 11 | Bond | South | S load |
| 13 | Flex-Shear | South | S load |
| 14 | Shear | North | N load |
| 16 | Flex-Shear | North | N load |
| 17 | Flexure | N/A | N load |
| 21 | Shear | South | S load |

## *C.2 Optotrak Data Correction*

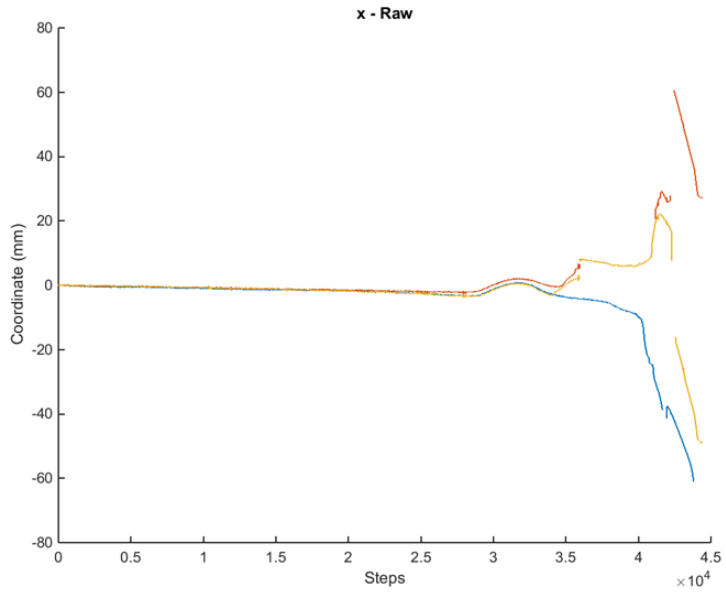
It was desired as part of this thesis to use the data collected from the NDI Optotrak Certus system for more accurate vertical CFST deflection determination and possibly detailed strain analysis of the experiments. While the strain analysis did not provide conducive results, the Optotrak data was used for all experimental deflection behaviors reported in this thesis. Before using though, the recorded data required filtering and correction due to apparent anomalies found in the raw data. Erroneous behaviors in the collected data could have been caused by multiple things. For example, the LED targets are susceptible to err when exposed to both bright light and/or changes in lighting. The testing performed at UW was done in a facility with high exposed windows and throughout the day the movement of the sun affected the data at times. Additionally, the cameras used to capture the movement of the LEDs were very sensitive to vibrations, that could have come from the mechanical equipment or lab assistant movements through the experiments. These and other unknown behaviors

created data that often contained random spikes, plateaus, and gaps. The following passages demonstrate these behaviors and how they were adjusted using a developed MATLAB script for use in this thesis.

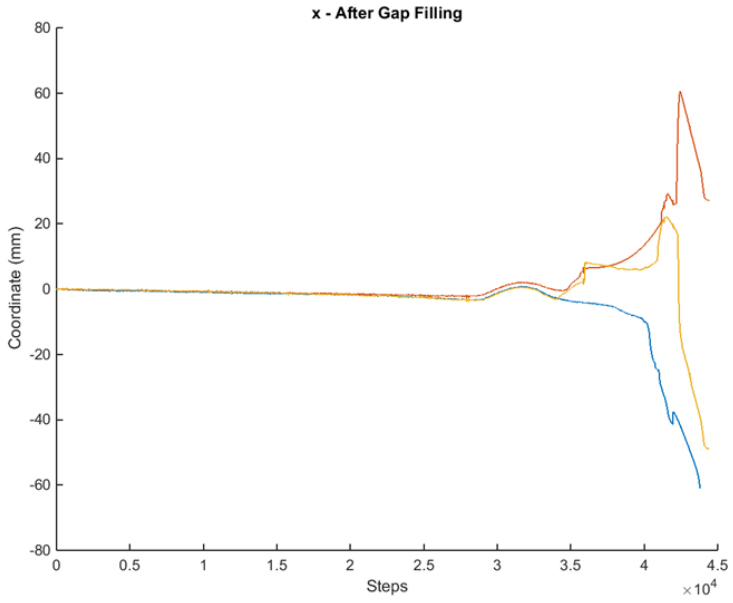
### *C.2.1 Step 1: Fill Gaps*

Frequently, small gaps in collected coordinate data were found, as shown in Figure C.2a. To remedy this, the MATLAB script used the 'pchip' function for interpolation to fill in the missing data. The 'pchip' function is a "Piecewise Cubic Hermite Interpolating Polynomial" that finds values at intermediate points that preserves the shape of the original data while maintaining monotonic behaviors. The result is a fit polynomial that not overshoot and produces less oscillation, when compared to other fitting functions like 'spline.' The function takes a specified number of data points from either side of a specified range in order to interpolate and create a continuous path. Typically, 50 data points was used, but could be changed as the user felt necessary for a given raw data set.

Before using 'pchip' though, MATLAB had to identify the blocks of missing data appropriately. This was done in two steps. First, 'NaN' groups were identified. Each coordinate of each target was checked for 'NaN' values ("Not a Number") at each step of the data collection. This output which steps had missing values. 'SplitVec' then organized these steps into groups, specifying the starting and ending step of consecutive 'NaN' values. Next, the 'NaN' groups were organized by where they occurred within the total collection time. Based on when these gaps occurred the 'pchip' interpolation needed to be adjusted. For example, if the gap was only 20 steps into the data collection period, the 50 point data range before the start of the gap would not work. So, a series of 'if' statements identified these location types. The methods of finding and how to handle each type are shown in the provided code at the end of this section. Figure C.2 shows a sample of three sets of x-coordinate data where this code was used.




(a) Before Correction

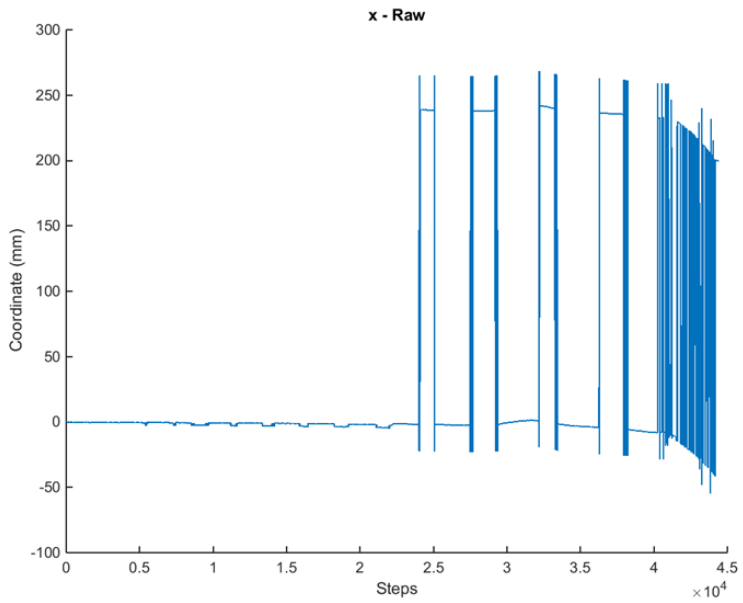



(b) After Correction

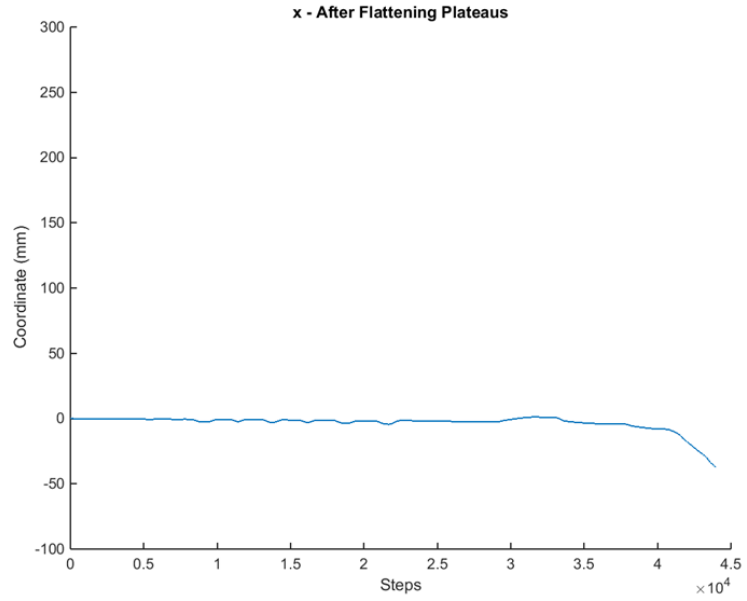
Figure C.2: Sample Correction for Gaps in Raw Data

### *C.2.2 Step 2: Smooth Spikes and Plateaus*

In order to flatten and smooth spikes and plateaus found in the raw Optotrak data, each of the three coordinates for a given target were adjusted separately. The developed code would search for instances where the coordinate value changed between steps by more than a specified percent limit. This limit would sometimes need to be iterated by the user until an acceptable fit was made. If this limit was exceeded, the code would replace the second data point with the first, so that the value remained constant across the two steps. After looping through each coordinate of each target across all steps of time, a moving average was used, with a window of 500 points, to smooth the data. The results of this adjustment are illustrated in Figure C.3.




(a) Before Correction

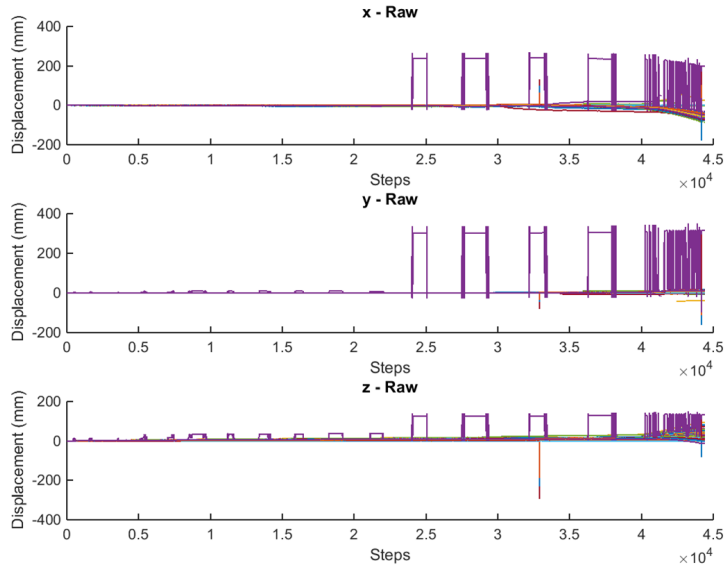



(b) After Correction

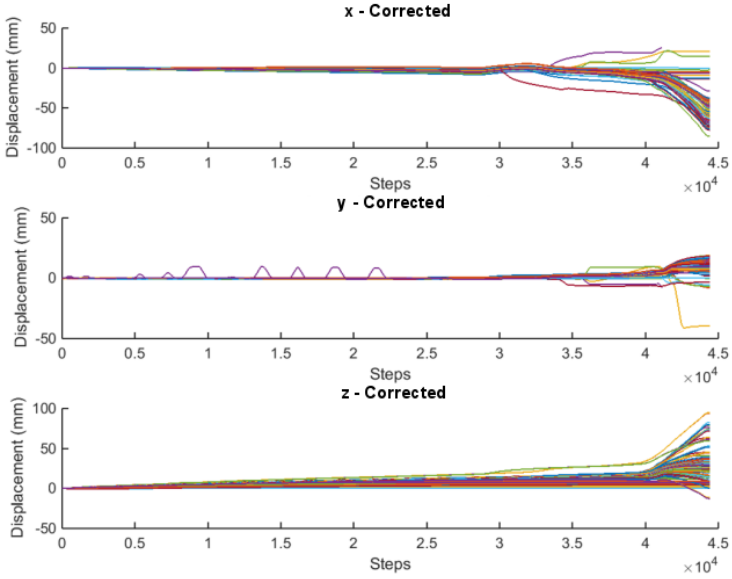
Figure C.3: Sample Correction for Spikes and Plateaus in Raw Data

### *C.2.3 Filtering Results*

A sample of completed filtering results for one experimental data set is shown in Figure C.4. The complete MATLAB script described here is also provided after this figure. Although all erroneous behavior was not corrected with this code, a significant amount was successfully altered. For this reason, before using any particular target's data in subsequent analyses, the data was plotted and assessed to ensure its use was justified for a given application.




(a) Before Correction




(b) After Correction

Figure C.4: Sample of Data after Complete Data Filtering

### *C.2.4 MATLAB Script*

```
close all; clear all; clc; tic;

%% FILTER/CORRECT OPTOTRACK DATA %%
% NOTE: 1. This file must be run before using for any calculations or plotting
%       with the optotrack targets.
%       2. Before running this file, one must adjust the raw Optotrack data
%       file. First, open the data in Excel, delete the first 4 rows, save
%       as .txt file, open in Notepad, and finally, save as 'file.'
%       3. This script works to fill in gaps in data (see NaN in raw data)
%       and to correct plateaus and spikes in data due to possible
%       light reflection on targets, cameras being tapped, or any other
%       disruptions to the data collection during testing.
%
%       4. OUTPUT: Opto_SXX_Fixed.txt - 2D matrix with x,y,z coordinates in
%       original/nonadjusted coordinates
%       example header: Frame   Marker1x   Marker1y    Marker1z   Marker2x...

%% INPUTS %%
OptoName = 'Opto_2_b';

num_targs = 144;
chan_O = 3*num_targs;
rawchan_O = chan_O+1;
delim_O = '\t';

%% LOAD RAW DATA %%
display('Processing Optotrak.......');
fid_O = fopen(OptoName);

% Get Optotrack Headers
O = repmat('%s ',1,rawchan_O);
headerline_O = fgetl(fid_O);
rawheaders_O = textscan(headerline_O, O,'Delimiter',delim_O);
headers_O = (rawheaders_O(:,1:rawchan_O));

% Fix Optotrak Headers
B = {'[+]' '[-]' '[\s]' '[_]';'pos' 'neg' '' ''};

for j = 1:chan_O+1
    correctedHeaders_O(j) = regexprep(headers_O{j}(:),B(1,1),B(2,1));
```

```
    correctedHeaders1_O(j) = regexprep(correctedHeaders_O(j),B(1,2),B(2,2));
    correctedHeaders2_O(j) = regexprep(correctedHeaders1_O(j),B(1,3),B(2,3));
    correctedHeaders3_O(j) = regexprep(correctedHeaders2_O(j),B(1,4),B(2,4));
end

headers_O = correctedHeaders3_O;

% Get Optotrack Data
dataTypeO = strcat(repmat('%f ',1,rawchan_O));
rawOptoData = textscan(fid_O,dataTypeO,'Delimiter',delim_O,'HeaderLines',O);
OptoData = rawOptoData(:,1:rawchan_O);
fclose(fid_O);

%% Create Optotrack Matrix %%
Opto_FullRaw = cell2mat(OptoData);

num_targs = (size(Opto_FullRaw,2)-1)/3

num_steps = size(Opto_FullRaw,1);

%% Remove NaN Columns %% -
% not all 144 targets plugged in were used, so this section removes those...
% targets from the data to be used to save on computation time
count_indexnan = 0;
for i = 1:size(Opto_FullRaw,2)
    if all(isnan(Opto_FullRaw(:,i)))==1
        count_indexnan = count_indexnan+1;
        index_nan(count_indexnan) = i;
    end
end

count_again = 0;
for i = 1:length(headers_O)
    for j = 1:length(index_nan)
        if i == index_nan(j)
            headers_O{i} = [];
        end
    end
end

headers_O(cellfun(@(headers_O) isempty(headers_O),headers_O))=[];
```

```
Opto_FullRaw(:,all(isnan(Opto_FullRaw),1))=[];

num_targs = (size(Opto_FullRaw,2)-1)/3

remove_index = input('Check for mostly NaN columns - input as vector here, from largest to smallest')
% example: remove_index = [244 243 242 172 171 170];

for i = 1:length(remove_index)
    headers_O{remove_index(i)} = [];
    Opto_FullRaw(:,remove_index(i)) = [];
end

headers_O(cellfun(@(headers_O) isempty(headers_O),headers_O))=[];

num_targs = (size(Opto_FullRaw,2)-1)/3

%% Scatter Plot Raw Data Initial Locations %%
figure()

for i = 1
   for j = 2:3:size(Opto_FullRaw,2)
       scatter3(Opto_FullRaw(i,j),Opto_FullRaw(i,j+1),Opto_FullRaw(i,j+2), 'filled'), hold on
       text(Opto_FullRaw(i,j),Opto_FullRaw(i,j+1),Opto_FullRaw(i,j+2),num2str(((j-2)/3)+1));
   end
   hold off

   axis equal
   view(225,33)
   xlabel('x') % x-axis label
   ylabel('y') % y-axis label
   zlabel('z') % z-axis label
   title('Specimen Optotrack Layout')
end

%% Plot Data before filter for target jumps %%
figure()
subplot(3,1,1)
hold on
for i = 2:3:size(Opto_FullRaw,2)
    plot(1:num_steps, Opto_FullRaw(:,i)-Opto_FullRaw(1,i), 'DisplayName', num2str(i))
end
xlabel('Steps')
```

```
ylabel('Displacement (mm)')
title('x - Raw')

subplot(3,1,2)
hold on
for i = 3:3:size(Opto_FullRaw,2)
    plot(1:num_steps, Opto_FullRaw(:,i)-Opto_FullRaw(1,i), 'DisplayName', num2str(i))
end
xlabel('Steps')
ylabel('Displacement (mm)')
title('y - Raw')

subplot(3,1,3)
hold on
for i = 4:3:size(Opto_FullRaw,2)
    plot(1:num_steps, Opto_FullRaw(:,i)-Opto_FullRaw(1,i), 'DisplayName', num2str(i))
end
xlabel('Steps')
ylabel('Displacement (mm)')
title('z - Raw')
print('Specimen2_OptoRaw(1)','-dpng')

%% Filter for Target Gaps %%
Opto_Raw = Opto_FullRaw;

display('Fix Target Gaps.....')

% find and fix gaps in data
countNaN = 0;
for k = 2:size(Opto_FullRaw,2)
   for i = 1:num_steps
        if isnan(Opto_Raw(i,k)) == 1
            countNaN = countNaN+1;
            Opto_RawNaN(countNaN,:) = [i k];
        end
   end
end

Opto_RawNaNSplitStart = SplitVec(Opto_RawNaN,'consecutive','firstval');
Opto_RawNaNSplitEnd = SplitVec(Opto_RawNaN,'consecutive','lastval');
Opto_RawNaNSplit = [Opto_RawNaNSplitStart(:,1) Opto_RawNaNSplitEnd(:,1) Opto_RawNaNSplitStart(:,2)];
```

```
NaNtargs = unique(Opto_RawNaNSplit(:,3));

pchip_range = 50;

for i = 1:size(Opto_RawNaNSplit,1)
    %if NaNs seen at all steps, create column of zeros
    if Opto_RawNaNSplit(i,1)==1 && Opto_RawNaNSplit(i,2)==num_steps
        Opto_Raw(:,Opto_RawNaNSplit(i,3))=0;
    else
        %if only see NaN at single step, then use value of previous step at NaN step
        if Opto_RawNaNSplit(i,1)==Opto_RawNaNSplit(i,2)
                Opto_Raw(Opto_RawNaNSplit(i,1),Opto_RawNaNSplit(i,3)) = Opto_Raw(Opto_RawNaNSplit(i,1)-1,...
                Opto_RawNaNSplit(i,3));
        else
            %if range of NaNs ends at final step - keep range at NaNs
            if Opto_RawNaNSplit(i,1)~=1 && Opto_RawNaNSplit(i,2)==num_steps
                Opto_Raw(Opto_RawNaNSplit(i,1):1:Opto_RawNaNSplit(i,2),Opto_RawNaNSplit(i,3)) =...
                Opto_Raw(Opto_RawNaNSplit(i,1):1:Opto_RawNaNSplit(i,2),Opto_RawNaNSplit(i,3));
            else
                %if NaNs do not end at final step and NaN range within range +/- pchip_range,use pchip
                if Opto_RawNaNSplit(i,2)~=num_steps && Opto_RawNaNSplit(i,2)+pchip_range<num_steps &&...
                   Opto_RawNaNSplit(i,1)-pchip_range>0
                     Opto_Raw(Opto_RawNaNSplit(i,1)-pchip_range:1:Opto_RawNaNSplit(i,2)+pchip_range,...
                     Opto_RawNaNSplit(i,3)) = pchip(1:num_steps,Opto_Raw(:,Opto_RawNaNSplit(i,3)),...
                     Opto_RawNaNSplit(i,1)-pchip_range:1:Opto_RawNaNSplit(i,2)+pchip_range);
                else
                    %if NaNs do not end at at final step, but lower end less than 0 when use pchip_range
                    if Opto_RawNaNSplit(i,2)~=num_steps && Opto_RawNaNSplit(i,2)+pchip_range<num_steps...
                       && Opto_RawNaNSplit(i,1)-pchip_range<0
                         Opto_Raw(1:1:Opto_RawNaNSplit(i,2)+pchip_range,Opto_RawNaNSplit(i,3)) = ...
                         pchip(1:num_steps,Opto_Raw(:,Opto_RawNaNSplit(i,3)),1:1:Opto_RawNaNSplit(i,2)...
                         +pchip_range);
                    else
                        %if NaNs do not end at at final step, but upper end with pchip_range would go...
                        %beyond num_steps
                        if Opto_RawNaNSplit(i,2)~=num_steps && Opto_RawNaNSplit(i,2)+pchip_range>...
                           num_steps && Opto_RawNaNSplit(i,1)-pchip_range>0
                             Opto_Raw(Opto_RawNaNSplit(i,1)-pchip_range:1:num_steps,Opto_RawNaNSplit(i,3))...
                             = pchip(1:num_steps,Opto_Raw(:,Opto_RawNaNSplit(i,3)),Opto_RawNaNSplit(i,1)-...
                             pchip_range:1:num_steps);
                        else
end end end end end end end
```

```
%% Filter for Target Spikes and Plateaus %%
display('Filter Target Spikes/Plateaus........')

% Method: if x,y,and z coordinates (checked separately) change between
% steps by more than plimit of the first value (percentage limit defined),...
% use the coordinate of the first step

% adjust x coordinate
plimitx = 0.01;

countfx = 0;
for i = 2:num_steps
    for k = 2:3:size(Opto_FullRaw,2)
        percentdiff(i,1) = abs((Opto_Raw(i,k)-Opto_Raw(i-1,k))/Opto_Raw(i,k));
        if percentdiff(i,1) > plimitx
            countfx = countfx+1;
            Opto_Raw(i,k) = Opto_Raw(i-1,k);
        else
        end
    end
end

% adjust y coordinate
plimity = 0.02;

countfy = 0;
for i = 2:num_steps
    for k = 3:3:size(Opto_FullRaw,2)
        percentdiff(i,2) = abs((Opto_Raw(i,k)-Opto_Raw(i-1,k))/Opto_Raw(i,k));
        if percentdiff(i,2) > plimity
            countfy = countfy+1;
            Opto_Raw(i,k) = Opto_Raw(i-1,k);
        else
        end
    end
end

% adjust z coordinate
plimitz = 0.01;

countfz = 0;
```

```
for i = 2:num_steps
    for k = 4:3:size(Opto_FullRaw,2)
        percentdiff(i,3) = abs((Opto_Raw(i,k)-Opto_Raw(i-1,k))/Opto_Raw(i,k));
        if percentdiff(i,3) > plimitz
            countfz = countfz+1;
            Opto_Raw(i,k) = Opto_Raw(i-1,k);
        else
        end
    end
end

% smooth data using a moving average
display('Smoothing Data......')
window = 500;

for k = 2:size(Opto_FullRaw,2)
    Opto_RawS(:,k) = movingmean(Opto_Raw(:,k),window,1,1);
end

Opto_RawS(:,1) = Opto_Raw(:,1);

%% Save OptoData to use in Main.m script %%
varA = headers_O; % cell array of strings that will be the column headers for the table
varB = Opto_RawS; % matrix of values to fill in the table columns
input = '';
for i = 1:size(varA,2)
    eval([varA{i},' = varB(:,',num2str(i),');']);
    if i < size(varA,2)
        input = [input,varA{i},','];
    else
        input = [input,varA{i}];
    end
end
eval(['myTable = table(',input,');']);
writetable(myTable,'Opto_S2_Fixed.txt','delimiter','\t');

toc;

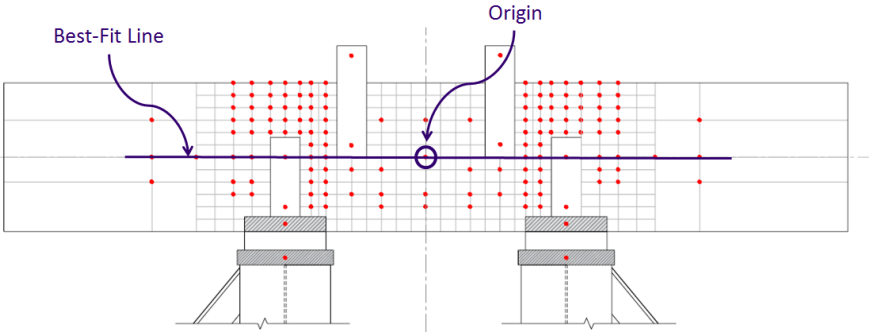
display('DONE')
```

### *C.3 Match Optotrak and LabVIEW Data*

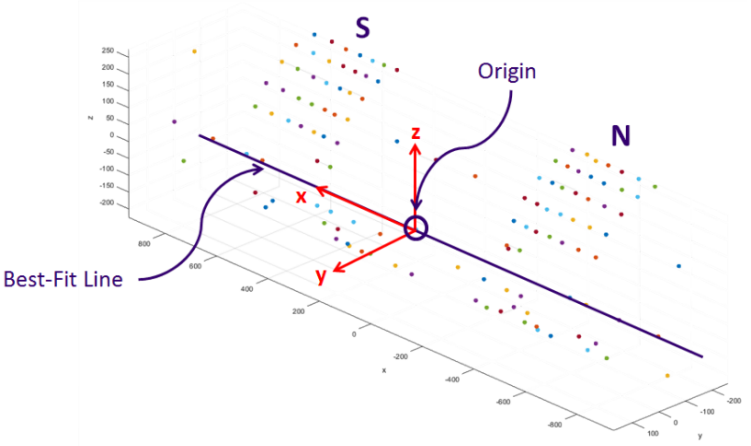
The Baldwin load data used in the analyses presented in this thesis were collected with the LabVIEW system. Although both the Optotrak and LabVIEW systems were set with a data collection rate of 5 $Hz$, there was often some inconsistencies in total steps of data collected between the two. So, in order to relate deflection with the Optotrak system to load with the LabVIEW system, the data needed to be coordinated by time, assuming their start times were exactly the same. This process is as follows:

1. Create time vectors for each data collection system
    - LabVIEW: change 'HH:MM:SS' to total seconds from start of test
    - Optotrak: create time vecto with an increment of 0.2 $sec$ (5 $Hz$)
2. Adjust data sets so that both end at same time, i.e. shop data set with longer time vector to match the shorter
3. Interpolate Optotrak data to match the number of points i n LabVIEW

This adjustment was completed immediately following the Optotrak filtering script above. It was added to the beginning of a script that rotated and translated the Optotrak data so that the origin of the coordinate system was situated midspan of the CFST specimen, as shown in Figure C.5. Only the portion of the script that coordinated the LabVIEW and Optotrak is given following the figure.




(a) Sketch of CFST in test rig with Optotrak layout




(b) Rendering of original target locations in MATLAB

Figure C.5: Illustration of Placement of Optotrak Data Origin for Subsequent Calculations

### *C.3.1 MATLAB Script*

```
close all; clear all; clc; tic;
%% MAIN DATA %%
% NOTE: 1. Must run OptoFilter.m before use of this file.

%% INPUT INFORMATION
%--------------------
SpecimenName = 'Specimen_1_a'; %Raw LabVIEW data file
chan_S = 68;
% fsamp_S = 5; %data sample rate
rawchan_S = chan_S + 7;
delim_S = '\t';
```

```
OptoName = 'Opto_S1_Fixed'; %Filtered Optotrak data file
num_targs = 144; %i.e. dim=433
chan_O = 3*num_targs;
% fsamp_O = 5; %data sample rate
rawchan_O = chan_O+1;
delim_O = '\t';

%% OPEN LABVIEW DATA FILE
%-------------------------
display('Processing Labview.......');
fid_S = fopen(SpecimenName);

% GET LABVIEW HEADERS
%--------------------
S = repmat('%s ',1,rawchan_S);
headerline_S = fgetl(fid_S);
rawheaders_S = textscan(headerline_S, S,'Delimiter',delim_S);
headers_S = (rawheaders_S(:,6:rawchan_S));

%Fix Labview Headers
A = {'[+]' '[-]' '[\s]' '[.]';'pos' 'neg' '' ''};

    for j = 1:chan_S+2
        correctedHeaders_S(j) = regexprep(headers_S{j}(:),A(1,1),A(2,1));
        correctedHeaders1_S(j) = regexprep(correctedHeaders_S(j),A(1,2),A(2,2));
        correctedHeaders2_S(j) = regexprep(correctedHeaders1_S(j),A(1,3),A(2,3));
        correctedHeaders3_S(j) = regexprep(correctedHeaders2_S(j),A(1,4),A(2,4));
    end

    headers_S = correctedHeaders3_S;

% GET LABVIEW DATA
%-----------------
dataTypeS = strcat('%s %s ',repmat('%f ',1,rawchan_S-2));
rawLabviewData = textscan(fid_S,dataTypeS,'Delimiter',delim_S,'HeaderLines',0);
LabviewData = rawLabviewData(:,6:rawchan_S);
LabviewDataClock = rawLabviewData(:,2);
LabviewDataSec = rawLabviewData(:,3);
fclose(fid_S);

%% OPEN OPTOTRAK DATA FILE
%-------------------------
```

```
display('Processing Optotrak.......');
fid_O = fopen(OptoName);

% GET OPTOTRAK HEADERS
%--------------------------
O = repmat('%s ',1,rawchan_O);
headerline_O = fgetl(fid_O);
rawheaders_O = textscan(headerline_O, O,'Delimiter',delim_O);
headers_O = (rawheaders_O(:,1:rawchan_O));

%Fix Optotrak Headers
B = {'[+]' '[-]' '[\s]' '[_]';'pos' 'neg' '' ''};

    for j = 1:chan_O+1
        correctedHeaders_O(j) = regexprep(headers_O{j}(:),B(1,1),B(2,1));
        correctedHeaders1_O(j) = regexprep(correctedHeaders_O(j),B(1,2),B(2,2));
        correctedHeaders2_O(j) = regexprep(correctedHeaders1_O(j),B(1,3),B(2,3));
        correctedHeaders3_O(j) = regexprep(correctedHeaders2_O(j),B(1,4),B(2,4));
    end

headers_O = correctedHeaders3_O;

% GET OPTOTRAK DATA
%---------------------
dataTypeO = strcat(repmat('%f ',1,rawchan_O));
rawOptoData = textscan(fid_O,dataTypeO,'Delimiter',delim_O,'HeaderLines',0);
OptoData = rawOptoData(:,1:rawchan_O);
fclose(fid_O);

%% MATCH LABVIEW AND OPTOTRAK DATA POINTS
%-----------------------------------------
display('Interpolating Data.......');

L_S = length(LabviewData{1,1}); %length of Optotrak data
L_O = length(OptoData{1,1}); %length of LabVIEW data

% modify time stamp in LabVIEW raw data for matching
LabviewDataClock_sep1 = datestr(LabviewDataClock{1,1},13);
LabviewDataClock_sep2 = datevec(LabviewDataClock_sep1);
LabviewDataClock_sep = LabviewDataClock_sep2(:,4:6);
LabviewDataClock_sep(:,3) = LabviewDataSec{1,1};
```

```
LabviewData_startTime = (3600*LabviewDataClock_sep(1,1))+(60*LabviewDataClock_sep(1,2))+...
LabviewDataClock_sep(1,3);

for i = 1:size(LabviewDataClock_sep,1)
    LabviewDataTime(i,1) = ((3600*LabviewDataClock_sep(i,1))+(60*LabviewDataClock_sep(i,2))+...
    LabviewDataClock_sep(i,3))-LabviewData_startTime;
end

%create time vector for Optotrak (not time step provided with raw data)
OptoDataTime = transpose(0:0.2:(L_O-1)*0.2);

% make data stop at same point in time
if OptoDataTime(end) >= LabviewDataTime(end)
    index_tend = find(OptoDataTime-LabviewDataTime(end)>0);
    OptoDataTime = OptoDataTime(1:index_tend(1)-1,1);
    for i = 1: size(OptoData,2)
        OptoData{1,i} = OptoData{1,i}(1:length(OptoDataTime),1);
    end
else
    index_tend = find(LabviewDataTime-OptoDataTime(end)>0);
    LabviewDataTime = LabviewDataTime(1:index_tend(1)-1,1);
    for i = 1: size(LabviewData,2)
        LabviewData{1,i} = LabviewData{1,i}(1:length(LabviewDataTime),1);
    end
end

% interpolate OptoData to match number of points in LabVIEW (match to
% LabVIEW because do not want to create force, would rather interpolate
% displacements in Optotrak data
L_S = length(LabviewData{1,1});
L_O = length(OptoData{1,1});

figure()
hold on
for i = 2:3:3*num_targs
plot(1:L_O,OptoData{1,i}(:,1)-OptoData{1,i}(1,1),'DisplayName', num2str(i))
xlabel('Steps')
title('OptoData Before Interpolation')
end

if L_O >= L_S
    z = 1:L_O/L_S:L_O;
```

```
    for i = 1 : size(OptoData,2)
        OptoData_r{1,i}(:,1) = interp1(OptoData{1,i}(:,1),z);
        i = i + 1;
    end
else
    z = 1:L_S/L_O:L_S;
    for i = 1 : size(OptoData,2)
        OptoData_r{1,i}(:,1) = interp1(OptoData{1,i}(:,1),z);
        i = i + 1;
    end
end
L_O_r = length(OptoData_r{1,1});

figure()
hold on
for i = 2:3:3*num_targs
% plot(1:L_S,LabviewData{1,i}(:,1),'x-')
plot(1:L_S,OptoData_r{1,i}(:,1)-OptoData_r{1,i}(1,1),'DisplayName', num2str(i))
xlabel('Steps')
title('OptoData After Interpolation')
end

figure()
hold on
for i = 2:3:3*num_targs
% plot(LabviewDataTime,LabviewData{1,i}(:,1),'x-')
plot(LabviewDataTime,OptoData_r{1,i}(:,1)-OptoData_r{1,i}(1,1),'DisplayName', num2str(i))
xlabel('Time (sec)')
title('OptoData After Interpolation')
end

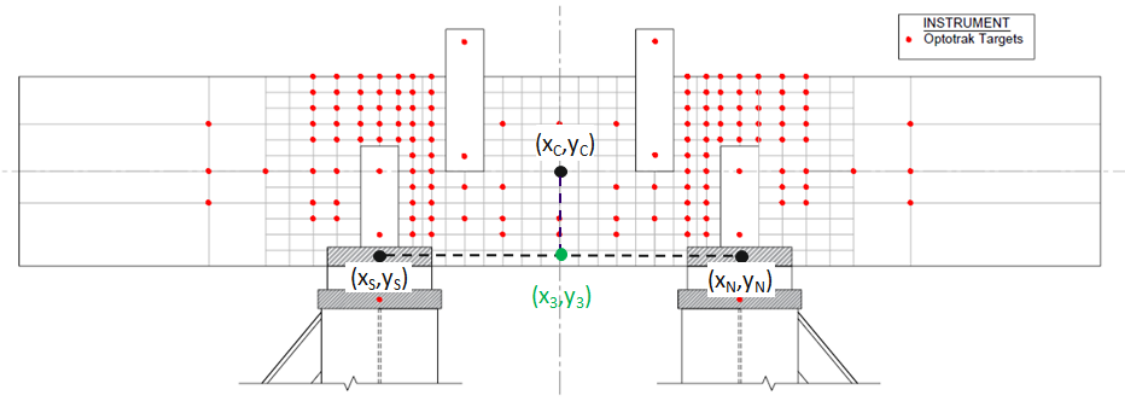
%Check plots for correct interpolation of data
```

## *C.4 CFST Deflection Correction Procedure*

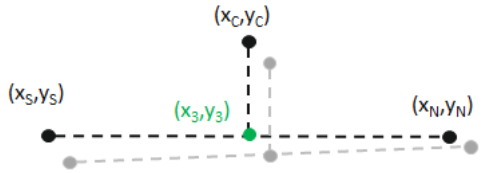
In order to appropriately report the CFST specimen deflection, it needs to be separated from the total deformation of the system captured in the raw Optotrak data. The total deformation includes the displacement of the steel base, elastomeric bearings, and cotton duck. The exact procedure used in this thesis is as described here, with the actual script

provided below. It follows closely in theory to that used in Maki (2015), with only some changes to calculation approach. Nevertheless, the corrected results closely matched those in the previous thesis. The correction occurs in two part. These procedures were created with the given instrumentation, and are definitely not perfected, but did ultimately provide reasonable estimates for global behavior.

The first part corrects for elastomeric bearing and steel base deflections. Because the bearings and steel base are located farther out from the midspan of the specimen than the targets used for deflection reporting and the deflections at each end of the specimen were often asymmetric, a linear relationship estimating the isolated specimen deflection at a given point between the center of each bearing was developed. When the displacement for the CFST was calculated as it relates to this line, rather than the global vertical axis, the deflections below this line, elastomeirc bearing and steel base, were essentially removed. An illustration of this procedure for the midspan deflection calculation, and accompanying equations, is given in Figure C.6 and Equation C.1, with $Disp_i$ being the midspan displacement at time step $i$ corrected for bearing and base deflecitons..




(a) Targets used as they relate to the test setup




(b) Movement of targets as they relate to the linear

Figure C.6: Illustration of Procedure for Elastomeric Bearing and Steel Base Correction (as demonstrated by the Optotrak layout for a/D = 0.25)

$$Solve\ for\ y_3: \quad \frac{y_3 - y_S}{x_3 - x_S} = \frac{y_N - y_S}{x_N - x_S} \tag{C.1a}$$

$$Disp_i = (y_{Ci} - y_{3i}) - (y_{C1} - y_{31})$$

$$where: \ i \ = \ current\ step\ and\ 1 \ = \ initial\ step \tag{C.1b}$$

The cotton duck deflection was then extracted from the CFST deflection by averaging the calculated deflection of the North and South support cotton duck pads and subtracting it from the new $Disp_i$ in Equation C.1. The cotton duck deflection at each support was estimated using a target on the support cradle and then just above the support cradle on the CFST itself. The difference in deflection of these two then roughly represented the amount of deflection seen in the cotton duck. An issue with this approach is the potential for rotation of the CFST out of the support cradle. However, the cotton duck typically completely tore before reaching significant rotations and by capping the cotton duck deflection calculation to 0.5 *in.*, the original thickness of the pad, this conflict was not present. The developed code and an illustration of the targets used for this correction procedure are provided in the next passage.

### *C.4.1 MATLAB Script*

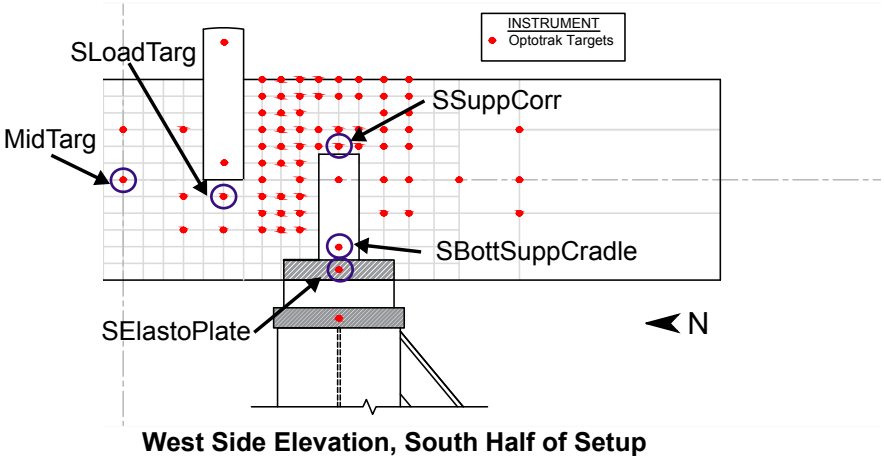



Figure C.7: Illustration of Targets used for CFST Deflection Correction in MATLAB Script (as demonstrated by the Optotrak layout for a/D = 0.375)

```
close all, clear all, clc, tic;

%% INPUTS %%
SpecimenData = 'Specimen_1_a.mat';
%MATLAB structure created with optotrak rotation and translation script

%% LOAD DATA %%
load(SpecimenData)

NDIxyzR = Data_S1.Optotrak.NDIxyzR;

num_targs = size(NDIxyzR,1);

num_steps = size(NDIxyzR,3);

%% 3D SCATTER PLOT FOR INITIAL TARGET NUMBER CHECK BELOW %%
figure()
for i = 1
   for j = 1:num_targs
       scatter3(NDIxyzR(j,1,i),NDIxyzR(j,2,i),NDIxyzR(j,3,i), 'filled'), hold on
       text(NDIxyzR(j,1,i),NDIxyzR(j,2,i),NDIxyzR(j,3,i),num2str(j)); %display target number
   end
```

```
   hold off

   axis equal
   view(225,33)
   xlabel('x') % x-axis label
   ylabel('y') % y-axis label
   zlabel('z') % z-axis label
end

%% DEFINE VARIABLES %%
BWLoad = Data_S1.Labview.BW2400kips; %LabVIEW Baldwin Data

input_targs = input('Check 3D Scatter Plot for Target Numbers. (Type "1" when complete.)')

MidTarg = 69;

NBottSuppCradle = 14;
NSuppCorr = 12;

SBottSuppCradle = 130;
SSuppCorr = 128;

NElastoPlate = 15;
SElastoPlate = 131;

NLoadTarg = 62;
SLoadTarg = 78;

for i = 1:num_steps %displacements
    NSuppCradle_z(i) = squeeze(NDIxyzR(NBottSuppCradle,3,i)-NDIxyzR(NBottSuppCradle,3,1));
    SSuppCradle_z(i) = squeeze(NDIxyzR(SBottSuppCradle,3,i)-NDIxyzR(SBottSuppCradle,3,1));

    NElastoVert(i) = squeeze(NDIxyzR(NElastoPlate,3,i)-NDIxyzR(NElastoPlate,3,1));
    SElastoVert(i) = squeeze(NDIxyzR(SElastoPlate,3,i)-NDIxyzR(SElastoPlate,3,1));
end

%% PLOT CURRENT 3D SCATTER DATA %%
for i = 1
   for j = 1:num_targs
       scatter3(NDIxyzR(j,1,i),NDIxyzR(j,2,i),NDIxyzR(j,3,i), 'filled'), hold on
       text(NDIxyzR(j,1,i),NDIxyzR(j,2,i),NDIxyzR(j,3,i),num2str(j));
   end
```

```
   hold off

   axis equal
   view(225,33)
% view(0,0)
   xlabel('x') % x-axis label
   ylabel('y') % y-axis label
   zlabel('z') % z-axis label
   title('Specimen Optotrack Layout')
end

%% OPTITRAK DISP CALCS OF SETUP PARTS %%
for i = 1:num_steps
    Disp_NSuppDuck(i) = min(0.5*25.4,NSuppCradle_z(i) - (NDIxyzR(NSuppCorr,3,i) - NDIxyzR(NSuppCorr,3,1)));
    Disp_SSuppDuck(i) = min(0.5*25.4,SSuppCradle_z(i) - (NDIxyzR(SSuppCorr,3,i) - NDIxyzR(SSuppCorr,3,1)));
    Disp_avgSuppDuck(i) = 0.5*(Disp_NSuppDuck(i)+Disp_SSuppDuck(i));
end

figure()
hold on
plot(1:num_steps,Disp_NSuppDuck,'--r')
plot(1:num_steps,Disp_SSuppDuck,':')
plot(1:num_steps,Disp_avgSuppDuck,'r')
xlabel('Steps')
ylabel('Vertical Displacement (mm)')
hline(25.4*0.5)
legend('NSuppDuck Disp','SSuppDuck Disp','AvgDuckDisp','location','NW')

%% CORRECT Optitrak Specimen Deflections %%
% deflection at midspan
for i = 1:num_steps
    Disp_uncorr(i) = NDIxyzR(MidTarg,3,i)-NDIxyzR(MidTarg,3,1);
    zcenter_elasto(i) = ((NDIxyzR(MidTarg,1,i)-NDIxyzR(SElastoPlate,1,i))*(NDIxyzR(NElastoPlate,3,i)-...
        NDIxyzR(SElastoPlate,3,i))/(NDIxyzR(NElastoPlate,1,i)-NDIxyzR(SElastoPlate,1,i))) +...
        NDIxyzR(SElastoPlate,3,i);
    Disp(i) = (NDIxyzR(MidTarg,3,i)-zcenter_elasto(i)+Disp_avgSuppDuck(i))-(NDIxyzR(MidTarg,3,1)-...
        zcenter_elasto(1)+Disp_avgSuppDuck(1));
end

figure()
hold on
plot(1:num_steps,Disp_uncorr)
```

```
plot(1:num_steps,Disp)
legend('Uncorrected','Corrected')
xlabel('Steps')
ylabel('Vertical Deflection (mm)')
ylim([-SLoadTarg 10])
title('Midspan Deflection')

%deflection at North load
for i = 1:num_steps
    DispN_uncorr(i) = NDIxyzR(NLoadTarg,3,i)-NDIxyzR(NLoadTarg,3,1);
    zNorth_elasto(i) = ((NDIxyzR(NLoadTarg,1,i)-NDIxyzR(SElastoPlate,1,i))*(NDIxyzR(NElastoPlate,3,i)-...
        NDIxyzR(SElastoPlate,3,i))/(NDIxyzR(NElastoPlate,1,i)-NDIxyzR(SElastoPlate,1,i))) +...
        NDIxyzR(SElastoPlate,3,i);
    DispN(i) = (NDIxyzR(NLoadTarg,3,i)-zNorth_elasto(i)+Disp_avgSuppDuck(i))-(NDIxyzR(NLoadTarg,3,1)-...
        zNorth_elasto(1)+Disp_avgSuppDuck(1));
end

figure()
hold on
plot(1:num_steps,DispN_uncorr)
plot(1:num_steps,DispN)
legend('Uncorrected','Corrected')
xlabel('Steps')
ylabel('Vertical Deflection (mm)')
ylim([-SLoadTarg 10])
title('North Load Deflection')

%deflection at South load
for i = 1:num_steps
    DispS_uncorr(i) = NDIxyzR(SLoadTarg,3,i)-NDIxyzR(SLoadTarg,3,1);
    zSouth_elasto(i) = ((NDIxyzR(SLoadTarg,1,i)-NDIxyzR(SElastoPlate,1,i))*(NDIxyzR(NElastoPlate,3,i)-...
        NDIxyzR(SElastoPlate,3,i))/(NDIxyzR(NElastoPlate,1,i)-NDIxyzR(SElastoPlate,1,i))) +...
        NDIxyzR(SElastoPlate,3,i);
    DispS(i) = (NDIxyzR(SLoadTarg,3,i)-zSouth_elasto(i)+Disp_avgSuppDuck(i))-(NDIxyzR(SLoadTarg,3,1)-..
    zSouth_elasto(1)+Disp_avgSuppDuck(1));
end

figure()
hold on
plot(1:num_steps,DispS_uncorr)
plot(1:num_steps,DispS)
legend('Uncorrected','Corrected')
```

```
xlabel('Steps')
ylabel('Vertical Deflection (mm)')
ylim([-SLoadTarg 10])
title('South Load Deflection')

%% System Behavior Plots %%
figure()
hold on
plot(-1*Disp,BWLoad)
plot(-1*DispN,BWLoad)
plot(-1*DispS,BWLoad)
xlabel('Deflection (mm)')
ylabel('BWLoad (kips)')
ylim([0 max(BWLoad)+100])
xlim([0 max([-1*Disp -1*DispN -1*DispS])+5])
legend('Midspan','North Load','South Load','location','SE')

%% Save Corrected Variables %%
save('Disp.mat','Disp') %displacement at midspan
save('DispN.mat','DispN') %displacement at north load target
save('DispS.mat','DispS') %displacement at south load target

display('DONE')
```

# Appendix D

# FURTHER VALIDATION OF ANALYTICAL MODEL

This appendix presents additional results from the refined base model. These include: shear force-deflection, shear force-relative displacement, and local deformation behaviors. All displacement behaviors shown are normalized by the clear span. $a$. These may serve as further validation of the proposed model. However, the model was largely calibrated for ultimate shear load because of the complexities of the experiments that the model cannot reasonably mimic, and so these relationships are not used for analysis in the parameter studies. The details of the validated specimens can be found in Table D.1. The remaining CFST parameters not noted in the table are: $D = 20\ in.$, $t = 0.25\ in.$, $F_{yt} \approx 50\ ksi$, $P/P_0 = 0\%$, $\rho_{int} = 0\%$, $L_T = 2D$, straight-seam tube, and clean interface condition. Chapter 4 provides additional details of the behaviors in these simulations, including the validated shear force magnitudes in Table 4.7.

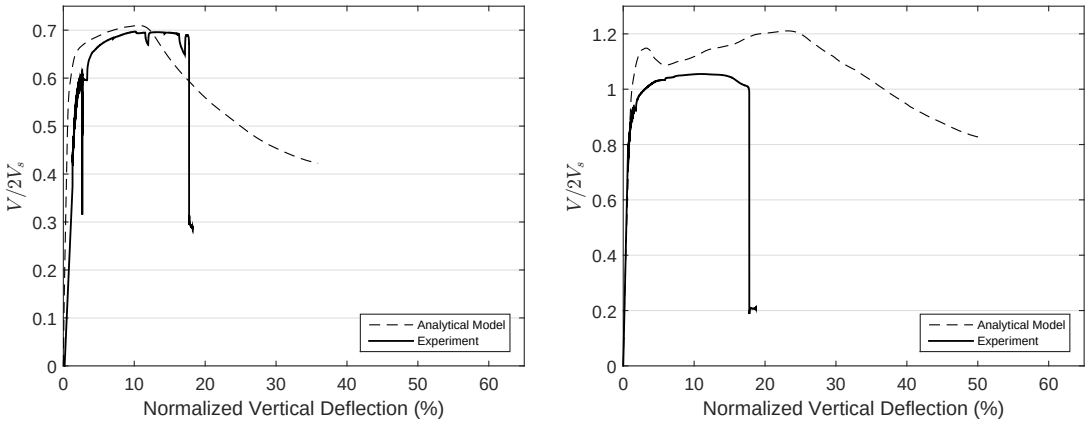
Table D.1: Summary of Specimens used for Analytical Model Validation

| a/D | Specimen | $F_{ytm}$ (ksi) | $f'_{cm}$(ksi) | $V_{exp}$ (kips) | $V_{ed}$ (kips) | $M_{ed}/M_{PSDM}$ | Failure Mode |
|---|---|---|---|---|---|---|---|
| 1.0 | 1 | 49.6 | 6.012 | 322.0 | 322.0 | 1.27 | Flexure |
| 0.5 | 17 | 55.4 | 9.450 | 549.3 | 544.5 | 1.10 | Flexure |
| | 2 | 49.6 | 6.220 | 550.8 | 549.0 | 1.26 | Flexure |
| 0.375 | 16 | 56.8 | 8.609 | 759.2 | 760.5 | 1.24 | Flex-Shear |
| | 10 | 53.9 | 6.151 | 668.9 | 660.0 | 1.16 | Flex-Shear |
| 0.250 | 14 | 55.4 | 8.596 | 874.9 | 788.4 | 1.03 | Shear |

### *D.1 Shear Force vs. Vertical Deflection*

Shear force versus vertical deflection relationships are provided in Figure D.1. Although it has been shown that maximum resistance of shear dominated specimens occurred at smaller deflections than predicted by the model, the plots do show good representation of the initial stiffness, onset of yielding, and reasonable predication of shear capacity seen in the experiments.

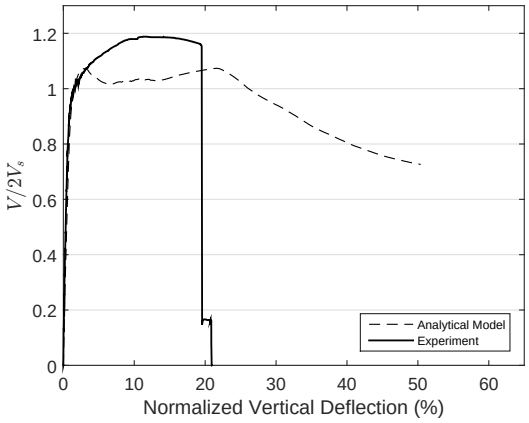
Note that the experimental results generated in this chapter were developed with a different approach than in Maki (2015) and, as a result, may differ slightly. Appendix C describes the methods of data analysis used to create the trends for the experiments. As mentioned in Chapter 4, the shear force in the simulation was taken from the sum of the vertical reactions on the fixed nodes of the "wire" supports in Figure 4.20.



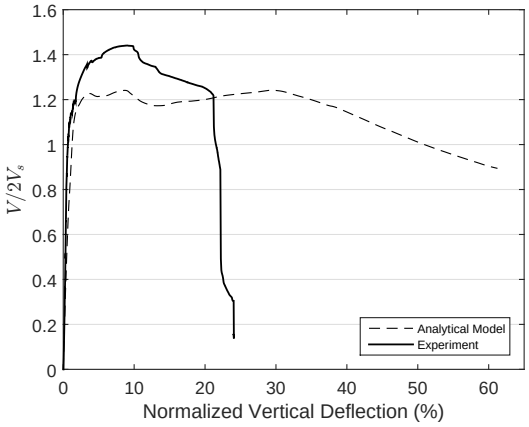

(a) Specimen 1



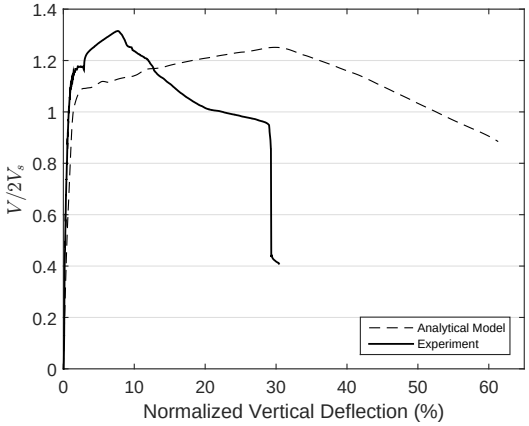

(b) Specimen 17



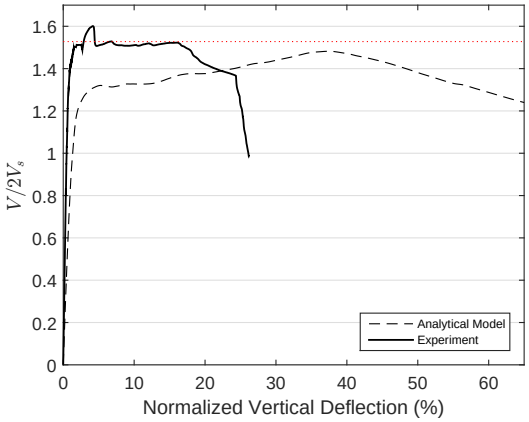

(c) Specimen 2




(d) Specimen 16




(e) Specimen 10

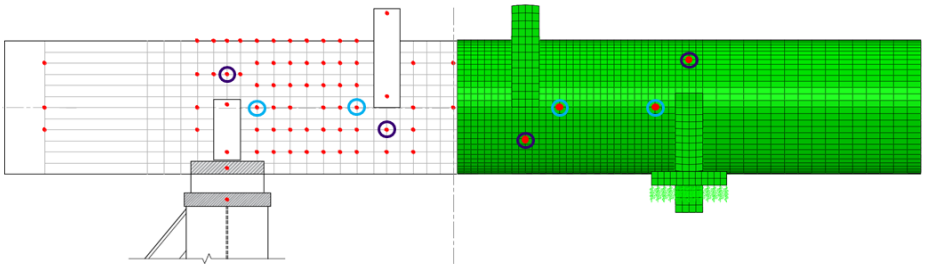



(f) Specimen 14

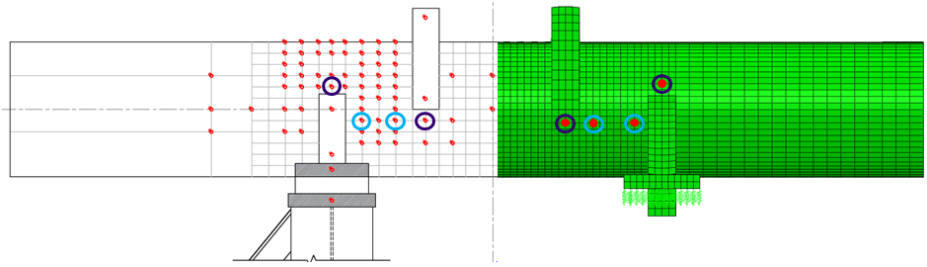
Figure D.1: Measured, $V_{ed}$, and Predicted Normlaized Shear vs. Vertical Deflection

### *D.2 Shear Force vs. Relative Displacement*

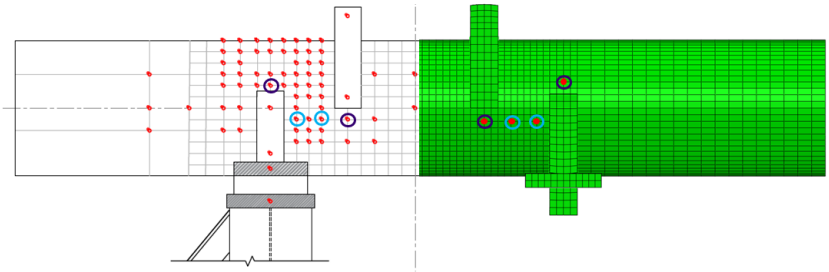
Since the global deformation behaviors are not well represented in the analytical models with shear span to depth ratios of 0.5 and less, the experimental and analytical specimen deformations were analyzed in greater detail. Figure D.2 shows the locations where the displacement comparisons are being made from in the experiment using Optotrak target data (left) and in the model using nodal vertical displacements (right). The two points found within the bounds of the load and support cradles are referenced for "inner" relative displacement calculations and those centered just above and below the cradles are considered for "outer" relative displacement calculations. The shear span used here corresponds to the side used for vertical deflection as shown in Appendix C. Refer to Figure D.3 and Equations D.1 and D.2 for these calculations. With the data from these locations, comparisons of shear force and relative displacements are presented in Figure D.4. This comparison intends to represent a measure of specimen local shear deformation that has better comparison between the experiments and simulations. The simulations show peak resistance occurring at similar relative displacements to the experimental specimens. Additionally, initial stiffness and yielding onset is comparable for most cases. Specimen 14 though experiences severe local deformations and the calculations here are likely directly related to issues with Optotrak instrumentation data collection at this stage. That is, frequently targets in the shear span would fall off the specimen in the presence of substantial local deformation.



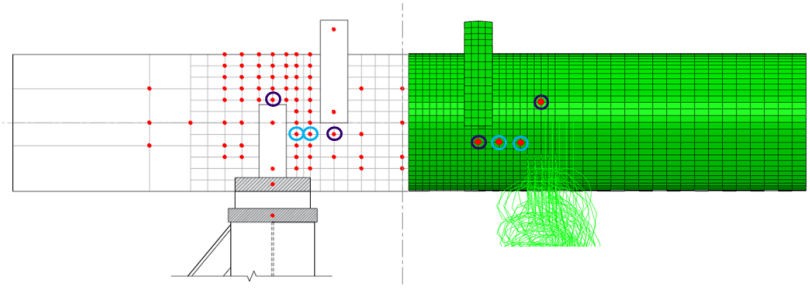
(a) $a/D = 1.00$



(b) $a/D = 0.50$



(c) $a/D = 0.375$



(d) $a/D = 0.250$

Figure D.2: Illustration of Locations of Points for Relative Displacement Calculation in Simulation and Experiments

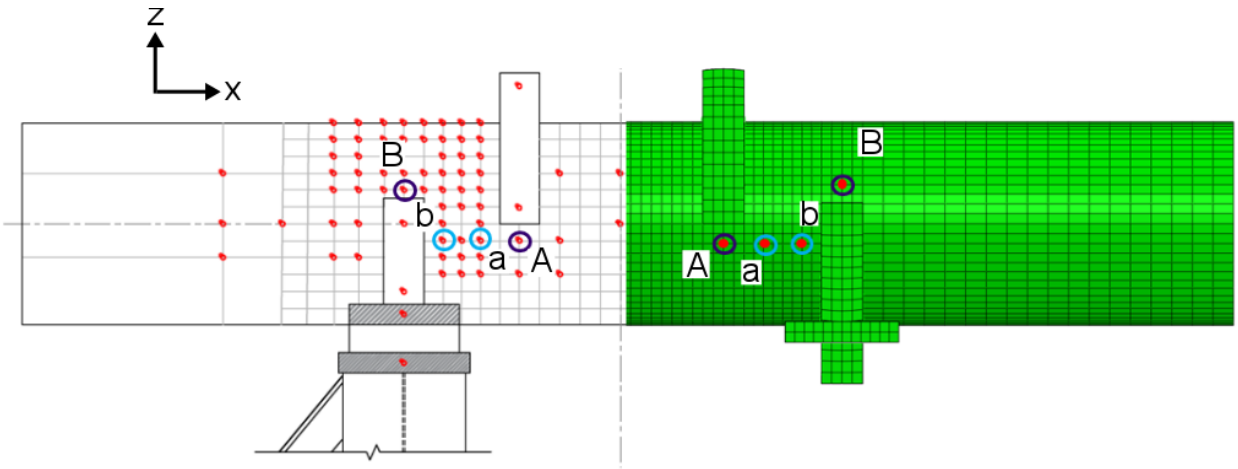



Figure D.3: Illustration of Points used For Calculation in Equations D.1 and D.2

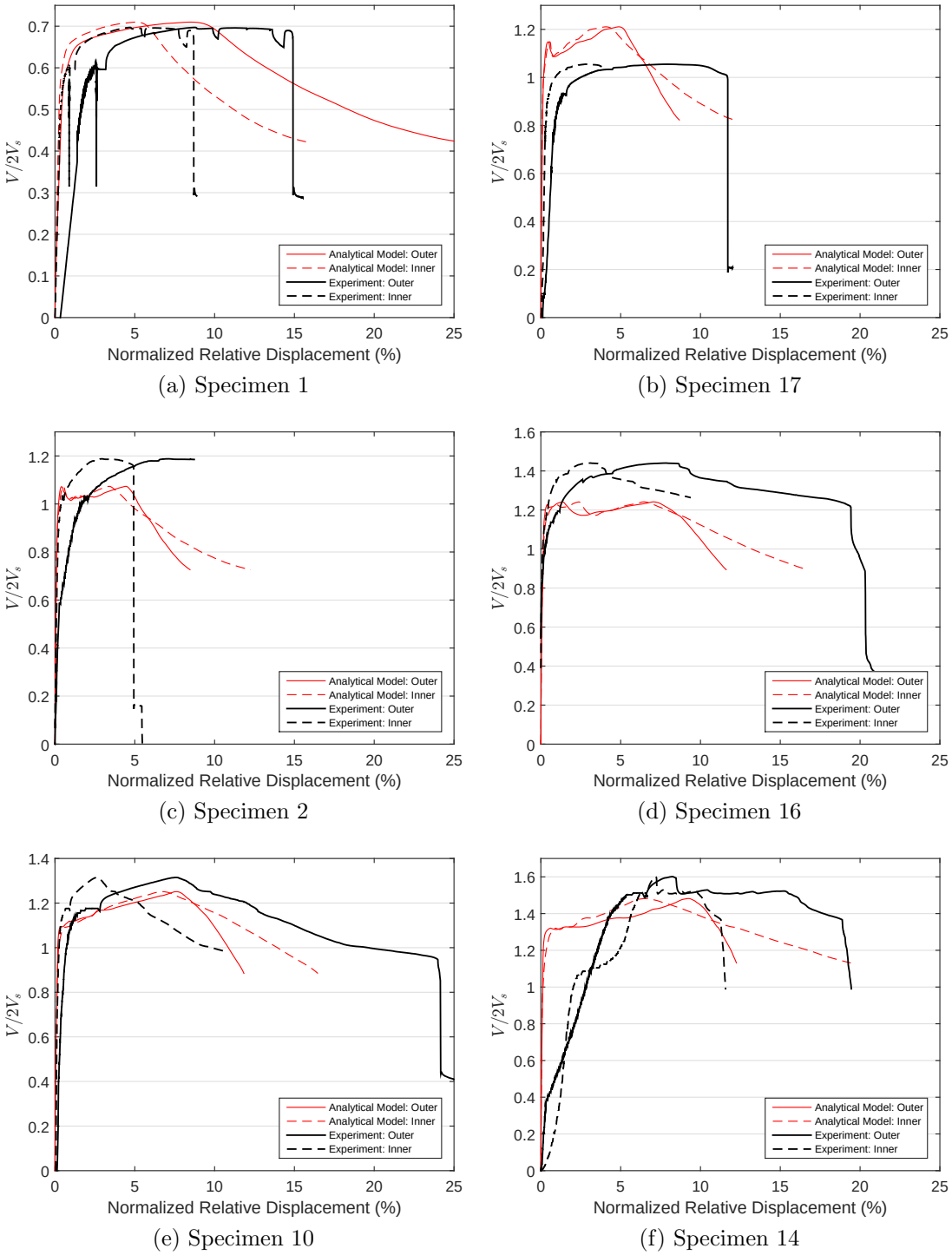
$$\text{Inner Relative Displacement} = Disp_a - Disp_b \tag{D.1a}$$

$$\text{Outer Relative Displacement} = Disp_A - Disp_B \tag{D.1b}$$

where: $Disp_n$ is either the vertical displacement directly exported from ABAQUS or that calculated by Equation D.2 for the experiments

$$Disp_{n(exp)} = z_{ni} - z_{n0} \tag{D.2a}$$

where: $n$ is either point a, b, A, or B; $z_{ni}$ is the z coordinate of point $n$ at a given step $i$; and $z_{n0}$ is the initial z coordinate of point $n$




(a) Specimen 1

(b) Specimen 17

(c) Specimen 2

(d) Specimen 16

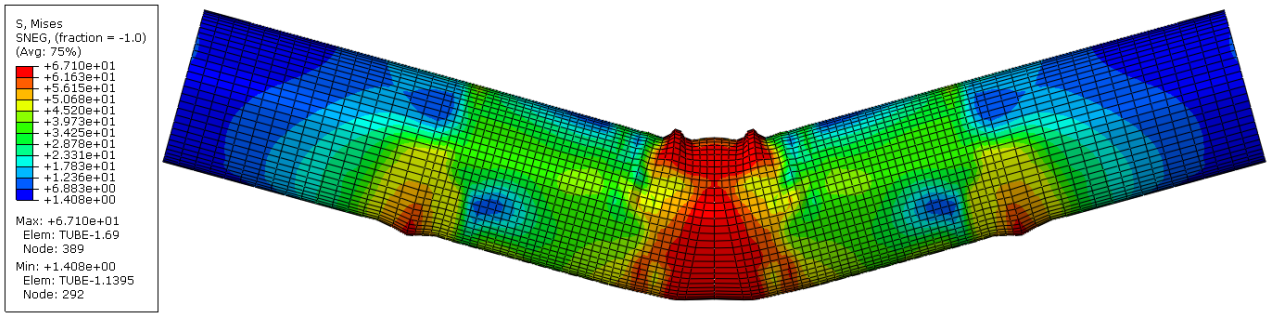
(e) Specimen 10

(f) Specimen 14

Figure D.4: Measured, $V_{ed}$, and Predicted Normalized Shear vs. Relative Displacement

### *D.3 Local Behaviors*

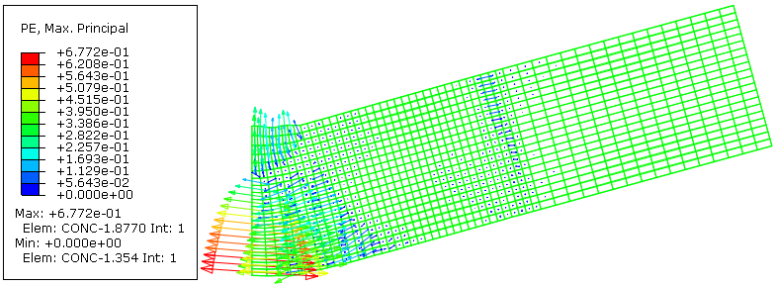
Figures D.5 to D.10 show the observed and predicted tube steel yield distribution and local buckling, and concrete fill cracking patterns for all models, starting with the flexurally dominated shear span ratio of 1.0 and down to the shear dominated ratio of 0.25. Reasonable comparisons are found between the model and experiment. With Specimen 1, a/D = 1.0 (Figure D.5), compression buckling at the top of the tube steel and both tensile and compressive cracking in the concrete, at the bottom and top of the pure moment region respectively, is predicted in the simulation, as expected with a flexurally controlled specimens. With shear influenced Specimens 16, 10, and 14 (Figures D.8 to D.10), elements in the shear span region exhibit severe shear deformations in the tube steel at the face of the load cradle, with extensive diagonal cracking of the concrete in the shear span. On the other hand, Specimens 2 and 17 have a shear span to depth ratio of 0.5 (Figures D.7 to D.6). The experiments showed that specimens with this span often fail in a transition zone between flexural and shear control, and the predictions do not appear to reflect the failure mode observed. That is, the experiments show to behave with more flexural-like behaviors and the model shows more shear-like behaviors. Specimens 16 and 10, on the other hand, appear to enter the observed failure mode, even though they too have shear span to depth ratio definitions that frequently fell into the flexure-shear zone of behavior. This is trend also noted with the shear resistance assessment.




(a) Predicted von mises stresses in tube steel



(b) Observed deformations of tube steel

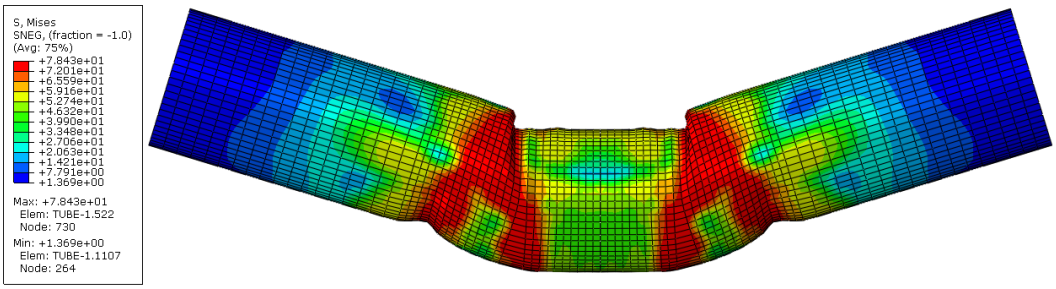



(c) Predicted maximum principal concrete strains at CFST centerline(cracks can be estimated perpendicular to arrows)

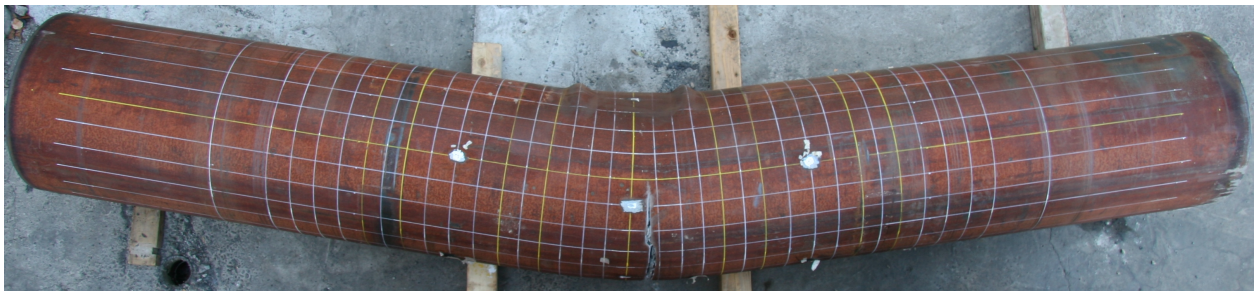



(d) Observed cracking patterns of concrete fill

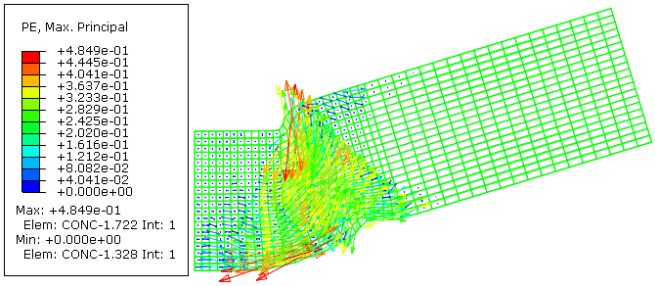
Figure D.5: Observed and Simulated Local Behaviors of Flexurally Dominated Specimen (Specimen 1, a/D = 1.0)



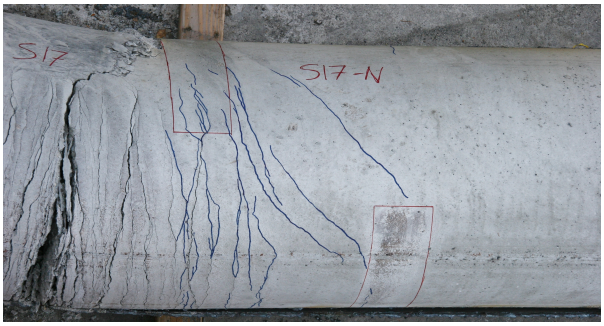

(a) Predicted von mises stresses in tube steel



(b) Observed deformations of tube steel

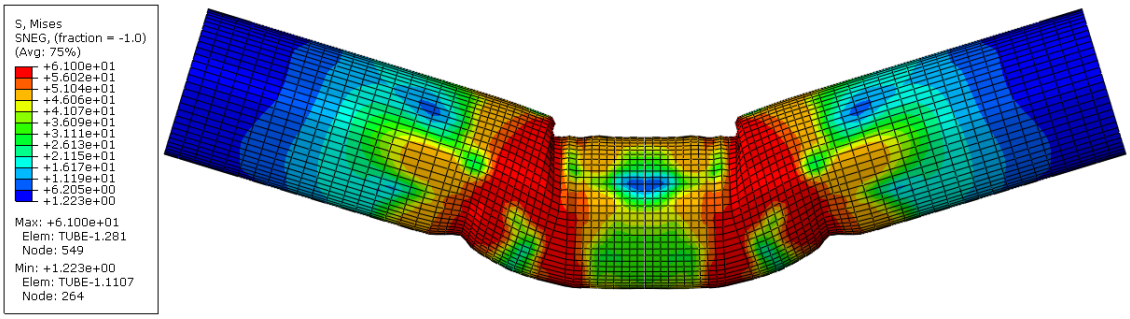



(c) Predicted maximum principal concrete strains at CFST centerline (cracks can be estimated perpendicular to arrows)

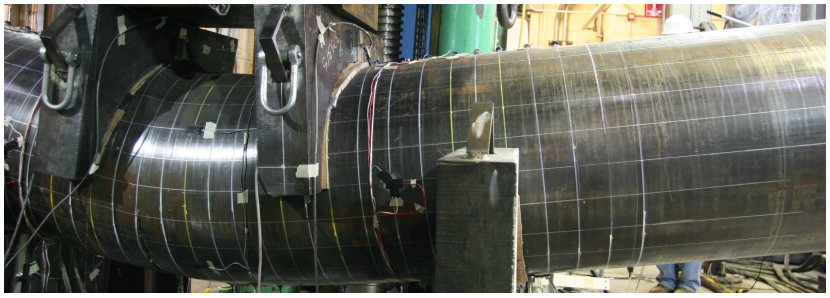



(d) Observed cracking patterns of concrete fill

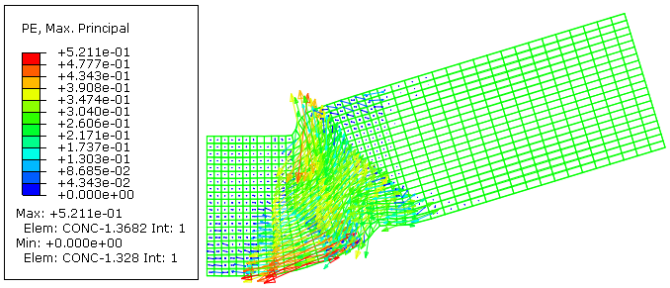
Figure D.6: Observed and Simulated Local Behaviors of Flexurally Dominated Specimen (Specimen 17, a/D = 0.5)




(a) Predicted von mises stresses in tube steel



(b) Observed deformations of tube steel

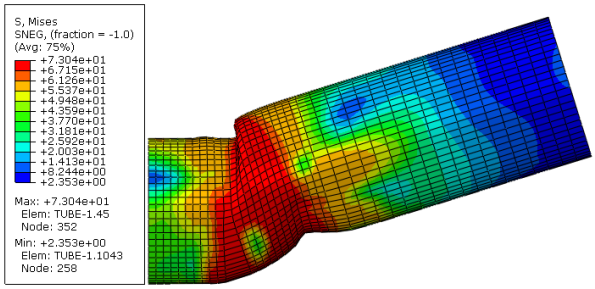



(c) Predicted maximum principal concrete strains at CFST centerline (cracks can be estimated perpendicular to arrows)

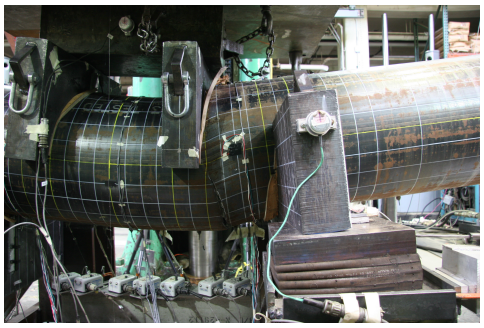


(d) Observed cracking patterns of concrete fill

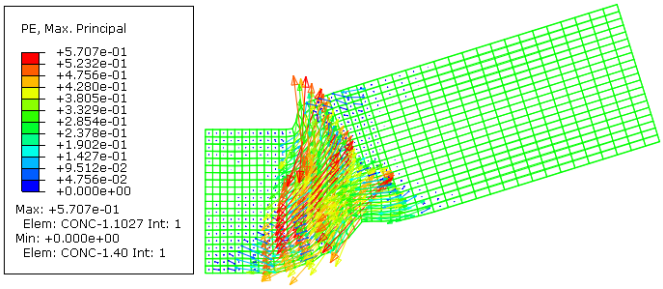
Figure D.7: Observed and Simulated Local Behaviors of Flexurally Dominated Specimen (Specimen 2, a/D = 0.5)




(a) Predicted von mises stresses in tube steel



(b) Observed deformations of tube steel

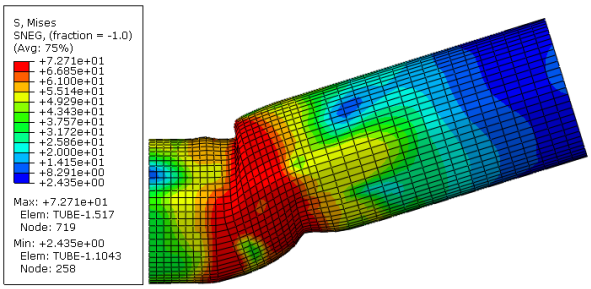



(c) Predicted maximum principal concrete strains at CFST centerline (cracks can be estimated perpendicular to arrows)

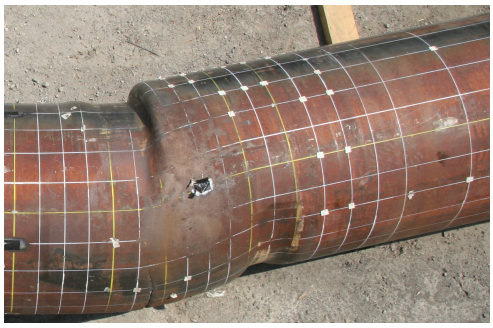


(d) Observed cracking patterns of concrete fill

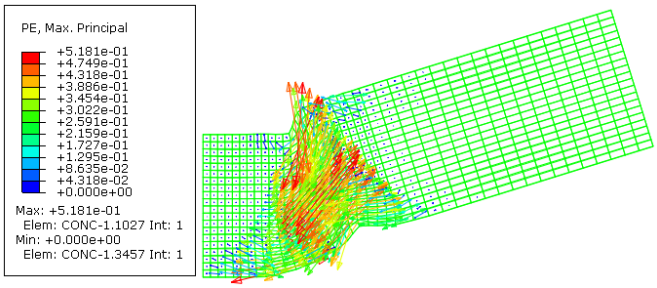
Figure D.8: Observed and Simulated Local Behaviors of Shear Yielding Specimen (Specimen 16, a/D = 0.375)




(a) Predicted von mises stresses in tube steel



(b) Observed deformations of tube steel

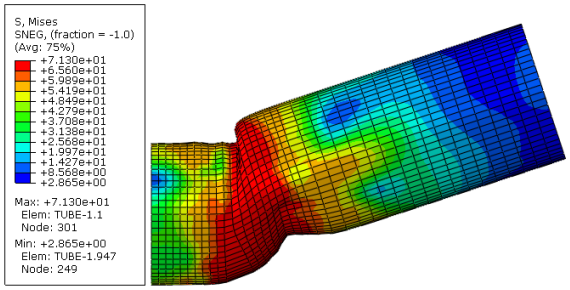



(c) Predicted maximum principal concrete strains at CFST centerline (cracks can be estimated perpendicular to arrows)




(d) Observed cracking patterns of concrete fill

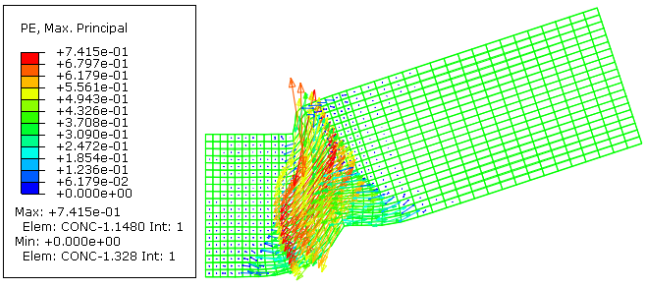
Figure D.9: Observed and Simulated Local Behaviors of Shear Yielding Specimen (Specimen 10, a/D = 0.375)



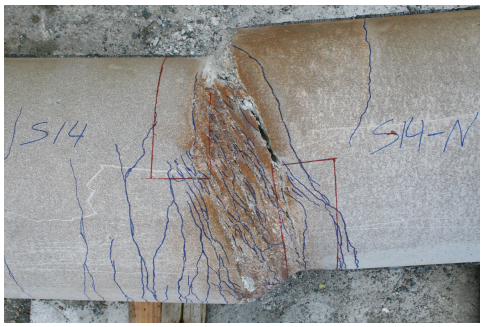

(a) Predicted von mises stresses in tube steel



(b) Observed deformations of tube steel




(c) Predicted maximum principal concrete strains at CFST centerline (cracks can be estimated perpendicular to arrows)




(d) Observed cracking patterns of concrete fill

Figure D.10: Observed and Simulated Local Behaviors of Shear Dominated Specimen (Specimen 14, a/D = 0.25)

# Appendix E

# SUPPLEMENTARY PARAMETER STUDY RESULTS

Within each parameter study, axial load was also varied so that a normalized axial-moment relationship could be observed. The axial load was initially calculated with the total load calculated as a percentage of the CFST nominal axial capacity, $P_0$ (Equation 2.3), of the base CFST in Table 5.1. For subsequent parameter studies, the loads calculated here were kept constant for the different CFSTs modeled. The resulting $P/P_0$ ratios for each model are provided in Appendix E, along with the shear and moment results plotted in the following sections.

Additional results from the models presented in Chapter 5 are provided in this Appendix. These results include: $P/P_0$, $M_{PSDM}$, $V_{prmax}$, $M_{pr}$ on the midspan and shear span sides of the load cradle, and $M_{pr}/M_{PSDM}$, using the midspan side $M_{pr}$ as it was used to determine failure mode. The shear-force deflection behaviors are also presented for reporting completion. However, they were not used explicitly in the final conclusions of this document, as the model used was not validated against deflections behaviors.

## *E.1 Axial Load Ratio,* $P/P_0$

### *E.1.1 Model Details and Results*

Table E.1: Summary of Models for $P/P_0$ Study

| $P/P_0$ | $M_{PSDM}$ (kip-in) | a/D = 0.375 | | | | a/D = 0.25 | | | |
|---|---|---|---|---|---|---|---|---|---|
| | | $V_{prmax}$ (kips) | $M_{prmax}$ (kip-in) | | $M_{pr}/M_{PSDM}$ | $V_{prmax}$ (kips) | $M_{prmax}$ (kip-in) | | $M_{pr}/M_{PSDM}$ |
| | | | Midspan Side | Shear Span Side | | | Midspan Side | Shear Span Side | |
| 0.0 % | 7068.0 | 655.6 | 7473.2 | 5358.4 | 1.06 | 788.7 | 6873.4 | 4460.4 | 0.97 |
| 5.0 % | 7970.4 | 701.8 | 8161.2 | 5844.0 | 1.02 | 836.7 | 7423.0 | 4808.6 | 0.93 |
| 8.5 % | 8520.8 | 740.0 | 8649.6 | 6177.0 | 1.02 | 877.1 | 7906.4 | 5114.6 | 0.93 |
| 10.0 % | 8736.4 | 751.8 | 8825.0 | 6300.2 | 1.01 | 887.9 | 8012.0 | 5179.4 | 0.92 |
| 15.0 % | 9372.6 | 800.6 | 9639.6 | 6892.0 | 1.03 | 954.1 | 8804.2 | 5685.0 | 0.94 |
| 20.0 % | 9867.9 | 838.8 | 10087.0 | 7192.0 | 1.02 | 1021.4 | 9662.8 | 6257.4 | 0.98 |
| 30.0 % | 10475.2 | 872.5 | 10457.0 | 7526.4 | 1.00 | 1067.4 | 10169.0 | 6512.6 | 0.97 |
| 40.0 % | 10565.1 | 885.3 | 10518.0 | 7584.8 | 1.00 | 1088.1 | 10252.0 | 6604.0 | 0.97 |
| 50.0 % | 10138.8 | 903.8 | 10668.0 | 7759.0 | 1.05 | 1094.1 | 10364.0 | 6656.0 | 1.02 |

### *E.1.2 Shear Force vs. Vertical Deflection*

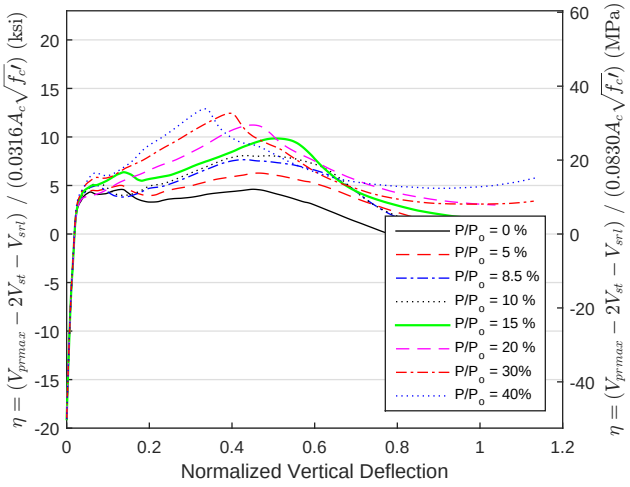



Figure E.1: Variation of Normalized Predicted Shear Force vs. Normalized Vertical Deflection with Axial Load Ratio for CFST with $a/D = 0.375$

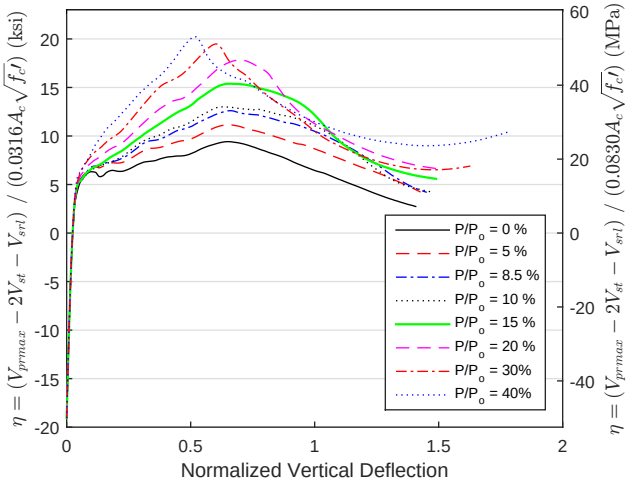



Figure E.2: Variation of Normalized Predicted Shear Force vs. Normalized Vertical Deflection with Axial Load Ratio for CFST with $a/D = 0.25$

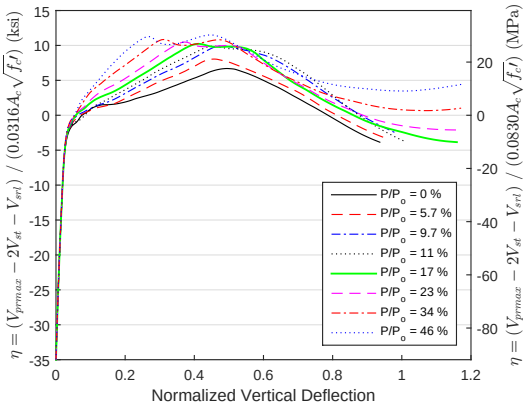
## *E.2 Tube Diameter to Thickness Ratio, $D/t$*

### *E.2.1 Model Details and Results*

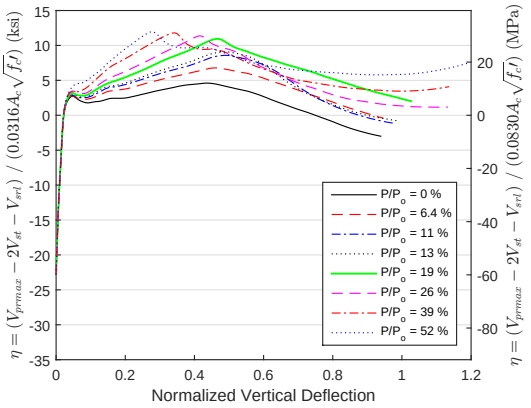
Table E.2: Summary of Models for $D/t$ Study

| $D/t$ | $P/P_0$ | $M_{PSDM}$ (kip-in) | a/D = 0.375 | | | | a/D = 0.25 | | | |
|---|---|---|---|---|---|---|---|---|---|---|
| | | | $V_{prmax}$ (kips) | $M_{prmax}$ (kip-in) | | $M_{pr}/M_{PSDM}$ | $V_{prmax}$ (kips) | $M_{prmax}$ (kip-in) | | $M_{pr}/M_{PSDM}$ |
| | | | | Midspan Side | Shear Span Side | | | Midspan Side | Shear Span Side | |
| 53.3 | 0.0 % | 9806.0 | 938.8 | 10703.0 | 7843.2 | 1.09 | 1121.6 | 10039.0 | 6764.0 | 1.02 |
| | 5.7 % | 10450.2 | 969.2 | 11201.0 | 8311.4 | 1.07 | 1183.7 | 10775.0 | 7263.2 | 1.03 |
| | 9.7 % | 10815.7 | 1011.6 | 11871.0 | 8716.2 | 1.10 | 1221.5 | 11236.0 | 7569.4 | 1.04 |
| | 11.5 % | 10950.8 | 1010.8 | 11854.0 | 8650.8 | 1.08 | 1238.0 | 11434.0 | 7700.0 | 1.04 |
| | 17.2 % | 11310.0 | 1018.4 | 11969.0 | 8757.4 | 1.06 | 1275.5 | 11917.0 | 7981.6 | 1.05 |
| | 23.0 % | 11521.5 | 1024.2 | 12009.0 | 8789.2 | 1.04 | 1285.0 | 12026.0 | 8010.6 | 1.04 |
| | 34.4 % | 11519.0 | 1032.4 | 12017.0 | 8860.6 | 1.04 | 1295.6 | 12101.0 | 8066.6 | 1.05 |
| | 45.9 % | 10943.3 | 1047.1 | 12812.0 | 9036.8 | 1.17 | 1303.0 | 12149.0 | 8104.2 | 1.11 |
| 80 | 0.0 % | 6872.1 | 634.5 | 7143.6 | 5195.2 | 1.04 | 746.3 | 6557.6 | 4304.6 | 0.95 |
| | 6.4 % | 7646.5 | 684.7 | 7875.7 | 5712.4 | 1.03 | 800.7 | 7166.6 | 4679.0 | 0.94 |
| | 10.9 % | 8087.4 | 726.3 | 8465.6 | 6125.6 | 1.05 | 855.0 | 7768.2 | 5113.6 | 0.96 |
| | 12.9 % | 8251.0 | 737.9 | 8640.8 | 6246.2 | 1.05 | 858.5 | 7834.2 | 5090.4 | 0.95 |
| | 19.3 % | 8689.9 | 780.9 | 9247.0 | 6641.6 | 1.06 | 932.3 | 8700.0 | 5692.6 | 1.00 |
| | 25.8 % | 8956.6 | 790.7 | 9378.6 | 6730.4 | 1.05 | 959.3 | 9032.4 | 5865.2 | 1.01 |
| | 38.6 % | 8997.0 | 800.7 | 9446.8 | 6839.0 | 1.05 | 973.9 | 9172.2 | 5962.4 | 1.02 |
| | 51.5 % | 8372.7 | 803.9 | 9350.2 | 6798.2 | 1.12 | 985.8 | 9239.8 | 6051.8 | 1.10 |
| 100 | 0.0 % | 5636.0 | 525.8 | 5934.6 | 4264.8 | 1.05 | 621.3 | 5399.4 | 3552.4 | 0.96 |
| | 6.8 % | 6477.6 | 571.7 | 6597.4 | 4763.8 | 1.02 | 680.4 | 6086.0 | 3993.6 | 0.94 |
| | 11.5 % | 6956.8 | 603.3 | 7066.8 | 5085.2 | 1.02 | 700.9 | 6344.8 | 4136.8 | 0.91 |
| | 13.6 % | 7134.9 | 624.0 | 7369.0 | 5304.4 | 1.03 | 736.6 | 6822.0 | 4482.8 | 0.96 |
| | 20.4 % | 7613.8 | 643.7 | 7605.6 | 5421.4 | 1.00 | 785.7 | 7402.4 | 4820.6 | 0.97 |
| | 27.2 % | 7908.0 | 659.6 | 7749.8 | 5544.6 | 0.98 | 820.2 | 7782.4 | 5041.4 | 0.98 |
| | 40.7 % | 7969.8 | 674.6 | 7836.6 | 5631.6 | 0.98 | 843.2 | 7972.6 | 5154.6 | 1.00 |
| | 54.3 % | 7321.4 | 690.0 | 7940.2 | 5734.2 | 1.08 | 855.7 | 8027.4 | 5231.6 | 1.10 |

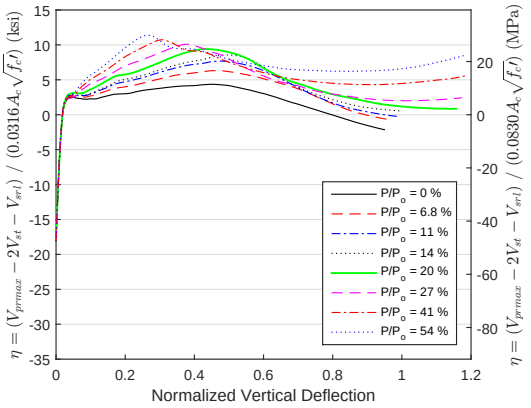
### *E.2.2 Shear Force vs. Vertical Deflection*




(a) $D/t = 53.3$

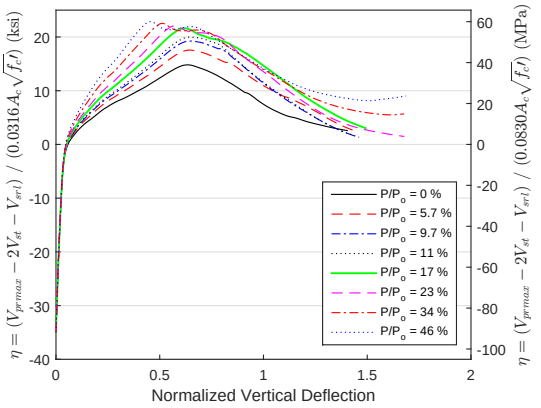



(b) $D/t = 80$

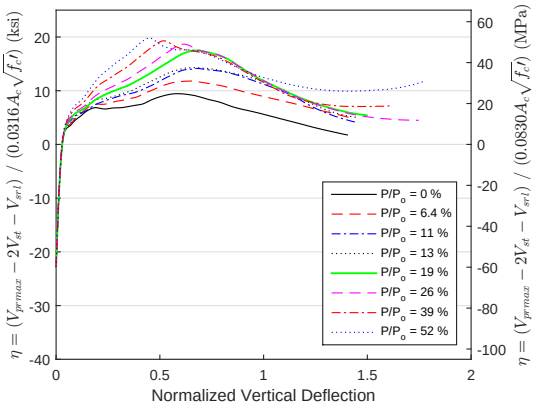



(c) $D/t = 100$

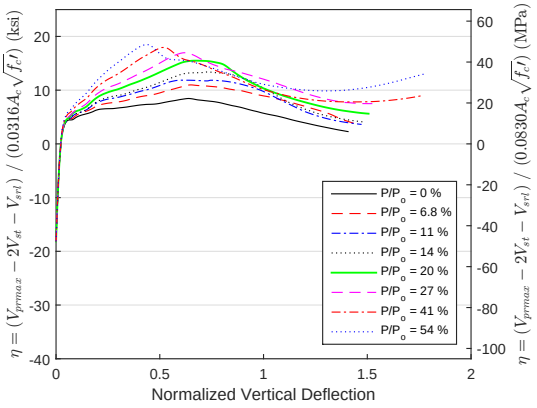
Figure E.3: Variation of Normalized Predicted Shear Force vs. Normalized Vertical Deflection with Axial Load and $D/t$ Ratios for CFST with $a/D = 0.375$




(a) $D/t = 53.3$




(b) $D/t = 80$




(c) $D/t = 100$

Figure E.4: Variation of Normalized Predicted Shear Force vs. Normalized Vertical Deflection with Axial Load and $D/t$ Ratios for CFST with $a/D = 0.25$

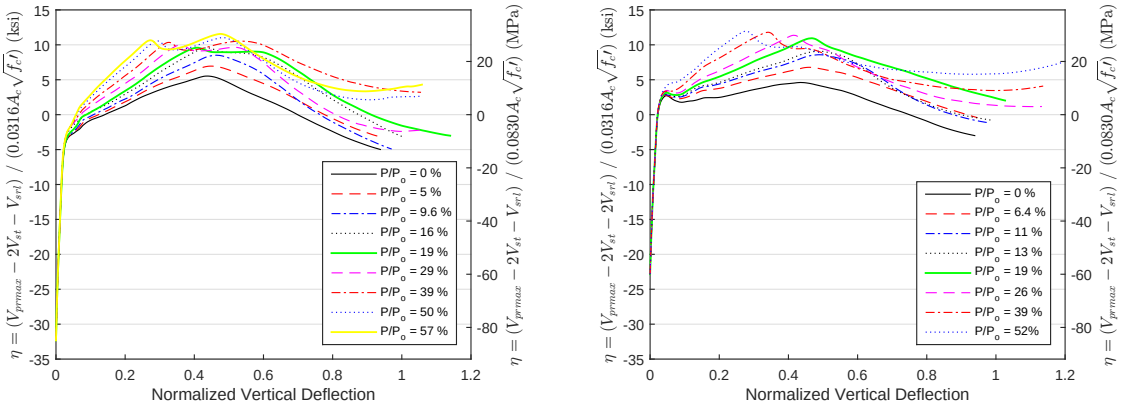
## *E.3 Concrete Strength, $f'_c$*

### *E.3.1 Model Details and Results*

Table E.3: Summary of Models for $f'_c$ Study

| $f'_c$ (ksi) | $P/P_0$ | $M_{PSDM}$ (kip-in) | a/D = 0.375 | | | | a/D = 0.25 | | | |
|---|---|---|---|---|---|---|---|---|---|---|
| | | | $V_{prmax}$ (kips) | $M_{prmax}$ (kip-in) | | $M_{pr}/M_{PSDM}$ | $V_{prmax}$ (kips) | $M_{prmax}$ (kip-in) | | $M_{pr}/M_{PSDM}$ |
| | | | | Midspan Side | Shear Span Side | | | Midspan Side | Shear Span Side | |
| 3 | 0.0 % | 6489.5 | 618.3 | 7054.2 | 5184.2 | 1.09 | 748.0 | 6668.4 | 4463.8 | 1.03 |
| | 5.0 % | 6785.7 | 641.6 | 7346.4 | 5369.6 | 1.08 | 783.0 | 7065.8 | 4717.6 | 1.04 |
| | 9.6 % | 6998.7 | 667.1 | 7676.8 | 5599.0 | 1.10 | 811.0 | 7438.0 | 4931.6 | 1.06 |
| | 16.3 % | 7208.3 | 684.4 | 7957.0 | 5794.4 | 1.10 | 835.4 | 7772.6 | 5114.8 | 1.08 |
| | 19.2 % | 7261.0 | 684.7 | 7963.6 | 5784.0 | 1.10 | 838.5 | 7831.6 | 5148.2 | 1.08 |
| | 28.9 % | 7275.3 | 691.2 | 8026.8 | 5898.2 | 1.10 | 848.1 | 8233.6 | 5275.0 | 1.13 |
| | 38.5 % | 7043.9 | 700.0 | 8425.8 | 5982.8 | 1.20 | 856.3 | 8439.2 | 5372.0 | 1.20 |
| | 50.1 % | 6429.7 | 708.4 | 8494.6 | 6055.4 | 1.32 | 867.3 | 8676.0 | 5514.6 | 1.35 |
| | 57.5 % | 5839.8 | 720.0 | 8606.6 | 6141.8 | 1.47 | 876.3 | 8966.2 | 5627.8 | 1.54 |
| 6 | 0.0 % | 6872.1 | 634.5 | 7143.6 | 5195.2 | 1.04 | 746.3 | 6557.6 | 4304.6 | 0.95 |
| | 6.4 % | 7646.5 | 684.7 | 7875.7 | 5712.4 | 1.03 | 800.7 | 7166.6 | 4679.0 | 0.94 |
| | 10.9 % | 8087.4 | 726.3 | 8465.6 | 6125.6 | 1.05 | 855.0 | 7768.2 | 5113.6 | 0.96 |
| | 12.9 % | 8251.0 | 737.9 | 8640.8 | 6246.2 | 1.05 | 858.5 | 7834.2 | 5090.4 | 0.95 |
| | 19.3 % | 8689.9 | 780.9 | 9247.0 | 6641.6 | 1.06 | 932.3 | 8700.0 | 5692.6 | 1.00 |
| | 25.8 % | 8956.6 | 790.7 | 9378.6 | 6730.4 | 1.05 | 959.3 | 9032.4 | 5865.2 | 1.01 |
| | 38.6 % | 8997.0 | 800.7 | 9446.8 | 6839.0 | 1.05 | 973.9 | 9172.2 | 5962.4 | 1.02 |
| | 51.5 % | 8372.7 | 803.9 | 9350.2 | 6798.2 | 1.12 | 985.8 | 9239.8 | 6051.8 | 1.10 |
| 8.6 | 0.0 % | 7068.0 | 655.6 | 7473.2 | 5358.4 | 1.06 | 788.7 | 6873.4 | 4460.4 | 0.97 |
| | 5.0 % | 7970.4 | 701.8 | 8161.2 | 5844.0 | 1.02 | 836.7 | 7423.0 | 4808.6 | 0.93 |
| | 8.5 % | 8520.8 | 740.0 | 8649.6 | 6177.0 | 1.02 | 877.1 | 7906.4 | 5114.6 | 0.93 |
| | 10.0 % | 8736.4 | 751.8 | 8825.0 | 6300.2 | 1.01 | 887.9 | 8012.0 | 5179.4 | 0.92 |
| | 15.0 % | 9372.6 | 800.6 | 9639.6 | 6892.0 | 1.03 | 954.1 | 8804.2 | 5685.0 | 0.94 |
| | 20.0 % | 9867.9 | 838.8 | 10087.0 | 7192.0 | 1.02 | 1021.4 | 9662.8 | 6257.4 | 0.98 |
| | 30.0 % | 10475.2 | 872.5 | 10457.0 | 7526.4 | 1.00 | 1067.4 | 10169.0 | 6512.6 | 0.97 |
| | 40.0 % | 10565.1 | 885.3 | 10518.0 | 7584.8 | 1.00 | 1088.1 | 10252.0 | 6604.0 | 0.97 |
| | 50.0 % | 10138.8 | 903.8 | 10668.0 | 7759.0 | 1.05 | 1094.1 | 10364.0 | 6656.0 | 1.02 |
| 12 | 0.0 % | 7236.0 | 725.7 | 7989.4 | 5857.4 | 1.10 | 817.1 | 7111.8 | 4565.6 | 0.98 |
| | 3.9 % | 8245.5 | 766.2 | 8920.4 | 6378.4 | 1.08 | 885.6 | 7899.0 | 5035.6 | 0.96 |
| | 6.6 % | 8886.4 | 750.2 | 8291.8 | 6124.2 | 0.93 | 926.2 | 8411.0 | 5361.4 | 0.95 |
| | 7.8 % | 9144.8 | 761.9 | 9009.6 | 6408.6 | 0.99 | 945.6 | 8653.0 | 5517.8 | 0.95 |
| | 11.7 % | 9941.6 | 819.4 | 9872.6 | 7025.4 | 0.99 | 1009.7 | 9545.8 | 6142.6 | 0.96 |
| | 15.5 % | 10621.3 | 859.1 | 10525.0 | 7483.2 | 0.99 | 1073.7 | 10400.0 | 6725.6 | 0.98 |
| | 23.3 % | 11680.2 | 923.8 | 11356.0 | 8047.4 | 0.97 | 1151.3 | 11151.0 | 7095.8 | 0.95 |
| | 31.0 % | 12331.2 | 944.3 | 11381.0 | 8044.2 | 0.92 | 1185.6 | 11446.0 | 7319.4 | 0.93 |
| | 40.0 % | 12582.8 | 979.8 | 11717.0 | 8317.4 | 0.93 | 1202.7 | 11590.0 | 7445.0 | 0.92 |
| | 50.0 % | 12231.4 | 999.9 | 11900 | 8486.2 | 0.97 | 1213.5 | 11396 | 7344.2 | 0.93 |

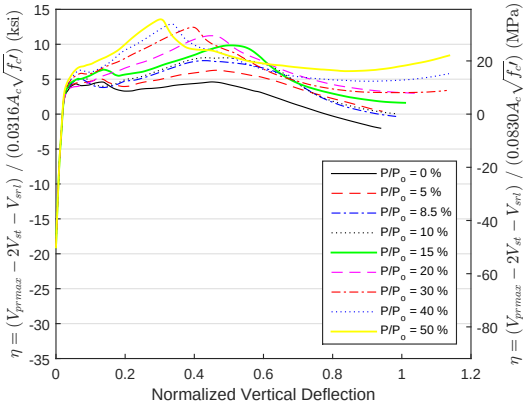
### *E.3.2 Shear Force vs. Vertical Deflection*



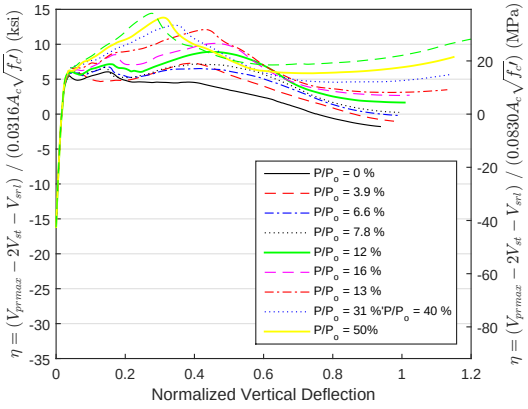

(a) $f'_c = 3\ ksi$




(b) $f'_c = 6\ ksi$

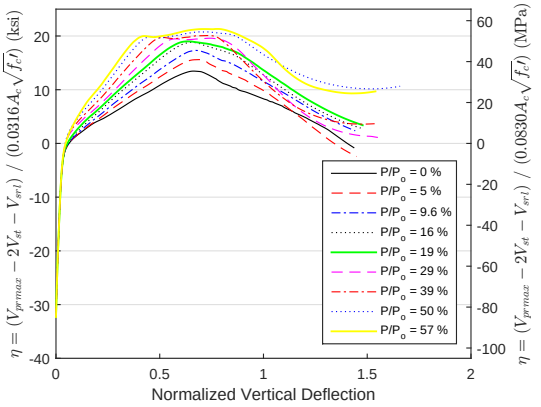



(c) $f'_c = 8.6\ ksi$

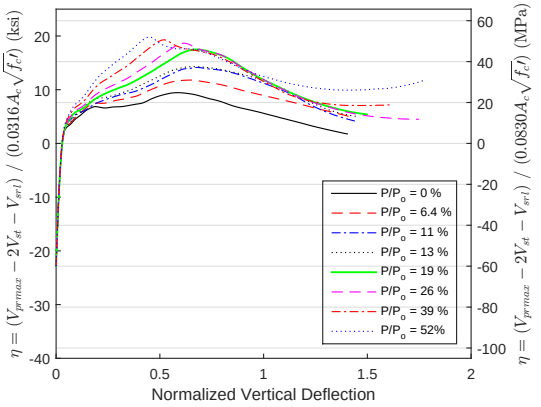



(d) $f'_c = 12\ ksi$

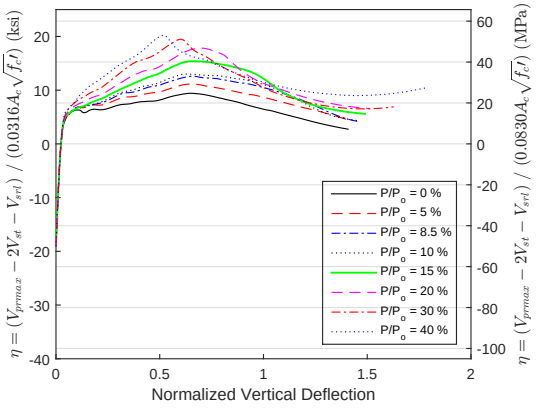
Figure E.5: Variation of Normalized Predicted Shear Force vs. Normalized Vertical Deflection with Axial Load Ratio and Concrete Strength, $f'_c$, for CFST with $a/D = 0.375$



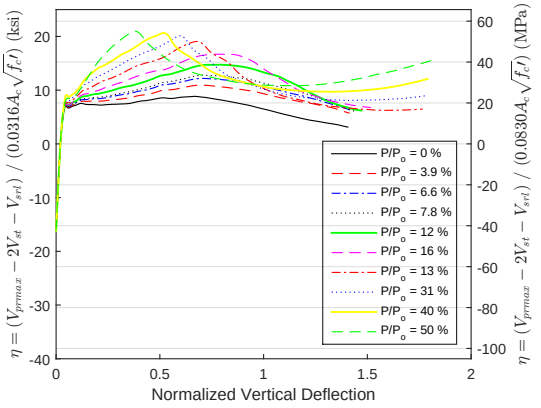

(a) $f_c' = 3\ ksi$




(b) $f_c' = 6\ ksi$




(c) $f_c' = 8.6\ ksi$




(d) $f_c' = 12\ ksi$

Figure E.6: Variation of Normalized Predicted Shear Force vs. Normalized Vertical Deflection with Axial Load Ratio and Concrete Strength, $f_c'$, for CFST with $a/D = 0.25$

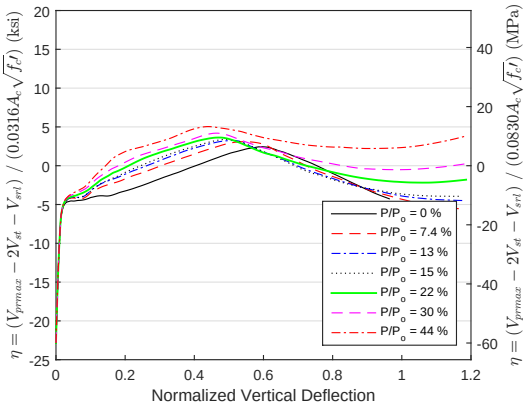
## *E.4 Tube Steel Yield Strength,* $F_{yt}$

### *E.4.1 Model Details and Results*

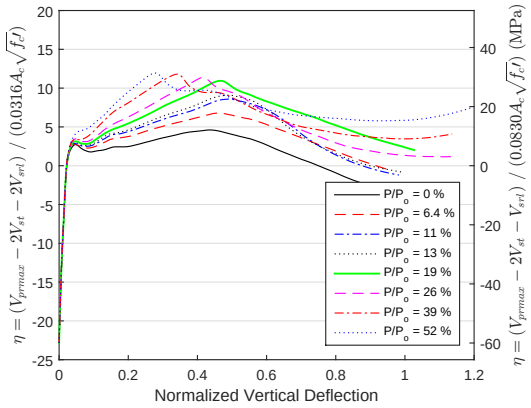
Table E.4: Summary of Models for $F_{yt}$ Study

| $F_{yt}$ (ksi) | $P/P_0$ | $M_{PSDM}$ (kip-in) | a/D = 0.375 | | | | a/D = 0.25 | | | |
|---|---|---|---|---|---|---|---|---|---|---|
| | | | $V_{prmax}$ (kips) | $M_{prmax}$ (kip-in) | | $M_{pr}/M_{PSDM}$ | $V_{prmax}$ (kips) | $M_{prmax}$ (kip-in) | | $M_{pr}/M_{PSDM}$ |
| | | | | Midspan Side | Shear Span Side | | | Midspan Side | Shear Span Side | |
| 35 | 0.0 % | 4394.7 | 584.4 | 6656.6 | 4935.2 | 1.51 | 672.9 | 5936.2 | 3948.0 | 1.35 |
| | 7.4 % | 5298.7 | 599.5 | 7144.4 | 5171.2 | 1.35 | 733.9 | 6683.4 | 4447.0 | 1.26 |
| | 12.6 % | 5810.8 | 603.2 | 7239.8 | 5167.4 | 1.25 | 771.4 | 7186.8 | 4757.2 | 1.24 |
| | 14.8 % | 6000.3 | 606.3 | 7269.0 | 5167.8 | 1.21 | 796.4 | 7244.6 | 4707.8 | 1.21 |
| | 22.3 % | 6507.6 | 611.9 | 7279.0 | 5110.8 | 1.12 | 767.2 | 7339.2 | 4671.0 | 1.13 |
| | 29.7 % | 6815.0 | 625.0 | 7477.2 | 5249.0 | 1.10 | 774.7 | 7543.4 | 4749.4 | 1.11 |
| | 44.4 % | 6861.5 | 644.6 | 7773.0 | 5506.0 | 1.13 | 787.3 | 7704.0 | 4880.8 | 1.12 |
| | 59.2 % | 6141.2 | 664.9 | 8297.2 | 5750.8 | 1.35 | 818.1 | 8217.2 | 5205.8 | 1.34 |
| 56.8 | 0.0 % | 6872.1 | 634.5 | 7143.6 | 5195.2 | 1.04 | 746.3 | 6557.6 | 4304.6 | 0.95 |
| | 6.4 % | 7646.5 | 684.7 | 7875.7 | 5712.4 | 1.03 | 800.7 | 7166.6 | 4679.0 | 0.94 |
| | 10.9 % | 8087.4 | 726.3 | 8465.6 | 6125.6 | 1.05 | 855.0 | 7768.2 | 5113.6 | 0.96 |
| | 12.9 % | 8251.0 | 737.9 | 8640.8 | 6246.2 | 1.05 | 858.5 | 7834.2 | 5090.4 | 0.95 |
| | 19.3 % | 8689.9 | 780.9 | 9247.0 | 6641.6 | 1.06 | 932.3 | 8700.0 | 5692.6 | 1.00 |
| | 25.8 % | 8956.6 | 790.7 | 9378.6 | 6730.4 | 1.05 | 959.3 | 9032.4 | 5865.2 | 1.01 |
| | 38.6 % | 8997.0 | 800.7 | 9446.8 | 6839.0 | 1.05 | 973.9 | 9172.2 | 5962.4 | 1.02 |
| | 51.5 % | 8372.7 | 803.9 | 9350.2 | 6798.2 | 1.12 | 985.8 | 9239.8 | 6051.8 | 1.10 |
| 70 | 0.0 % | 8325.8 | 768.4 | 8671.6 | 6325.0 | 1.04 | 912.6 | 8065.4 | 5412.8 | 0.97 |
| | 6.0 % | 9040.0 | 810.1 | 9300.0 | 6790.0 | 1.03 | 976.9 | 8814.4 | 5781.2 | 0.98 |
| | 10.1 % | 9447.2 | 848.3 | 9848.6 | 7167.0 | 1.04 | 1009.6 | 9195.8 | 6106.2 | 0.97 |
| | 11.9 % | 9598.5 | 864.7 | 10086.0 | 7329.0 | 1.05 | 1030.1 | 9457.6 | 6178.0 | 0.99 |
| | 17.9 % | 10004.5 | 909.0 | 10722.0 | 7723.2 | 1.07 | 1079.0 | 10041.0 | 6614.4 | 1.00 |
| | 23.9 % | 10251.5 | 920.7 | 10891.0 | 7843.2 | 1.06 | 1119.7 | 10584.0 | 6918.4 | 1.03 |
| | 35.7 % | 10288.9 | 928.4 | 10980.0 | 7986.6 | 1.07 | 1131.8 | 10676.0 | 6985.8 | 1.04 |
| | 47.7 % | 9711.0 | 940.2 | 11002.0 | 8074.6 | 1.13 | 1140.7 | 10705.0 | 7046.4 | 1.10 |

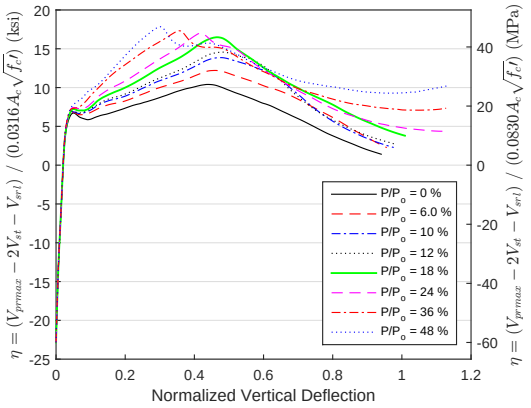
### *E.4.2 Shear Force vs. Vertical Deflection*




(a) $F_{yt} = 35\ ksi$

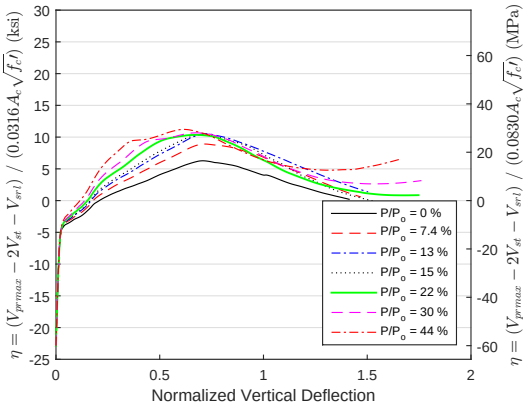



(b) $F_{yt} = 56.8\ ksi$

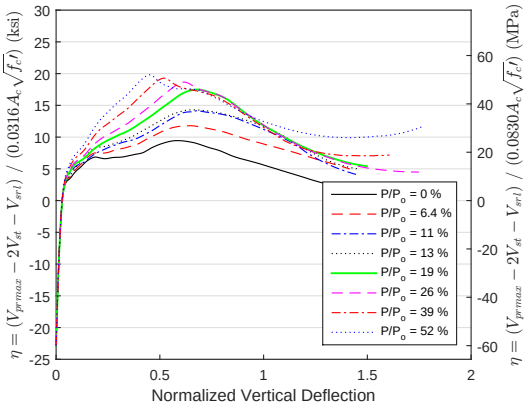



(c) $F_{yt} = 70\ ksi$

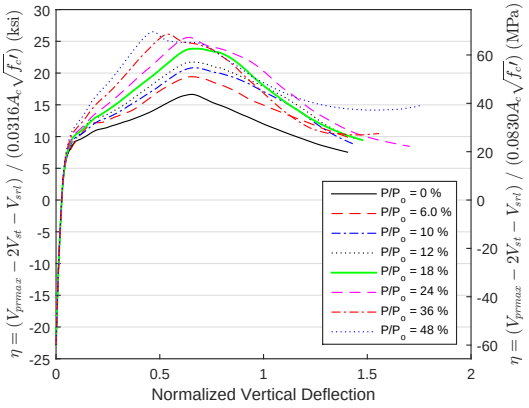
Figure E.7: Variation of Normalized Predicted Shear Force vs. Normalized Vertical Deflection with Axial Load Ratio and Steel Tube Strength, $F_{yt}$, for CFST with $a/D = 0.375$




(a) $F_{yt} = 35\ ksi$




(b) $F_{yt} = 56.8\ ksi$




(c) $F_{yt} = 70\ ksi$

Figure E.8: Variation of Normalized Predicted Shear Force vs. Normalized Vertical Deflection with Axial Load Ratio and Steel Tube Strength, $F_{yt}$, for CFST with $a/D = 0.25$

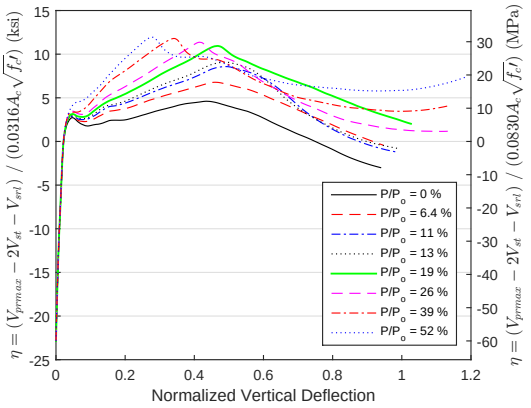
## *E.5 Internal Reinforcement Ratio,* $\rho_{int}$

### *E.5.1 Model Details and Results*

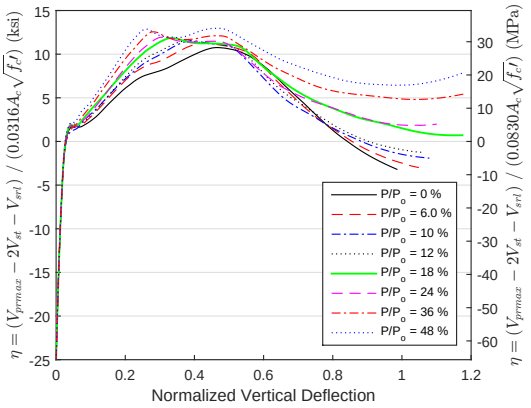
Table E.5: Summary of Models for Internal Reinforcement Ratio, $\rho_{int}$, Study

| $\rho_{int}$ | $P/P_0$ | $M_{PSDM}$ (kip-in) | a/D = 0.375 | | | | a/D = 0.25 | | | |
|---|---|---|---|---|---|---|---|---|---|---|
| | | | $V_{prmax}$ (kips) | $M_{prmax}$ (kip-in) | | $M_{pr}/M_{PSDM}$ | $V_{prmax}$ (kips) | $M_{prmax}$ (kip-in) | | $M_{pr}/M_{PSDM}$ |
| | | | | Midspan Side | Shear Span Side | | | Midspan Side | Shear Span Side | |
| 0% | 0.0 % | 6872.1 | 634.5 | 7143.6 | 5195.2 | 1.04 | 746.3 | 6557.6 | 4304.6 | 0.95 |
| | 6.4 % | 7646.5 | 684.7 | 7875.7 | 5712.4 | 1.03 | 800.7 | 7166.6 | 4679.0 | 0.94 |
| | 10.9 % | 8087.4 | 726.3 | 8465.6 | 6125.6 | 1.05 | 855.0 | 7768.2 | 5113.6 | 0.96 |
| | 12.9 % | 8251.0 | 737.9 | 8640.8 | 6246.2 | 1.05 | 858.5 | 7834.2 | 5090.4 | 0.95 |
| | 19.3 % | 8689.9 | 780.9 | 9247.0 | 6641.6 | 1.06 | 932.3 | 8700.0 | 5692.6 | 1.00 |
| | 25.8 % | 8956.6 | 790.7 | 9378.6 | 6730.4 | 1.05 | 959.3 | 9032.4 | 5865.2 | 1.01 |
| | 38.6 % | 8997.0 | 800.7 | 9446.8 | 6839.0 | 1.05 | 973.9 | 9172.2 | 5962.4 | 1.02 |
| | 51.5 % | 8372.7 | 803.9 | 9350.2 | 6798.2 | 1.12 | 985.8 | 9239.8 | 6051.8 | 1.10 |
| 1% | 0.0 % | 7977.9 | 832.4 | 8634.0 | 6674.8 | 1.08 | 1013.0 | 8395.0 | 5961.2 | 1.05 |
| | 6.0 % | 8701.1 | 843.9 | 8793.8 | 6758.0 | 1.01 | 1036.9 | 8686.8 | 6076.6 | 1.00 |
| | 10.2 % | 9114.6 | 850.2 | 8887.4 | 6838.4 | 0.98 | 1055.1 | 8862.8 | 6232.8 | 0.97 |
| | 12.0 % | 9268.5 | 850.2 | 8869.6 | 6825.4 | 0.96 | 1053.1 | 8828.8 | 6206.0 | 0.95 |
| | 18.0 % | 9683.5 | 857.7 | 8940.0 | 6884.6 | 0.92 | 1067.9 | 8976.2 | 6301.4 | 0.93 |
| | 24.0 % | 9939.0 | 859.9 | 8959.6 | 6911.4 | 0.90 | 1072.7 | 9012.0 | 6333.6 | 0.91 |
| | 35.9 % | 9992.8 | 874.1 | 9139.0 | 6954.8 | 0.91 | 1081.6 | 9082.6 | 6396.6 | 0.91 |
| | 47.9 % | 9430.5 | 883.4 | 9600.6 | 6980.0 | 1.02 | 1098.1 | 9230.8 | 6530.4 | 0.98 |
| 2% | 0.0 % | 8972.2 | 923.5 | 8844.2 | 7161.8 | 0.99 | 1137.0 | 8809.2 | 6505.0 | 0.98 |
| | 5.6 % | 9653.1 | 930.1 | 8940.2 | 7145.4 | 0.93 | 1145.0 | 8878.6 | 6552.2 | 0.92 |
| | 9.6 % | 10043.8 | 935.8 | 8996.0 | 7152.2 | 0.90 | 1150.2 | 8925.0 | 6587.4 | 0.89 |
| | 11.3 % | 10189.7 | 934.0 | 8964.8 | 7089.6 | 0.88 | 1154.1 | 8960.0 | 6610.4 | 0.88 |
| | 16.9 % | 10584.5 | 943.7 | 9089.6 | 7129.8 | 0.86 | 1158.9 | 8991.0 | 6599.8 | 0.85 |
| | 22.6 % | 10830.3 | 949.8 | 9170.0 | 7166.0 | 0.85 | 1166.9 | 9059.2 | 6663.2 | 0.84 |
| | 33.8 % | 10895.0 | 954.4 | 9223.6 | 7140.8 | 0.85 | 1180.6 | 9187.4 | 6809.8 | 0.84 |
| | 45.1 % | 10383.9 | 958.2 | 9309.4 | 7103.2 | 0.90 | 1191.5 | 9255.2 | 6867.0 | 0.89 |

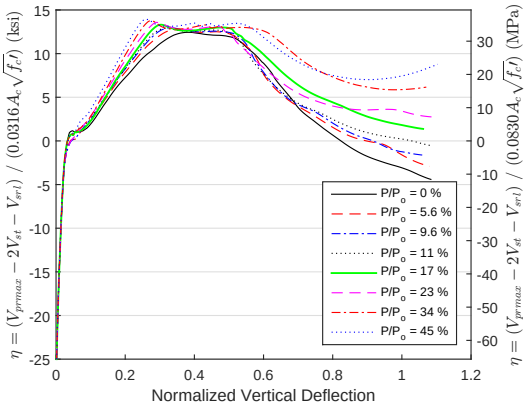
### *E.5.2 Shear Force vs. Vertical Deflection*




(a) $\rho_{int} = 0\%$

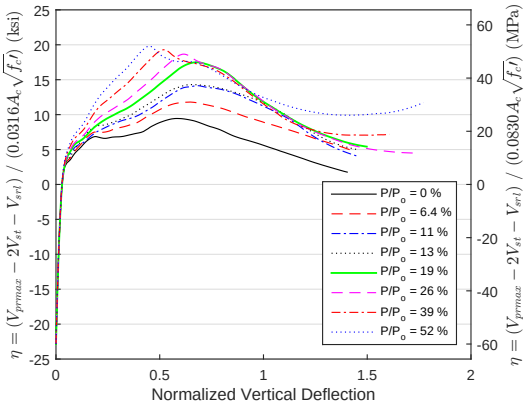



(b) $\rho_{int} = 1\%$

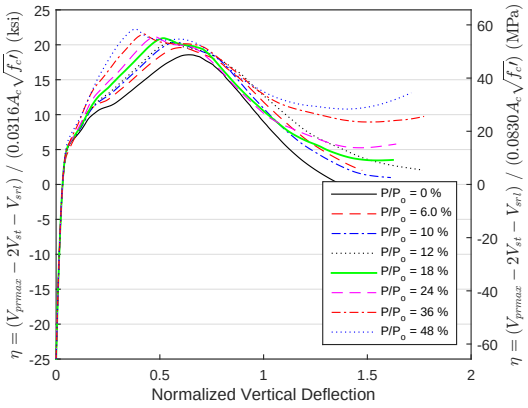



(c) $\rho_{int} = 2\%$

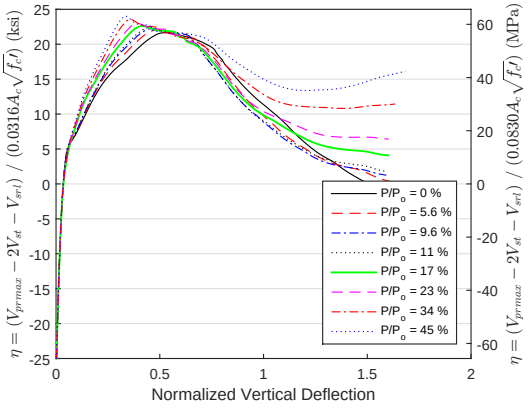
Figure E.9: Variation of Normalized Predicted Shear Force vs. Normalized Vertical Deflection with Axial Load Ratio and Internal Reinforcement Ratio, $\rho_{int}$, for CFST with $a/D = 0.375$




(a) $\rho_{int} = 0\%$




(b) $\rho_{int} = 1\%$




(c) $\rho_{int} = 2\%$

Figure E.10: Variation of Normalized Predicted Shear Force vs. Normalized Vertical Deflection with Axial Load Ratio and Internal Reinforcement Ratio, $\rho_{int}$, for CSFT with $a/D = 0.25$

# Appendix F

# DESIGN EXPRESSION RESULTS

## *F.1 Linear Regression of Shear Controlled Models*

Simulations from the parameters studies in Chapter 5 that resulted in $M_{pr} < 1.1M_{PSDM}$ and were subject to 20% axial load or less were put through a least squares linear regression analysis for the determination of the $\eta$-$P/P_0$ relationship to be used in $V_{n(prop2)}$. The individual results for each CFST composition are presented in the following sections. Some of these models use the same CFST composition and are grouped simply for reference to changes based on individual parameters. A summary of these results is provided at the end of this section, noting only unique CFST designs. The simulations used for the fit line determination, meet proposed limit state criterion of $M_{pr}/M_{PSDM} < 1.1$ and $V_{pr}/2V_{st} > 1.2$, are noted in the plots with a double diamond marker. Appendix E can be referenced for exact $M_{pr}/M_{PSDM}$ and $P/P_0$ values.

### *F.1.1 Axial Load Ratio, $P/P_0$*

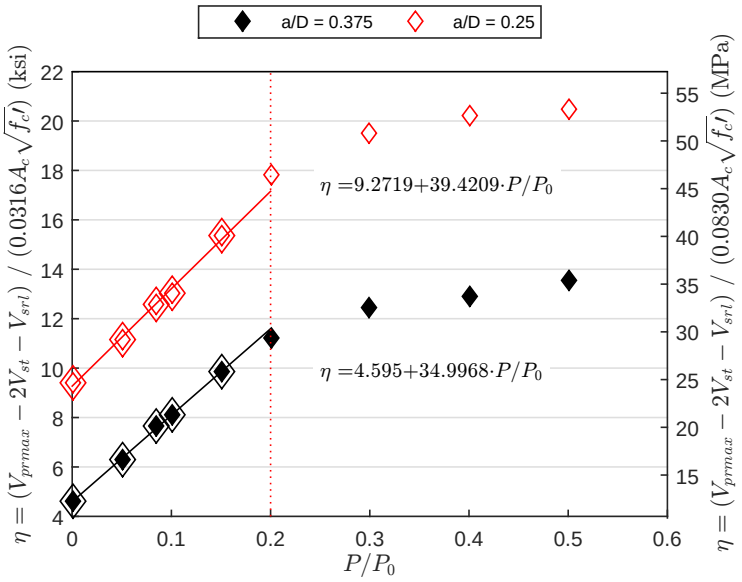
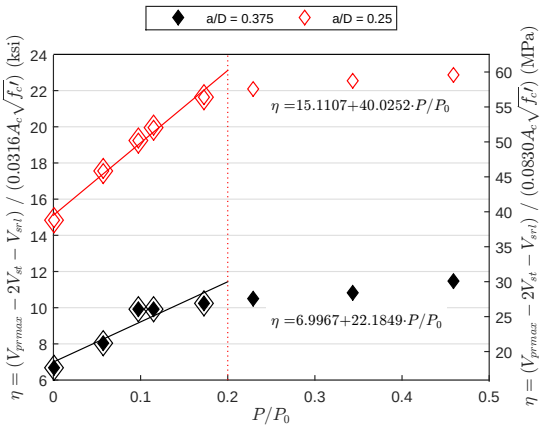
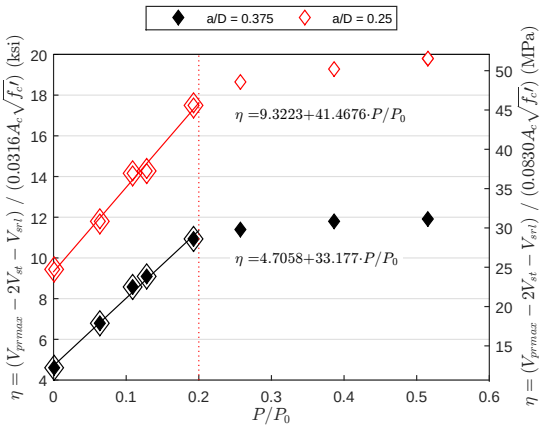



Figure F.1: Least Squares Linear Regression with Different Axial Load Ratios, $P/P_0$

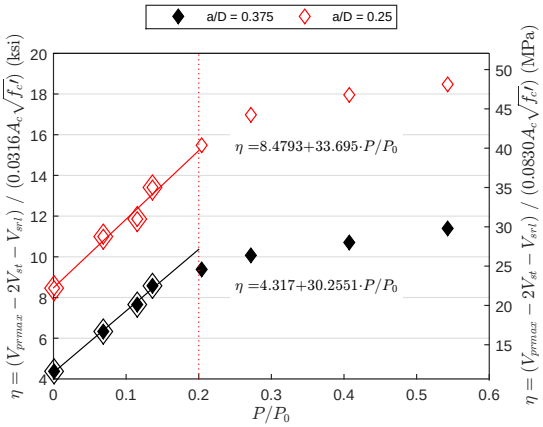
### *F.1.2 Tube Diameter to Thickness Ratio, $D/t$*




(a) $D/t$ = 53.3



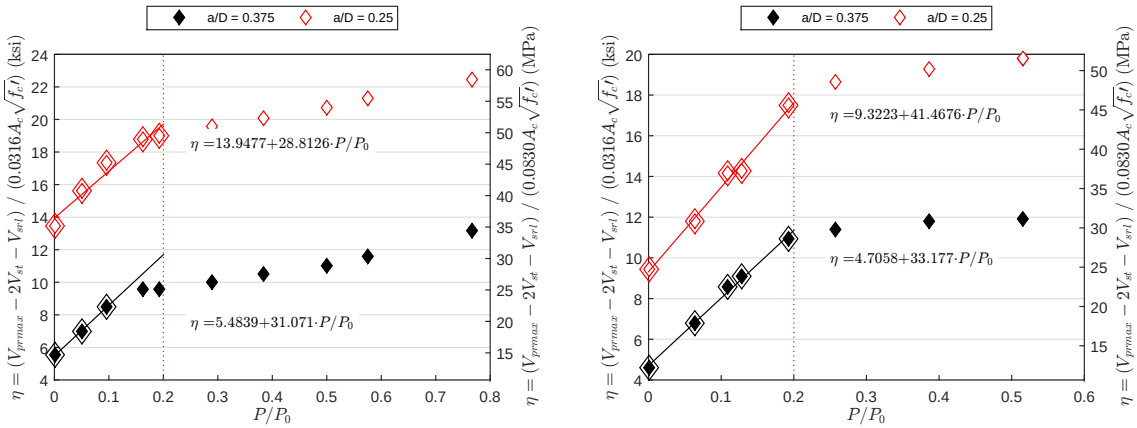

(b) $D/t$ = 80




(c) $D/t$ = 100

Figure F.2: Least Squares Linear Regression with Different $D/t$ Ratios

### *F.1.3 Concrete Strength, $f'_c$*

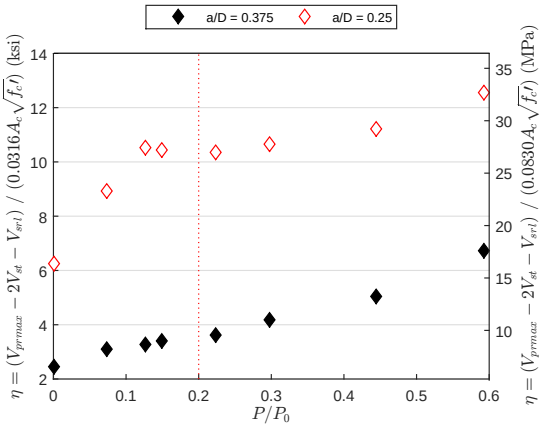



(a) $f'_c = 3\ ksi$ (b) $f'_c = 6\ ksi$

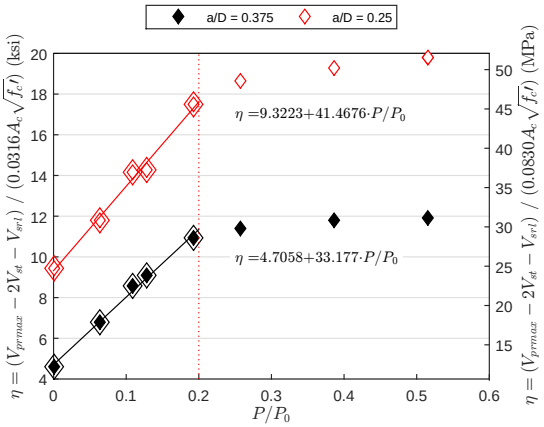
(c) $f'_c = 8.6\ ksi$ (d) $f'_c = 12\ ksi$

Figure F.3: Least Squares Linear Regression with Different Concrete Strengths, $f'_c$

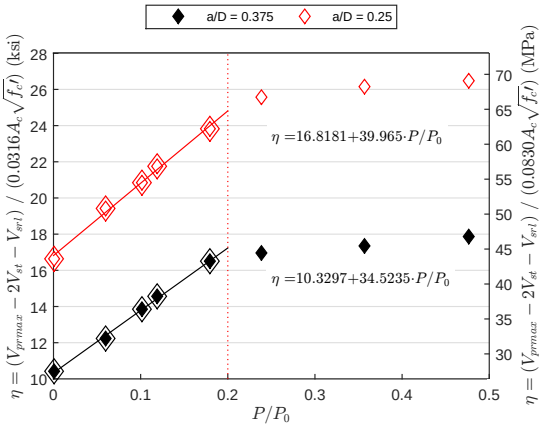
### *F.1.4 Tube Steel Yield Strength, $F_{yt}$*




(a) $F_{yt} = 35\ ksi$



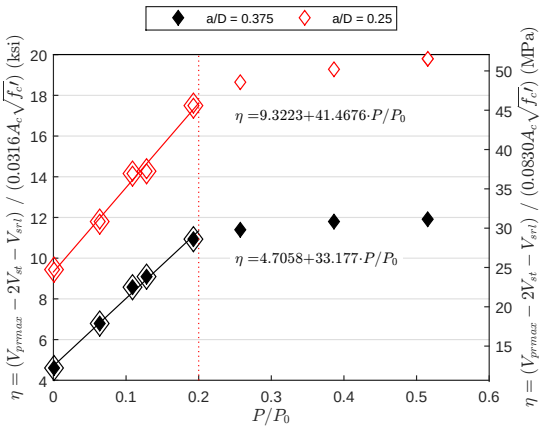

(b) $F_{yt} = 56.8\ ksi$



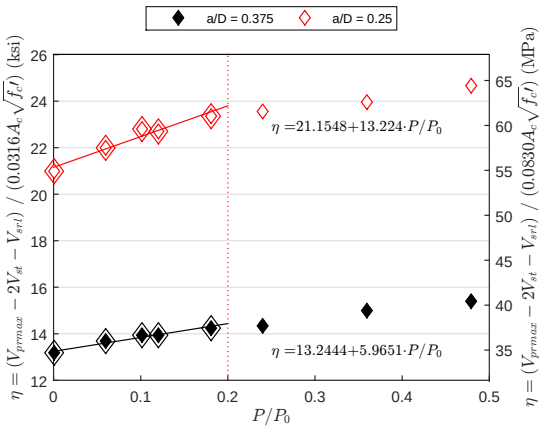

(c) $F_{yt} = 70\ ksi$

Figure F.4: Least Squares Linear Regression with Different Tube Steel Strengths, $F_{yt}$

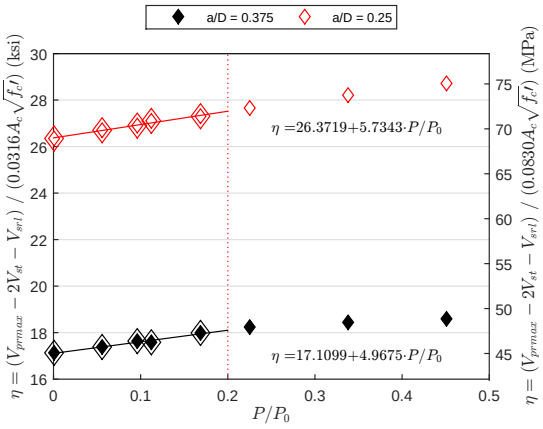
### *F.1.5 Internal Reinforcement Ratio, $\rho_{int}$*




(a) $\rho_{int} = 0\%$




(b) $\rho_{int} = 1\%$




(c) $\rho_{int} = 2\%$

Figure F.5: Least Squares Linear Regression with Different Internal Reinforcement Ratios, $\rho_{int}$

### *F.1.6 Summary of Fit Lines*

Table F.1: Summary of Fit Lines for Models with $M_{pr}/M_{PSDM} < 1.1$ and $P/P_0 \leq 0.2$

| Model | a/D = 0.375 | | a/D = 0.25 | |
|---|---|---|---|---|
| | Slope | $\eta$-Intercept | Slope | $\eta$-Intercept |
| D/t 80 - $f'_c$ 3.0 - $F_{yt}$ 56.8 - Reinf 0% | 31.07 | 5.48 | 28.81 | 13.95 |
| D/t 80 - $f'_c$ 6.0 - $F_{yt}$ 35.0 - Reinf 0% | −− | −− | −− | −− |
| D/t 80 - $f'_c$ 6.0 - $F_{yt}$ 70.0 - Reinf 0% | 34.52 | 10.33 | 39.97 | 16.82 |
| D/t 80 - $f'_c$ 6 .0 - $F_{yt}$ 56.8 - Reinf 0% | 33.18 | 4.71 | 41.47 | 9.32 |
| D/t 80 - $f'_c$ 8.6 - $F_{yt}$ 56.8 - Reinf 0% | 35.00 | 4.60 | 39.42 | 9.27 |
| D/t 80 - $f'_c$ 12 - $F_{yt}$ 56.8 - Reinf 0% | 28.68 | 5.45 | 50.16 | 8.90 |
| D/t 100 - $f'_c$ 6.0 - $F_{yt}$ 56.8 - Reinf 0% | 30.26 | 4.32 | 33.70 | 8.48 |
| D/t 53.3 - $f'_c$ 6.0 - $F_{yt}$ 56.8 - Reinf 0% | 22.18 | 7.00 | 40.03 | 15.11 |
| Mean | 30.70 | 5.98 | 39.08 | 11.69 |
| Min | 22.18 | 4.32 | 28.81 | 8.48 |
| Max | 35.00 | 10.33 | 50.16 | 16.82 |
| D/t 80 - $f'_c$ 6.0 - $F_{yt}$ 56.8 - Reinf 1% | 5.97 | 13.24 | 13.22 | 21.15 |
| D/t 80 - $f'_c$ 6.0 - $F_{yt}$ 56.8 - Reinf 2% | 4.97 | 17.11 | 5.73 | 26.37 |
| Mean | 5.47 | 15.18 | 9.48 | 23.76 |
| Min | 4.97 | 13.24 | 5.73 | 21.15 |
| Max | 5.97 | 17.11 | 13.22 | 26.37 |

## *F.2 Equation Evaluation Results for All Models*

Table F.2: Previous Experimental Research Summary

| $P/P_0$ | $D/t$ | $F_{yt}$ (ksi) | $f'_c$ (ksi) | $\rho_{int}$ | a/D = 0.375 | | | | a/D = 0.25 | | | |
|---|---|---|---|---|---|---|---|---|---|---|---|---|
| | | | | | $M_{pr}/M_{PSDM}$ | $V_{pr}/2V_{st}$ | $V_{prmax}$ (kips) | $V_{pr}/V_{n(prop2)}$ | $M_{pr}/M_{PSDM}$ | $V_{pr}/2V_{st}$ | $V_{prmax}$ (kips) | $V_{pr}/V_{n(prop2)}$ |
| 0.0 % | 80 | 56.8 | 3 | 0 % | 1.090 | 1.17 | 618.3 | 1.01 | 1.030 | 1.41 | 748.0 | 1.23 |
| 5.0 % | 80 | 56.8 | 3 | 0 % | 1.080 | 1.21 | 641.6 | 1.02 | 1.040 | 1.48 | 783.0 | 1.24 |
| 9.6 % | 80 | 56.8 | 3 | 0 % | 1.100 | 1.26 | 667.1 | 1.03 | 1.060 | 1.53 | 811.0 | 1.25 |
| 16.3 % | 80 | 56.8 | 3 | 0 % | 1.104 | 1.29 | 684.4 | 1.01 | 1.080 | 1.58 | 835.4 | 1.23 |
| 19.2 % | 80 | 56.8 | 3 | 0 % | 1.097 | 1.30 | 684.7 | 0.99 | 1.080 | 1.59 | 838.5 | 1.22 |
| 28.9 % | 80 | 56.8 | 3 | 0 % | 1.100 | 1.31 | 691.2 | 1.00 | 1.130 | 1.60 | 848.1 | 1.23 |
| 38.5 % | 80 | 56.8 | 3 | 0 % | 1.200 | 1.32 | 700.0 | 1.01 | 1.200 | 1.62 | 856.3 | 1.24 |
| 50.0 % | 80 | 56.8 | 3 | 0 % | 1.320 | 1.34 | 708.4 | 1.02 | 1.350 | 1.64 | 867.3 | 1.25 |
| 57.5 % | 80 | 56.8 | 3 | 0 % | 1.470 | 1.36 | 720.0 | 1.04 | 1.540 | 1.66 | 876.3 | 1.27 |
| 0.0 % | 80 | 56.8 | 6 | 0 % | 1.040 | 1.20 | 634.5 | 0.98 | 0.950 | 1.41 | 746.3 | 1.16 |
| 6.4 % | 80 | 56.8 | 6 | 0 % | 1.030 | 1.30 | 684.7 | 1.00 | 0.940 | 1.51 | 800.7 | 1.18 |
| 10.9 % | 80 | 56.8 | 6 | 0 % | 1.050 | 1.37 | 726.3 | 1.03 | 0.960 | 1.62 | 855.0 | 1.21 |
| 12.9 % | 80 | 56.8 | 6 | 0 % | 1.050 | 1.40 | 737.9 | 1.03 | 0.950 | 1.62 | 858.5 | 1.19 |
| 19.3 % | 80 | 56.8 | 6 | 0 % | 1.060 | 1.48 | 780.9 | 1.03 | 1.000 | 1.76 | 932.3 | 1.23 |
| 25.8 % | 80 | 56.8 | 6 | 0 % | 1.050 | 1.50 | 790.7 | 1.04 | 1.010 | 1.81 | 959.3 | 1.26 |
| 38.6 % | 80 | 56.8 | 6 | 0 % | 1.050 | 1.51 | 800.7 | 1.05 | 1.020 | 1.84 | 973.9 | 1.28 |
| 51.5 % | 80 | 56.8 | 6 | 0 % | 1.120 | 1.52 | 803.9 | 1.06 | 1.100 | 1.86 | 985.8 | 1.30 |
| 0.0 % | 80 | 56.8 | 8.609 | 0 % | 1.060 | 1.24 | 655.6 | 0.98 | 0.970 | 1.49 | 788.7 | 1.18 |
| 5.0 % | 80 | 56.8 | 8.609 | 0 % | 1.020 | 1.33 | 701.8 | 1.00 | 0.930 | 1.58 | 836.7 | 1.19 |
| 8.5 % | 80 | 56.8 | 8.609 | 0 % | 1.020 | 1.40 | 740.0 | 1.02 | 0.930 | 1.66 | 877.1 | 1.21 |
| 10.0 % | 80 | 56.8 | 8.609 | 0 % | 1.010 | 1.42 | 751.8 | 1.02 | 0.920 | 1.68 | 887.9 | 1.21 |
| 15.0 % | 80 | 56.8 | 8.609 | 0 % | 1.030 | 1.51 | 800.6 | 1.04 | 0.940 | 1.80 | 954.1 | 1.24 |
| 20.1 % | 80 | 56.8 | 8.609 | 0 % | 1.020 | 1.59 | 838.8 | 1.04 | 0.980 | 1.93 | 1021.4 | 1.27 |
| 30.0 % | 80 | 56.8 | 8.609 | 0 % | 1.000 | 1.65 | 872.5 | 1.08 | 0.970 | 2.02 | 1067.4 | 1.33 |

Continued on next page

Table F.2 – Continued from previous page

| $P/P_0$ | $D/t$) | $F_{yt}$ (ksi) | $f'_c$ (ksi) | $\rho_{int}$ | a/D = 0.375 | | | | a/D = 0.25 | | | |
|---|---|---|---|---|---|---|---|---|---|---|---|---|
| | | | | | $M_{pr}/M_{PSDM}$ | $V_{pr}/2V_{st}$ | $V_{prmax}$ (kips) | $V_{pr}/V_{n(prop2)}$ | $M_{pr}/M_{PSDM}$ | $V_{pr}/2V_{st}$ | $V_{prmax}$ (kips) | $V_{pr}/V_{n(prop2)}$ |
| 40.0 % | 80 | 56.8 | 8.609 | 0 % | 1.000 | 1.67 | 885.3 | 1.10 | 0.970 | 2.06 | 1088.1 | 1.35 |
| 50.0 % | 80 | 56.8 | 8.609 | 0 % | 1.050 | 1.71 | 903.8 | 1.12 | 1.020 | 2.07 | 1094.1 | 1.36 |
| 0.0 % | 80 | 56.8 | 12 | 0 % | 1.100 | 1.37 | 725.7 | 1.05 | 0.980 | 1.55 | 817.1 | 1.18 |
| 3.9 % | 80 | 56.8 | 12 | 0 % | 1.080 | 1.45 | 766.2 | 1.06 | 0.960 | 1.68 | 885.6 | 1.22 |
| 6.6 % | 80 | 56.8 | 12 | 0 % | 0.930 | 1.42 | 750.2 | 1.01 | 0.950 | 1.75 | 926.2 | 1.24 |
| 7.8 % | 80 | 56.8 | 12 | 0 % | 0.990 | 1.44 | 761.9 | 1.01 | 0.950 | 1.79 | 945.6 | 1.25 |
| 11.7 % | 80 | 56.8 | 12 | 0 % | 0.990 | 1.55 | 819.4 | 1.04 | 0.960 | 1.91 | 1009.7 | 1.28 |
| 15.6 % | 80 | 56.8 | 12 | 0 % | 0.990 | 1.63 | 859.1 | 1.05 | 0.980 | 2.03 | 1073.7 | 1.31 |
| 23.3 % | 80 | 56.8 | 12 | 0 % | 0.970 | 1.75 | 923.8 | 1.08 | 0.950 | 2.18 | 1151.3 | 1.35 |
| 31.0 % | 80 | 56.8 | 12 | 0 % | 0.920 | 1.79 | 944.3 | 1.10 | 0.930 | 2.24 | 1185.6 | 1.39 |
| 40.0 % | 80 | 56.8 | 12 | 0 % | 0.930 | 1.85 | 979.8 | 1.15 | 0.920 | 2.28 | 1202.7 | 1.41 |
| 50.0 % | 80 | 56.8 | 12 | 0 % | 0.970 | 1.89 | 999.9 | 1.17 | 0.930 | 2.30 | 1213.5 | 1.42 |
| 0.0 % | 53.3 | 56.8 | 6 | 0 % | 1.090 | 1.19 | 938.8 | 1.04 | 1.02 | 1.42 | 1121.6 | 1.25 |
| 5.7 % | 53.3 | 56.8 | 6 | 0 % | 1.070 | 1.23 | 969.2 | 1.04 | 1.03 | 1.50 | 1183.7 | 1.27 |
| 9.7 % | 53.3 | 56.8 | 6 | 0 % | 1.100 | 1.28 | 1011.6 | 1.06 | 1.04 | 1.55 | 1221.5 | 1.28 |
| 11.5 % | 53.3 | 56.8 | 6 | 0 % | 1.080 | 1.28 | 1010.8 | 1.05 | 1.04 | 1.57 | 1238.0 | 1.28 |
| 17.3 % | 53.3 | 56.8 | 6 | 0 % | 1.060 | 1.29 | 1018.4 | 1.02 | 1.05 | 1.62 | 1275.5 | 1.28 |
| 23.0 % | 53.3 | 56.8 | 6 | 0 % | 1.040 | 1.30 | 1024.2 | 1.01 | 1.04 | 1.63 | 1285.0 | 1.27 |
| 34.4 % | 53.3 | 56.8 | 6 | 0 % | 1.040 | 1.31 | 1032.4 | 1.02 | 1.05 | 1.64 | 1295.6 | 1.28 |
| 45.9 % | 53.3 | 56.8 | 6 | 0 % | 1.170 | 1.33 | 1047.1 | 1.03 | 1.11 | 1.65 | 1303.0 | 1.29 |
| 0.0 % | 100 | 56.8 | 6 | 0 % | 1.050 | 1.24 | 525.8 | 0.97 | 0.960 | 1.47 | 621.3 | 1.15 |
| 6.8 % | 100 | 56.8 | 6 | 0 % | 1.020 | 1.35 | 571.7 | 0.99 | 0.940 | 1.60 | 680.4 | 1.17 |
| 11.5 % | 100 | 56.8 | 6 | 0 % | 1.020 | 1.42 | 603.3 | 0.99 | 0.910 | 1.65 | 700.9 | 1.15 |
| 13.6 % | 100 | 56.8 | 6 | 0 % | 1.030 | 1.47 | 624.0 | 1.01 | 0.960 | 1.74 | 736.6 | 1.19 |
| 20.4 % | 100 | 56.8 | 6 | 0 % | 1.000 | 1.52 | 643.7 | 0.98 | 0.970 | 1.85 | 785.7 | 1.19 |

Continued on next page

Table F.2 – Continued from previous page

| $P/P_0$ | $D/t$) | $F_{yt}$ (ksi) | $f'_c$ (ksi) | $\rho_{int}$ | a/D = 0.375 | | | | a/D = 0.25 | | | |
|---|---|---|---|---|---|---|---|---|---|---|---|---|
| | | | | | $M_{pr}/M_{PSDM}$ | $V_{pr}/2V_{st}$ | $V_{prmax}$ (kips) | $V_{pr}/V_{n(prop2)}$ | $M_{pr}/M_{PSDM}$ | $V_{pr}/2V_{st}$ | $V_{prmax}$ (kips) | $V_{pr}/V_{n(prop2)}$ |
| 27.2 % | 100 | 56.8 | 6 | 0 % | 0.980 | 1.56 | 659.6 | 1.00 | 0.980 | 1.93 | 820.2 | 1.25 |
| 40.7 % | 100 | 56.8 | 6 | 0 % | 0.980 | 1.59 | 674.6 | 1.03 | 1.000 | 1.99 | 843.2 | 1.28 |
| 54.3 % | 100 | 56.8 | 6 | 0 % | 1.080 | 1.63 | 690.0 | 1.05 | 1.100 | 2.02 | 855.7 | 1.30 |
| 0.0 % | 80 | 35 | 6 | 0 % | 1.510 | 1.79 | 584.4 | 1.32 | 1.350 | 2.07 | 672.9 | 1.52 |
| 7.4 % | 80 | 35 | 6 | 0 % | 1.350 | 1.84 | 599.5 | 1.24 | 1.260 | 2.25 | 733.9 | 1.52 |
| 12.6 % | 80 | 35 | 6 | 0 % | 1.250 | 1.85 | 603.2 | 1.17 | 1.240 | 2.37 | 771.4 | 1.50 |
| 14.8 % | 80 | 35 | 6 | 0 % | 1.210 | 1.86 | 606.3 | 1.15 | 1.210 | 2.44 | 796.4 | 1.51 |
| 22.3 % | 80 | 35 | 6 | 0 % | 1.120 | 1.88 | 611.9 | 1.10 | 1.130 | 2.36 | 767.2 | 1.38 |
| 29.7 % | 80 | 35 | 6 | 0 % | 1.100 | 1.92 | 625 | 1.12 | 1.110 | 2.38 | 774.7 | 1.39 |
| 44.4 % | 80 | 35 | 6 | 0 % | 1.130 | 1.98 | 644.6 | 1.16 | 1.120 | 2.42 | 787.3 | 1.41 |
| 59.2 % | 80 | 35 | 6 | 0 % | 1.350 | 2.04 | 664.9 | 1.19 | 1.340 | 2.51 | 818.1 | 1.47 |
| 0.0 % | 80 | 70 | 6 | 0 % | 1.040 | 1.18 | 768.4 | 1.00 | 0.970 | 1.40 | 912.6 | 1.19 |
| 6.0 % | 80 | 70 | 6 | 0 % | 1.030 | 1.24 | 810.1 | 1.01 | 0.980 | 1.50 | 976.9 | 1.22 |
| 10.1 % | 80 | 70 | 6 | 0 % | 1.040 | 1.30 | 848.3 | 1.03 | 0.970 | 1.55 | 1009.6 | 1.22 |
| 12.0 % | 80 | 70 | 6 | 0 % | 1.050 | 1.33 | 864.7 | 1.03 | 0.990 | 1.58 | 1030.1 | 1.23 |
| 17.9 % | 80 | 70 | 6 | 0 % | 1.070 | 1.40 | 909 | 1.04 | 1.000 | 1.66 | 1079.0 | 1.24 |
| 23.9 % | 80 | 70 | 6 | 0 % | 1.060 | 1.41 | 920.7 | 1.04 | 1.030 | 1.72 | 1119.7 | 1.27 |
| 35.7 % | 80 | 70 | 6 | 0 % | 1.070 | 1.43 | 928.4 | 1.05 | 1.040 | 1.74 | 1131.8 | 1.28 |
| 47.7 % | 80 | 70 | 6 | 0 % | 1.130 | 1.44 | 940.2 | 1.07 | 1.100 | 1.75 | 1140.7 | 1.29 |
| 0.0 % | 80 | 56.8 | 6 | 1 % | 1.080 | 1.57 | 832.4 | 1.19 | 1.050 | 1.92 | 1013.0 | 1.45 |
| 6.0 % | 80 | 56.8 | 6 | 1 % | 1.010 | 1.60 | 843.9 | 1.15 | 1.000 | 1.96 | 1036.9 | 1.41 |
| 10.2 % | 80 | 56.8 | 6 | 1 % | 0.980 | 1.61 | 850.2 | 1.12 | 0.970 | 2.00 | 1055.1 | 1.39 |
| 12.0 % | 80 | 56.8 | 6 | 1 % | 0.960 | 1.61 | 850.2 | 1.10 | 0.950 | 1.99 | 1053.1 | 1.37 |
| 18.0 % | 80 | 56.8 | 6 | 1 % | 0.920 | 1.62 | 857.7 | 1.07 | 0.930 | 2.02 | 1067.9 | 1.33 |
| 24.1 % | 80 | 56.8 | 6 | 1 % | 0.900 | 1.63 | 859.9 | 1.05 | 0.910 | 2.03 | 1072.7 | 1.32 |

Continued on next page

Table F.2 – Continued from previous page

| $P/P_0$ | $D/t$) | $F_{yt}$ (ksi) | $f'_c$ (ksi) | $\rho_{int}$ | a/D = 0.375 | | | | a/D = 0.25 | | | |
|---|---|---|---|---|---|---|---|---|---|---|---|---|
| | | | | | $M_{pr}/M_{PSDM}$ | $V_{pr}/2V_{st}$ | $V_{prmax}$ (kips) | $V_{pr}/V_{n(prop2)}$ | $M_{pr}/M_{PSDM}$ | $V_{pr}/2V_{st}$ | $V_{prmax}$ (kips) | $V_{pr}/V_{n(prop2)}$ |
| 36.0 % | 80 | 56.8 | 6 | 1 % | 0.910 | 1.65 | 874.1 | 1.07 | 0.910 | 2.05 | 1081.6 | 1.33 |
| 48.0 % | 80 | 56.8 | 6 | 1 % | 1.020 | 1.67 | 883.4 | 1.08 | 0.980 | 2.08 | 1098.1 | 1.35 |
| 0.0 % | 80 | 56.8 | 6 | 2 % | 0.990 | 1.75 | 923.5 | 1.230 | 0.980 | 2.15 | 1137.0 | 1.51 |
| 5.6 % | 80 | 56.8 | 6 | 2 % | 0.930 | 1.76 | 930.1 | 1.190 | 0.920 | 2.17 | 1145.0 | 1.46 |
| 9.6 % | 80 | 56.8 | 6 | 2 % | 0.900 | 1.77 | 935.8 | 1.160 | 0.890 | 2.18 | 1150.2 | 1.42 |
| 11.3 % | 80 | 56.8 | 6 | 2 % | 0.880 | 1.77 | 934.0 | 1.140 | 0.880 | 2.18 | 1154.1 | 1.41 |
| 17.0 % | 80 | 56.8 | 6 | 2 % | 0.860 | 1.79 | 943.7 | 1.110 | 0.850 | 2.19 | 1158.9 | 1.36 |
| 22.6 % | 80 | 56.8 | 6 | 2 % | 0.850 | 1.80 | 949.8 | 1.090 | 0.840 | 2.21 | 1166.9 | 1.34 |
| 33.9 % | 80 | 56.8 | 6 | 2 % | 0.850 | 1.81 | 954.4 | 1.100 | 0.840 | 2.23 | 1180.6 | 1.36 |
| 45.2 % | 80 | 56.8 | 6 | 2 % | 0.900 | 1.81 | 958.2 | 1.100 | 0.890 | 2.25 | 1191.5 | 1.37 |